NDOT Research Report

Report No. 593-18-803

Column and Footing Pocket Connections for Cast-in-Place and Precast Construction

June 2021

Nevada Department of Transportation
1263 South Stewart Street
Carson City, NV 89712

Disclaimer

This work was sponsored by the Nevada Department of Transportation. The contents of this report reflect the views of the authors, who are responsible for the facts and the accuracy of the data presented herein. The contents do not necessarily reflect the official views or policies of the State of Nevada at the time of publication. This report does not constitute a standard, specification, or regulation.

TECHNICAL REPORT DOCUMENTATION PAGE

1. Report No. 593-18-803	2. Government Accession No.	3. Recipient's Catalog No.
4. Title and Subtitle DEVELOPMENT AND SEISMIC EVALUATION OF CAST-IN-PLACE EMULATING ABC POCKET CONNECTIONS AND SMA REINFORCED TWO-WAY HINGES		5. Report Date June 30, 2021 6. Performing Organization Code
7. Author(s) Christian Camarena, M. Saiid Saiidi, and Mohamed Moustafa		8. Performing Organization Report No. CCEER 20-06
9. Performing Organization Name and Address University of Nevada, Reno Reno, NV 89557		10. Work Unit No. 11. Contract or Grant No. P593-18-803
12. Sponsoring Agency Name and Address Nevada Department of Transportation 1263 South Stewart Street Carson City, NV 89712		13. Type of Report and Period Covered Final Report 14. Sponsoring Agency Code
15. Supplementary Notes		

16. Abstract

Accelerated bridge construction (ABC) and may be preferable to conventional cast-in-place (CIP) construction because it can significantly expedite project delivery. The design of precast member connections is critical as the connections must maintain structural integrity and provide for ductile behavior under strong earthquakes. Pocket/socket connections are a type of ABC connection that eliminates the need to thread bars through the column cage which can be time consuming and cause rebar congestion. The primary goal of this study was to evaluate the performance and viability of a CIP column-cap joint that was detailed similar to ABC pocket/socket connections to reduce steel congestion. Another objective of the study was to explore the use of superelastic Copper-Aluminum-Manganese (CAM) shape memory alloy (SMA) bars at two-column base hinges. Superelastic SMA bars are known to have reduced permanent deformation of concrete bridges under seismic loads.

To achieve the primary goal of the study, a CIP emulating ABC pocket connection design was developed and implemented in a 0.33-scale test model. The test model was a two-column bent, wherein one of the column-cap connections utilized the novel CIP pocket connection and the other utilized a traditional ABC pocket connection. Both connections were designed identically according to existing guidelines for ABC pocket connections. Auxiliary transverse cap beam reinforcement was placed around the connections to reduce joints stresses and address prying forces. The secondary objective of the study was achieved by implementing two-way hinges reinforced with CAM bars at the base of both columns. The test specimen was instrumented with strain gauges, displacement transducers, accelerometers, and cameras to measure local and global responses. The experimental study involved shake table testing of the test bent subjected to multiple runs of simulated, scaled versions of the 1940 Imperial Valley El Centro record. The bent reached a drift ratio of 11.2 percent, yet the connections were effective in forming the plastic hinge in the columns while the joints remained damage-free. Capacity-protected behavior was also observed in the cap beam for both connections as the cap beam reinforcement around the connection remained elastic. The CAM reinforced two-way hinges maintained the integrity of the column bases with substantial yielding and energy dissipation. Post-test analytical studies of the bent were conducted by using actual material properties and shake table motions. Comparison of the calculated and measured results showed that a relatively routine OpenSees model can be used to obtain an approximate response for moderate and strong earthquakes of up to approximately twice the design earthquake. Finally, the design of CIP pocket connections emulating ABC was evaluated in light of the measured seismic performance of the bent.

17. Key Words	18. Distribution Statement
ABC, accelerated bridge construction, seismic loading, pocket connections, cast-in-place concrete, Copper-Aluminum-Manganese alloy, shape memory alloy	No restrictions. This document is available through the: National Technical Information Service Springfield, VA 22161

19. Security Classif. (of this report)	20. Security Classif. (of this page)	21. No. of Pages	22. Price
Unclassified	Unclassified		

Report No. CCEER 20-06

DEVELOPMENT AND SEISMIC EVALUATION OF CAST-IN-PLACE EMULATING ABC POCKET CONNECTIONS AND SMA REINFORCED TWO-WAY COLUMN HINGES

Christian Camarena
M. Saiid Saiidi
and
Mohamed Moustafa

Nevada Department of Transportation and the Federal Highway Administration, Contract number P593-18-80

Center for Civil Engineering Earthquake Research

University of Nevada, Reno
Department of Civil and Environmental Engineering, MS 258
1664 N. Virginia St.
Reno, NV 89557

August 2020

Abstract

Utilization of precast members in bridge construction is also known as accelerated bridge construction (ABC) and may be preferable to conventional cast-in-place (CIP) method because it can significantly expedite project delivery. The design of precast member connections is critical as they must maintain structural integrity and have ductile behavior in regions of moderate and high seismic activity. Among different connections for ABC, pocket/socket connections are preferred because they allow precast members to be inserted into adjacent members uninhibited eliminating the need to thread bars through the column cage, which can be time consuming and cause congestion. The primary goal of this study was to evaluate the performance and viability of a CIP column-cap joint that was designed using existing ABC pocket/socket connection design guidelines. Depending on the performance of the connection, this alternative connection may be used to simplify and expedite CIP construction as well.

Another objective of the study was to determine the seismic performance of a new generation of shape memory alloy (SMA) bars. Bridge designers may be inclined to use SMA bars within critical regions of a column to reduce residual drifts due to the superelastic characteristic of SMA. Reducing the residual drifts of structures may minimize damage and allow structures to remain in service after seismic events. Due to the significantly higher costs of SMA bars relative to traditional steel bars, SMAs have only been implemented in critical regions of bridge columns in past studies. Recent research has shown that post-earthquake serviceability is significantly enhanced when SMA is combined with ductile types of concrete in plastic hinges. As a secondary objective of this study, the performance and viability of two-way hinges reinforced with Copper-Aluminum-Manganese (CAM) shape memory alloy (SMA) bars coupled to traditional rebar using headed rebar couplers was evaluated.

To achieve the primary goal of the study, a CIP emulating ABC pocket connection design was developed and implemented in a 0.33-scale test model. The test model was a two-column bent, wherein one of the column-cap connections utilized the novel CIP pocket connection and the other utilized a traditional ABC pocket connection. Both connections were designed identically according to existing guidelines for ABC pocket connections. Auxiliary transverse cap beam reinforcement was placed around the connections to reduce joints stresses and address prying forces. The secondary objective of the study was achieved by implementing two-way hinges reinforced with CAM bars at the base of both columns. CAM bars were attached to #4 (Ø13 mm) steel bars at both ends using headed bar couplers and were placed at the two-way hinges at the base of each column. As CAM bars can only be manufactured to limited lengths, are smooth, and are expensive relative to traditional steel bars, they were connected to steel bars using headed bar couplers to ensure sufficient development and anchorage. Before the design of the bent was finalized, a nonlinear analytical model of the bent was created in OpenSees. The response history of the analytical model under various ground motions was analyzed to develop the shake table testing protocol and to ensure the bent could be tested to failure. The test specimen was instrumented with strain gauges, displacement transducers,

accelerometers, and cameras to measure local and global responses. The experimental study involved shake table testing of the test bent. The specimen was subjected to multiple runs of simulated, scaled versions of the 1940 Imperial Valley-02 earthquake event recorded at the El Centro Array #9 Station. The displacement history and peak curvatures of the columns obtained from the experimental study showed the bent reached a drift ratio of 11.2 percent, and the connection was effective in forming the plastic hinge in the column while the joint remained damage-free. The strains and curvatures of the connections and columns were comparable up until the final two runs, where the CIP connection had smaller longitudinal bar strains due to its lower stiffness. Capacity-protected behavior was also observed in the cap beam for both connections as the cap beam reinforcement around the connection remained elastic. The CAM reinforced two-way hinges performed well under seismic loading as they maintained the integrity of the column bases with substantial yielding and energy dissipation. Post-test analytical studies of the bent were conducted by developing a more accurate representation of the bent in OpenSees by using actual material properties and shake table motions. Comparison of the calculated and measured results showed that a relatively routine OpenSees model can be used to obtain an approximate response for moderate and strong earthquakes of up to approximately twice the design earthquake. Finally, the design of CIP pocket connections emulating ABC was evaluated in light of the measured seismic performance of the bent.

Acknowledgements

This study was funded by the Nevada Department of Transportation (NDOT) and the Federal Highway Administration (FWA) through agreement no. P593-18-803. The study was conducted at the University of Nevada, Reno (UNR) with Dr. M. Saiid Saiidi as the PI and Dr. Mohamed Moustafa as the Co-PI.

Special thanks to Mr. Troy Martin, of NDOT, for his involvement and technical contributions throughout this study, and Azin Ghaffary, Taylor Schwartz, and Jared Jones for their assistance with the instrumentation, testing of the specimen, and input.

The experimental portion of this study was made possible with the support of the UNR Earthquake Engineering Laboratory staff members Dr. Patrick Laplace, Mr. Chad Lyttle, and Mr. Todd Lyttle. They were very involved in the larger-scale aspects of the test setup, provided guidance, and made testing possible.

This report is based on a master's thesis by the first author under supervision of the other authors.

Table of Contents

List of Tables

List of Figures

Chapter 1. Introduction

1.1 Background

Accelerated bridge construction (ABC) may be preferable to conventional cast-in-place (CIP) construction because it can significantly expedite the construction process. CIP construction requires onsite formwork, shoring, casting, and curing of concrete, which usually have to be done sequentially and lengthen the construction time. ABC utilizes precast elements and reduces or eliminates the need for some of these processes. Thus, ABC shortens traffic delays and extended route closures. ABC has been adopted in low seismic regions, but high seismic regions have been generally hesitant in embracing ABC techniques. The joints connecting precast elements are particularly of concern for bridge designers as it is critical that they maintain structural integrity and result in ductile performance of columns. Research has been conducted in the past two decades to evaluate the viability of ABC in regions of moderate and high seismic. Various types of ABC connections have been developed to satisfy the seismic performance criteria. Studies conducted by Tazarv and Saiidi [1], Mohebbi et al. [2], and Mehrsoroush et al. [3] have shown that the pocket and socket connection type results in ductile performance of bridge columns while requiring the least amount of construction time. These connections consist of a partially (pocket connections) or fully precast columns (socket connections) inserted into an opening in an adjacent element and securing them together using concrete or high strength grout in socket and pocket connections, respectively.

In contrast to ABC pocket/socket connections, CIP column joints can be more difficult and time-consuming to construct because the longitudinal cap beam reinforcement must be threaded through the column longitudinal reinforcement within the relatively small joint area. Additional joint reinforcement is also required to resist principle stresses that develop in the joint, which can lead to congestion that slows construction. Emulating ABC pocket connections by adapting the design guidelines for ABC pocket/socket connections alleviates the joint reinforcement congestion. Question is raised: Could the design guidelines details for ABC pocket/socket connections be used in CIP joints to simplify the CIP construction process? Research conducted by Schwartz et al. [4] has shown that CIP joints constructed this way results in ductile performance of bridge columns when loaded in the out-of-plane direction of the bent.

ABC present innovation in bridge construction and detailing method. Innovation in bridge engineering could also be realized through the use of advanced materials. Superelastic shape memory alloy (SMA) bars are such materials that could be used to improve the bridge seismic performance. Bridge designers may be inclined to use SMA bars within critical regions of a column to reduce residual drifts after seismic events. This can be attributed to SMAs superelastic properties. Reducing the residual drifts of structures may reduce damage and allow structures to remain in service after seismic events. Research has been conducted to evaluate the viability of implementing SMA bars in critical regions, but the subject is still in its infancy. Various types of SMAs have been developed but most research for structural applications has focused on Nickel-Titanium (Ni-Ti) and Copper-Aluminum-Manganese (CAM) alloy bars. Due to the significantly higher costs of SMA bars relative to traditional rebar, SMA bars have been implemented only in critical regions of bridge columns. Studies conducted by Varela and Saiidi. [5]

and Tazarv and Saiidi [6] have shown that SMAs substantially reduce residual drafts and damage in plastic hinges when combined with ductile types of concrete.

1.2 Literature Review

A literature review of previous investigations of the seismic performance of pocket/socket connections and the performance of SMAs was conducted and summarized in this section.

1.2.1 Pocket Connections

Connections that utilize partially-cast columns are also known as pocket connections according to AASHTO LRFD guide specifications for ABC [7]. Typically, pocket connections will have columns cast up to the section that extends into the joint area and are then cast with the pier cap. Extensive research has been conducted on the performance of pocket connections as they have been the subject of many projects. Restrepo et al. [8] tested two 0.42-scale, beam-column pocket connections between precast pier caps and partially-cast columns. The performance of the connections was evaluated under cyclic loading and compared to a reference CIP column. One connection was designed to provide high ductility and the other low ductility. Stirrups and hoops were included around the joint region of the high ductility connection, and cap beam longitudinal reinforcement was threaded through the column cage as the cap bars were not bundled. The columns of both connections developed plastic hinges but the low ductility connection underwent more damage due shear cracking. It was concluded that corrugated steel pipes could provide joint shear resistance

Mehraein and Saiidi [9] also investigated pocket connections with partially-cast columns and precast cap beams. Two 0.27-scale two-column bents were subjected to seismic loading through shake table tests. Each bent consisted of a precast column and a CIP column. The longitudinal reinforcement of the cap beam was bundled to allow the protruding column cage of the partially-cast column to extend into the pocket uninhibited, after which it was cast with self-consolidating concrete (SCC). A spiral was placed around the lower one-third of the pocket depth to ensure proper confinement. Both the precast and CIP columns formed plastic hinges and had similar performances. As the cap beams are capacity protected members, they are designed based on the column overstrength moment. The tests rendered the connections effective and the cap beams remained elastic and no damage was observed.

1.2.2 Socket Connections

According AASHTO LRFD guide specifications for ABC [7], connections that utilize fully precast columns are also known as socket connections. Fully precast columns are precast for the entirety of the column cage length which means the portion that extends into the joint is also precast. Socket connections have been the subject of many research projects and further accelerates construction speed as there is no threading of cap beam longitudinal bars through the column cage. Design guidelines for column-cap socket connections were developed by Tazarv and Saiidi [1] after extensive review of previous projects. The design guidelines propose that all bridge components be analyzed according to the AASHTO LRFD (2013) or AASHTO Guide Specifications (2014). Equations to determine the minimum pocket were also proposed to ensure the socket

connection can develop the full plastic moment in the column and the depth is to be no less than the largest column dimension. Additional transverse reinforcement with same volumetric ratio of column transverse reinforcement is to be placed on the lower half of the cap beam. The use of bundled bars in the cap beam to allow fully precast columns to enter the socket are to be continuous over the bent length. A more recent document presents specific proposed AASHTO seismic guidelines for design of ABC column connections [8]. The guidelines provide specific connection detailing recommendations for different earthquake-resistant column connections.

Mohebbi et al. [2] also conducted research on the performance of fully precast column-cap connections to further develop design guidelines for square column-cap beam pocket connections and pocket connections using advanced materials. The performance of 0.33-scale single-column model and a two-column bent model was evaluated when subjected to seismic loading on a shake table. The single-column model used a socket connection between the column and the footing, while the two-column bent model used socket connections between the columns and the precast footing and cap beam. The damage in both models was concentrated in the columns, and the connections were relatively undamaged. Mohebbi et al. [2] recommend that diagonal bars be used in socket connections of square columns to alleviate cracking due to stress concentration at the corners of the openings. Additional transverse reinforcement was placed around the cap beam openings, but it was concluded that this reinforcement was unnecessary, and the column transverse reinforcement provided sufficient confinement. Longitudinal cap beam reinforcement outside the connection was also recommended to reduce temperature and shrinkage cracks.

A 0.33-scale two-column bent model was tested on a shake table and evaluated by Mehrsoroush et al. [3]. The model consisted of two precast columns, a precast cap, and a precast footing to which the columns were connected to using socket connections. The main difference between the two columns consisted of the rebar hinge connection of one column and a novel pipe-pin connection of the other. Both the rebar hinge and the pipe-pin connection provide partial moment transfer and were located at the column-cap pocket connections. The footing socket connections utilized full moment connections. The pipe-pin connection performed well and remained undamaged, while the rebar hinge failed during latter runs similarly to CIP hinges. The cap beam remained elastic demonstrating that both connections were effective in transferring moment. The footing connections maintained structural integrity throughout testing even under large drift ratios.

1.2.3 Copper-Aluminum-Manganese Shape Memory Alloys

Copper-Aluminum-Manganese alloy (CAM) bars are relatively new subject of interest due to their potential use in earthquake-resistant structures. CAM bars are one of the few shape memory alloys (SMA) that have superelastic properties. That is to say that they can recover large deformations, a feature that can reduce residual drifts of structures, thus allowing the bridge to remain in use. Although other SMAs exist, CAM is of particular interest due to its relatively low cost and ease of machining. Despite being cost effective relative to other SMAs, CAM is still more costly than traditional reinforcement and has been manufactured to limited lengths as of this writing. Thus, CAM bars have to

be connected to steel bars utilizing mechanical couplers to provide anchorage to concrete outside plastic hinges of columns.

Varela and Saiidi. [5] evaluated the performance of a 0.25-scale single-column model with a plastic hinge reinforced with Engineered Cementitious Composite (ECC) and CAM bars. The model was subjected to one of the 1994 Northridge ground motions at various design levels on a shake table. The CAM bars served as the longitudinal reinforcement of the column in the plastic hinge region and were coupled to mild steel that served as the remaining longitudinal reinforcement using threaded rod coupling nuts. Samples of the CAM bars were also tested to obtain CAM material properties to be used in analytical modeling. The model exhibited a high self-centering ability even when exposed to large drift ratios. It was concluded that ECC and CAM bar use in the plastic hinge region of columns is a feasible alternative for reducing permanent displacements and damage under strong earthquakes.

Mohebbi et al. [10] conducted research to evaluate the performance of CAM bars spliced to steel reinforcement using headed bar couplers. The performance of two large diameter (1.18 in, Ø15 mm) and two small diameter (0.5 in, Ø13 mm) CAM bars was investigated. The bars were tested utilizing a hydraulic load frame and subjected to either static monotonic or static cyclic loading. Superelastic behavior was observed in both large and small diameter CAM bars. The rupture strain of the large bars was significantly lower than the small bars, but this may have been due to difficulties in the heading process of large diameter bars. It was concluded that while large diameter bars are feasible for use in structural applications, the manufacturing process of large diameter CAM and the heading process of large diameter CAM still needs refining.

1.2.4 Shape Memory Alloys with Headed Bar Couplers

As SMA bars are costly and typically only implemented in critical regions such as the plastic hinges of columns, mechanical splices are used to provide continuity with remaining column longitudinal reinforcement. Although various mechanical splices exist, SMA bars are preferred to be spliced using headed bar couplers because no machining is involved, and the full diameter of the bars are utilized. The recently published proposed AASHTO guidelines for design of ABC column connections [8] provide specific guidelines for coupler design in moderate and high seismic zones. The guidelines show that the displacement ductility of columns utilizing headed bar couplers is higher than that of columns with other types of couplers.

As mentioned previously, research conducted by Mohebbi et al. [10] focused on the performance of CAM bars coupled using headed bar couplers. The bar couplers worked well with the small diameter bars but not the large diameter bars. The process of heading large diameter CAM bars can result in inconsistencies and must be refined for practical use in structural applications.

Tazarv and Saiidi [6] evaluate the performance of several 0.5-scale single column models under seismic loading; one of which incorporated Ni-Ti SMA bars and ECC in the plastic hinge region of the column. The Ni-Ti bars were spliced to the longitudinal reinforcement using headed bar couplers. The plastic hinge damage of this model was substantially lower than the others. Additionally, the model performed well under seismic loading, and its residual displacements were 79% lower than the CIP reference model. The report also developed recommendations for implementation of SMA bars for use in

structural applications. No damage of the headed bar couplers was observed. It was recommended that SMA bars only be used in critical regions such as the plastic hinge of a column for economic reasons and the preferred mechanical splices are headed bar couplers.

A study conducted by Nakashoji and Saiidi [11] evaluated the performance of two CIP Ni-Ti reinforced ECC single-column models under cyclic loading. The Ni-Ti bars of the two models were spliced to mild steel using headed bar couplers and the length of the Ni-Ti bars varied between the two models. An additional CIP model was created for reference. The residual displacements of both SMA models were significantly lower than the reference model, demonstrating the self-centering ability of Ni-Ti bars and ECC. Both columns also demonstrated larger displacement capacities than the reference model indicating the headed bar couplers allow the columns to develop the full plastic moment. The results of that research led to field deployment of 1.25 in (30 mm) Ni-Ti bars with headed bar couplers in the SR-99 off-ramp bridge in downtown, Seattle, Washington [12].

1.3 Objective and Scope

The main objectives of this study were to: (1) develop and compare the performance of a CIP emulating ABC pocket connection to an ordinary ABC socket connection when subjected to in-plane seismic loading, (2) refine design recommendations as necessary based on the results of shake table testing, and (3) determine the seismic performance of CAM bars when coupled with mild steel using headed rebar couplers in two-way concrete hinges.

To achieve the first objective, existing design guidelines for ABC pocket connections were adopted to develop a CIP joint that emulates ABC pocket connections. Transverse hoops were added to provide confinement, and cap beam longitudinal reinforcement was bundled to avoid threading through the column cage of the CIP column and the corrugated metal pipe (CMP) of the ABC column. Additional reinforcement around the joint, not typical to the design of CIP joints or ABC pocket connections, were included to address prying forces. A near identical ABC pocket connection was included in the test model to compare the performance of the two connections. A two-column bent which included a cap beam, two columns, and a footing was constructed. The two columns differed in the construction of their connection to the cap beam. The CIP column was cast up to the column-cap interface above which the column cage that extended into the cap-beam was cast with the cap-beam. The ABC column was fully cast and then grouted to a CMP before the cap-beam was cast. The longitudinal reinforcement ratio of the columns was increased from the prototype to place a relatively high demand on the connections. This study focused on the in-plane performance of the connections under seismic loading. A parallel study focused on the out-of-plane response of ABC-emulating CIP cap-column joints.

The specimen was instrumented with strain gauges, displacement transducers, and accelerometers to evaluate and compare the performances of the connections. As the cap beam is a capacity-protected member, it was essential that the strains of joint reinforcement and the longitudinal column bars were measured. These strains were used to determine if plastic hinges were developed in the columns. Measuring displacement of the specimen was necessary to ensure the specimen was tested to large drift ratios and

adequate demand was placed on the connections. The displacement histories measured by these instruments was also used to develop an analytical model capable of capturing the global response of the system.

The second objective required that the performance of joint reinforcement be evaluated to determine if the design of the CIP pocket connection was adequate. The strains of the reinforcement surrounding the joints were monitored to determine to what extent they were necessary for in-plane loading. These strains were also used to evaluate the effectiveness of the connection to concentrate ductility in the plastic hinges of the columns. Design recommendations for CIP pocket connections were discussed based on the connection performance.

To achieve the third objective, existing guidelines for the design of two-way hinges using steel reinforcement were adapted to develop a two-way hinge that utilizes CAM longitudinal reinforcement. The two-way hinges of the columns were instrumented with strain gauges and displacement transducers to determine the effectiveness of CAM bars in maintaining hinge integrity and the hinge seismic performance when coupled with mild steel using headed rebar couplers. The strains along the CAM bars were evaluated to ensure that the moments transferred to the footing were reduced and that the HRC couplers provided continuity between the CAM bars and the mild steel.

1.4 Thesis Outline

This report is organized into seven chapters. Chapter 1 provides an introduction, problem statement and the objectives of this research. Additionally, a literature review on pocket connections, socket connections, CAM SMA, and the use of SMA with headed bar couplers was conducted. Chapter 2 presents the design and construction process of the test specimen. The pre-test analytical studies are presented in Chapter 3. Chapter 4 describes the instrumentation and test setup of the experimental study. The measured results from testing are reported and analyzed in Chapter 5. Chapter 6 presents further analytical studies and discussion of design recommendations. Finally, Chapter 7 provides a summary, observations, and conclusions of the study.

Chapter 2. Specimen Description

2.1 Overview

A large-scale two-column bent model was constructed and tested to assess the viability of designing and constructing an ABC column-to-cap beam pocket connection detail for use in CIP bridge construction. The test served the secondary purpose of evaluating the viability of using superelastic CAM SMA bars in place of traditional rebar at the column-to-footing two-way hinge connection to reduce moment transfer to the footing. The in-plane seismic performance of different connections was the primary focus of the study. The study permitted the specimen to utilize a traditional two-column bent configuration. This chapter describes the configuration, design, and construction of the test specimen.

2.2 Specimen Configuration

The specimen was of 1/3rd geometric scale consisting of two columns, a cap beam, and a footing. The bent was designed and built for in-plane shake table testing under axial load. Figure 2.1 shows elevation of the specimen. The specimen was configured in a traditional two-column bent configuration, with one column being CIP and the other being partially precast (Fig. 2.1). When positioned on the shake table, the former column was on the north and latter was on the south of the model. The orientation of the bent columns was selected arbitrarily. A footing was designed to support the columns and attach the test specimen to the shake table. Under in-plane shaking, the bent deformed in double curvature, as the cap beam behaved essentially as a rigid member because of its relatively large stiffness, and the column-to-cap pocket connections were designed to behave as rigid connections to fully transfer moments.

2.2.1 Prototype Bridge

A significant part of the design of the specimen was based on a prototype bridge developed by Nevada Department of Transportation (NDOT) bridge engineers. The prototype represents an existing bridge located in Carson City, Nevada at the intersection of U.S. Route 395 and Clearview Drive. The location of this bridge would later be utilized in determining the seismic design response spectrum of the specimen, for which the selected ground motion would be scaled. The prototype bridge is a concrete box-girder bridge with an integral bent cap. Figure 2.2 shows a cross-section of the prototype bridge. A 1/3rd geometric scale of the prototype bridge was used to design the columns and cap beam of the specimen and select the column spacing. The longitudinal and transverse reinforcement ratios of the prototype bridge were used in the initial iterations of the specimen design.

Dead loads of the prototype bridge, which consisted of the box girder self-weight and the railings, were estimated. The ratio of the dead load to the product of the cross-sectional area of the columns and the compressive strength of concrete was obtain and referred to as axial load index (ALI). The compressive force due to the dead loads was 67.3 kips (300 kN) and resulted in an ALI of 8.3 percent. Typical ALI in concrete bridge columns range from 5 to 10 percent.

2.3 Design

2.3.1 Dimensions

2.3.1.1 Columns

The specimen was primarily a 1/3rd scale model of the pier and the associated superstructure of the prototype bridge. Elevation views with the dimensions of the specimen are shown in Fig. 2.1 and Fig. 2.3. The columns had a clear height of 80 in (2038 mm) and a 16-in (406 mm) diameter circular-cross section, i.e. exact 1:3 ratio to the 240-in (6096 mm) clear height and 48-in (1219 mm) diameter columns of the prototype bridge.

2.3.1.2 Hinges

The diameter of the circular two-way hinges located at the bottom of the specimen columns was 10 in (254 mm), which was one-third of the 30-in (762 mm) diameter two-way hinges in the prototype bridge. The hinge thickness was designed in accordance with the recommendations of Cheng et al to ensure that the rotation of the column would not result in the edge of the column base bearing on the footing [13]. Spacing of the columns was intended to be 72 in (1829 mm), a 1/3rd scale of the prototype column spacing, but an error during construction of the specimen resulted in a spacing of 78 in (1981 mm). A closeup of the elevation of one of the hinges is shown in Fig. 2.4 with an arrow pointing to the hinge throat.

2.3.1.3 Cap Beam

The cross section of the cap beam was I-shaped with flanges representing portions of the top and bottom superstructure slabs. An I-shaped cross-section is a better representative of an integral cap than the typical rectangular cross-section used in most studies. Bridge superstructures typically consist of thicker top flanges, i.e. deck slab, for the cap beam cross-section than the lower flange, i.e. soffit slab. However, the thicknesses of the top and bottom flanges in the model were the same to simplify the construction process. The depth of the cross-section was 18 inches (457 mm), which conformed to a 1:3 ratio with the 54-in (1372 mm) integral cap of the prototype bridge. The flanges of the cross-section were 3 in (76 mm) thick, which slightly exceeded the 1:3 ratio with the thickness of the prototype bridge top deck slab to ensure sufficient cover concrete was provided for the flange reinforcement.

2.3.1.4 Footing

The footing in the specimen was not designed to represent the prototype, but rather provide support for the rest of the bent. The footing reinforcement and dimensions were designed to avoid footing damages and provide the necessary height to connect the specimen to the mass rig (a part of the shake table testing system described in subsequent chapters). The width of the footing was selected to allow anchoring of the footing to the shake table with sufficient friction resistance at the base to avoid slippage during shake table testing. Because of the anchorage to the shake table, the load path within the footing is substantially different than that of real footings. The footing reinforcement was designed to avoid flexural and shear failure with a relatively large factor of safety.

Figure 2.5 shows the plan of the specimen on the shake table and the tie down locations. The red holes in the figure represent the unused strong tie-down points of the table, the blue holes represent the strong-tie down points that were engaged, and black holes represent the weak-tie down points that were not used. Strong tie-down points have a maximum clamping force of 30 kips (133 kN) and weak tie-down points have maximum clamping force of 10 kips (44 kN). The tie downs are capable of handling approximately 20 percent of their clamping force as shear force. The expected plastic shear of the bent controlled the number of tie-down points to engage. The shear was estimated by conducting a pushover analysis of the pre-test analytical model.

2.3.2 Reinforcement Details

2.3.2.1 Columns

Table 2.1 summarizes the reinforcement design of the columns and Fig. 2.6 shows the column cross-section. Initially, the column was designed to have an equal longitudinal reinforcement ratio to that of the columns in the prototype bridge bent. The longitudinal reinforcement ratio of the prototype bridge was 1.1 percent but was increased to 1.59 percent in the specimen to increase the shear and moment demands of the column-to-cap connections. An increase in the shear and moment demands allows performance of the connections to be evaluated under a more critical condition. The target column reinforcement ratio of 1.59 percent was achieved by using 16-#4 (Ø13 mm) bars. Larger bar sizes were considered but were dismissed as changing the proposed design resulted in a substantial reduction of the number of the bars. The number of longitudinal bars need to be sufficiently large to produce the cage effect that is similar to that of the prototype. The transverse reinforcement of the column was designed similarly. The transverse reinforcement ratio of the prototype bridge columns was 0.7 percent and was increased to 1.3 percent for the specimen columns. The relatively large transverse steel ratio increased the column ductility capacity, and in turn, allowed to test the model under larger lateral displacement demands without failing the columns. The final reinforcement design of the specimen columns consisted of 16-#4 (Ø13 mm) longitudinal bars and a #3 (Ø9.5 mm) spiral at a pitch of 2.25 in (57 mm).

2.3.2.1.1 Moment-Curvature Analysis of Columns.

For the cap beam to behave as a capacity-protected member (meaning essentially elastic behavior), the flexural capacity of the cap beam had to be at least 20 percent larger than the column moment capacity [14]. A moment-curvature analysis of the column cross-section was conducted to determine the plastic moment of the column in both SAP2000 [15] and OpenSees [16] to ensure an accurate analysis was conducted, although one analysis would be sufficient. The analysis of the cross-section included a 67.3 kip (300 kN) compressive axial load on the column to represent the gravity load effect. Table 2.2 shows the results of the analysis from the two programs. The analyses provided very similar yield and plastic moments, therefore the results were assumed to be accurate. The results of the moment curvature-analysis and the idealized curve are shown in Figure 2.7. Using the plastic moment obtained from this analysis, an overstrength moment (calculated by increasing the column plastic moment obtained from the idealized curve by 1.2) was calculated and used for the design of the capacity protected cap beam.

2.3.2.2 Two-Way Hinges

Reinforcement design of the two-way hinges followed the design of the column. Fig. 2.8 shows the hinge cross-section. The two-way hinges placed at the bottom of the columns are unique in that they were longitudinally reinforced with superelastic Copper-Aluminum-Manganese (CAM) shape memory alloy (SMA) bars in place of traditional steel bars. CAM bars were only used for the longitudinal reinforcement, and the hinges were confined with a mild steel spiral. The CAM bars were provided by Furukawa Techno Material Co., Ltd. of Japan. CAM bars are superelastic and are desirable for reducing permanent drift under seismic loads. Nonetheless, they were used in the present study to determine their effectiveness in reducing hinge moment and their seismic performance when coupled with mild steel using HRC. The prototype bridge hinge reinforcement ratio was 1.36 percent but did not utilize CAM bars. Since the prototype bridge was not reinforced with CAM bars, an appropriate amount of longitudinal reinforcement was determined to be six 0.59-in (Ø15 mm) CAM bars. The number of CAM bars in the hinges was selected according to the ACI minimum requirement of six longitudinal bars for circular cross sections [17]. The shear capacity of the proposed section was then compared to the expected shear demand. It was found that the shear demand over capacity was 0.7, which provided a large margin against hinge shear failure. The calculated longitudinal reinforcement ratio of the two-way hinges was 2.6 percent. Reinforcement ratios of the specimen hinges and the prototype bridge hinges cannot be equated as they consist of different materials.

CAM bars are smooth with no ribs and very small bond strength if embedded in concrete without another mechanism for anchorage. However, because CAM bars are only needed in critical part of the hinge (in this case the hinge throat area), relatively short CAM bars were used to cover the hinge throat region. The CAM bars were headed and coupled to allow for HRC connection to the #4 (Ø13 mm) steel bars, which provided sufficient development length and reduced the effects of bond-slip. Figure 2.9 shows an image of the CAM bars and the HRC connection to the #4 (Ø13 mm) rebar.

Number 3 (Ø9.5 mm) spirals were used as smaller bars were not available. The transverse reinforcement ratio of the prototype was 1.36 percent. This reinforcement ratio was considered in initial designs of the hinges but resulted in a relatively large pitch of 4 in (102 mm). The pitch of the spiral was reduced to 2 in (51.mm) to prevent buckling of the longitudinal bars and resulted in a transverse reinforcement ratio of 2.6 percent.

2.3.2.2.1 Moment-Curvature Analysis of Hinge.

Similar to the column cross-section, a moment-curvature analysis of the hinge cross section was conducted to determine its plastic moment capacity. The moment-curvature analysis of the hinge was only conducted in OpenSees as SAP2000 does not have the required options to accurately define the material properties of the CAM bars in the hinges. Table 2.3 shows the results of the analysis. The analysis of the cross section included a 67.3 kip (300 kN) axial load, which is the same as that used in the column analysis. Figure 2.10 shows the result of the moment-curvature analysis and the idealized curve. The ratio of the hinge plastic moment and the column plastic moment was 0.22. Note the substantially lower moment capacity of the hinges relative to the main columns. This allows the hinges to essentially behave as partial pins and significantly lowers the

moment transferred to the footing. Multiplying the plastic moment from the moment-curvature analysis by a factor of 1.2 provided the overstrength moment used to design the test specimen footing. It is noted that because the footing in the specimen was not modeled to represent the prototype footing, its flexural capacity was substantially higher.

2.3.2.3 Cap Beam

The cap beam was designed for both shear and flexure as a capacity-protected member with a minimum positive and negative moment capacity equal to that of the overstrength moment of the column section. Figure 2.11 shows a typical cross-section of the cap beam outside of the column-to-cap pocket joint. The cap beam was reinforced with 10-#5 (Ø16 mm) bars in both the top and bottom portions of the cap beam to resist positive and negative moments. The configuration of the top and bottom longitudinal reinforcement of the cap beam differs in that some of the bottom reinforcement was bundled to leave space for a pocket. This configuration of the bottom reinforcement accommodates the extended column reinforcement (for CIP column) and the socket formed by corrugated metal pipe (CMP) (for ABC column) in the cap beam joint. Two #3 (Ø9.5 mm) longitudinal bars were added to the bottom portion of the cap beam cross-section outside of the joint region to resist shrinkage and temperature cracking. Figure 2.12 shows the cross-section of the cap beam with the columns extending into pocket.

Recall that the ABC column was fully precast but the CIP column was precast up to the bottom of the cap beam (as indicated by the dash line in the figure) with the remaining part of the column cage extending into a “pocket” in the cap beam. The reinforcement in the top portion of the cap beam was distributed across the width of the I-shaped cross section. Additional longitudinal reinforcement was placed within the web of the I-shaped cross section for torsion of a similar previously tested specimen [4]. Although no torsion of the cap beam was expected in the present study because the specimen was loaded in the in-plane direction, the reinforcement was unchanged for consistency. The transverse reinforcement required to accommodate shear was a #3 (Ø9.5 mm) stirrup at 4-in (102 mm) spacing. Additional transverse reinforcement that was placed within the web of the I-shaped cross section of a previously tested specimen [4] was also used in the present specimen for consistency. A transverse straight #3 (Ø9.5 mm) bar was added in both the top and bottom portions of the cap beam to support the longitudinal bars of the flanges. Figures 2.13 through 2.16 show different cross-section reinforcement layouts throughout the cap beam and their locations.

2.3.2.3.1 Pocket Connections

In traditional CIP connections, the reinforcement of the cap beam intersects with that of the column reinforcement cage, causing congestion and longer construction time. In ABC connections, reinforcement within the pocket is arranged in a way that permits a precast column to extend into another precast member without running into reinforcement. The remaining space in the joint is filled with either grout (in socket connections) or concrete (in pocket connections). Thus, reducing steel congestion, eliminating intersecting bars, and expediting construction. The idea of reducing steel congestion and expediting construction through ABC connections was adopted and implemented into a CIP column in the present study for performance assessment. The CIP column to cap joint of the specimen utilized reinforcement detailing of a pocket

connection to eliminate the need for intersecting bars without using a precast member. The ABC column to cap joint of the specimen consists of the same detailing as the CIP column to cap joint but was grouted to an 18 in (457 mm) diameter CMP

Figure 2.17 shows the reinforcement detailing of the pocket connections. To form the pocket connection, the transverse reinforcement of the cap beam was adjusted. The #3 (Ø9.5 mm) horizontal ties, vertical ties, and straight bars at the bottom of the cap beam were removed within the joint. Two additional #3 (Ø9.5 mm) horizontal ties were placed adjacent to the pockets on each side of the columns to accommodate potential prying. Five #3 (Ø9.5 mm) hoops, vertically spaced at 1.5 in (38 mm), were placed in the lower half of the joint and a single #3 (Ø9.5 mm) hoop was centered at the upper half of the joint to ensure the pockets were properly confined. The location of the hoops is shown in Fig. 2.13 and Fig. 2.15. An elevation of the cap beam transverse reinforcement layout is shown in Fig. 2.18.

The protruded portion of the column cage of the CIP column and the upper portion of the ABC column extended 15 in (381 mm) into the cap beam to ensure that the column longitudinal bars in both columns were sufficiently developed. The spacing between the column cage and the cap beam reinforcement was not determined by any design recommendations, but empirically selected to allow concrete to flow between reinforcement. Figure 2.12 shows the CIP and ABC columns within the pocket.

2.3.2.3.2 Additional Column-Cap Connection Configurations Considered

The first proposed column-cap connection configuration was two CIP columns. One column would be a traditionally constructed CIP column that had intersecting bars, while the other column would be the CIP column with no intersecting bars as was selected. To obtain this configuration, some of the bottom longitudinal bars of the cap beam would have to bent at an angle to transition from unbundled at one column to unbundled at the other. The final selection of an ABC column and a CIP column that emulates ABC was based on ease of construction in addition to the columns being directly comparable with nearly identical joint detailing.

2.3.2.4 Footing

As indicated before, the footing in the specimen was designed to be strong and rigid to avoid any footing damage and deformation. Figure 2.19 shows a typical cross-section of the footing. The footing was reinforced with 10-#4 (Ø13 mm) longitudinal U bars in both the top and bottom resist positive and negative moments. The configuration of the top and bottom longitudinal reinforcement differed in that the top reinforcement consisted of more closely spaced bars and a gap that allowed for the placement of the hinge reinforcement cage. Although this was similar to the cap beam to column joint, this reinforcement layout was selected as the hinge reinforcement cage was too congested to have intersecting bars. Figure 2.20 shows a cross-section of the footing with the hinge reinforcement cage extending into the footing. Two #3 (Ø9.5 mm) transverse U bars at 8-in (203 mm) spacing were added to the top and bottom portions of the footing cross-section to support the longitudinal bars and provide confinement. The transverse reinforcement required to accommodate shear was 2-#3 (Ø9.5 mm) vertical cross ties at 8-in (203 mm) spacing and were only placed outside of the joint. To ensure the footing remained undamaged during testing, the transverse reinforcement was spaced 4 inches

adjacent to the joint. Figures 2.21 through 2.27 show an elevation and plan view of the locations of the different cross sections along the footing.

2.4 Construction

The specimen was constructed at the University of Nevada, Reno fabrication yard outside the Earthquake Engineering Laboratory (EEL) from July 2019 to August 2019. Grade 60 A706 Steel was used for all reinforcement. The first member to be constructed was the footing. Forms for the footing were built and the reinforcement for the footing was tied within the forms. After the footing reinforcement was completed, the hinge reinforcement cage was constructed and placed within the footing reinforcement. Figures 2.28 and 2.29 show the footing reinforcement as well as the hinge reinforcement cage. Note that the footing reinforcement had an opening in which the hinge reinforcement cage could enter uninhibited. The clearance between the footing reinforcement and the hinge reinforcement cage was minimal (Fig. 2.30). Figure 2.31 shows the CAM bars connected to #4 (Ø13 mm) bars using HRC couplers and the spirals. The cardboard tube in the photo is to form the hinge throat. Note that the HRC couplers were larger in diameter than the #4 (Ø13 mm) rebar as and the 0.59-in (Ø15 mm) CAM bars. This resulted in a slight gap between the CAM bar and the spiral, which could have caused the bars to prematurely buckle. This was alleviated by placing high strength steel nuts in the gap (Fig. 2.32).

Lifting anchors were attached to the footing forms at specific locations to allow the specimen to be lifted with a forklift and placed into the lab for testing. Twenty 1.5-in (38mm) nominal diameter PVC pipes were placed in the footing to allow the specimen to be anchored to the shake table. Ten pipes were used to fit the anchors used to attach the specimen to the shake table, and ten pipes to pass the rods that applied vertical loading. Figure 2.33 shows the placement of the pipes and Fig. 2.34 shows a photo of the pipes within the footing. After all components of the footing and the two-way hinges were in place, concrete with a specified strength of 4,500 psi (31 MPa) was poured into the footing and the 2-in (51 mm) thick hinge throats. The concrete was then consolidated with a concrete stinger vibrator. After the concrete was poured and consolidated, the exposed surfaces of the concrete were smoothed and finished. Figures 2.35 through 2.38 show the process of pouring, consolidating, and finishing of the footing.

After two weeks of curing, the wooden forms were stripped, and the construction of the columns began. Small wooden platforms the height of the hinge gap were placed at the bases of the columns. The platforms were used to elevate the Sonotube that would form the main columns. An image of a platform can be seen in Fig. 2.39. Once the platforms were built, the column reinforcement cages were tied and erected with the Sonotube. Figures 2.40 and 2.41 show the reinforcement of a column and the erected columns, respectively. Note that one Sonotube extended to the top of the column cage (ABC), while the other did not (CIP). Once the columns were correctly positioned, concrete with a specified strength of 4,500 psi (31 MPa) was poured and consolidated within the Sonotube. These processes are shown in Fig. 2.42.

The Sonotube was stripped from the columns after two weeks of curing, and the wooden platforms on which the columns rested were also removed. Figure 2.43 shows the stripped columns. The two-way hinge gaps can be seen at the base of the columns.

The final stage of construction was that of the cap beam. Initially, only the base of the wooden form was built for ease of access to the cap beam reinforcement. After the base of the form was placed, an 18-in (457 mm) diameter CMP was installed and the gap between the ABC column and CMP was filled with non-shrink, high-strength grout.

Typically, in ABC construction, precast columns are grouted to a precast cap beam. Since the specimen did not consist of a precast cap beam, the CMP was grouted to the ABC column before casting of the rest of the cap beam. The grouted CMP can be seen in Fig. 2.44. Once the CMP was grouted to the ABC column, the bottom portion of the cap beam reinforcement was placed. After tying the bottom cap beam reinforcement, the middle cage of the cap beam was constructed and tied to the bottom portion of the cap beam reinforcement (Fig 2.45). Figures 2.46 and 2.47 show the CIP column cage extending into the cap beam and the CMP, respectively. The CIP column cage was placed inside the cap beam without being inhibited by the cap beam reinforcement, effectively forming a pocket connection. Once this was completed, the remaining formwork and reinforcement for the cap beam was placed. Ten 1.5-in (38mm) nominal diameter PVC pipes were placed through the cap beam flanges to allow vertical load rods to pass through the specimen and load the cap beam. These PVC pipes were positioned identically to the footing pipes to allow the vertical load rods to pass through the entire specimen. Figures 2.48 and 2.49 show the completed cap beam formwork, cap beam reinforcement, and PVC pipes.

Finally, five groups of four 0.75-in (19 mm) diameter threaded rods were positioned on the cap beam. These rods were used to connect a load transfer steel beam to the top of the bent, which allowed the specimen to be attached to a mass rig through a rigid link, which is discussed in subsequent chapters. Figures 2.49 and 2.50 show a group of the rods as well as their position within the cap beam. Once all components were placed, concrete of equal specified strength to that of the columns and footing was poured, consolidated, and finished. Figures 2.51 to 2.53 show these processes. After a week, the wooden forms were removed. Figure 2.54. shows an elevation of the completed specimen.

Two construction errors were noted after the specimen was completed. A small portion of one of the cap beam flanges was missing, exposing some of the rebar in the cap beam flange. The missing piece patched by the contractor and had no significant effect on the performance of the connection being assessed. Figure 2.55 and Fig. 2.56 show the exposed rebar and the repaired flange. The other error consisted of the columns being spaced incorrectly. The columns were spaced 78 inches (1981 mm) apart instead of 72 inches (1829 mm) apart. This did not affect the performance of the connections being evaluated but did slightly change the results of the pretest analysis and was accounted for when selecting the ground motion simulated in testing.

Chapter 3. Pre-Test Analytical Studies

3.1 Overview

Static and dynamic nonlinear analyses of the pier model were conducted in OpenSees [16]. The performance of the bent under various ground motions was evaluated to determine a loading protocol that would impose sufficient demands and capture the different limit states of the specimen up to or near failure. This chapter describes the analytical model, the analyses, and the results.

3.2 Analytical Modeling

A two-dimensional fixed-base frame was used for the analytical model. The frame consisted of two identical columns with two-way hinges near the base and a cap beam. The footing was not modeled as it essentially behaves as a part of the ground as it was designed to remain undamaged and not slip. The columns were composed of fiber sections applied to a force-based beam-column elements with five Gauss-Lobatto integration points to capture the nonlinear behavior of the columns. P-Delta effects were included to simulate the effects of the secondary moments caused by eccentricity of column axial loads as the specimen is displaced. The fiber sections of the columns were composed of two concrete patches and a circular layer of longitudinal reinforcement. Two patch sections were defined to represent confined and unconfined concrete respectively. Transverse reinforcement was not modeled directly but its confining effect was implicit in the confined concrete properties. Furthermore, the transverse reinforcement was assumed to provide sufficient shear strength and stiffness, hence shear springs were not included in the model.

OpenSees provides various material models to represent concrete and reinforcing steel. *Concrete01* was selected to model the behavior of confined and unconfined concrete used in the analytical model. The stress-strain relationship for the material, *Concrete01*, is shown in Fig. 3.1. *Concrete01* was selected, as the major stress-strain points of the material can be defined manually to account for both confined and unconfined concrete behavior. The material model *ReinforcingSteel* was used to model the longitudinal reinforcement of the columns. The stress-strain relationship of *ReinforcingSteel* is shown in Fig. 3.2. This material was selected as it is a more accurate representation of the behavior of steel than a bilinear material model. *ReinforcingSteel* allows the user to define the stresses and strains at various points along a typical steel stress-strain curve. Since the analytical model was developed before the construction of the specimen, the expected material properties from AASHTO guide specifications [14] were used in the pretest analytical studies. The Mander et al. [18] model was used to calculate the material properties of confined concrete. Tables 3.1 and 3.2 list the properties of the concrete and reinforcement used in the model columns, respectively.

The two-way hinges of the specimen were modeled similarly to the columns. The primary modeling differences between the columns and the two-way hinges were the material properties of the hinge concrete and reinforcement. Similar to the column fiber sections, the hinge utilized two patches representing the outer and core concrete and a circular layer for the longitudinal reinforcement. Due to the hinge being adjacent to the core concrete of the column, the outer layer of the hinge was essentially confined because of the restraining effect of the column concrete against dilation of hinge concrete. Hence,

the confined concrete properties of the column were used for the outer layer of hinge concrete. As the hinge had its own transverse reinforcement, the core concrete of the hinge was effectively doubly confined. *SelfCentering* material was used to model the CAM bars of the hinge, as CAM bars do not behave like traditional rebar. The stress-strain relationship of *SelfCentering* material is shown in Fig 3.3. *SelfCentering* material was selected to represent the CAM bars as it is capable of modeling the flag-shaped behavior of superelastic materials. The input material properties of CAM bars referenced previous studies conducted by Varela and Saiidi [5]. Tables 3.3 and 3.4 list the concrete and reinforcement properties of the hinge

Because the cap beam was designed as a capacity-protected member and expected to remain elastic during testing, a linear elastic beam-column element was used in the analytical model of the cap beam. The area, moment of inertia, and Young's modulus of were calculated and defined within the model for elements representative of the cap beam. Because the specimen would be exposed to external vertical loads representative of the dead loads of the prototype bridge, nodal masses were defined along the cap beam at locations at which the vertical load rods would pass through the specimen. Additionally, an extremely rigid member was used to connect the top of the columns to the center height of the cap beam, to capture displacements accurately. Details of the analytical model are shown in Fig. 3.4.

3.3 Pre-Test Analyses

3.3.1 Pushover Analysis

A pushover analysis, which is a nonlinear lateral static analysis, of the model was conducted in the in-plane direction to estimate the lateral load and displacement capacity of the specimen. The pushover curve is calculated by applying a lateral displacement at the centroidal axis of the cap beam to a desired drift level and determining the associated lateral load. To obtain an accurate pushover curve representative of the specimen, gravity loads were applied before the analysis was conducted. The gravity loads imposed on the model included the self-weight of the cap beam, half the weight of the columns, half the weight of the mass rig link, and 100 kips (444 kN) of vertical loading. Note that the vertical loads were reduced from 67.3 kips (333 kN) per column to 46 kips per column (222 kN) as only 100 kips total (444 kN) could be allocated to the mass rig during testing of the actual specimen. Once gravity loads were applied, the pushover analysis calculates the stresses along the fiber sections at each displacement increment until the specified displacement is reached. Figure 3.5 shows the results of this analysis. The pushover analysis provided an idea of the force-displacement response of the specimen during dynamic loading.

The stress-strain response of an extreme tensile bar at various locations along the column length is shown in Fig. 3.6. This was done to verify the local behavior of the column longitudinal reinforcement by demonstrating the expected inelastic response of the column reinforcement in the plastic hinge region and to estimate the cracked stiffness of the specimen. The cracked stiffness was calculated by converting the static pushover analysis result to an equivalent elasto-plastic relationship, which was done by locating the point on the pushover curve at which the extreme tension bar yields and assuming a linear slope.

3.3.2 Dynamic Analysis

After conducting the static pushover analysis and verifying the model, a dynamic analysis of the bent model was conducted to select an adequate determine the earthquake acceleration record and inform the loading protocol for the shake table testing. A damping ratio of 5 percent was applied to the model using the *Rayleigh* damping command in OpenSees. The model was subjected to five previously measured earthquake acceleration records as candidates for potential use during shake table testing.

3.3.3 Ground Motion Search Parameters

All earthquake records used in this exercise were obtained from the NGA-West2 ground motion database provided by the Pacific Earthquake Engineering Research (PEER) Center [19]. The ASCE Code Spectrum [20] model option was used to define a target spectrum when searching the PEER database [19]. The intersection of US 395 and Clearview Drive, which was the location of the prototype, has a peak ground acceleration coefficient of 0.4 g and a type II soil classification. These values were used to calculate seismic parameters of S_{DS} = 1.25 and S_{D1} = 0.5 g, where S_{DS} is the design spectral acceleration at a 0.2 second period and S_{D1} is the design spectral acceleration at a one-second period. The design response spectrum is shown in Fig. 3.7. Once the design spectrum was defined, the period of the specimen was estimated. The specimen was assumed to behave as a single degree of freedom system, and the period was calculated according to Equation 3-1.

$$T = 2\pi\sqrt{M/K_{total}} \tag{3-1}$$

where,

M = Mass due to dead load
K_{total} = lateral stiffness of the system
T = period of the system

The cracked stiffness of the structure was calculated from the pushover curve, while the mass of the structure was calculated from a portion of the self-weight of the specimen, as discussed in the pushover curve section, and the vertical loads. The manually estimated period of the specimen was 0.364 seconds while the period calculated from the OpenSees model was 0.243 seconds. This large discrepancy is due to OpenSees use of gross section rather than cracked section stiffness of the columns, which resulted in the significantly lower period.

Once the period of the specimen was determined, the period of the prototype bridge pier was estimated. The period of the prototype was determined by dividing the specimen period (0.364 seconds) by the square root of the specimen geometric scale factor ($1/3^{rd}$). This provided an estimated period of 0.631 seconds for the prototype period, which was used in the PEER database to search for and scale earthquake records. A period range (0.631 to 4 seconds) was input when searching the database to scale and match earthquake spectra to the design spectra for more than just a single period. The purpose of the search was to identify earthquakes that would have similar spectral accelerations to that of the design spectra at the initial period and beyond. Once all parameters were input, the database was searched for earthquake records with appropriate

scale factors and acceleration histories. Accordingly, five different ground motions were selected as potential candidates for this study. A discussion of analyses for the five earthquake records is presented in subsequent sections starting with the record that was eventually selected among the five for the shake table tests.

3.3.3.1 1940 Imperial Valley-02 at El Centro Array #9, H1 Component

The ground motion selected for simulation for the shake table testing of the specimen was the 1940 Imperial Valley-02 (El Centro) earthquake record at the El Centro Array #9 station. The first horizontal component (H1) of this ground motion was selected instead of the second horizontal component (H2) as peak ground acceleration (PGA) of H2 was relatively low and may not have imposed sufficient demands on the specimen without an unreasonably large amplification factor. This record was selected due to its symmetric acceleration history and reasonable scale factor. A symmetrical acceleration history was highly desired as it would result in comparable displacement in both directions of the specimen placing comparable demands on the two column cap beam connections, which were different. A reasonable amplification factor for the input record is preferred as the ground motion is more representative of a real earthquake. An unreasonably large amplification factor would lead to a false sense that the amplified record represents a very strong earthquake, whereas in reality strong earthquakes have additional characteristics that are not captured by merely amplifying the acceleration. The selected record is from well-known seismic event and has been used in many other shake table tests. The unscaled acceleration history of the ground motion and its response spectrum are shown in Fig. 3.8 and 3.9.

A nonlinear dynamic analysis of the bent model was conducted using the ground motion. To meet similitude requirements for the specimen, the time axis of the input acceleration history was compressed. The timestep of the ground motion was multiplied by the square root of the specimen geometric scale factor (1/3) to achieve this. The amplification factor used to match the ground motion design spectrum to the design spectrum was also applied to the acceleration history. The amplification factor of 1.464 was calculated by the PEER database according to the user-defined inputs. A comparison of the design response spectrum and the scaled response spectrum are shown in Fig. 3.10, while the compressed and scaled acceleration history of the motion is shown in Fig. 3.11. This acceleration history is representative of the 100 percent design earthquake used in shake table testing. The hysteretic force-displacement relationship and the lateral displacement history at the top of the specimen show the dynamic response of the model subjected to the ground motion and are presented in Fig 3.12 and Fig 3.13, respectively. Note the relatively symmetric response of the specimen. The peak drift ratio of 1.5% is reasonable and represent typical drift levels seen in past research projects when bridge bent models are subjected to a design level earthquake. Based on this analysis, a loading protocol was developed in which the design earthquake would be applied successively at different scales to capture the different limit states of the specimen.

3.3.3.2 Additional Earthquake Records Considered

Four other earthquake records were considered and applied to the model in the pre-test dynamic analysis. The dynamic response of the model under each of these ground motions was compared to the response from others before ultimately selecting the H1 Imperial Valley-02 earthquake record. These records were considered due to their

reasonable amplification factors, symmetric acceleration histories, and peak ground accelerations. The records were ultimately not selected due to one or more of the following: sufficient demands were not placed on the specimen; the response of the specimen was not symmetrical; significant residual displacements in the response of the specimen, or the duration of the ground motion was overly short. Information of the considered earthquake records are listed in Table 3.5. All earthquake records were time compressed and scaled according to the previously described method before each dynamic analysis.

3.3.3.2.1 1971 San Fernando at Castaic – Old Ridge Route, H1 Component

Figure 3.14 provides the unmodified ground motion record of the event, while Fig 3.15 shows a comparison of the design spectrum and the amplified response spectrum of the record. The displacement history and the force-displacement relationship are shown in Fig. 3.16 and 3.17, respectively. Although this earthquake is of historical significance, the ground motion did not place symmetric demands on the bent and resulted in minor residual displacements. This was likely due to the high amplitude accelerations caused by the relatively large amplification factor. Therefore, the ground motion was not suitable for use in shake table testing.

3.3.3.2.2 1979 Imperial Valley-06 at El Centro Array #11, H1 Component

The unmodified acceleration history of this event is shown in Fig. 3.18, the amplified response spectrum is shown in Fig. 3.19, and the response of the specimen is shown in Fig. 3.20 and Fig 3.21. The Imperial Valley-06 results of the dynamic analysis showed symmetric displacement demands on the column and the response spectrum closely matched that of the design spectrum, but the demands were not sufficiently large to induce significant yielding of the columns. Additionally, the significant accelerations of the ground motion occurred in a relatively short time frame. For these reasons, this Imperial Valley-06 was not selected for shake table simulation.

3.3.3.2.3 1980 Mammoth Lakes-01 at Convict Creek, H1 Component

Figure 3.22 provides the unmodified ground motion record of the event, while Fig 3.23 shows a comparison of the design spectrum and the amplified response spectrum of the record. The displacement history and the force-displacement relationship are shown in Fig. 3.24 and 3.25, respectively. The response spectrum matched the design spectrum well, but the ground motion resulted in asymmetric displacement demands on the specimen. Therefore, this ground motion was not used for shake table testing.

3.3.3.2.4 1994 Northridge-01 at Sylmar – Converter Station, H1 Component

The unmodified record of this event is shown in Fig. 3.26 and a comparison of the amplified response spectrum and the design spectrum is shown in Fig. 3.27. The dynamic response of the specimen is shown in Fig. 3.28 and Fig 3.29. Although the response spectrum matched the design spectrum closely and the dynamic response of the specimen was symmetric, t the displacement demand was relatively small when compared to typical drift levels seen for design level earthquakes. For this reason, this ground motion was not selected for use in shake table testing.

3.3.3.3 Loading Protocol

A loading protocol was developed for shake table simulation and was based on the dynamic analysis of the test specimen model under the H1 component of the 1940 Imperial Valley-02 event recorded at El Centro Array #9. The design level ground motion was reduced or amplified by various scale factors and spliced in order of increasing peak acceleration. Sufficient time was inserted between subsequent earthquake runs to allow the bent model to return to a resting position before being subjected to the next ground motion. This was done to duplicate the shake table testing setting where long pauses typically occur between earthquake runs to assess and document the damage. The spliced acceleration history for the loading protocol is shown in Fig. 3.30. Each ground motion is referred to as a percentage of the design level earthquake in accordance to the scale factor (e.g., a 0.33 scale factor = 33% design level). The loading protocol consisted of seven runs representative of 33, 67, 100, 150, 200, 250, and 300 percent of the design level earthquake. These levels were selected to capture different limit states of the specimen based on the estimated response obtained from the pushover analysis. Before each earthquake motion and after the last motion, white noise motions with an amplitude of approximately 0.1g were applied to estimate the period and damping ratio of the specimen. The details of the loading protocol are listed in Table 3.6. Additional ground motions were applied to the actual specimen until the specimen reached higher drift levels that caused substantial damage.

3.3.3.4 Estimated Response

The spliced motion was applied to the model to estimate the response of the specimen during shake table testing. The 33 percent design level earthquake was intended to capture the response under a relatively minor earthquake with no yielding of the reinforcement The remaining earthquake amplitudes were intended to capture various limit states of the specimen, (as guided by the pushover analysis) including, yielding, strain hardening, and near failure.

Table 3.7 lists the estimated maximum displacement at the top of the specimen, the maximum drift ratios, the residual drift ratios, and the base shear for each run. The drift of the specimen increased with each run, while residual drifts first appeared during run 4 but remained relatively small thereafter. Figure 3.31 demonstrates the increase in peak displacement in successive runs and the minimal residual drift. The hysteresis loops for each run are shown in Figures 3.32 through 3.38. Figure 3.32 shows that the specimen remained linear for the 33% design earthquake (DE). The 67% DE showed some nonlinearity caused by the concrete as well as minor yielding of the CAM bars and extreme column reinforcement. The DE caused some yielding and reached a drift ratio of 1.64%. A slight residual drift arose during the 150% DE (run 4). Significant yielding of the specimen did not occur until the 200% DE, which also resulted in a somewhat asymmetric response. Figures 3.37 and 3.38 show the specimen was approaching the plastic lateral force and that the response became highly asymmetric with dominant displacement being in the negative direction.

An envelope of the accumulated hysteresis curves was determined and compared to that of the pushover curve and is shown in Fig. 3.39. The envelope captures the maximum displacements in the negative direction (which was the dominant displacement

direction for all runs) and its associated lateral force for each run. The two curves are similar, with the envelope having a near-identical base shear capacity.

Chapter 4. Experimental Studies

4.1 Overview

Shake table testing was conducted to evaluate and compare the performance of the ABC-emulative CIP connection to the ABC socket connection at the cap-to-column joints under in-plane seismic loading of the test model. The secondary focus of this testing was to evaluate the CAM bars effectiveness in reducing hinge moments and their seismic performance when coupled with mild steel using HRC couplers. Testing was conducted on one of the shake tables at the EEL at UNR. The specimen material properties, experimental setup, and instrumentation used to capture the specimen response are described in the following sections of this chapter.

4.2 Measured Material Properties

To determine if the materials in the specimen met the specified properties and are representative of those used in typical bridges, samples of each material were taken and tested. These measured properties were later used to update the material models in the post-test analysis. The sampled materials included concrete, reinforcing steel, and the CAM bars. The 28-day compressive strength of the high-strength non-shrink grout used to grout the corrugated metal pipe to the ABC column was 10,000 psi (69.5 MPa) according to the product specification sheet.

4.2.1 Concrete

The compressive strength of concrete for each casting (footing, columns, and cap beam) was determined at 7, 14, and 28 days. Additionally, the compressive strength of each casting was measured the day after shake table testing to determine the properties around the day of testing. Standard 6×12 in (152 × 305 mm) cylinder molds were used to sample concrete during construction. As the specimen was cast in three separate pours, samples were collected for each. Twelve samples each were collected for the footing, columns, and cap beam pours respectively. All cylinders were sampled and tested to the ASTM C39 [21] concrete compressive strength testing standards, but cylinders were not kept in moisture room and neoprene pads were used instead of sulfur caps. The average measured compressive strength for all members at 7-day, 14-day, 28-day, and test-day are listed in Table 4.1. Note the compressive strengths of the 14-day footing pour and the 7-day were not possible to obtain on time. Also note that the test day strength of the footing was slightly lower than the 28-day strength due to scatter in the data.

4.2.2 Reinforcing Steel

Three samples of each reinforcing steel bar size used in the specimen were collected and tested at UNR. All bars were tested to the ASTM A370 tensile testing standard for steel [22]. Bars were tested to obtain the stress-strain plots for each bar size to determine their yield stress, ultimate stress, strain at hardening, and ultimate strain. Figures 4.1 through 4.3 show the measured stress strain relationships of the #3 (Ø9.5 mm), #4 (Ø13 mm), and #5 (Ø16 mm) bars, respectively. Note that only #4 (Ø13 mm) bars demonstrated a clear yield plateau, so the yield stress for the #3 and #5 bars was

taken to be the intersection of stress-strain curve with a parallel secant line drawn from 0.2% strain. Table 4.2 lists the average measured properties of each bar size.

4.2.3 Copper-Aluminum-Manganese (CAM) Bars

4.2.3.1 Loading Protocol

Four extra CAM bars provided by Furukawa Techno Material Co., Ltd. of Japan were tested at UNR. As there is no standard procedure for testing of CAM bars used for seismic application, the testing procedure used in Mohebbi et al. [10] was applied. The ends of all CAM bars tested were flattened and the bars were linked to #4 (Ø13 mm) steel bars using HRC couplers to exactly match the CAM bars used in the specimen. Three bars underwent static cyclic loading at a rate of .02%/second, that consisted of loading the samples at two, half cycles at strain intervals of 0.25%, 0.5%, 0.75%, 1%, 2%, 3%, 4%, 5%, 6%, 7%, 8%, and then pulling to failure. The fourth CAM bar was to undergo static single-cycle loading, but had an abnormally high ultimate strength. Testing of this bar was not completed, and the results were not used in the determination of material properties.

4.2.3.2 Instrumentation

A standard extensometer with a gage length of 8 in (203 mm) was used to measure strain in the first two tested CAM bars. Figure 4.4 shows the setup. Note that the bars were gripped at the #4 (Ø13 mm) steel bars and not the CAM bars. A laser extensometer was used for the third CAM bar. Although the steel bars would elongate as well during testing, the extensometer only captured the elongation of the CAM bar. In addition to the extensometer, strain gauges (two on CAM 1 and 2, four on CAM 3) were applied to at mid length of each CAM bar to obtain local strain data and compare with the data measured by the extensometer.

4.2.3.3 Results

The stress-strain relationships of each bar during static full-cycle loading are shown in Fig. 4.5. through 4.7. As the strain gauges tended to fail after significant elongation of the CAM bars, only the data from the extensometer was used in determining the CAM bar material properties. The strain gauge data was compared to that of the extensometer (before strain gauges reached failure), and the results were agreeable. The signature flag-shaped stress-strain curve of the CAM bars is apparent and demonstrates the superelastic CAM bars' ability to return to a near-zero strain. Although the results of the tests are mostly consistent, there is a large difference in the ultimate stress of the bars. The second CAM bar was not pulled to failure, but the stress at 10% strain exceeded the fracture stress of the other bars. As the bar was not tested to failure, it was not taken considered when determining the average fracture stress of the bars. The ultimate stresses of the other bars were used to obtain an average ultimate stress for the CAM bars, and the stress-strain relationships for the 5% half cycles were used to determine the average yield stress, elastic modulus, post yield-modulus, yield strain, and rupture strain. Table 4.3 lists the material properties of individual bars and the average material properties.

4.3 Experimental Setup

The shake table test setup is shown in Figs. 4.8 and 4.9. The specimen was tested in the in-plane direction, which aligned with the north-south orientation in the laboratory. A standard grout tolerance gap of 1.5 in (38 mm) was allotted between the top of the shake table and the bottom of the footing. This gap allowed high strength non-shrink grout to be placed around the footing, which ensured that the specimen would be placed on a level surface. After the grout was cured, the specimen was anchored to the shake table using ten threaded rods that passed through the PVC pipes in the footing. Each rod was then tensioned to 30 kips (133 kN).

A steel load transfer beam was placed on top of the specimen cap-beam to connect the specimen to the mass rig using a rigid link and provide a realistic vertical loading distribution on the cap beam. Drawings and a photo of the load transfer beam are shown in Figs. 4.10 through 4.12. The load transfer beam consisted of short steel elements perpendicular to the cap beam to mimic longitudinal girders of superstructures. These elements were connected to each other by other steel elements parallel to the cap beam. The connection between the latter and the former was pinned to avoid any flexural rigidity for the load transfer beam that would affect the column-cap beam connection behavior. To prevent slippage of the load transfer beam during dynamic loading, the beam was connected to the cap beam with threaded anchors. The anchors were developed to a length of 7.5 in (191 mm) in the cap beam with 0.75-in (19 mm) nuts at the ends to serve as mechanical anchorage inside the cap beam concrete.

The load transfer beam also allowed the specimen to be vertically loaded. Vertical loads were applied to the specimen through ten 0.75-in (19 mm) diameter high-strength threaded rods post-tensioned by 10 single acting hollow plunger hydraulic jacks. The jacks were then connected to an accumulator installed on top of the load transfer beam to minimize the fluctuation of vertical loads during shake table testing. The rods were post-tensioned to a total of 92 kips (410 kN) or 9.2 kips (41 kN) per rod. Before the rods were tensioned, the rods were aligned with the cap-beam flange and footing PVC pipes to allow the rods to pass through the specimen and be anchored to 6 × 6 inch (152 × 152 mm), 1-in (25 mm) thick bearing plates under the footing.

As previously mentioned, the load transfer beam was used to connect the specimen to the mass rig using a rigid link. The mass rig provided inertial mass during dynamic loading tests, thus inducing lateral loads on the specimen. One hundred kips (444 kN) of inertial mass were provided by the mass rig and was achieved by placing four 20 kip (89 kN) concrete blocks on the rig. The rig itself weighs an additional 20 kips (89 kN), but because it is supported on a mechanism with hinges at base, its entire inertial force is transferred to the specimen through the rigid link connected to the load transfer beam. The rigid link included a load cell that measured the lateral loads applied at the top of the specimen.

Two steel columns were placed on one side of the table and were used to restrain the specimen in the out-of-plane direction. These columns were connected to the load transfer beam using compression rods and were oriented in the strong direction to better resist out-of-plane loads as illustrated in Fig. 4.13. Figure 4.14 shows the complete experimental setup on the shake table.

To capture the response of the specimen during testing, cameras were placed on and around critical specimen regions. GoPro cameras were placed on the bottom face of

the cap and aimed at the plastic hinge regions of the columns (two cameras each). Additional GoPro cameras were placed at the top of the footing and were aimed at the column-hinge interface to capture the damage of the two-way hinges (two cameras each). The cameras were placed on the north-west and south-east sides of the ABC column and the north-east and south-west sides of the CIP column. Two video cameras were setup on the east and west sides of the shake table to capture the overall response of the specimen. Additional photos of the observed damage were taken between each run.

4.4 Instrumentation

The specimen was instrumented to measure its response during dynamic loading. Strain gauges, string potentiometers, displacement transducers, and accelerometers were applied to the specimen to collect data. Additionally, the vertical load accumulator, lateral load cell, and the shake table itself are instrumented to measure forces, displacements, velocities, and accelerations. All data was continuously recorded throughout each run using 240 channels connected to multiple data acquisition systems (DAQs). During the tests, the data was acquired at 256 Hz sampling rate.

4.4.1 Strain Gauges

Strain gauges were installed to column and cap beam reinforcement to measure the local behavior of the bar as the specimen underwent shake table testing. The strain gauges were manufactured by Tokyo Measuring Instruments Laboratory Co., Ltd. YEFLA-5 gauges with a gauge length of 0.2 in (5 mm) were used. This gauge type is rated for dynamic loading and provides adequate strain capacity. Application of the strain gauges involved grinding a small portion of the bars (until smooth), cleaning of the target location using isopropyl alcohol, attachment of the strain gauge using cellophane tape and the manufacturer provided cyanoacrylate glue, and wrapping of the strain gauge using rubber mastic tape. Figures 4.15 to 4.18 show the locations of 112 gauges applied to one side of the specimen, this configuration was replicated for the other side, i.e. a total of 224 gauges were used in the full specimen. Strain gauge data was differentiated using N for the northern column and S for the southern column.

Figure 4.15 shows the strain gauges placed at six different heights (layers) along the longitudinal column reinforcement. These gauges were installed to capture yielding of the reinforcement within the plastic hinge region as well as the strain penetration into the cap beam. Two layers of gauges located above the cap-column interfaces at 4.5-in (114 mm) spacings were placed on the longitudinal column reinforcement extending into the cap beam pockets. The remaining four layers of gauges were placed on the longitudinal reinforcement at or below the cap-column interfaces at 6-in (152 mm) spacings. The gauges located above the cap-column interfaces were placed to capture the strain penetration of yielding into the cap beam pockets and to evaluate the connections' ability to redistribute strains. Gauges located at or below the cap-column interfaces captured the yielding of reinforcement within the plastic hinge region. Three bars on the north and south sides of each column were instrumented for redundancy.

Additional gauges were installed on to the column spirals at the same heights as those of the longitudinal gauges. Gauges were placed on the north, south, east, and west sides of the column spirals. These gauges captured the maximum spiral strains caused by confinement and shear. Strain gauges were also installed around the cap beam pocket

connection to evaluate the performance of the different pocket connections. The confinement provided by the hoops was measured by instrumenting the hoops at two layers (Fig 4.15) similarly to the column spirals.

Transverse vertical and horizontal ties adjacent to the pocket connections and pocket stirrups were instrumented to measure the behavior of this reinforcement during in-plane loading (Figs. 4.16 and 4.17). Transverse reinforcement adjacent (vertical ties, horizontal ties, and stirrups) to and at the pocket connections (stirrups only) were instrumented to measure the engagement of reinforcement during in plane loading to evaluate the performance of the pocket connections.

Similar to the column reinforcement, strain gauges were placed on the hinge reinforcement of each column (Fig. 4.18). Strain gauges were placed at three different heights on the hinge reinforcement (spiral and CAM bars): (1) 5 in (127 mm) above the center of the two-way hinge gap to measure the spread of strain from the hinge gap to a location within the main column, (2) at the center of the hinge gap to measure yielding of the CAM bars, and (3) 5 in (127 mm) below the center of the two-way hinge gap to measure the spread of strains into the footing. The strain gauges on the spiral were used to capture strains caused by confinement and shear.

4.4.2 Displacement Transducers

TR-75 mm (2.95 in) and TR-100 mm (3.94 in) Novotechnik displacement transducers were used on the columns to measure the local displacements, which was used to calculate curvature, rotations, and shear displacements (Fig. 4.19). Transducers were attached to 5/16-in (8 mm) threaded rods that had been inserted into the columns during construction at the following locations: (1) three vertical pairs on the north and south (in-plane directions) sides of each column along the plastic hinge region to calculate curvature, (2) one vertical pair on the north and south sides of each column near the base to calculate rotations, and (3) one horizontal pair on the east and west sides of each column near the base to determine hinge shear displacements. Only a single pair of vertical transducers was placed near the column base as the two-way hinges would effectively eliminate curvature of the column bases and only cause rotations.

4.4.3 String Potentiometers and Accelerometers

Four string potentiometers were attached to the corners of the north face of the cap beam. These string potentiometers were used to measure the absolute (relative to the fixed laboratory floor) horizontal displacement of the cap beam during shake table testing. Four string potentiometers were used for redundancy and their results were averaged to determine the lateral displacement of the specimen relative to the shake table after subtracting the shake table displacements. Locations of the string potentiometers are shown in Fig. 4.19.

Three tri-axial accelerometers were placed on the specimen to measure accelerations during shake table testing. The locations of the accelerometers are shown in Fig. 4.19. The accelerometers were placed on the northern and southern ends of the specimen on top of the cap beam to capture accelerations at the top of the specimen. The remaining accelerometer was placed at the center of the top of the footing for redundancy and was used to verify the accelerations measured by the shake table itself.

Chapter 5. Experimental Results

5.1 Overview

The specimen was tested in the in-plane direction on a shake table at the EEL at UNR. A scaled and time-compressed version of the H1 component of the 1940 Imperial Valley-02 event was simulated in several runs with increasing amplitudes. All shake table testing was conducted on October 8th, 2019. Although the initial loading protocol specified seven runs, a misinterpretation of the protocol resulted in additional low-level runs with amplitudes below 100% of design level. The amplitude of the runs following the 150% design were increased by 75% design rather than 50% to increase drifts of the specimen. Table 5.1 lists the planned and actual loading protocols. The observed and measured seismic performance of the specimen are discussed in this chapter.

5.2 Observed Damage

In addition to visual inspection, GoPro video cameras and camcorders were used to record the movements and damage progression of the specimen during testing. Before testing, existing cracks caused by shrinkage or the vertical loads were marked in black crayon and labeled with a number zero to document the damage took place before testing. After each run, new cracks were marked with a new color and the run number was written adjacent to the crack to track the progression of damage. Photos were taken from different directions at the column-cap joints, column top plastic hinges, and column base hinges after each run. Additional photos of the overall specimen were taken from the east and west direction. The following sections discuss the observed damage of the individual columns and connections.

5.2.1 ABC Column

No cracks were noted along the cap beam at the joint before testing of the ABC column. Construction-related cracks, i.e. long spiral crack running along the Sonotube form (Fig. 5.1) as well as some minor cracks and voids (Fig 5.2), were marked in black crayon with the number zero before testing. As the first three runs were under-scaled due to the loading protocol misinterpretation, the peak ground accelerations of these runs were small and did not significantly damage the column. Figure 5.3 shows the minor spalling of the ABC column two-way hinge at a drift ratio of 1.64 percent during run 4. After reaching a drift ratio of 2.3 percent during run 5, significant spalling of the two-way hinge was observed (Fig. 5.4) and a significant number of flexural cracks were noted in the plastic hinge of the column (Figs. 5.5 and 5.6). During run 6, additional flexural cracks formed, and the flexural cracks developed in run 5 began to widen and extend around the column. Additionally, cracking of the pocket grout was marked, but this was later observed to be a pre-existing crack (Fig 5.7). Figures 5.8 and 5.9 show the flexural cracks of the column after run 6, when the column reached a drift ratio of 2.6 percent.

A large albeit shallow portion of the north face and a small portion of the southern face of the column spalled during run 7 (3.8 percent drift). The spalling of the column in addition to the elongated and widened flexural cracks can be seen in Figs. 5.10 and 5.11. Concrete spalling expanded in both the two-way hinge and north face of the column during run 8, where the column reached a drift ratio of 7.1 percent. Figures 5.12 and 5.13 show the exposed reinforcement in the two-way hinge and the column after the run.

Additionally, Fig. 5.14 shows small shear cracks that developed during run 8 as well. Run 9 resulted in a drift ratio of 12.6 percent and caused significant spalling of two-way hinge concrete, significant spalling of southern face of column that exposed rebars, widening of all existing cracks, development of additional shear cracks, and development of cracks on the grout connection. Figures 5.15 through 5.19 show photos of the damage caused by the run. Note that run 9 resulted in significant residual drift of 2.62 in (67 mm, 2.94 percent), whereas run 8 only had a residual drift of 0.4 in (10 mm), i.e. 0.46 percent drift ratio. The large residual drift in run 9 caused some safety concerns. As a result, testing was terminated after the white-noise motion that followed run 9. An overview of the specimen from the west is shown in Fig. 5.20.

The photos show that damage in the specimen was essentially concentrated in the plastic hinge region and the two-way hinge of the column. The minimal cracking of the column adjacent to the two-way hinge demonstrates the reduced moment-capacity of the hinge (see Fig. 5.19). Figures 5.21 and 5.22 show the southern cap beam joint from the east and west directions after run 9 where no cracks or other signs of non-linearity were observed. The lack of joint damage in the ABC column connection is particularly important because the cap beam column joint design and detailing deviated from the standard ABC practice.

5.2.2 CIP Column

In contrast to the ABC column, there were several relatively large cracks in the plastic hinge region of CIP column before testing. The large cracks were likely caused by over-vibration of concrete near the top during construction. Just as the ABC column was marked before testing, the existing cracks in the CIP column were marked using a black crayon and labeled with the number zero. Pre-test damage photos of the column are shown in Figs. 5.23 to 5.26. As the first three runs of dynamic testing had significantly lower peak ground accelerations than the target per the planned loading protocol, the column did not experience significant damage. Figure 5.27 shows the minor elongation of pre-existing cracks after run 2, when the specimen reached a drift ratio of 0.32 percent. The specimen reached a drift ratio of 1.4 percent during run 4, and a few new flexural cracks were observed on the southern face of the column (Fig. 5.28). During run 5, where the specimen reached a drift ratio of 2.3 percent, there was significant spalling of the two-way hinge concrete (Fig. 5.29 and Fig. 5.30). The existing cracks propagated, and many thin flexural cracks were formed on both sides of the column plastic hinge as well (Fig. 5.31 and Fig. 5.32). Run 6, during which the specimen reached a drift ratio of 2.6 percent resulted in minor spalling of the column southern face, elongation of existing cracks around the column, and more spalling of the two-way hinge concrete. Figure 5.33 to 5.35 show the flexural cracks of the column and the spalling of the two-way hinge.

The specimen reached a drift ratio of 3.8 percent during run 7, which resulted in major spalling of both sides of the column and cracking of the cap beam soffit (Fig. 5.36 to 5.38). Small shear cracks were also developed during the run and are shown in Fig. 5.36. Run 8 with 7.1 percent drift, resulted in major spalling at the column-cap connection on the southern side of the column as seen in Fig. 5.39. The spalling was no longer isolated to the cover concrete of the column and propagated deeper into the cap beam and column core. Additional shear cracks were observed on both sides of the column and spalling of the northern side was expanded as well (Fig. 5.40). The specimen

reached a drift ratio of 12.6 percent during run 9 and experienced significant expansion of existing damage. The run caused major spalling of the column and bottom cap face on the northern side (Fig. 5.41), further extension of spalling into the column core and cap beam, buckling of longitudinal bars on the southern side (Fig. 5.42), and spalling of the two-way hinge concrete into the hinge core (Fig. 5.43). Additional photos of the damage are shown in Figs. 5.44 to 5.46.

The photos show that damage in the specimen was mostly concentrated in the plastic hinge region and the two-way hinge of the column, but high intensity ground motions caused the damage to extend into the cap beam. The minimal cracking of the column adjacent to the two-way hinge demonstrates the reduced moment-capacity of the hinge (Fig. 5.43). Additional photos of the cap beam joint were taken between each run to determine if the cap beam remained elastic. This was in lieu of strain gauges on the cap beam longitudinal bars that would have provided more direct data. Figures 5.47 and 5.48 show the northern cap beam joint from the east and west directions after run 9 and no cracks or other signs of non-linearity were observed. As no cracking was observed at the northern or southern column-cap joints, the cap beam was confirmed to have remained essentially elastic. The observed damage indicated, while there was no joint damage, the lower part of the cap beam at the connection to CIP column underwent some damage under very strong earthquakes. This trend was not observed in ABC column.

5.3 Shake Table Accelerations

Internal instrumentation in the shake table measure accelerations, velocities, and displacement of the table. The actual shake table accelerations typically vary slightly from the target motions due to the shake table mass and the interaction of the table and the specimen. The shake table achieved slightly higher PGAs than that of the loading protocol (used for the pre-test dynamic analyses) for the first three runs, but lower PGAs for the remaining ones, i.e. run 4 through run 9. Table 5.2 lists the target and achieved PGA for each run as well as the percent difference. The percent difference of the achieved and target motion was relatively small during the first few runs but worsened as the runs progressed to a maximum of 25 percent (run 8). The target and achieved spectral accelerations of the specimen were also compared and listed in Table 5.3. This was done by generating the achieved and target response spectra and comparing the spectral acceleration values at the initial period of the specimen. The initial period of the specimen for each run was estimated using frequency response factors (FRF) as well as Fast Fourier Transform (FFT) from the accelerations measured at the top of the specimen during the white noise test preceding each run.

Figures 5.49 to 5.57 show the target and achieved response spectra for each earthquake run and identify the specimen period. The achieved spectral acceleration was consistently lower than the target spectral acceleration for all runs but no trend was observed in the percent difference. There was generally good correlation between the shape of the target and achieved response spectra for most runs. A collection of the achieved response spectra in addition to the time-compressed seismic design response spectrum is shown in Fig. 5.58. Even though the target and achieved motions differed, the most important aspect of loading, which is imposing large drift ratios on the specimen, was successfully achieved. Furthermore, it should be noted that once the structure yields, it does not have a single period because its stiffness changes during each motion.

Therefore, comparison of spectral acceleration is merely a measure of the correlation of the overall target and achieved motions.

5.4 Force-Displacement Relationship

The lateral-force displacement relationship of the specimen is an effective indicator of the seismic performance of a structure. Hysteretic force-displacement figures are generated to provide insight of yielding, energy dissipation, and lateral force and displacement capacities of a structure. The displacement data of four string potentiometers attached to the north face of the specimen cap beam was averaged to obtain the absolute displacement at the top of the specimen. This data was then filtered to remove high-frequency noise which may have been caused by the movement of the shake table or the instruments themselves. The displacement of the shake table recorded by the internal instruments of the shake table was then subtracted from this displacement to obtain the displacement of the top of the specimen relative to the footing. Lateral forces applied at the top of the specimen were measured by the load cell of the mass rig link. As the mass rig has a four-hinge mechanism at the base, the entire inertial force of the mass rig is transferred to the specimen and the total base shear of the specimen can be assumed to be equal to the lateral force recorded by the load cell.

The measured force-displacement relationships for all nine runs are shown in Figs. 5.59 through 5.67. Negative displacements are representative of relative displacements to the north and positive displacements of relative displacements to the south. The response of the specimen for the first run is shown in Fig. 5.59. As can be observed, very little energy was dissipated and the response of the specimen was linear, which indicates no yielding of reinforcement. During run two, the specimen appears to be slightly softer than what was observed during run one, but the response was still essentially linear (Fig. 5.60). A similar change was observed in run 3; The specimen softened further, little energy was dissipated, and the response of the specimen remained essentially linear (Fig. 5.61). During run four, the response of the specimen became softer and very slightly nonlinear, indicating that some of the longitudinal column reinforcement had yielded. This can be observed in the slight widening of the hysteretic loops shown in Fig. 5.62. The response of the specimen also started to become slightly asymmetric during run four, with larger displacements to the north. Run five showed a similar response, with the hysteretic loops widening further and the response becoming softer indicating further yielding of the column longitudinal reinforcement (Fig. 5.63). The continuous softening of the specimen was to be expected as the specimen was progressively damaged and longitudinal bar strains in the columns increased.

During run six, the column response become symmetric and the general shape of the hysteresis loops began to curve, indicating more substantial yielding than was previously observed (Fig. 5.64). Additionally, the peak lateral forces of the specimen did not significantly increase from run five, which shows that the specimen was beginning to reach its force capacity. Figure 5.65 shows the response of the specimen for run seven. In run seven, the specimen response remained symmetrical, and the force-displacement loops significantly widened. Run eight showed significant widening of the force-displacement loops, a very slight increase in the peak lateral force, and the response of the specimen was asymmetric with significantly larger displacements to the south. Additionally, run 8 resulted in a residual drift of 0.44 in (11.2 mm) to the south (positive

displacement). The force-displacement relationship of the specimen during run eight is shown in Fig. 5.66. During run nine, the residual displacement to the north continued to increase and a large residual displacement of 2.6 in (66 mm) was observed after the run was completed (Fig. 5.67). This is indicated by the cluster of low-amplitude loops in the 2 to 5 in (51 to 127 mm) displacement range. The response of this specimen was highly asymmetric due to this residual displacement with the displacement to the north being significantly lower than what was observed in run eight.

Overall, the specimen force-displacement relationship showed the gradual widening of the hysteresis loops from runs four to nine, which indicates good energy dissipation and stable ductile response with no strength degradation. Figures 5.68 and 5.69 show the individual and cumulative energy dissipation of each run, respectively, which was determined by calculating the area within the force-displacement loops. Note that the individual energy dissipation increased with the progression of runs. The ground motions induced significant displacements in both directions despite the asymmetric response during the last two runs and little residual drift was observed after the first eight runs.

The envelope of cumulative hysteresis curves was obtained to capture the overall force-displacement response of the specimen in both the north and south directions (Fig. 5.70). The envelope of the south direction response (dominant response) was used as the "effective experimental pushover" curve for the specimen, which was used to determine the lateral load and displacement/drift capacity. An elasto-plastic relationship was then used to idealize the curve and is shown in Fig. 5.71. The elastic portion of the idealized curve was formed by passing a line from the origin to the point where yielding of column longitudinal reinforcement first occurred and the plastic portion of the curve was formed by balancing the areas of the curves. The effective yield point of the specimen was 42.1 kips (187 kN) at 0.95 in (24.1 mm) and the maximum measured displacement of the specimen was 11.2 in (284 mm), which equates to a drift ratio of 12.6 percent.

5.5 Displacement History

The specimen relative displacement history for runs one through nine is shown in Fig. 5.72. Positive displacements indicate movement to the south. Although slight residual drift was accumulated over the later runs, significant residual drift was not observed until the final run (run 9). Run eight resulted in a small residual drift of 0.44 in (11.2 mm, 0.5% drift ratio) and run nine resulted in a large residual displacement of 2.6 in (66 mm, 12.6% drift ratio). This is evidence that the specimen did not reach a high level of displacement through the accumulation of residual displacements and was tested to high levels of displacement in both directions prior to run nine. Thus, lateral displacement was fully cyclic and placed cyclic force and deformation demand on the column-cap connections during testing.

The maximum relative displacements, lateral forces, and drift ratios for all the runs are listed in Table 5.4. Note that the displacements were measured at the top and bottom of the northern cap beam face and averaged to coincide with the effective specimen height, which was taken as the column clear height plus one-half of the cap beam height. The effective specimen height was 89 in (2261 mm). Drift ratio was calculated by dividing the specimen displacement by the specimen effective height.

To determine the effect of hinge shear deformation on the overall displacement of the column, horizontal displacement transducers were placed on the east and west side of the columns near the base. The measured local hinge displacements were then averaged for each column. Because these transducers were located above the two-way hinges, the data included displacement due to column base rotation. The horizontal displacement due to rotation of the columns, which was measured with vertical transducers, was subtracted from the average displacement readings to obtain hinge throat shear deformation. The horizontal displacement due to rotation was calculated by multiplying the rotation at the base of the columns by the vertical distance of the transducers from the footing top face. Figures 5.73 to 5.81 show the shear deformation histories of both columns for each run. Note that deformations to the south are represented by positive values. As can be seen, the shear deformation histories of the two columns are consistent, which indicates similar demands were imposed on both columns. Note that one of the displacement transducers on the southern column had significantly different readings during run nine; this was likely caused by spalling of the concrete columns landing on the transducer. Thus, the data for the transducer was deemed invalid and was not used. Table 5.5 lists the maximum absolute hinge shear deformation of each column for each run and the percent contribution of shear to the total relative displacement measured at the top of the specimen. The contribution of shear to the total displacement of the specimen was relatively small, but not negligible. The maximum contribution of 6.57 percent was measured during run 5. The percent contributions of shear to the total displacement fluctuated between runs and no trend was observed.

5.6 Strains

The peak strain values in compression and tension, or minimum and maximum for cases when tension only or compression only happened, as recorded by all gauges in each run are listed in Tables 5.6 through Table 5.29. Each strain gauge is prefaced with an N or an S indicative of the north (CIP) and south (ABC) columns. The locations of all strain gauges are shown in Figs. 4.15 through 4.18. Negative values indicate tensile strain and are bolded if they exceed the measured yield strain. All strains are reported as microstrain. The dashed lines indicate invalid data from strain gauges that were damaged or malfunctioned before or during testing.

5.6.1 ABC Column (South)

Tables 5.6 through 5.10 show the peak strains of the column longitudinal reinforcement at various sections. No yielding occurred at any of the longitudinal cross sections of the south column (see Fig. 4.15) during the first three runs. Additionally, the maximum tensile strains on the north and south sides of the column were close. This is attributed to the symmetric displacements of the specimen for these runs. Yielding first occurred during run four at every section except 9 in (229 mm) above the cap-column interface (Section 1-1). The maximum tensile strains of the northern side of the column were higher as a result of the larger displacement to the north for this run. Similar observations were made for the maximum tensile strains during run five, i.e. yielding at all sections except at 9 in (229 mm) above cap-column interface. Larger strains were observed due to larger displacements, and larger strains of northern reinforcement were attributed to slightly higher displacements to the north. The magnitude of the maximum

tensile strains continued to increase as the runs progressed due to the larger displacements. The specimen had symmetric displacement response during run six and the maximum tensile strains were no longer dominated by the northern column reinforcement as a result. The maximum tensile strains of run seven were also symmetric as the specimen response was symmetric. Many of the strain gauges reached their limit during run eight and were no longer providing valid data. From the remaining gauges, it can be observed that significantly larger maximum tensile strains were measured on the southern longitudinal reinforcement. This was caused by the largely asymmetric response of the specimen during this run. Run nine damaged more strain gauges, but it can be observed that the peak strains of the northern longitudinal reinforcement were lower than those observed during run eight. The peak northern displacement of the specimen during run nine was lower than run eight, which resulted in lower strains at these gauges.

Strain gauge profiles were generated to visually compare the minimum and maximum longitudinal reinforcement strains at various sections along the column cage. Figures 5.82 and 5.83 show the strain profiles for runs one through five and six through nine, respectively. The measured yield strain was 2255 microstrains. Note that negative distances represent sections below the column-cap interface, while positive ones represent sections within the cap beam. Larger peak strains were observed with the progression of the runs except for run nine during which some of the gages failed and did not provide reliable data. Typically, the largest strains were seen at the column-cap interface (Section 3-3) and 6 in (152 mm) below the interface (Section 4-4) in the plastic hinge region.

Tables 5.11 to 5.15 show the peak strains of the column spiral at various sections. The spiral did not yield during shake table testing. Figures 5.84 and 5.85 show the spiral strain profiles at various sections along the column cage for runs one through five and six through nine, respectively. Note that negative distances represent sections below the column-cap interface, while positive ones represent sections within the cap beam. The peak strains of each run were typically measured at 12 in (305 mm) below the column-cap interface and increased with the progression of runs.

The peak strains of the hoops located at 4.5 in (114 mm) and 9 in (228 mm) above the column-cap interface are shown in Table 5.16 and Table 5.17, respectively. The peak strain of these hoops was about 20 percent of yield, indicating some contribution to confinement. The strains increased with each run, but neither hoop had strictly higher strains than the other.

Tables 5.18 to Table 5.23 show the peak strains of the cap beam transverse reinforcement (stirrups, vertical ties, horizontal ties). Yielding was observed in one of the stirrups at 14 in (356 mm) inward from the center of the column, but the data was not reliable because the yielding was measured during run 1, which is not expected. Furthermore, the data was not consistent with those of other nearby bars. The largest tensile strains were measured on the stirrups within the pocket region and reached 55 percent of the yield strain. The strain gauges on the horizontal and vertical ties, which were located outside of the cap beam pocket, only reached a peak strain of about 12 percent of yield. This indicates that there was low demand placed on the cap beam.

5.6.2 CIP Column (North)

Tables 5.6 through 5.10 show the peak strains of the column longitudinal reinforcement at various sections. No yielding occurred at any of the bars in the north column (see Fig. 4.15) during the first run. Yielding was first measured by one strain gauge (N SG 40) 6 in (152 mm) below the cap-column interface (Section 4-4) during run 2. Note that this strain gauge measured much larger strains than other gauges on this longitudinal bar (N SG 30 and 50) and other gauges at this section. Thus, the data from this strain gauge may not be valid. The remaining gauges measured similar maximum tensile strains on the north and south sides of the column during runs one to three. This can be attributed to the symmetric displacements of the specimen for these runs. Yielding was measured at most sections during run four and all sections during run five. The maximum tensile strains in the northern side of the column were higher during these runs as a result of larger displacements to the north. The magnitude of the maximum tensile strains continued to increase as the runs progressed due to the larger displacements. The displacement response was symmetric during run six, and the maximum tensile strains were no longer dominated by the northern longitudinal reinforcement as a result. Many of the strain gauges stopped functioning properly during run seven and were no longer providing valid data. From the remaining gauges, it can be observed that the peak strains of the northern longitudinal reinforcement during run nine were lower than those observed during run eight. The peak northern displacement of the specimen during run nine was lower than run eight, which resulted in lower strains at these gauges.

Figures 5.86 and 5.87 show the maximum longitudinal column strain profiles for runs one through five and six through nine, respectively. Larger peak strains were observed with the progression of the runs except for run seven due to the absence of sufficient data. Typically, the largest strains were seen at the column-cap interface (Section 3-3) and six inches below the interface (Section 4-4) in the plastic hinge region.

Tables 5.11 to 5.15 show the peak strains of the column spiral at various sections. The spiral yielded at one location (N SG 57) during run three but remained below yield for the remaining runs. Considering the trend in all other gages, the data from this gage is unreliable. Figures 5.88 and 5.89 show the spiral strain profiles at various sections along the column cage for runs one through five and six through nine, respectively. The measured yield strain was 2070 microstrains. The peak strains in runs one to six were typically measured at 12 in (305 mm) below the column-cap interface and above the column-cap interface for runs seven to nine.

The peak strains of the hoops located at 4.5 in (114 mm) and 9 in (228 mm) above the column-cap interface are shown in Table 5.16 and Table 5.17, respectively. The peak strain in these hoops was about 16 percent of yield, indicating some contribution to confinement. The strains typically increased with each run and the lower hoop had higher strains than the other.

Table 5.18 to Table 5.23 list the peak strains of the cap beam transverse reinforcement (stirrups, vertical ties, horizontal ties). Yielding was observed in one of the stirrups at 14 in (356 mm) inward from the center of the column, but the strain gauge was likely damaged as the yielding was measured during run 1, which was unlikely. The largest tensile strains were measured on the stirrups within the pocket region and reached 61 percent of the yield strain. The strain gauges on the horizontal and vertical ties, which

were outside of the cap beam pocket, only reached a peak strain of about 8 percent of yield. This indicates that there was low shear demand placed on the cap beam.

5.6.3 CAM Bars

Recall that CAM bars were used as the longitudinal reinforcement at the column base hinges. The peak strains of the two-way hinge longitudinal reinforcement (CAM bars) at various sections are shown in Tables 5.24 through 5.26. Note that most strain gauge labels were lost during construction, but the remaining strain gauges were organized with the assumption that the largest compressive strains would be measured at the center of the hinge throat due to the reduced section size of the two-way hinge. This assumption was made based on larger compressive strains measured by S SG 102 (located at the center height of the two-way hinge) during run 1 and the large tensile strains measured during other runs. The yield strain of the CAM bars was determined by dividing the average yield stress by the average elastic modulus (Table 4.3) and was estimated to be 5300 microstrains. The maximum strains exceeding the yield strain are shown in bold font.

During the first few runs, large compressive strains relative to the column longitudinal bars were measured at the center length of the two-way hinge. This was due to the reduced diameter of the two-way hinges and the vertical loads and the lower modulus of elasticity of CAM compared to that of steel. Yielding of the CAM bars did not occur until run four at the hinge throats. Typically, the peak strains increased from runs six through nine but there were some instances where the maximum tensile strain decreased during run nine. This is likely due to the decrease in peak displacement to the north from run eight to run nine.

Figures 5.90 to 5.93 show the strain profiles of the north column CAM bars and the south column CAM bars. The strain profiles of both columns for runs one through five show that both the maximum and minimum strains were measured at the mid-height of the two-way hinges, which coincided with the center of the hinge throat. The large tensile strains at this location are due to small cross section of the hinge that concentrate rotation of the column bases at this section, while the large compressive strains are due to the reduced diameter of the two-way hinge. The tensile (negative) portions of the strain profiles remained similar for runs six through nine, but the compressive (positive) portions did not.

Tables 5.27 through 5.29 list the minimum and maximum strains of the two-way hinge spirals for each run at various sections. Note that the spirals were made out of mild steel and not CAM. The measured yield strain in the spiral steel was 2069 microstrains. Yielding was seen at one strain gauge located at the center height of the two-way hinge in the north column. This strain gauge was located along the axis of loading (north-south), which indicates that these strains were due to confinement. Additional peak strain profiles of the two-way hinge spiral are shown in Figs. 5.94 through 5.97. The peak strains typically occurred at the center height of the two-way hinge.

5.7 Curvature and Rotations

Curvatures in the plastic hinge region and rotations at the base of the columns were determined for the direction of loading using data recorded by the Novotechnik displacement transducers. Curvatures were calculated over the top 21 in (533 mm) of the

columns. Three pairs of displacement transducers were used to measure curvature at three sections along the plastic hinge zone of the column. Curvature was calculated using Equation 5-1 and rotation was calculated using Equation 5-2.

$$_i = \frac{\frac{\Delta_{i,1}}{l_{i,1}} - \frac{\Delta_{i,2}}{l_{i,2}}}{x_{i,1} + D + x_{i,2}} \quad (5\text{-}1)$$

$$= \frac{\Delta_{i,1} + \Delta_{i,2}}{x_{i,1} + D + x_{i,2}} \quad (5\text{-}1)$$

where,

ϕ_i = average curvature at section i
θ_i = average rotation at section i
$\Delta_{i,1}$, $\Delta_{i,2}$ = measured displacements from Novotechnik at section i
$l_{i,1}$, $l_{i,2}$ = gauge lengths at section i
$x_{i,1}$, $x_{i,2}$ = distance from column face to Novotechnik at section i
D = column diameter

The peak positive and negative curvatures at each pair of displacement transducers was calculated for each run and is shown in Tables 5.30 and 5.31, respectively. Note that positive curvatures are directed to the south. The opposite is true for the rotations at the base of the specimen.

5.7.1 ABC Column

As can be seen from Tables 5.30 and 5.31, larger curvatures were measured with the progression of runs except during run nine. Some of the minimum curvatures were lower than what was observed during run eight as the displacement of the specimen to the north was smaller during run nine. Note that the maximum curvatures were also reduced during run nine at the two lowermost sections. Curvature profiles were generated to show the minimum and maximum curvatures at the top of the column at the three sections instrumented. Figures 5.98 and 5.99 show the curvature profiles for runs one through five and runs six through nine, respectively. The curvature profiles show that the plastic hinge is formed near the column-cap connection, indicated by the decrease in peak curvature values the further the section is from the interface.

Rotations at the base of the columns were also estimated and shown in Fig. 5.100 and Tables 5.32 and 5.33. Note that the sign convention switches for the rotations measured at the base, which means that positive rotations are toward north. As can be seen the maximum rotations were slightly larger than minimum rotations during runs four and five as a result of the slightly asymmetric displacement response of these runs (slightly higher displacements to north). The opposite is apparent during runs eight and nine, where the minimum rotations are much larger than the maximum rotations due to the largely asymmetric response of these runs (significantly larger displacements to south).

5.7.2 CIP Column (North)

A very similar curvature response was observed at the top of the north column: larger curvatures with progression of runs except minimum curvatures during run nine, both the maximum and minimum curvatures decreased from run eight to run nine at the lower sections, larger curvatures were measured close to column-cap interface. Figures 5.101 and 5.102 show the curvature profiles for runs one through five and runs six through nine, respectively.

The rotation response at the base of the north column (Fig. 5.103) resembled the response of the south column, i.e. maximum rotations larger than minimum during runs four and five, much larger minimum rotations during runs eight and nine, and a decrease in maximum rotation from run eight to run nine.

5.8 Accelerations

Acceleration was measured at three locations on the specimen during testing using triaxial accelerometers. Data was collected for the X (north-south), Y (east-west), and Z (vertical) axes at each location. One of the accelerometers was placed on the footing top face for redundancy in measuring the shake table acceleration. The peak accelerations recorded along the Y and Z axes of the footing were only 0.027g and 0.057g, respectively. These accelerations were deemed negligible. The small accelerations in these directions indicate that the test setup was properly aligned as intended.

Figure 5.104 compares the accelerations measured by the footing accelerometer in the X direction and the shake table for run 9. There was very close correlation between the measurements of the instruments, indicating that the shake table internal instruments were a reliable source of input ground motion acceleration data. Accelerometers were also installed on the north and south ends of the specimen top. Figures 5.105 through 5.113 show the acceleration history in the X direction measured by both accelerometers at the top of the specimen for each run. Because of the large axial stiffness of the cap beam, the acceleration histories were expected to be the same. It can be seen that there was good correlation between the two accelerometers, which indicates similar accelerations were seen on both ends of the specimen and that the accelerometers were oriented correctly. It should be noted that large out-of-plane accelerations were measured at the top of the specimen during the last two runs with the peaks being about 50 and 100 percent of the in-plane accelerations in runs eight and nine, respectively. These accelerations are attributed to the out-of-plane displacements induced by the safety frame pulling the specimen eastward by approximately 0.7 in (18 mm) and 1 in (25.4 mm) in runs eight and nine, respectively.

5.9 White Noise

In addition to the nine runs simulated on the shake table, white noise motions with an amplitude of approximately 0.1g were applied before each run and after the last. The specimen response during the white noise motions was used to estimate its low-amplitude fundamental period and to detect any irregularity is the progression of the test, realizing that once the structure becomes nonlinear, the effective period depends on the amplitude of displacements. Extracting the low-amplitude period was done through the use of FFT

of the acceleration data at the top of the specimen. The Fourier amplitude spectrum of the column acceleration data was plotted for each white noise run. These plots showed noticeable peaks with characteristics of possible effective fundamental frequencies. The fundamental frequency and period were estimated from the peaks in these plots. Table 5.34 lists the fundamental period from each white noise test. The measured initial period of the specimen (0.40 seconds) showed good correlation with the hand calculation for cracked period of the specimen determined during the pretest analysis (0.364 seconds). As the specimen accumulated damage, the period of the specimen continued to increase and reached a maximum period of 1.14 seconds after the final run.

5.10 Comparison of Performance of ABC and CIP Columns

One of the primary objectives of this study was to evaluate and compare the performance of the novel CIP pocket connection to that of the ABC connection. This section summarizes the primary differences in the observed damage, measured strains, and measured curvatures of the columns to determine the viability of CIP pocket connections. Note that this section will only focus on the cap-column connections and not the CAM reinforced two-way hinges since the details of the two-way hinges in both columns were the same.

5.10.1 Observed Damage

The observed damage in the plastic hinge zone of the columns was similar for runs 1 through 6 and showed the typical formation and extension of flexural cracks. All apparent damage of these runs was concentrated in the plastic hinges. Run 7 resulted in significant spalling of the cover concrete on north and south faces of the CIP column plastic hinge (Figs. 5.10 and 5.11), while only minor spalling was observed on the north and south faces of the ABC column (Figs. 5.36 and 5.37). The most notable difference of the damage after run 7 was the cracking of the cap beam soffit at the CIP pocket connection (Fig. 5.37). Run 8 resulted in the progression of spalling in both columns, exposing the transverse column spirals. The spalling was more significant on the south side of the CIP column and the north side of the ABC column (Fig. 5.12 and Fig. 5.39). Additionally, the damage of the cap beam soffit at the CIP connection was exacerbated during run 8. Run 9 shows the most apparent damage difference between the two connections. Although there was major spalling of both columns, the spalling of the cap beam soffit at the CIP connection spread deeper into the cap beam (Fig. 5.42). While this was not seen at the ABC connection, there was significant cracking of the high-strength grout in the socket connection. There was no apparent damage in either joint for the entirety of testing.

5.10.2 Strains

In addition to the observed damage, the peak strains of the longitudinal column bars, transverse column spirals, and transverse cap beam bars were compared. From Fig. 5.82 and 5.86, it can be observed that the peak longitudinal columns strains of the two columns were similar during runs 1 through 5. The largest strains were typically measured at the column-cap interface and 6 in (127 mm) below it in both columns. As strain gauges began to fail with the progression of runs, viable strain data became scarce. Figures 5.83 and 5.87 show similar magnitude strains for run 6, but larger strains in the

ABC column in run 7, with the peak being 35 percent higher. It appears that the ABC column connection was stiffer than the CIP column connection, hence allowing for development of larger longitudinal bars strains in the ABC column. Sufficient data was not available for the CIP column to make a conclusive statement for runs 8 and 9.

Figures 5.84 and 5.85 for ABC column, and Figs. 5.88 and 5.89 for the CIP column show the peak spiral bar strain profiles for runs 1 through 9. The peak strains in the ABC column were typically measured at 12 in (305 mm) below the column-cap interface, while peak strains of the CIP column spiral were typically measured at 4.5 in (114 mm) above and 12 in (305 mm) below the interface. This is further evidence of the higher stiffness of the ABC column connection. Although the peak strains of the column spirals were typically measured at different locations, the peak strains were similar of similar magnitude and close to the yield strain.

Tables 5.16 and 5.17 show the peak strains of the hoops within the connections. The peak strains in the hoops of the ABC connection at 9 in (229 mm) above the column-cap interface exceeded those of the CIP connection, with the difference during run 9 being 300 percent. The strain of the hoops at 4.5 in (114 mm) above the interface were comparable in both connections. Note that the peak strains of the hoops were only about 20 percent of the yield strain (2070 microstrains). Tables 5.18 to 5.23 show the peak strains of the cap beam transverse reinforcement. In both connections, the peak strains were measured on the stirrups surrounding the pockets. The magnitudes of these strains were comparable and approximately 60 percent of the yield strain.

5.10.3 Curvature

Figures 5.98 and 5.99 for the ABC column, and Figs. 5.101 and 5.102 for the CIP column, show the peak curvature profiles for runs 1 through 9. The largest curvatures were measured at 7 in (178 mm) below the column-cap interface in both columns. Similar magnitudes were measured in both columns during runs 1 through 5 with the CIP column curvatures being slightly higher. The CIP column typically had larger peak curvatures than the ABC column in runs 6 through 9 as well. It should be noted that the CIP column curvatures at 14 in (356 mm) below the interface, which was not larger than the curvatures measured at 7 in (178 mm) below the column-cap interface, were significantly larger than their counterpart curvatures in the ABC column.

5.10.4 Summary

The experimental results and analysis indicate that the CIP connection can perform well under seismic loading. However, under large drifts exceeding 7 percent, the stiffness of the CIP connection appeared to be lower than the ABC connection stiffness, which resulted in smaller column longitudinal bar strains. Damage in the ABC pocket was more concentrated to the plastic hinge zone of the column in contrast to the CIP pocket, which had significant spalling at the cap beam soffit.

Chapter 6. Post-Test Analytical Studies and Design Recommendations

6.1 Overview

A post-test analytical model was developed after shake table testing to explore where simplified modeling techniques could be applied to estimate the response of the tested specimen under earthquake loading. The post-test analytical model assumptions were similar to the pre-test analytical model and adopted using OpenSees. However, additional features were added, and input parameters were modified to more accurately represent the test setup, actual achieved loading, and material properties. To evaluate the ability of the model to determine the specimen responses, the analytical results were compared to the measured results. Additionally, the performance of the test specimen was revisited to determine if the design method used was appropriate and identify any necessary refinement. This chapter includes the information about the revised analytical model, a comparison of the new analytical results with the measured data, and a discussion of recommendations for the design of CIP pocket connections.

6.2 Refined Analytical Model for Post-Test Analysis

A schematic of the updated analytical computer model is shown in Fig. 6.1. The material properties of the analytical model were updated to reflect the measured material properties discussed in Chapter 4. These changes were made to the constitutive properties of the *Concrete01*, *ReinforcingSteel*, and *SelfCentering* CAM material models. Tables 4.1 through 4.3 summarize the measured material properties of the test specimen used for the three aforementioned material models, respectively.

The model was also updated to utilize the achieved acceleration histories of the runs measured by the internal instruments of the shake table. The input earthquake records were changed using the achieved shake table acceleration histories and were filtered and spliced with 15 seconds added before each successive run. The acceleration histories were filtered using a low-pass band filter with a cut-in frequency of 15 Hz to eliminate high frequency noise as can be seen in Fig. 6.2. Utilizing the spliced input acceleration history allowed the model to capture the accumulation of damage as testing progressed and adding time in between runs was done to allow for free vibration and response damping. This is a realistic representation of the actual testing procedure where damage accumulated with each run and the specimen returned to a resting position between runs.

The elements representative of the cap beam were not changed from the linear elements originally adopted for the pre-test analysis. As there was no observable damage of the cap beam and the joints, and the strains of the transverse reinforcement did not yield, the cap beam was confirmed to have remained essentially elastic. Thus, modeling of the cap beam using linear elastic elements remained consistent between the pre and post-test analytical models.

The effects of bond-slip were added to the post-test analytical model. The effects of bond-slip were only included at the top of the columns. The bases of the columns consisted of the two-way hinges reinforced with CAM bars spliced to rebar using headed bar couplers, which provided proper mechanical anchorage and effectively eliminated

bond-slip at this location. Bond-slip at the top column connections was accounted for using the method proposed by Tazarv and Saiidi [6]. To include bond-slip using this method, a geometrically identical column section with a different *ReinforcingSteel* model is created and applied to the integration point at which the effects of bond-slip are expected. The *ReinforcingSteel* model used in the bond-slip column section differs in that the elastic modulus of the longitudinal reinforcement is reduced, and the strain hardening and ultimate strains are slightly increased. Including bond-slip in the model essentially softens it.

Another important change to the model was the addition of the steel load transfer beam at the top of the specimen and the relocation of mass nodes to the centroidal axis of this beam. This was done as the inertial force of the mass rig was applied to the centroid of the load transfer beam during testing, not directly to the cap beam (Figs. 4.8 and 4.14). This was not accounted for in the pre-test analytical model to expedite the analysis. The horizontal elements, representative of the load transfer beam, were modeled using truss elements with *ReinforcingSteel* properties. A large area was defined for the truss elements as axial shortening was negligible due to the relatively low axial force. The load transfer beam was vertically connected to the cap beam elements using rigid elements. Inherent damping was still modeled using Rayleigh damping, which used the first two modes of the model and a 5 percent damping ratio for calculating the Rayleigh coefficients. The damping ratio of 5 percent was used as it is representative typical bridges and common practice.

6.3 Comparison of Test and Analytical Results

The calculated displacement histories and peak responses of the model were compared to the measured results for each run and are shown in Figs. 6.3 through 6.11. In the first four runs, the model overestimated the lateral displacement of the top of the specimen as seen in Figs. 6.3 through 6.6. Note that the first two runs had very small accelerations representing only 14 and 27 percent of the design earthquake. These small runs would keep the analytical model in the linear range, whereas in reality slight nonlinear actions are expected in the cementitious materials, which could lead to some energy dissipation. The damping ratio of 5 percent in the analytical model was not able to make up for that energy dissipation. It can be seen that although the analytical model was not accurately replicating the measured results, the model was gradually able to yield more accurate results from runs 3 and after. In run 5 (representing the design earthquake), the model led to a very close correlation with the measured displacement history of the specimen and this is shown in Fig. 6.7. The correlation was close in terms of overall trend as well as amplitudes, the waveforms, and time windows with relatively large displacements. The model captured the response of the specimen relatively well during runs 6 and 7 but slightly underestimated the peak displacements. A comparison of the analytical and measured results for runs 6 and 7 are shown in Figs. 6.8 and 6.9, respectively. The model did not capture the response for the runs 8 and 9 accurately and this is shown in Figs. 6.10 and 6.11. This is likely due to the largely asymmetric response of the specimen and possibly the relatively large out of plane accelerations observed during these runs; an effect that was not accounted for. Note that these runs represented unrealistically large earthquakes of 300 percent and 350 percent of the design motion.

In addition to the displacement histories, the force-displacement hysteretic relationship of the analytical model and the test specimen were compared. Table 6.1 and 6.2 summarize and compare the analytical model and the test specimen in terms of peak displacement and peak lateral force, respectively. Figures 6.12 to 6.14 show the force displacement relationship of the first three runs. Both peak forces and displacements were largely overestimated by the analytical model for these runs. The analytical model overestimated the peak displacements for run 4 as well, but only slightly overestimated the peak lateral force (Fig. 6.14). Figure 6.16 shows a much better correlation for run 5 and demonstrates that the analytical model only slightly overestimated the peak displacement but not the peak lateral force. Figure 6.17 and 6.18 show that the analytical model results closely resembled the measured hysteresis loops during runs 6 and 7. The analytical model slightly underestimated the peak lateral force and displacement of the test specimen during these runs. During run 8, the analytical model began to significantly underestimate the peak displacement of the specimen. This is only the case for when the specimen displaced to the south as the analytical model accurately captured the peak force and displacement to the north (Fig 6.19). This may be due to the largely asymmetric response of the test specimen during this run. Similarly, the analytical model accurately captured the peak force and displacement to the north but not the south during run 9. The comparison is shown in Fig. 6.20 and the difference is likely due to the large residual displacement of the test specimen during this run, which was not captured by the analytical model.

The relatively simple OpenSees [16] model was able to capture the global response of the specimen to some extent, but accuracy for very low-amplitude and very high-amplitude earthquakes was inadequate. Of course, it can be argued that the high-amplitude runs of the test are not representative of real earthquake properties, and accurate estimation of the response might not be of interest. The implementation of bond-slip using the method proposed by Tazarv and Saiidi [6] was effective in essentially softening the computer model of the specimen. Modeling of the load transfer beam did not change the results of the analysis significantly. One aspect of the model that could have improved the results includes more accurate material modeling of the CAM bars. The *SelfCentering* material model used for the CAM bars only allows two stress-strain slopes to be defined (Fig. 3.3), whereas the measured stress-strain curves (Fig. 4.5 to 4.7) indicate that the stress-strain curve is curvilinear. Although more accurate modeling of the CAM bars is preferred, the effect of the CAM bars on the global response of the specimen was minimal and may result in only minor improvements to the model. A more important part of testing that was not accounted for in the analytical model was the out-of-plane accelerations observed at the top of the specimen during runs 8 and 9. To account for these accelerations, a three-dimensional analytical model is necessary that accounts for the links in the safety frame restraining the top of the specimen under very strong motions.

6.4 Comments on Connection Design Method

As no guidelines existed for the design of the CIP pocket connection tested in this study, the design was developed using a combination of the ABC pocket connections design recommendations by Tazarv and Saiidi [1] and the AASHTO Guide Specifications for LRFD Seismic Bridge Design [14]. The performance of the connection was evaluated and used to develop preliminary design recommendations for CIP pocket connections emulating ABC pocket connections. The primary differences between the CIP pocket connection and a standard CIP joint are: (1) the bundling of cap beam longitudinal reinforcement, (2) the elimination of vertical joint reinforcement within the joint, and (3) the addition of transverse reinforcement adjacent to and near the joint.

Bundling of cap beam longitudinal bars followed the requirements for bundled rebar as specified in Section 5.10.3.1.5 of the AASHTO LRFD Bridge Design Specification [23]. Bundling of bars was done to allow the column reinforcement cage to extend into the joint unimpeded. As the bundling of bars resulted in a relatively large unreinforced around the pocket, additional bars were placed to reduce temperature and shrinkage cracking (Fig 2.11). These bars were designed in compliance with Section 5.10.6 of AASHTO [23] and were only included outside of the pocket connections. The connection demonstrated capacity protected behavior and minimal temperature and shrinkage cracks were observed in the cap beam. A previous study conducted by Schwartz et al. [4] tested the same connection in the out-of-plane direction and had similar results. Thus, it was deemed that the AASHTO design specifications for bundled bars and temperature and shrinkage bars are appropriate for use in the design of CIP pocket connections.

Typically, CIP connections are reinforced with vertical bars to help resist joint shear forces, but they were eliminated within the joint of the CIP pocket connection tested. These bars were removed within the joint as they would need to be threaded through the column reinforcement cage. This further improved the constructability of the connection. The tests showed that the vertical ties that were adjacent to the joint did not experience significant demands. The maximum tensile strain in the vertical ties outside of the CIP joint region (Fig. 2. 11 and 2.14) was observed to be only 108 microstrains, which is about 5 percent of the yield strain. The study conducted by Schwartz et al. [4] demonstrated larger, but still relatively small, tensile strains in the vertical ties adjacent to the connection when tested out-of-plane, i.e. about 20 percent of the yield strain. Thus, the removal of the vertical joint reinforcement was deemed appropriate for the design of CIP pocket connections because the bars placed adjacent to the joint provided sufficient strength.

Additional transverse reinforcement was placed around the pocket connection due to the removal of horizontal ties normally used in conventional CIP joints. Transverse hoops surrounding the pocket connection were added to ensure the joint was properly confined and can be seen in Fig. 2.15. The hoops were designed as per Tazarv and Saiidi [1] design recommendations for ABC pocket connection and had a transverse reinforcement ratio equal to that of the column transverse reinforcement. The design recommendations only required that hoops be placed in the lower half of the cap beam. The hoops surrounding the CIP pocket connection reached a maximum tensile strain of 332 microstrains, which 17 percent of yield. This indicated that the extra hoops were engaged in confining the connection. The study conducted by Schwartz et al.[4] resulted

in larger strains of the hoops surrounding the connection when tested out-of-plane, reaching 30 percent of yield. Thus, it was deemed that the hoops surrounding the pockets are necessary in providing confinement and the design guidelines proposed by Tazarv and Saiidi [4] are appropriate for use in the design of CIP pocket connections.

Horizontal ties were also added adjacent to the joints (Fig. 2.14). These ties are normally not included in the design of ABC pocket connections or CIP joints, but were included to address any prying force. Note that these bars were included and designed by Schwartz et al. [4] to address the prying forces that would result from torsion when testing out-of-plane but were not removed for this in-plane loading test for consistency. The horizontal ties were designed to match the same bar size, spacing, and number of bars as the vertical ties and were placed to at two layers on each side of the pockets. The peak tensile strain measured in the horizontal ties adjacent to the CIP pocket connection was 158 microstrains, or 8 percent of yield. These bars appeared unnecessary for in-plane loading, but the horizontal ties of the connection tested by Schwartz et al. [4] reached 47 percent of yield. Thus, it is recommended that additional horizontal ties should be placed around CIP pocket connections.

As the specimen cap beam and column were not considered precast elements, not all guidelines for the design of ABC pocket connections proposed by Tazarv and Saiidi were implemented. The connection should be designed to have sufficient embedment depth for the column to ensure a full-moment connection is developed. In the case of this connection, the reinforcement cage extended 15 in (381 mm) into the cap beam, which was about 30 times the diameter of the longitudinal column bars. Additionally, there was no specified spacing between the column reinforcement cage and the cap beam transverse reinforcement. It is advised that sufficient clearance of between 1.5 to 2 in (38 to 50 mm) be provided to ensure that the cage installed with ease and concrete can flow between the reinforcement. Alternatively, the spacing required between the CMP and the cap beam transverse reinforcement of traditional ABC pocket connections may be used.

Chapter 7. Summary and Conclusions

7.1 Summary

Accelerated Bridge Construction (ABC) expedites the construction of bridges for faster project delivery using precast members. The joint connections of precast members are of interest to bridge designers as they are critical to ensure structural integrity. Joints of bridges in moderate and high seismic regions must also ensure ductile behavior of the columns. Research has shown that ABC is a viable alternative to conventional cast-in-place (CIP) bridge construction. Many types of ABC connections between precast members have been developed with pocket connections having proven to perform well in seismic regions while considerably simplifying the construction process. The construction of joints in traditional CIP construction can be difficult and time-consuming due to reinforcement congestion resulting from the intersection of cap beam and column bars.

The primary objective of this study was to adapt the design and detailing guidelines for ABC pocket connections in CIP construction and evaluate CIP column-cap beam connections that adhere to ABC detailing methods. One 0.33-scale two-column pier model was built to evaluate and compare the seismic performance of a CIP column-to-cap beam pocket connection to that of a similarly designed ABC column-to-cap beam pocket connection. The present study focused on the in-plane performance of the connections but was complementary to a recent study conducted by Schwartz et al. [4] that assessed this type of connection under out-of-plane loading.

The secondary objective of this study was to determine the effectiveness of Copper-Aluminum-Manganese (CAM) alloy shape memory alloy (SMA) bars in reducing hinge moment transfer and their seismic performance when coupled with mild steel using headed rebar couplers. The same pier model used to address the primary objective of the study incorporated SMA reinforced two-way hinges to evaluate their performance under seismic loading.

The first task of this project consisted of a literature review to develop an in-depth understanding of the subjects pertinent to this research. These subjects consisted of different earthquake-resistant ABC connections and their design guidelines, structural applications of CAM bars, and the use of mechanical splices with SMAs.

Design and detailing of the two-column pier model served as the second task of this project. A novel CIP pocket connection was developed and incorporated into the 0.33-scale two-column bent representative of a prototype bridge pier. The bridge pier was a component of an actual CIP box girder bridge with an integral bent cap located in Carson City, Nevada. The proposed design guidelines for ABC pocket connections [1] was used to develop the CIP pocket connection and the ABC pocket connection. The specimen was a two-column bent comprised of two columns, a cap beam, and a footing. The columns and pockets had identical reinforcement but were constructed differently (CIP and ABC). A two-column bent layout was used as this would allow the two different connections to be compared directly for the in-plane testing direction. Design guidelines for steel rebar hinges were used to develop the two-way hinges of the specimen despite being reinforced with SMA bars. There were no guidelines available for design of SMA-reinforced two-way hinges. The design and construction of the SMA hinges in the two columns was identical.

Before the design of the test model was finalized, a preliminary analytical model of the specimen was developed under the third task to estimate its response under seismic loading and ensure that the test is feasible considering the shake table capacity. The test specimen was subjected to several earthquake records using the analytical model to develop a loading protocol that would impose high demands on the specimen and eventually failure. A ground motion from the 1940 Imperial Valley-02 earthquake event recorded at the El Centro Array #9 station was selected, based on the pre-test analysis, and used for the shake table testing.

Investigation of the seismic performance and behavior of the connections when exposed to shake table testing was the fourth task of the project. The specimen was subjected to nine runs at increasing amplitudes, with the fourth run corresponding to the design level earthquake. The performance of the specimen was evaluated through observed damage as well as strain, displacements, forces, and acceleration data collected by 240 instrument channels during testing. Following the experimental studies, the measured data was analyzed. This included analysis of the force-displacement relationship, rotations, curvatures, peak strains, strain profiles, and energy dissipation. The results were utilized to compare the performances of the two connections and determine the feasibility and any drawbacks of ABC pocket simulated CIP cap-column connections.

The fifth task of this project involved refining and expanding the preliminary analytical model of task three. Material properties were updated to match the measured material properties and additional elements and modeling techniques were implemented to more accurately capture the response of the specimen under seismic loading.

In the sixth task of the study, design of CIP pocket connections and SMA reinforced hinges was reviewed and discussed in light of the experimental and analytical studies and the seismic performance of the connections. The results of the study were summarized subsequently, and key observations and conclusions are provided next.

7.2 Observations

The primary observations from the experimental and analytical parts of the study were as follows:

1) Construction of the CIP connection was facilitated by using the design guidelines for ABC pocket connections to bundle longitudinal cap beam bars around the pocket.
2) The CIP emulating ABC pocket connections performed well under in-plane dynamic loading and had a similar response to that of the ABC connection. Additionally, an identical connection tested by Schwartz et al. [4] performed well when dynamically loaded in the out-of-plane direction.
3) Plastic hinges in both columns developed under the cap beam and met the expectation that columns should be the source of earthquake energy dissipation.
4) The transverse cap beam stirrups surrounding the pocket approached 60 percent of the yield strain when the connection was subjected to in-plane loading and 40 percent when loaded out-of-plane [4].
5) The transverse hoops surrounding the pocket reached 16 percent of the yield strain when loaded in-plane and 30 percent when loaded out-of-plane [4].

6) The transverse vertical cap beam ties placed outside the joint did not exceed 5 percent of the yield strain when loaded in-plane and reached 20 percent when loaded out-of-plane [4].
7) The transverse horizontal cap beam ties placed outside the joint did not exceed 8 percent of the yield strain when loaded in-plane but reached 47 percent when loaded out-of-plane [4].
8) The CAM reinforced two-way hinges using headed rebar couplers performed well under seismic loading. The CAM bars yielded substantially, but the joint integrity was maintained.
9) The post-test analytical model was capable of accurately capturing the displacement and hysteretic force-displacement response of the specimen under moderate and strong earthquakes. However, it was not able to reproduce the response under extremely strong earthquakes that correspond to over three times the design ground motions.

7.3 Conclusions

The primary experimental and analytical conclusions of the study were as follows:

1) Bundling of longitudinal cap beam bars is viable in reducing construction time and rebar congestion for CIP construction.
2) CIP emulating ABC pocket connections are viable for use in bridge column-cap connections.
3) The proposed guidelines for detailing of ABC pocket connections [1] can be adapted for use in the design of CIP pocket connections, but the more recently proposed AASHTO guidelines for design of ABC column connections [8] should be used.
4) Recommendations for auxiliary reinforcement adjacent to and around the pocket connection are as follows.
    a. The transverse stirrups around the pocket connections are required for CIP pocket connections.
    b. The transverse hoops around the pocket connection are necessary for CIP pocket connections.
    c. The vertical cap beam ties adjacent to the connection may be reduced by perhaps 50 percent for CIP pocket connections.
    d. The horizontal cap beam ties adjacent to the connection are necessary for CIP pocket connections.
5) CAM bars are viable for use in two-way hinges and can be spliced to traditional rebar using headed rebar couplers to provide continuity between bars and anchorage.
6) The existing guidelines for design of rebar hinges by Cheng et al. [13] are applicable for us with CAM bars.
7) For moderate and strong earthquakes of up to approximately twice the design earthquake, a relatively routine OpenSees model using existing constitutive relationships can be used to obtain an approximate response.

7.4 Future Research

Although this study has provided valuable insight into the performance of CIP emulating ABC pocket connections and CAM reinforced two-way hinges, future studies

may seek to further validate the performance of such connections with slight alterations. As CIP pocket connections have been tested in the in-plane and out-of-plane directions separately, a future study may include testing under triaxial seismic loading to account for the combined effects of three earthquake components. Another study could focus on the self-centering capabilities of SMA when implemented in both the column top and base two-way hinges, an effect that could not be evaluated in the present study because the plastic hinging of the column tops dominated the response. As the post-test analytical model was not capable of replicating the results obtained from testing for low and very high amplitude motions, a three-dimensional analytical model may be developed.

References

[1] Tazarv, M., Saiidi, M. (2015) "Design and Construction of Precast Bent Caps with Pocket Connections for High Seismic Regions." Center for Civil Engineering Earthquake Research, Department of Civil and Environmental Engineering, University of Nevada, Reno, Report No. CCEER 15-06.

[2] Mohebbi, A., Saiidi, M., and Itani, A. (2017). "Development and Seismic Evaluation of Pier Systems w/Pocket Connections, CFRP Tendons, and ECC/UHPC Columns." Center for Civil Engineering Earthquake Research, Department of Civil and Environmental Engineering, University of Nevada, Reno, Report No. CCEER-17-02.

[3] Mehrsoroush, A., Saiidi, M., and Ryan, K. (2017). "Development of Earthquake Resistant Precast Pier Systems for Accelerated Bridge Construction in Nevada." Center for Civil Engineering Earthquake Research, Department of Civil and Environmental Engineering, University of Nevada, Reno, Report No. CCEER-17-03.

[4] Schwartz, T., Saiidi, M., and Moustafa, M., "Simplifying Cast-in-Place Joint Design Using ABC Pocket Connection Details in High Seismic Regions," Center for Civil Engineering Earthquake Research, Department of Civil and Environmental Engineering, University of Nevada, Reno, Nevada, Report No. CCEER-20-01, January 2020.

[5] Varela, S., and Saiidi, M., "Dynamic Performance of Innovative Bridge Columns with Superelastic CuAlMn Shape Memory Alloy and ECC," International Journal of Bridge Engineering Vol. 2, No. 3, 2014, pp. 29-58.

[6] Tazarv, M., Saiidi, M. (2014) "Next Generation of Bridge Columns for Accelerated Bridge Construction in High Seismic Zones." Center for Civil Engineering Earthquake Research, Department of Civil and Environmental Engineering, University of Nevada, Reno, Report No. CCEER 14-06

[7] American Association of State Highway and Transportation Officials (AASHTO) (2018). "AASHTO LRFD Guide Specifications for Accelerated Bridge Construction (1st Ed.)," Washington, D.C.

[8] Saiidi, M., M. Mehraein, G. Shrestha, E. Jordan, A. Itani, M. Tazarv, T. Murphy, M. Reno, and M. Pohll, "Proposed AASHTO Seismic Specifications for ABC Column Connections," National Cooperative Highway Research Program, NCHRP Report 935,Transportation Research Board, Washington, DC, April 2020.

[9] Mehraein, M., Saiidi, M. (2016) "Seismic Performance of Bridge Column-Pile Shaft Pin Connections for Application in Accelerated Bridge Construction." Center for Civil Engineering Earthquake Research, Department of Civil and Environmental Engineering, University of Nevada, Reno, Report No. CCEER 16-01.

[10] Mohebbi, A., Jordan, E., and Saiidi, M., "Exploratory Experimental Studies of Spliced Cam Shape Memory Alloy Bars for Seismic Application," Center for Civil Engineering Earthquake Research, Department of Civil and Environmental Engineering, University of Nevada, Reno, Nevada, Report No. CCEER-18-04, September 2018.

[11] Nakashoji, B. and Saiidi, M.S., "Seismic Performance of Square Nickel-Titanium Reinforced ECC Columns with Headed Couplers," Center for Civil Engineering Earthquake Research, Department of Civil and Environmental Engineering, University of Nevada, Reno, Nevada, Report No. CCEER-14-05, July 2014.

[12] Baker, T., M. Saiidi, B. Nakashoji, J. Bingle, T. Moore, and B. Khaleghi, "Precast Spliced Girder Bridge in Washington State using Superelastic Materials in Bridge Columns to Improve Seismic Resiliency - From Research to Practice," PCI Journal, Precast/Prestressed Concrete Institute, January-February 2018, pp. 57-71.

[13] Cheng, Z., Saiidi, M., and Sanders, D., "Development of a Seismic Design Method for Reinforced Concrete Two-Way Bridge Column Hinges," Center for Civil Engineering Earthquake Research, Department of Civil Engineering, University of Nevada, Reno, Nevada, Report No. CCEER-06-01, February 2006.

[14] American Association of State Highway and Transportation Officials (AASHTO) (2011). "AASHTO Guide Specifications for LRFD Seismic Bridge Design (2nd Ed.)," Washington, D.C.

[15] SAP2000, CSI Computer & Structures Inc. Linear and nonlinear static and dynamic analysis of three-dimensional structures. Berkeley (CA): Computer & Structures, Inc., V18.1.1, 2018.

[16] OpenSees (2016) [Computer software]. Berkeley, CA, Pacific Earthquake Engineering Research Center, Univ. of California–Berkeley.

[17] ACI Committee 318 (2014). "Building Code Requirements for Structural Concrete (ACI 318-14) and Commentary (ACI 318R-14)," American Concrete Institute, Farmington Hills, MI.

[18] Mander, J. B., Priestley, M. J. N., and Park, R. (1988). Theoretical stress strain model for confined concrete. Journal of Structural Engineering, 114(8), 1804–1826.

[19] PEER. (2014). Pacific Earthquake Engineering Research Center (PEER) Ground Motion Database. Retrieved from https://ngawest2.berkeley.edu/

[20] ASCE7-10 (2013), ASCE 7-10, “Minimum Design Loads for Buildings and Other Structures,” American Society of Civil Engineers, Reston, VA.

[21] ASTM C39 / C39M-20, “Standard Test Method for Compressive Strength of Cylindrical Concrete Specimens,” ASTM International, West Conshohocken, PA, 2020

[22] ASTM A370-19e1, “Standard Test Methods and Definitions for Mechanical Testing of Steel Products,” ASTM International, West Conshohocken, PA, 2019,

[23] American Association of State Highway and Transportation Officials (AASHTO) (2017). “AASHTO LRFD Bridge Design Specifications (8th Ed.),” Washington, D.C.

Chapter 2 Tables

Table 2.1 Column Design

Scale Factor	1/3
Column diameter, inch (mm)	16 (406)
Column clear height, inch (mm)	80 (2032)
Cover, inch (mm)	0.75 (19)
Column longitudinal bar, US size (mm)	16 - #4 (Ø13)
Column long. steel ratio	1.59%
Column transverse steel, US size, inch (mm)	#3 @ 2.25 (Ø9.5 @ 57)
Column transverse steel ratio	1.35%

Table 2.2 Moment-curvature results of column-section under axial load

	SAP2000	**OpenSees**	**Difference (%)**
My, effective yield moment (kip-in)	1206	1209	0.25
(kN-mm)	(136260)	(136599)	
φy, yield curvature (rad/in)	0.0002603	0.0002654	1.94
(rad/mm)	(0.0000102)	(0.0000104)	
Mp, effective plastic moment (kip-in)	1706	1725	1.11
(kN-mm)	(192752)	(194899)	
φp, plastic curvature (rad/in)	0.0003683	0.0003721	1.03
(rad/mm)	(0.0000145)	(0.0000146)	

Table 2.3 Moment-curvature results of hinge-section under axial load.

	OpenSees
My, effective yield moment (kip-in)	163.44
(kN-mm)	(18466)
φy, yield curvature (rad/in)	0.000212
(rad/mm)	(0.0000083)
Mp, effective plastic moment (kip-in)	370
(kN-mm)	(41804)
φp, plastic curvature (rad/in)	0.000452
(rad/mm)	(0.0000178)

Chapter 2 Figures

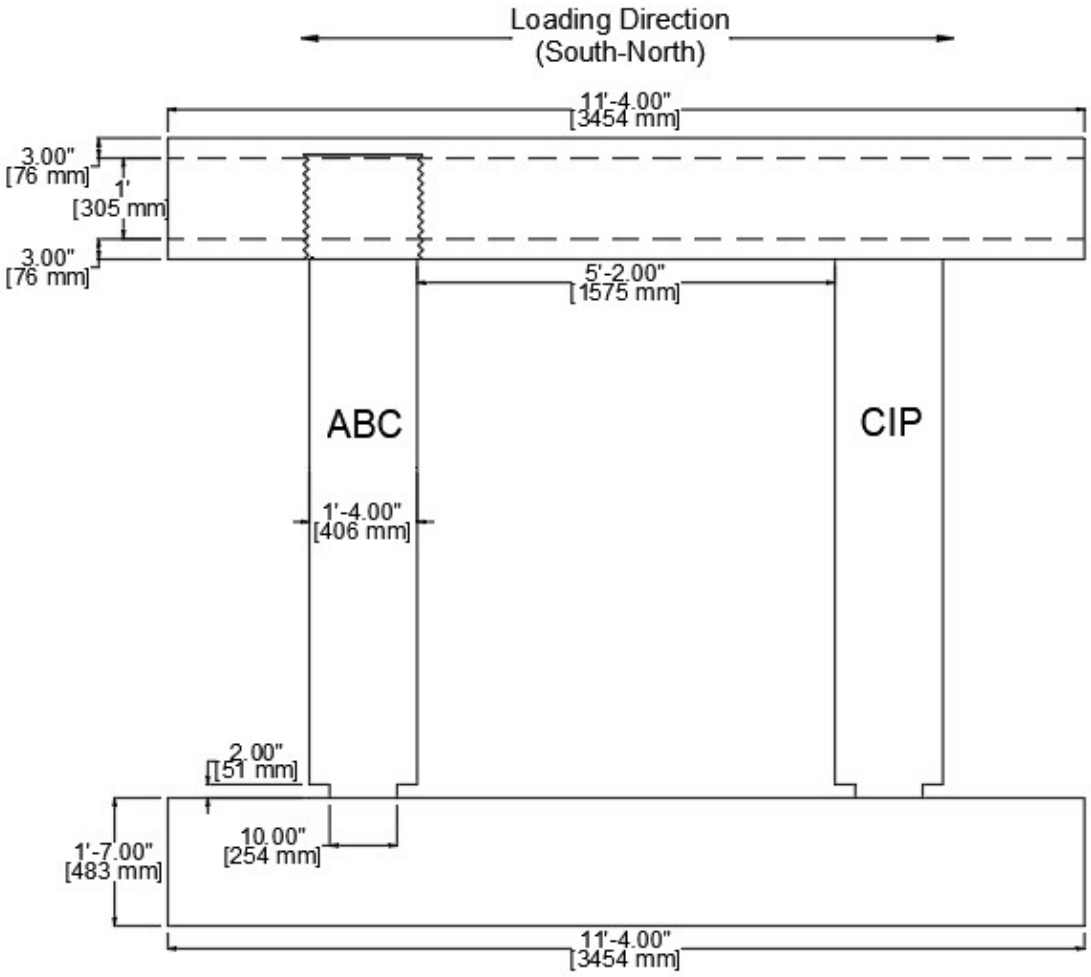

Figure 2.1 Specimen configuration and dimensions

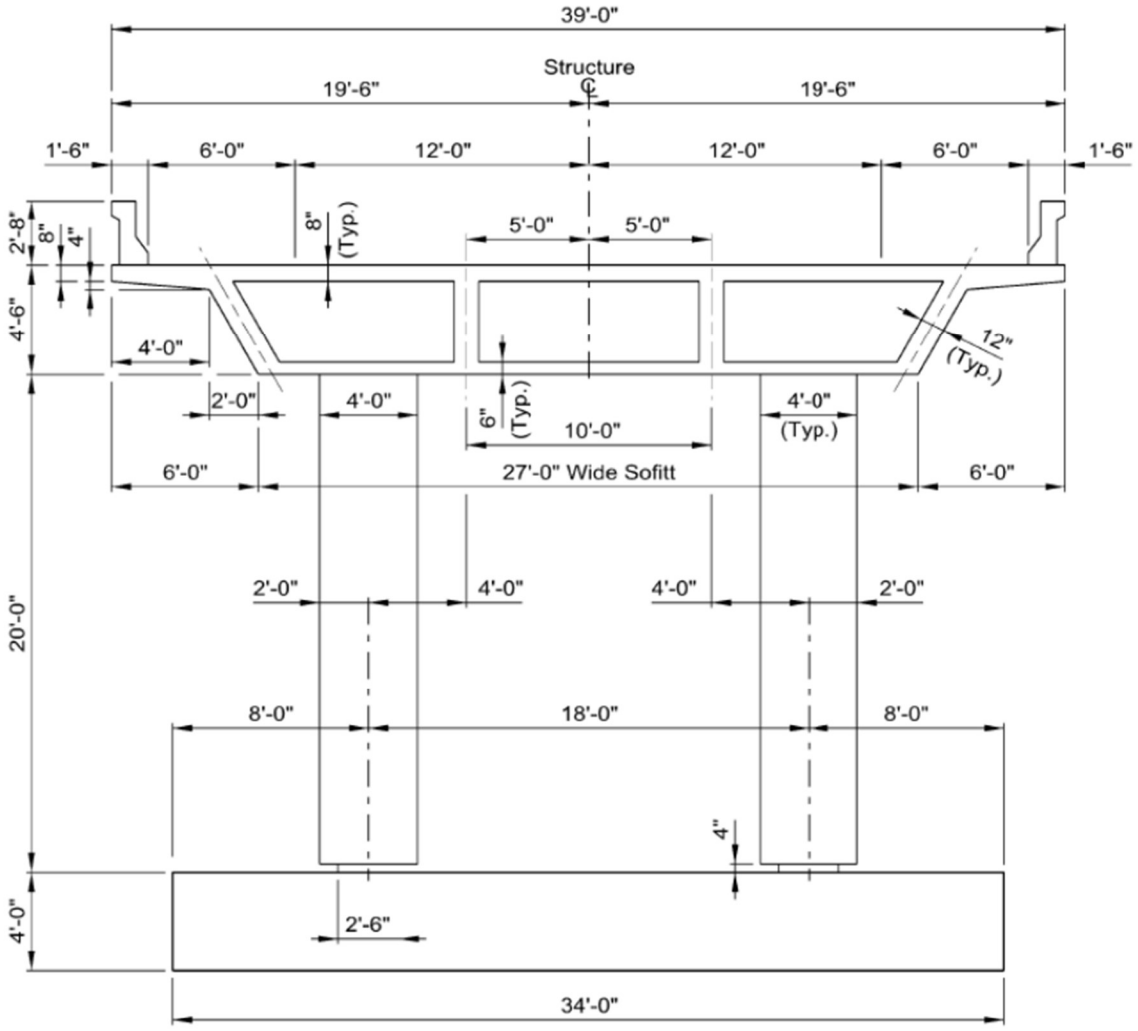

Figure 2.2 Prototype bridge typical cross-section

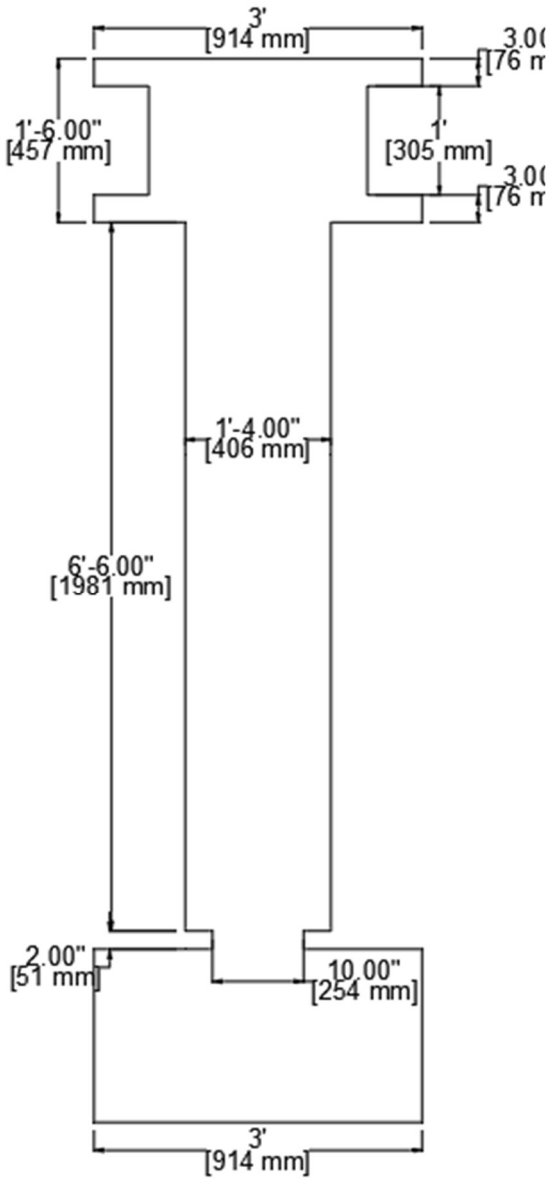

Figure 2.3 Specimen Dimensions

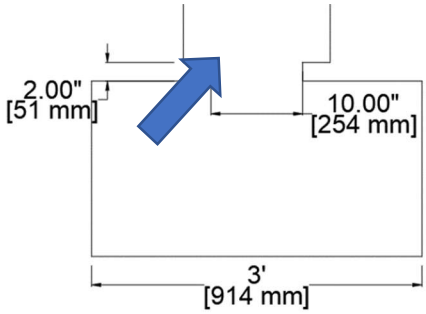

Figure 2.4 Elevation view closeup of two-way hinge

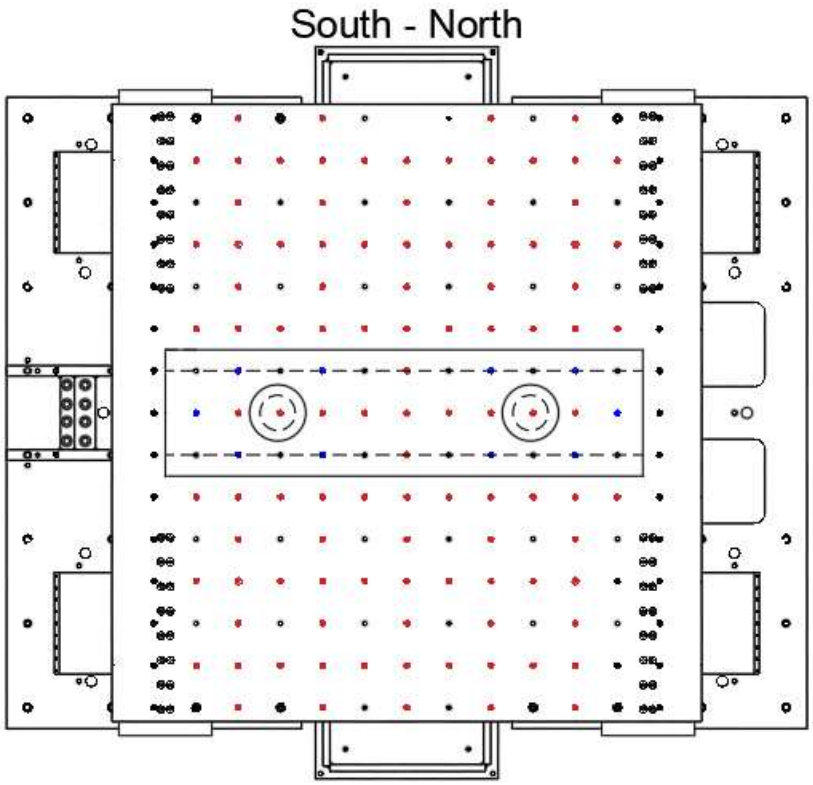

Figure 2.5 Plan view of specimen on shake table

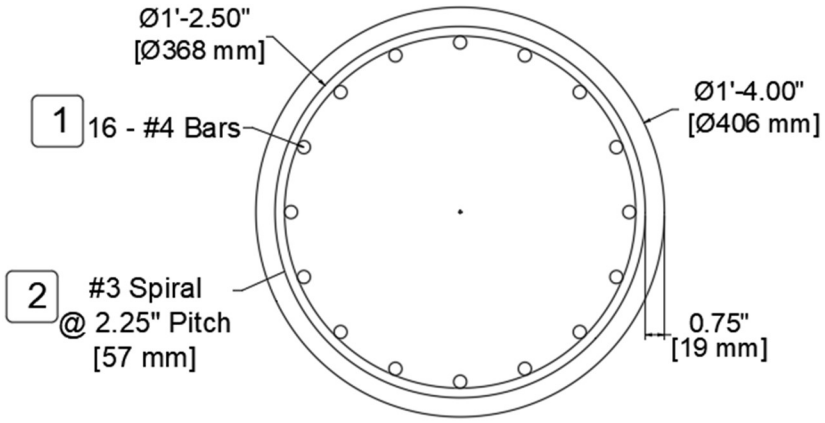

Figure 2.6 Cross-section of column

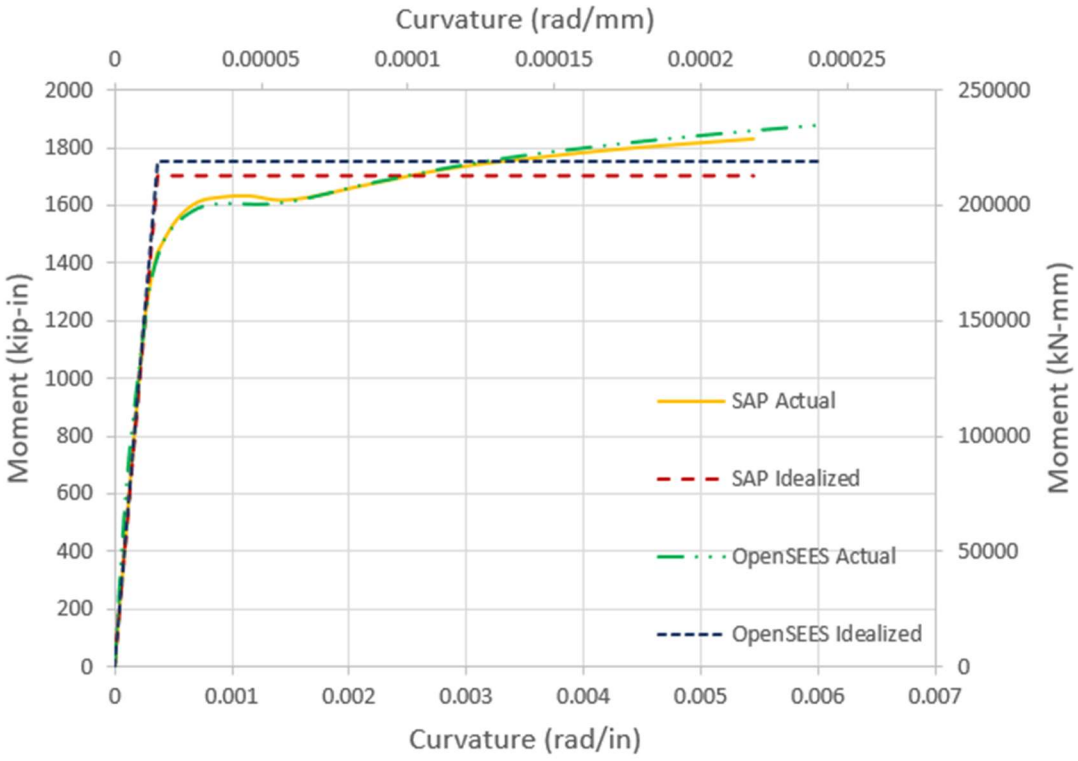

Figure 2.7 Moment-curvature analysis of column section under axial load

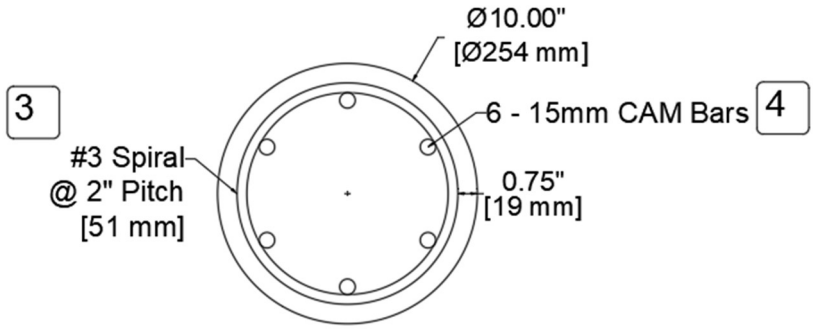

Figure 2.8 Cross-section of two-way hinge

Figure 2.9 HRC connection between rebar and CAM bar

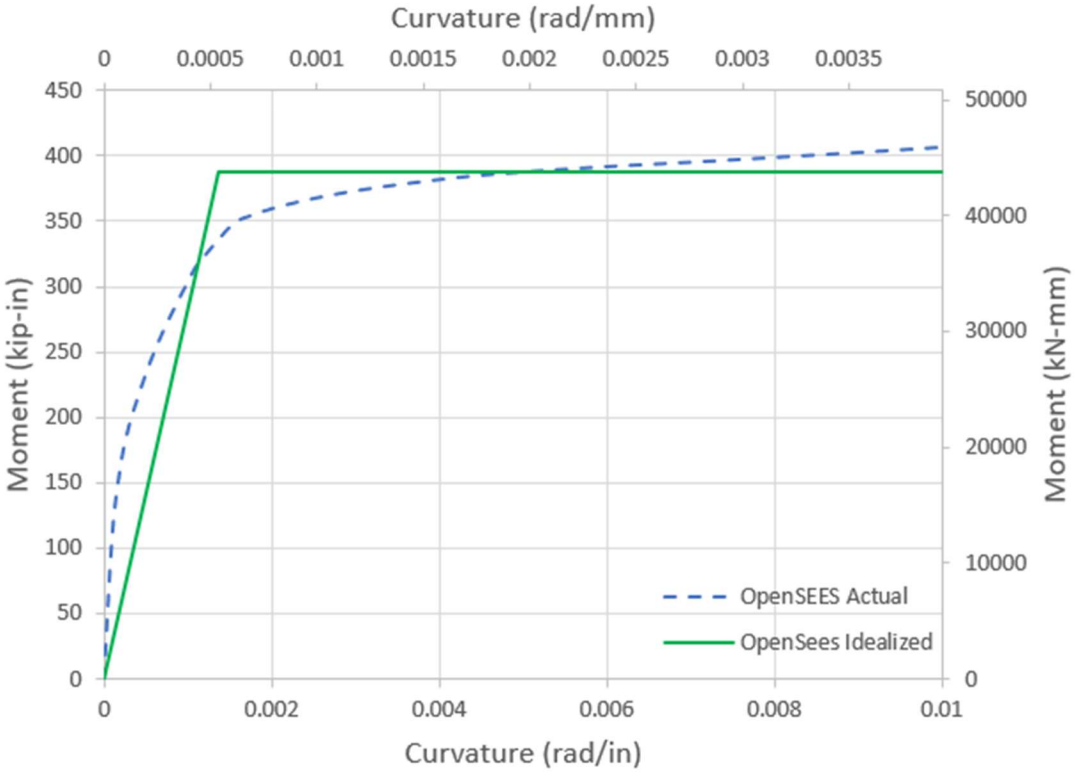

Figure 2.10 Moment-curvature analysis of hinge section under axial load

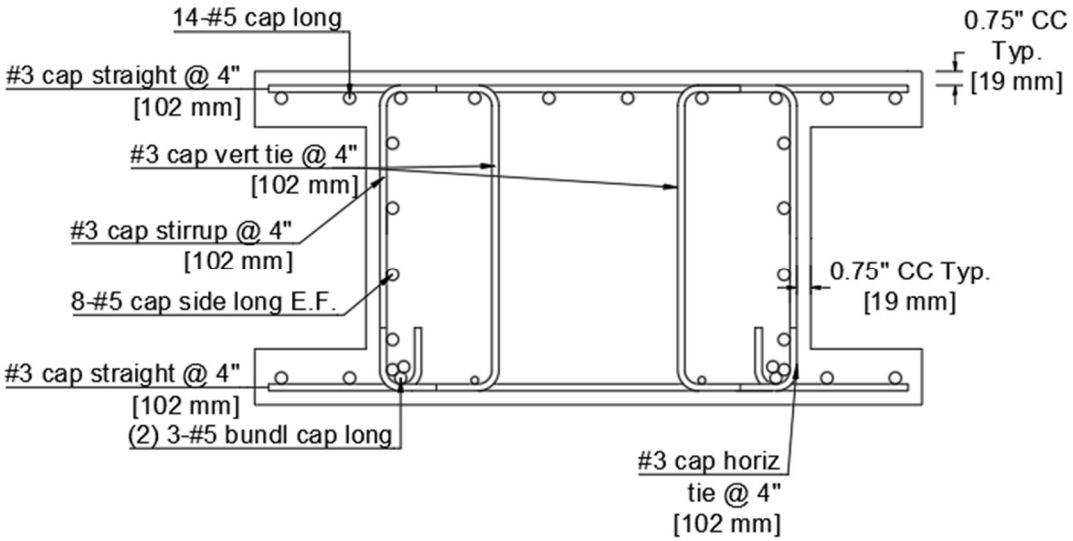

Figure 2.11 Typical cap beam cross-section out of joint area

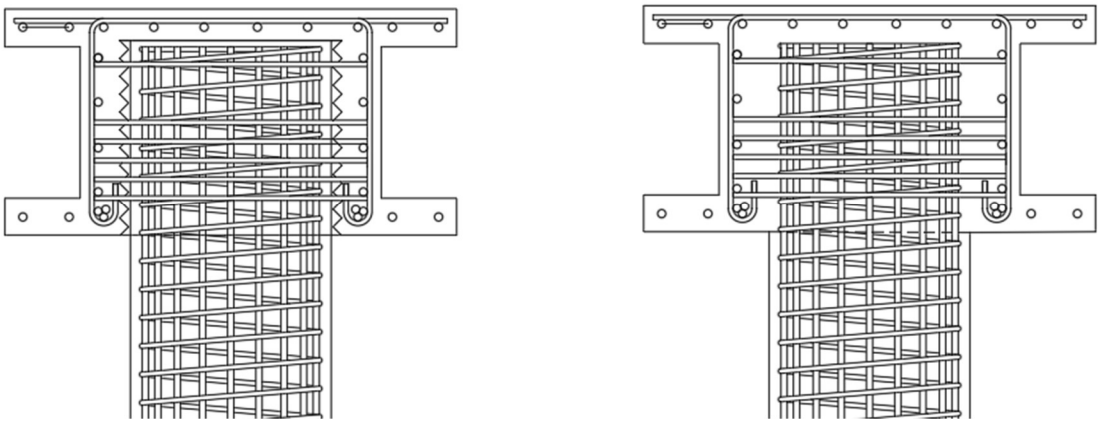

Figure 2.12(a) ABC column (left) and (b) CIP Column (right

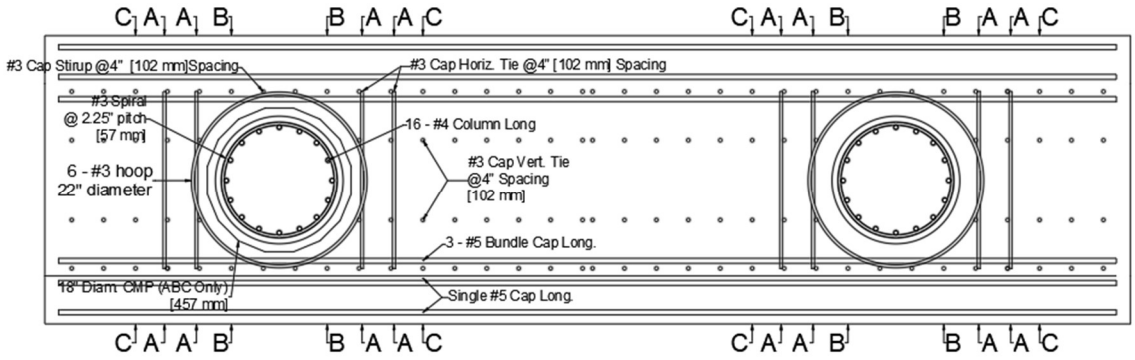

Figure 2.13 Plan view of cap beam reinforcement and locations of cross-sections

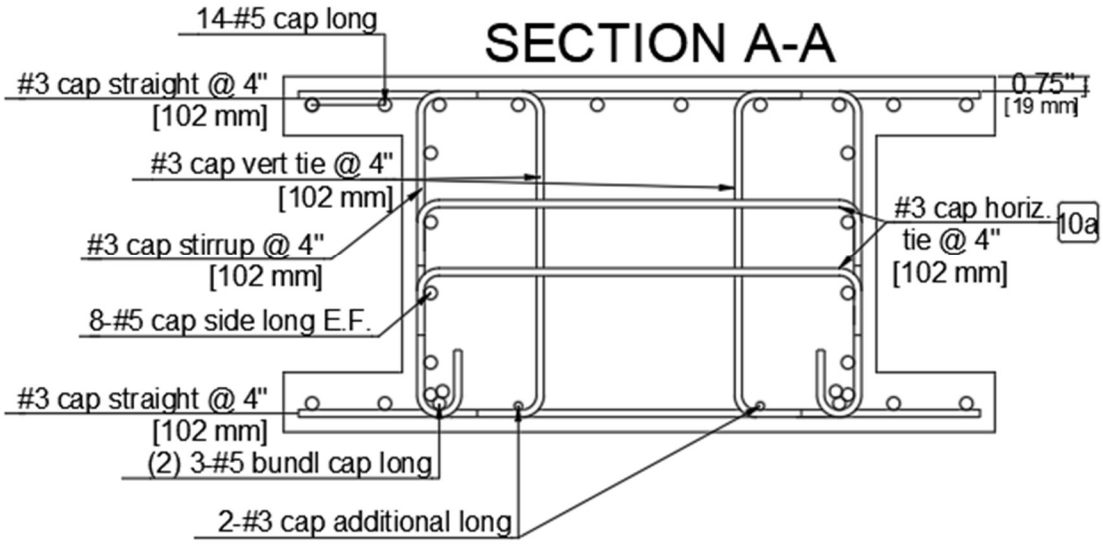

Figure 2.14 Cap beam cross section A-A, adjacent to pockets

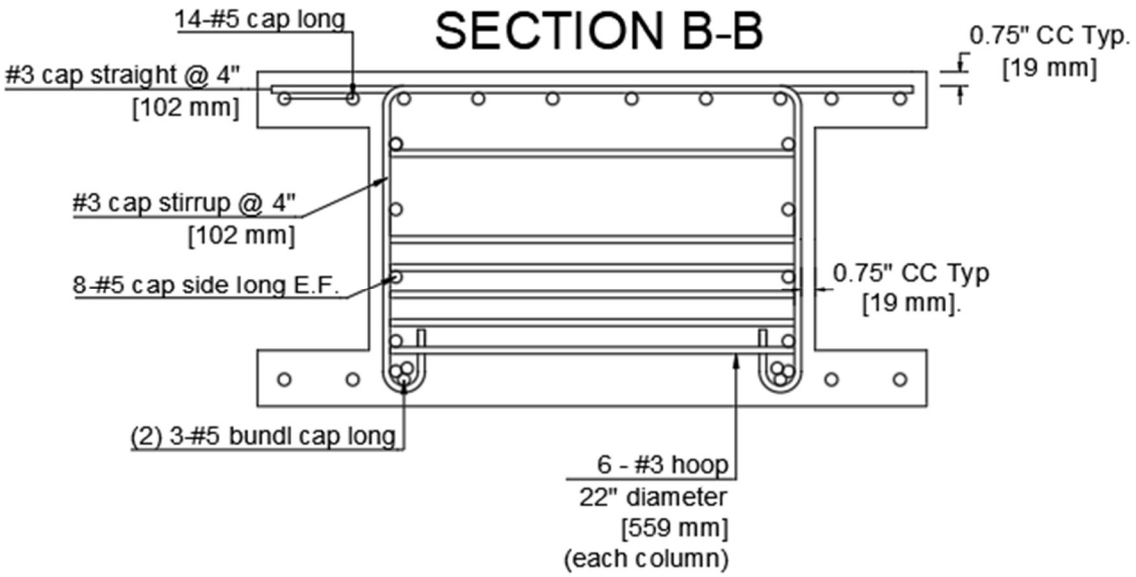

Figure 2.15 Cap beam cross section B-B, pocket and hoops

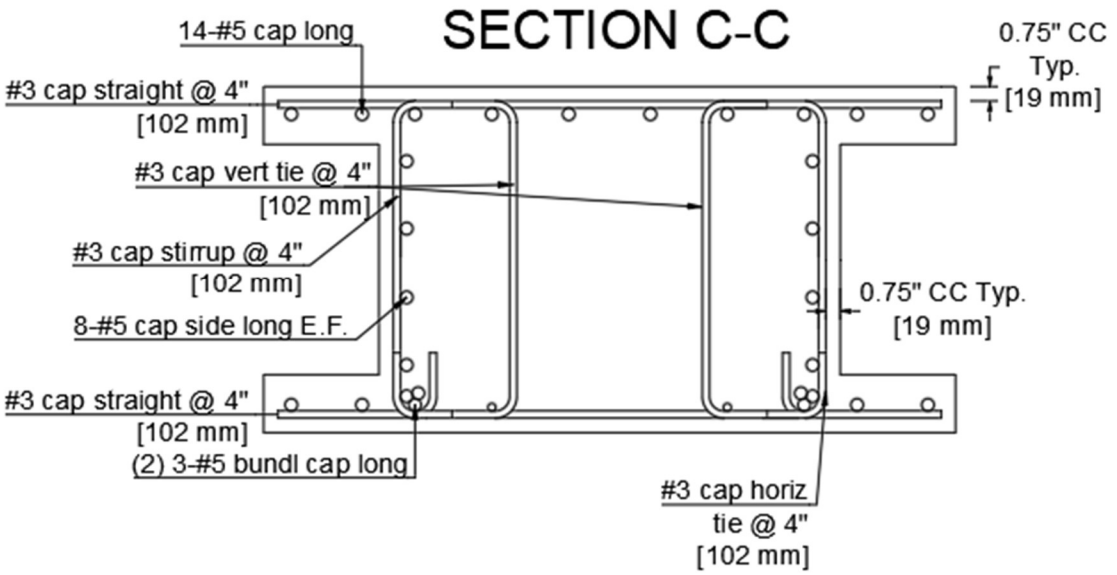

Figure 2.16 Cap beam cross section C-C, away from pockets

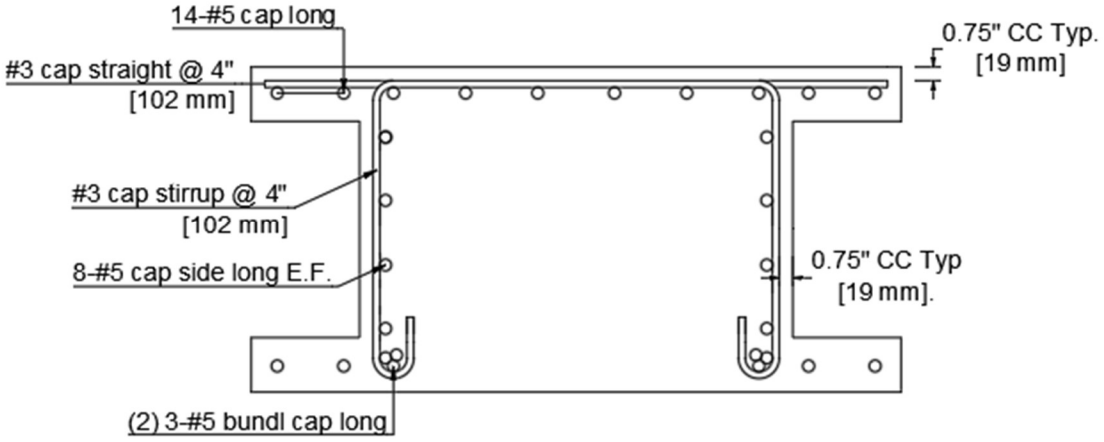

Figure 2.17 Longitudinal and transverse reinforcement at pocket

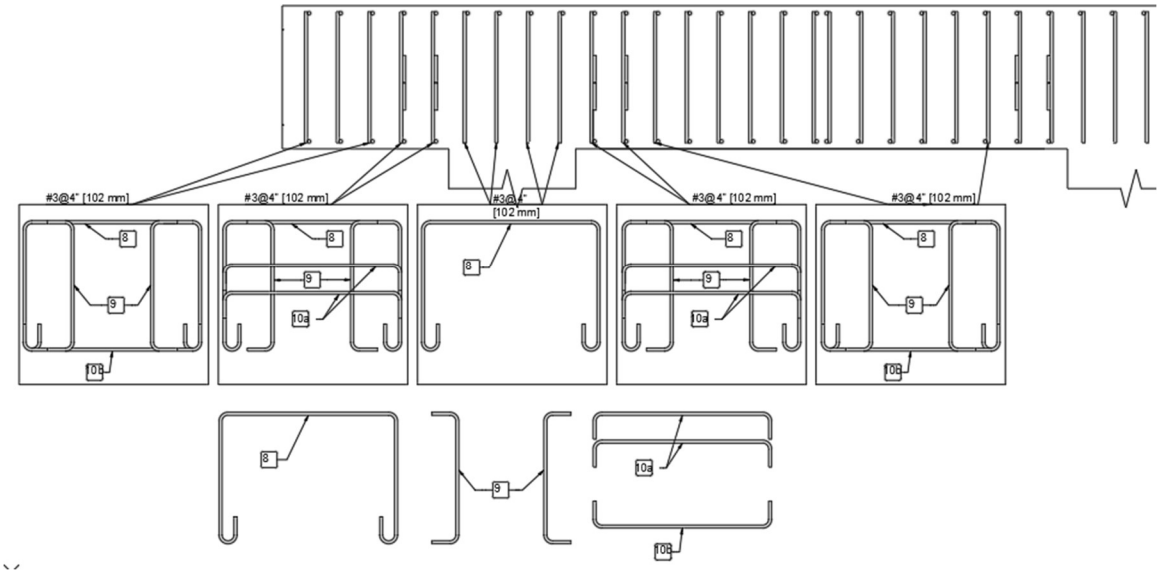

Figure 2.18 Elevation view of locations of cap beam transverse reinforcement cross-sections

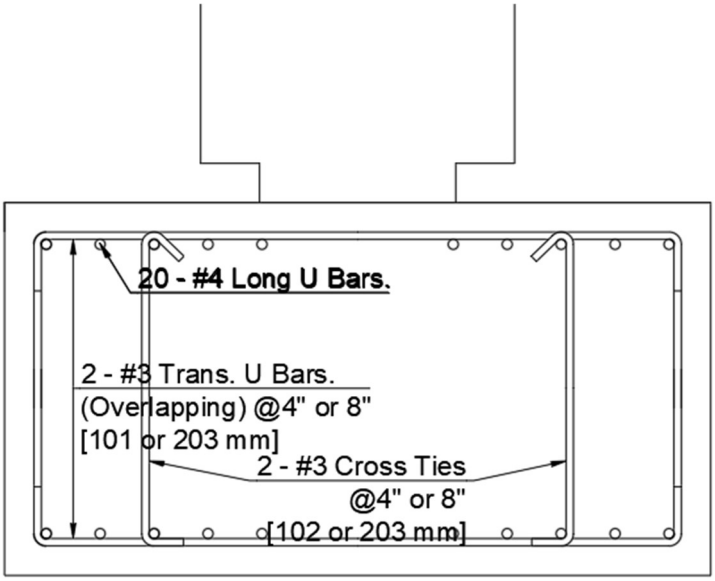

Figure 2.19 Typical footing cross section

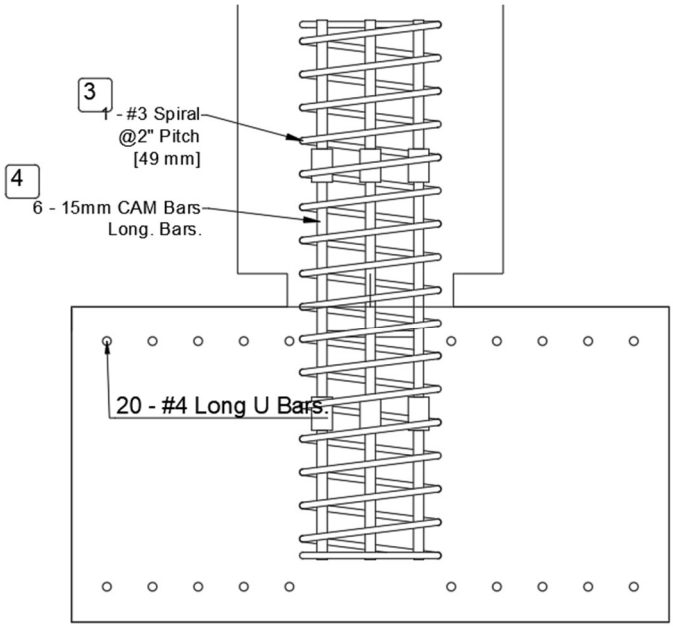

Figure 2.20 Hinge reinforcement caged extending into footing

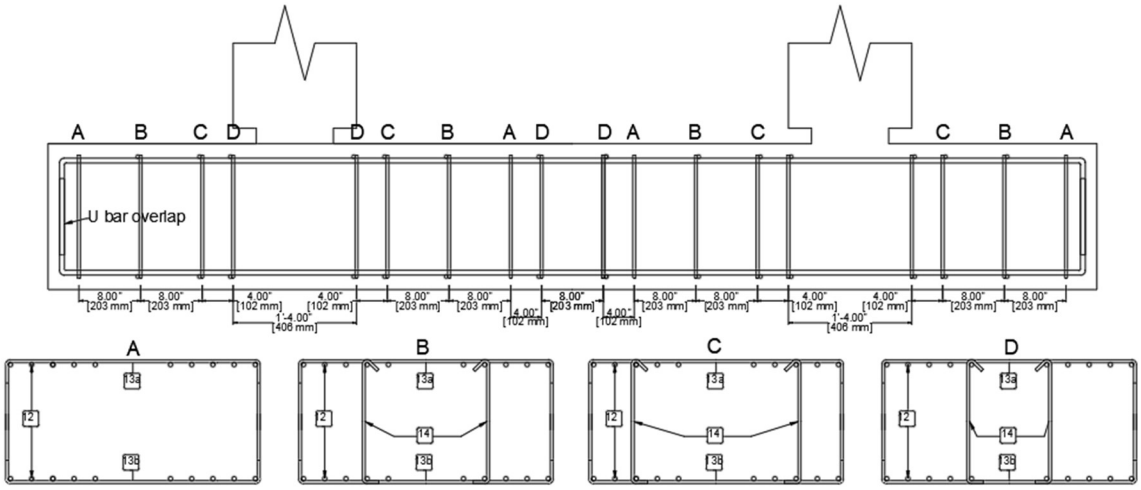

Figure 2.21 Elevation view of locations of footing reinforcement cross-sections

Figure 2.22 Footing cross-section A-A, far from joint

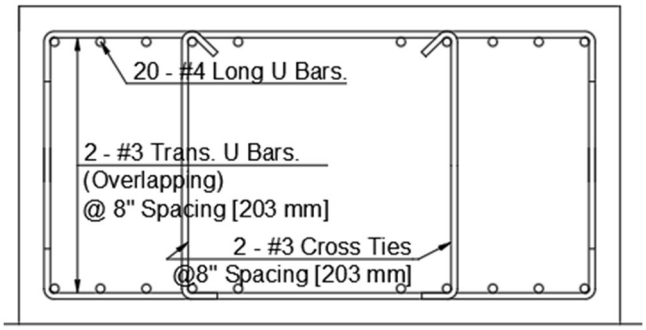

Figure 2.23 Footing cross-section B-B, medium distance from joint

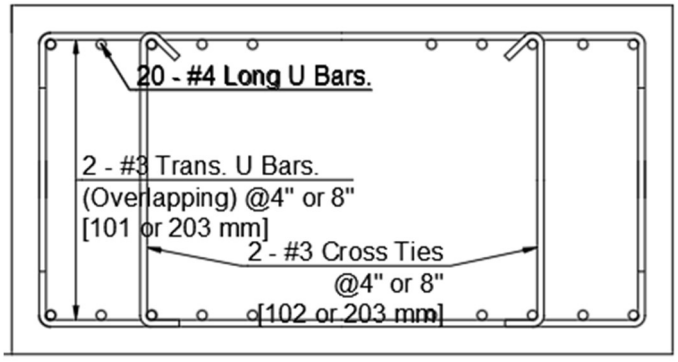

Figure 2.24 Footing cross-section C-C, near joint

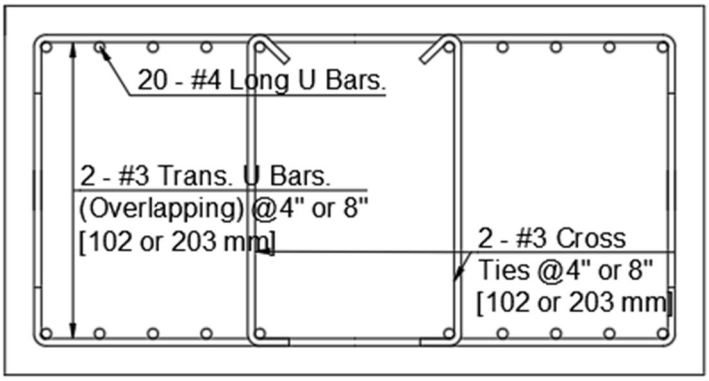

Figure 2.25 Footing cross-section D-D, adjacent to joint

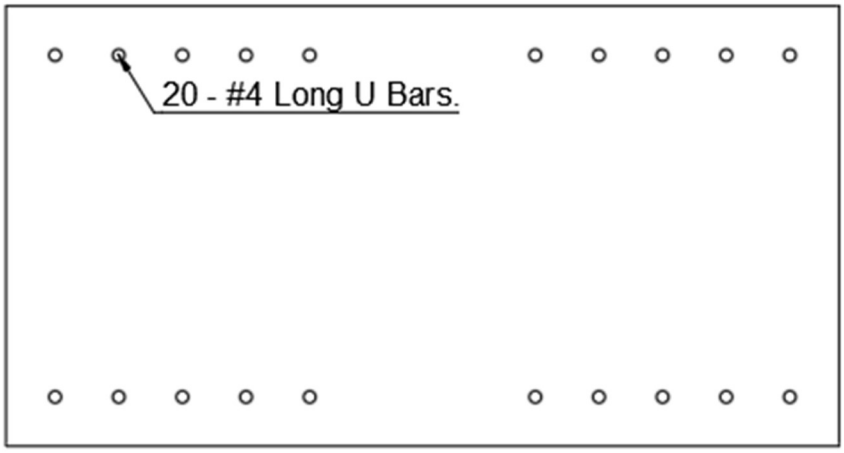

Figure 2.26 Footing cross-section E-E, at hinge-to-footing joint

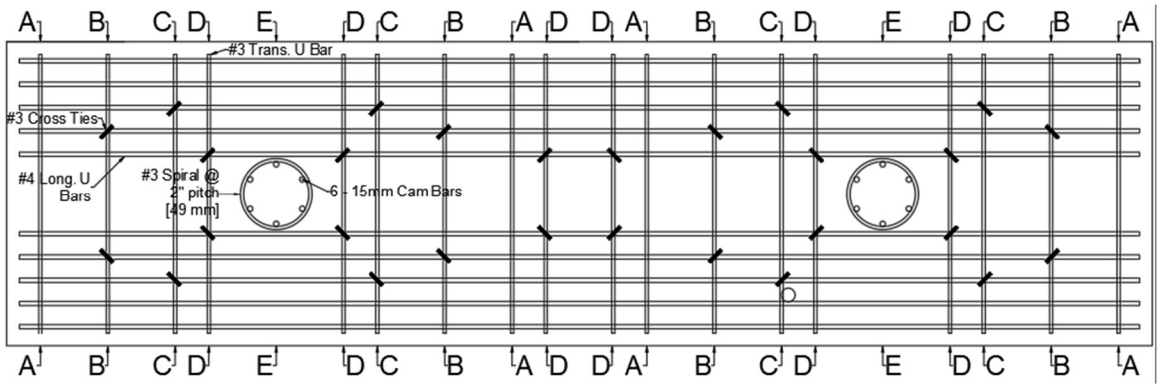

Figure 2.27 Plan view of locations of footing reinforcement cross sections

Figure 2.28 Footing reinforcement

Figure 2.29 Hinge reinforcement cage residing in footing reinforcement

Figure 2.30 Clearance between hinge reinforcement cage and footing reinforcement

Figure 2.31 CAM bars HRC coupled to #4 rebar within hinge spiral

Figure 2.32 High strength steel nut placed in gap between CAM bar and hinge spiral

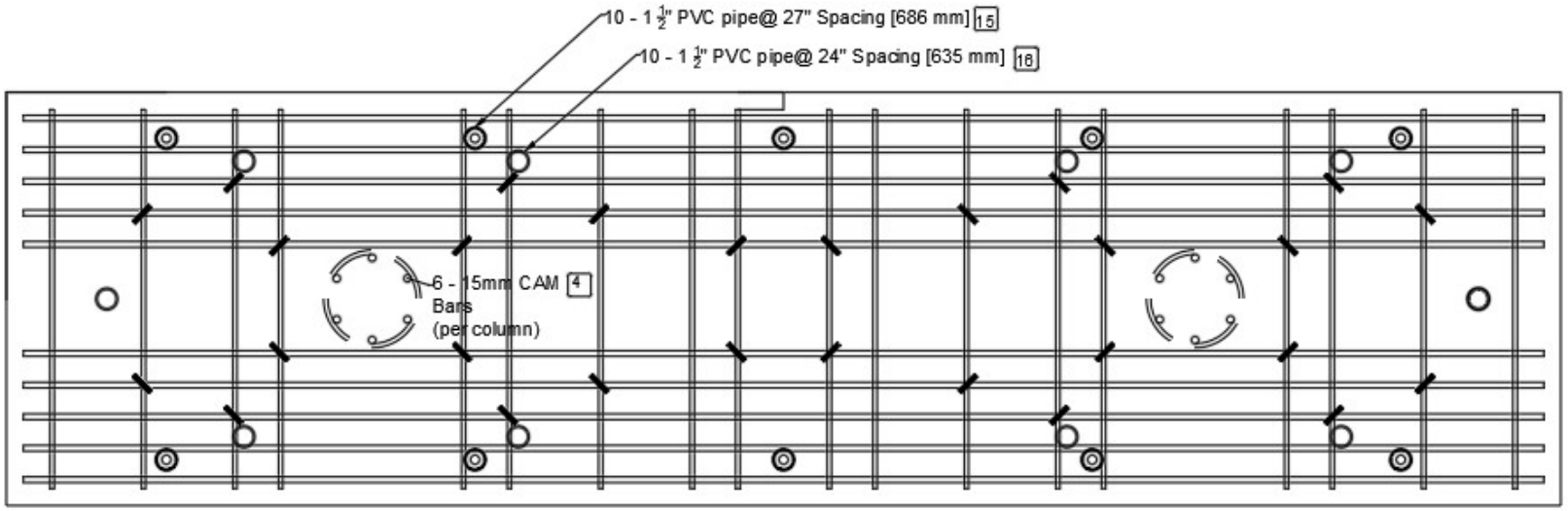

Figure 2.33 Positions of PVC pipes within footing

Figure 2.34 PVC pipes within footing

Figure 2.35 Pouring of footing concrete

Figure 2.36 Vibrating of footing concrete

Figure 2.37 Finished footing concrete

Figure 2.38 Water based cure spread on finished concrete

Figure 2.39 Wooden platform to elevate column

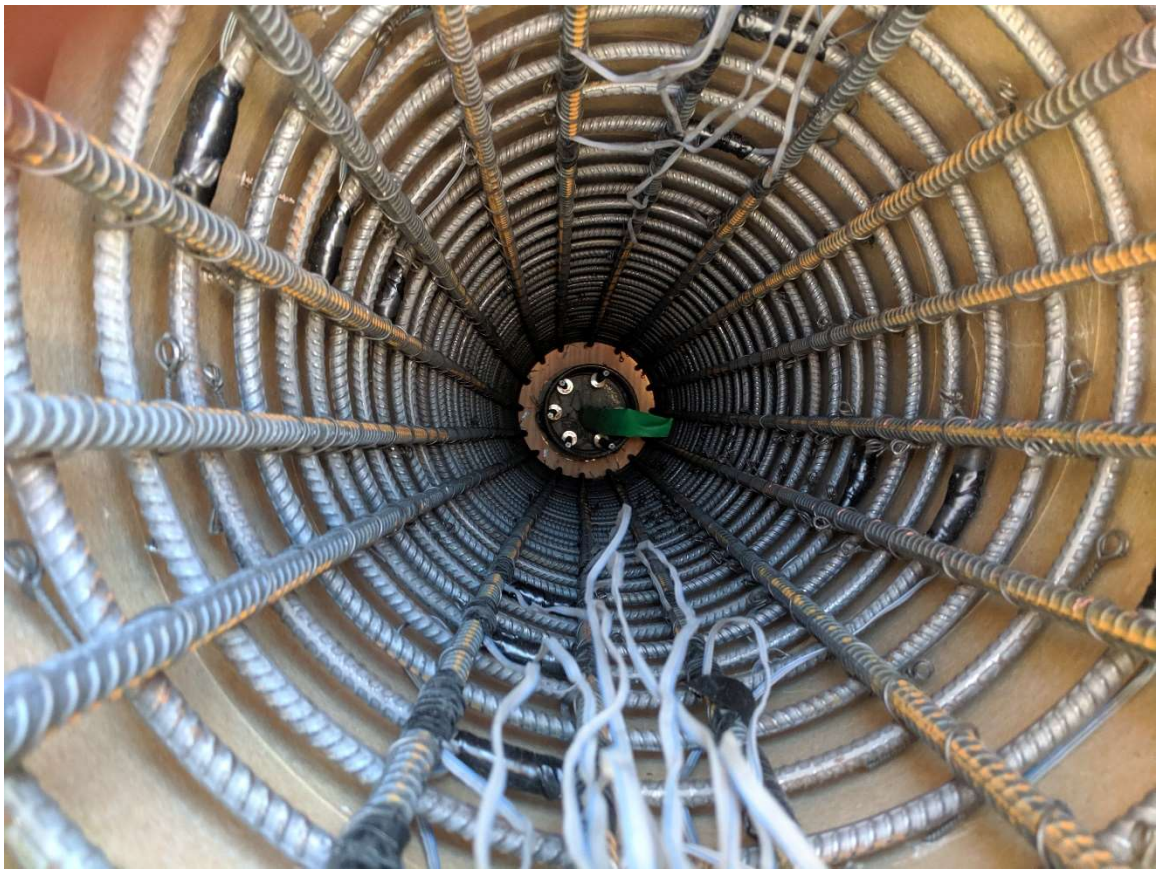

Figure 2.40 Inside view of column reinforcement cage

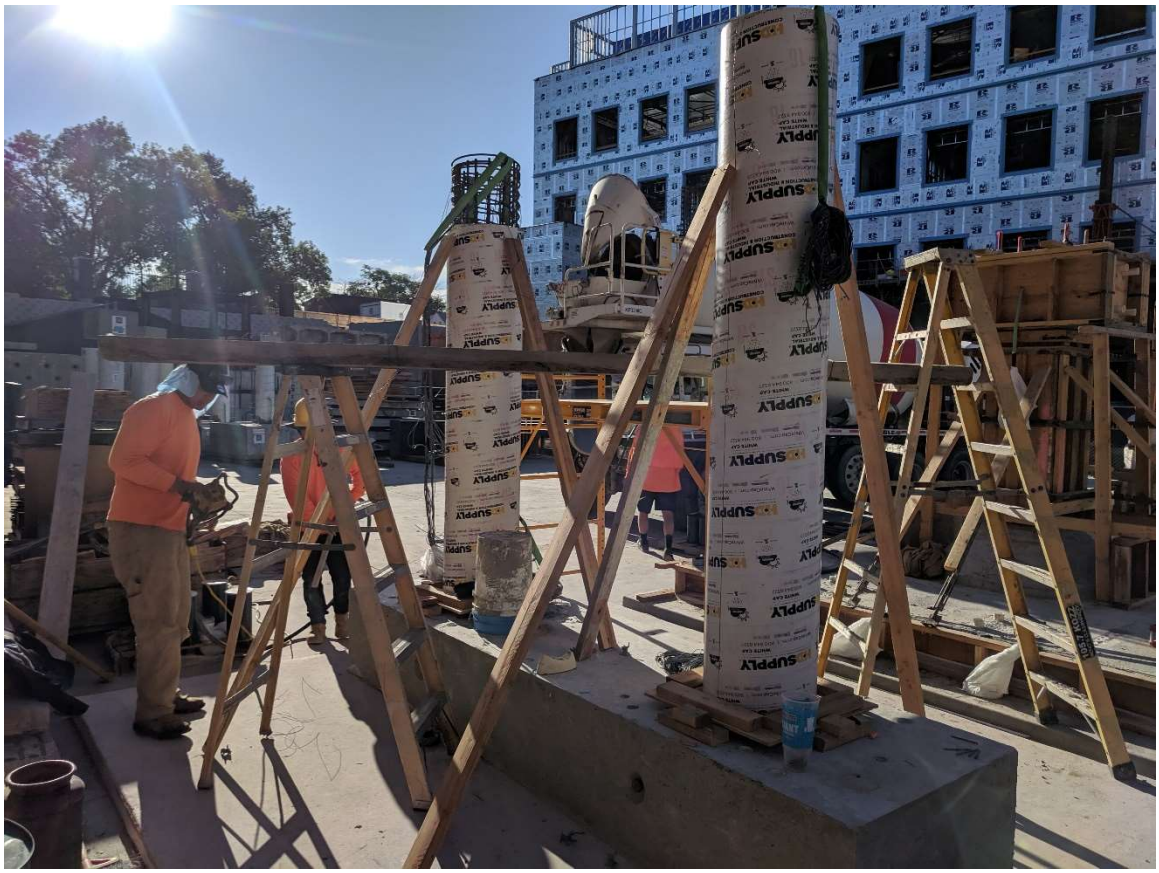

Figure 2.41 Erected column cages and Sonotube

Figure 2.42 Pouring and vibrating of column concrete

Figure 2.43 Columns stripped of their formwork

Figure 2.44 CMP grouted partially precast column (ABC).

Figure 2.45 Tying of bottom and middle cap beam reinforcement

Figure 2.46 CIP column reinforcement cage passing into cap beam pocket unobstructed

Figure 2.47 ABC column and CMP passing into cap beam pocket unobstructed.

Figure 2.48 Completed cap beam formwork and PVC pipes

Figure 2.49 Completed cap beam reinforcement

Figure 2.50 Group of ¾” (19 mm) steel studs.

Figure 2.51 Pouring of cap beam concrete

Figure 2.52 Vibrating of cap beam concrete

Figure 2.53 Finished cap beam concrete

Figure 2.54 Completed specimen

Figure 2.55 Exposed cap beam flange rebar

Figure 2.56 Repaired cap beam flange rebar exposure

Chapter 3 Tables

Table 3.1 Column concrete properties

	Confined	Unconfined
f'c, 28-day compressive strength (ksi)	-7.84	-5.2
(MPa)	(-54.1)	(-36.9)
f'cu, crushing strength (ksi)	-6.96	0
(MPa)	(-48)	(0)
εc0, strain at maximum strength	-0.0073	-0.002
εcu, strain at crushing strength	(-0.0174)	(-0.005)

Table 3.2 Column reinforcing steel properties

fy, yield stress (ksi)	68
(MPa)	(469)
fu, ultimate stress (ksi)	95
(MPa)	(655)
Es, Elastic modulus (ksi)	29000
(MPa)	(199950)
Esh, Elastic modulus at strain hardening (ksi)	6090
(MPa)	(42000)
εsh, strain at strain hardening	0.015
εsu, ultimate strain	(0.12)

Table 3.3 Hinge concrete properties

	Confined	Unconfined
f'c, 28-day compressive strength (ksi)	-10.6	-7.84
(MPa)	(-73.15)	(-54.1)
f'cu, crushing strength (ksi)	-10.5	-6.96
(MPa)	(-72.41)	(-48)
εc0, strain at maximum strength	-0.02108	-0.0073
εcu, strain at crushing strength	(-0.02884)	(-0.0174)

Table 3.4 Hinge CAM bar properties and OpenSEES "SelfCentering" input

k1, Elastic Modulus (ksi)	4500
(MPa)	(31052)
k2, Post-Yield Modulus (ksi)	280
(MPa)	(1932)
SigAct, forward activation (yield) stress (ksi)	24
(MPa)	(166)
β, ratio forward to reverse activation	0.2

Table 3.5 Earthquake records considered in pre-test analysis

Event Name	**Station Name**	**Year**	**Component**	**Unscaled PGA (g)**	**Amp. Factor**	**Amp. PGA (g)**
Imperial Valley-02	El Centro Array #9	1940	H1	0.28	1.46	0.41
San Fernando	Castaic - Old Ridge Route	1971	H1	0.32	3.80	3.80
Imperial Valley-06	El Centro Array #11	1979	H1	0.37	1.44	1.44
Mammoth Lakes-01	Convict Creek	1980	H1	0.42	1.94	1.94
Northridge-01	Sylmar Converter Station	1994	H1	0.62	0.40	0.40

Table 3.6 Loading protocol details

Run #	Test Type	Design Level, %	PGA (g)
WN 1	White Noise		
1	El Centro - H1	33	0.14
WN 2	White Noise		
2	El Centro - H1	67	0.27
WN 3	White Noise		
3	El Centro - H1	100	0.41
WN 4	White Noise		
4	El Centro - H1	150	0.62
WN 5	White Noise		
5	El Centro - H1	200	0.82
WN 6	White Noise		
6	El Centro - H1	250	1.03
WN 7	White Noise		
7	El Centro - H1	300	1.23
WN 8	White Noise		

Table 3.7 Predicted maximum displacement and base shear

Run #	Test Type	Design Level, %	Max Disp, in (mm)	Base Shear, kips (kN)	Drift Ratio, %	Residual Drift Ratio, %
1	El Centro - H1	33	0.21 (5.43)	23.43 (104.21)	0.27	0.00
2	El Centro - H1	67	1.00 (25.45)	44.34 (197.21)	1.25	0.01
3	El Centro - H1	100	1.31 (33.36)	45.16 (200.88)	1.64	0.01
4	El Centro - H1	150	2.34 (59.37)	50.31 (223.79)	2.92	0.14
5	El Centro - H1	200	3.44 (87.48)	52.97 (235.62)	4.31	0.15
6	El Centro - H1	250	4.34 (110.12)	53.84 (239.47)	5.42	0.22
7	El Centro - H1	300	5.21 (132.24)	54.09 (240.59)	6.51	0.20

Chapter 3 Figures

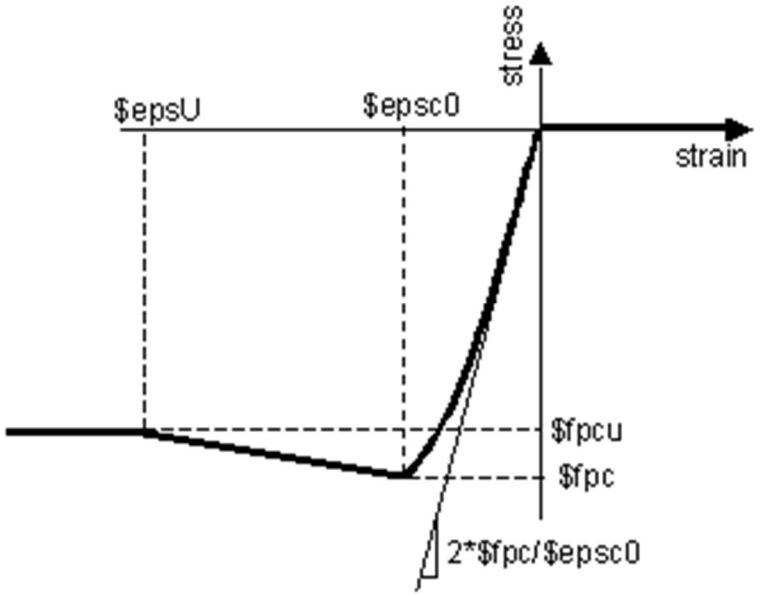

Figure 3.1 OpenSEES material Concrete01 stress-strain relationship

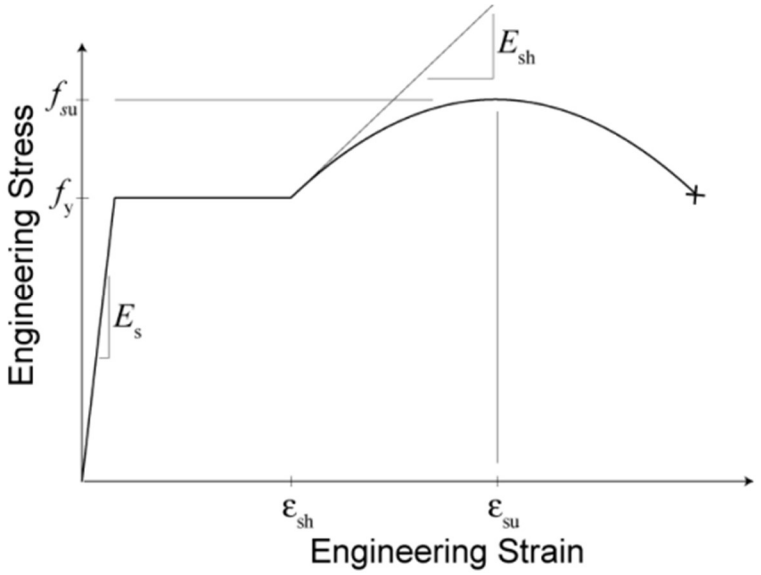

Figure 3.2 OpenSEES material ReinforcingSteel stress-strain relationship

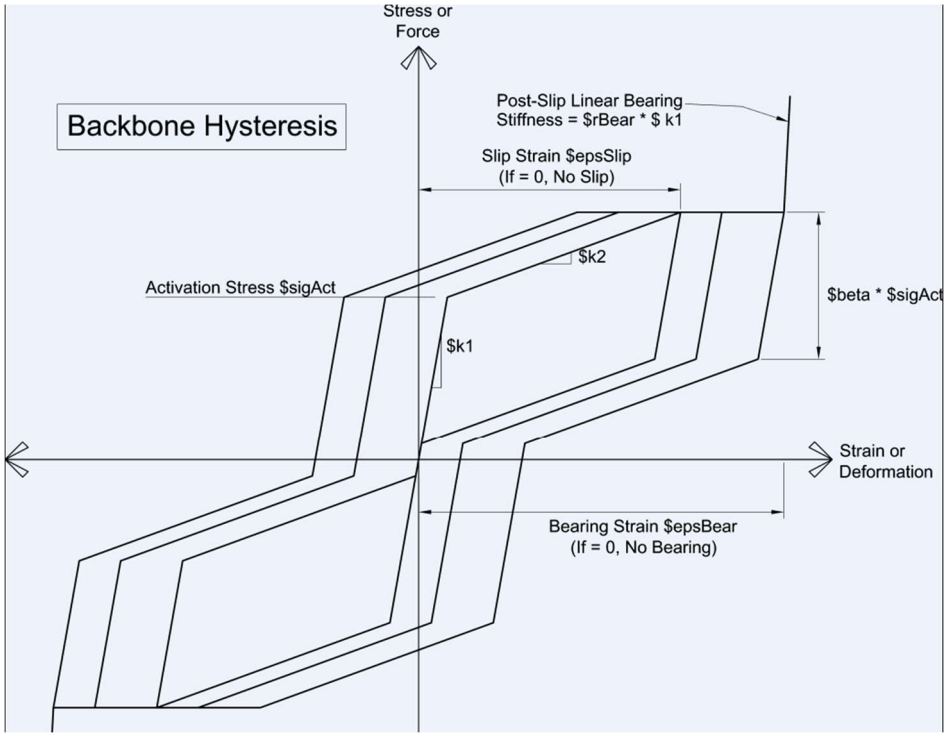

Figure 3.3 OpenSEES material SelfCentering stress-strain relationship

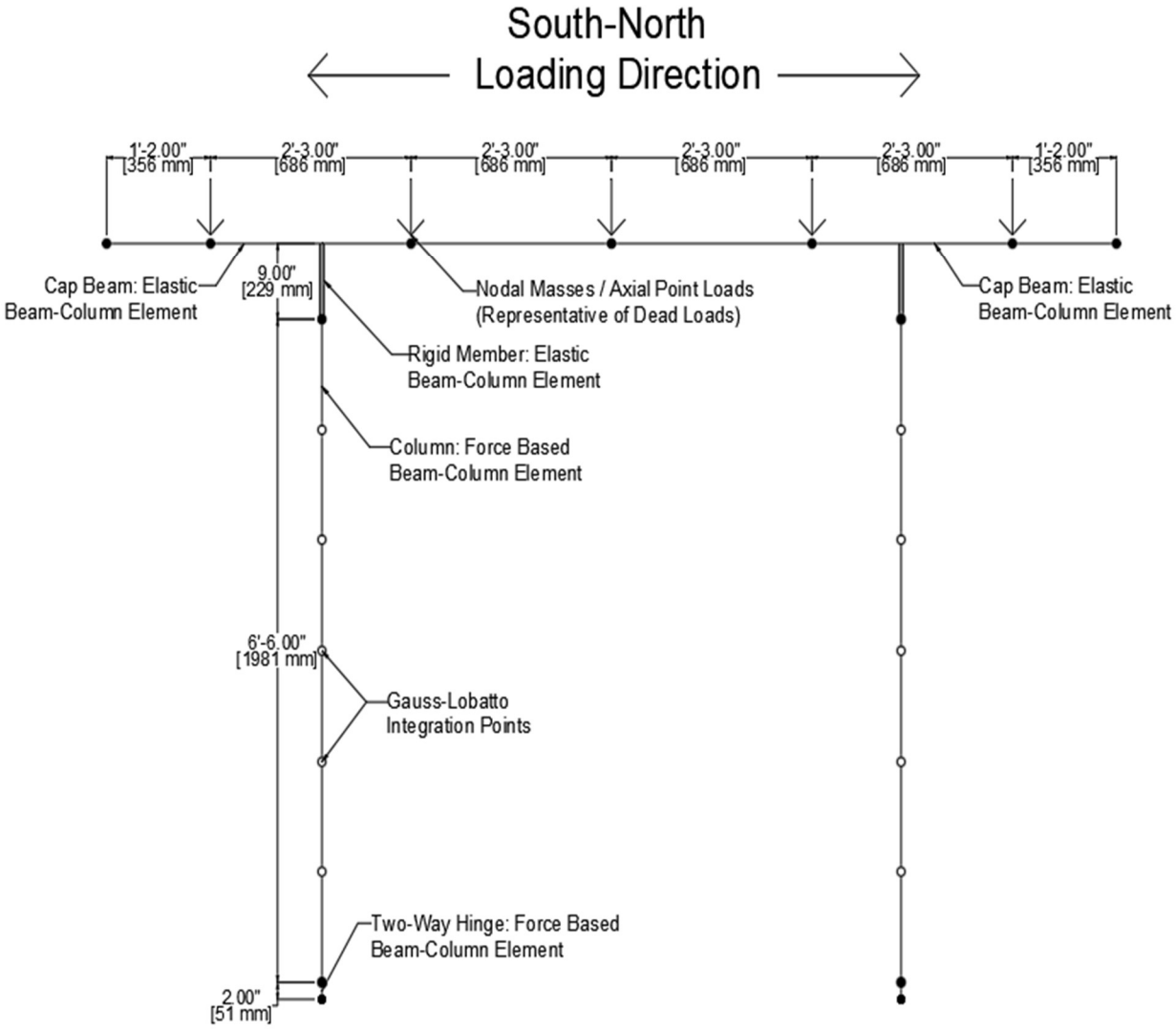

Figure 3.4 Analytical model details

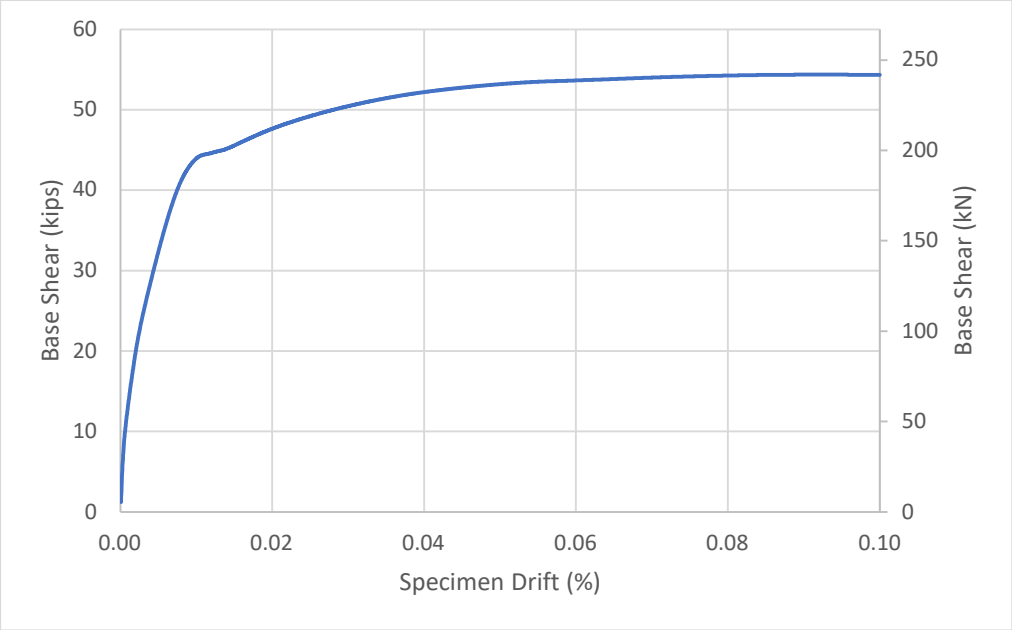

Figure 3.5 Analytical model pushover analysis

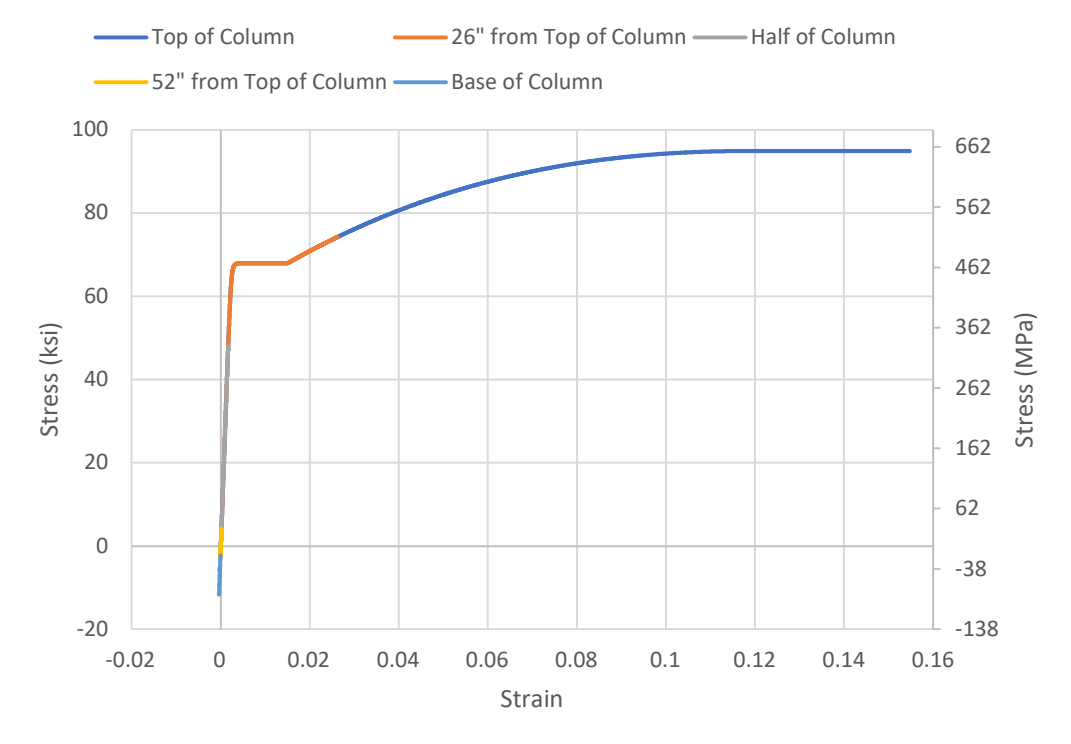

Figure 3.6 Stress-strain relationship of an extreme tensile bar along column length

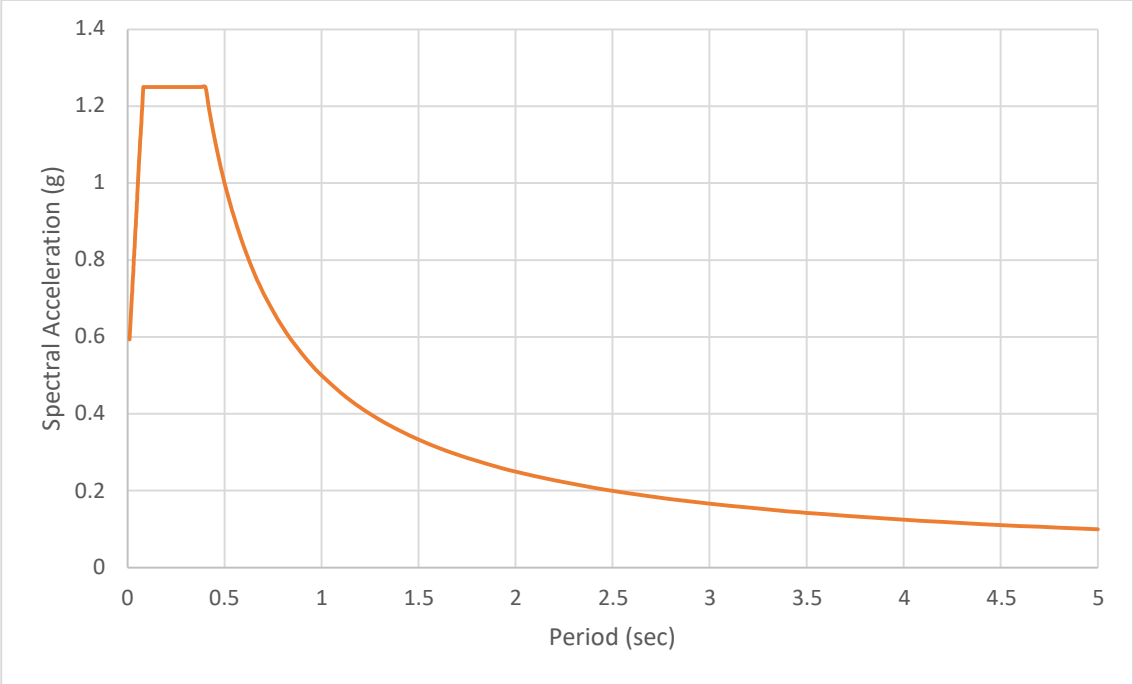

Figure 3.7 Design response spectrum

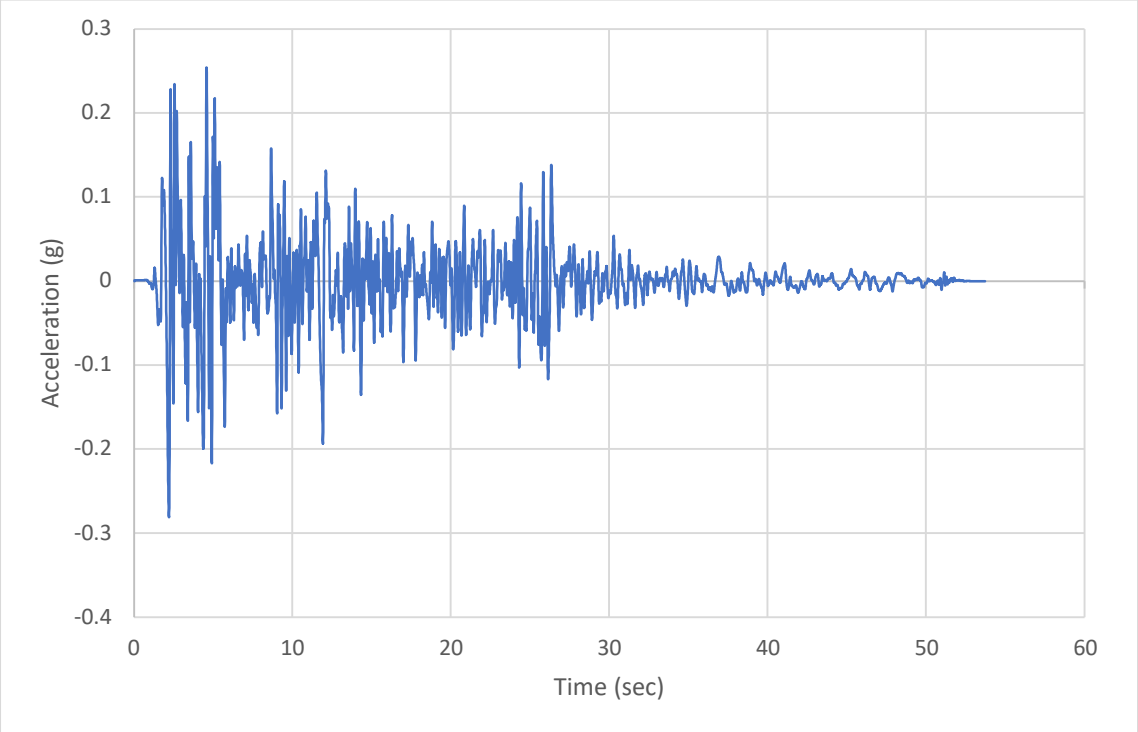

Figure 3.8 Imperial Valley-02 El Centro H1 acceleration history, unscaled and uncompressed

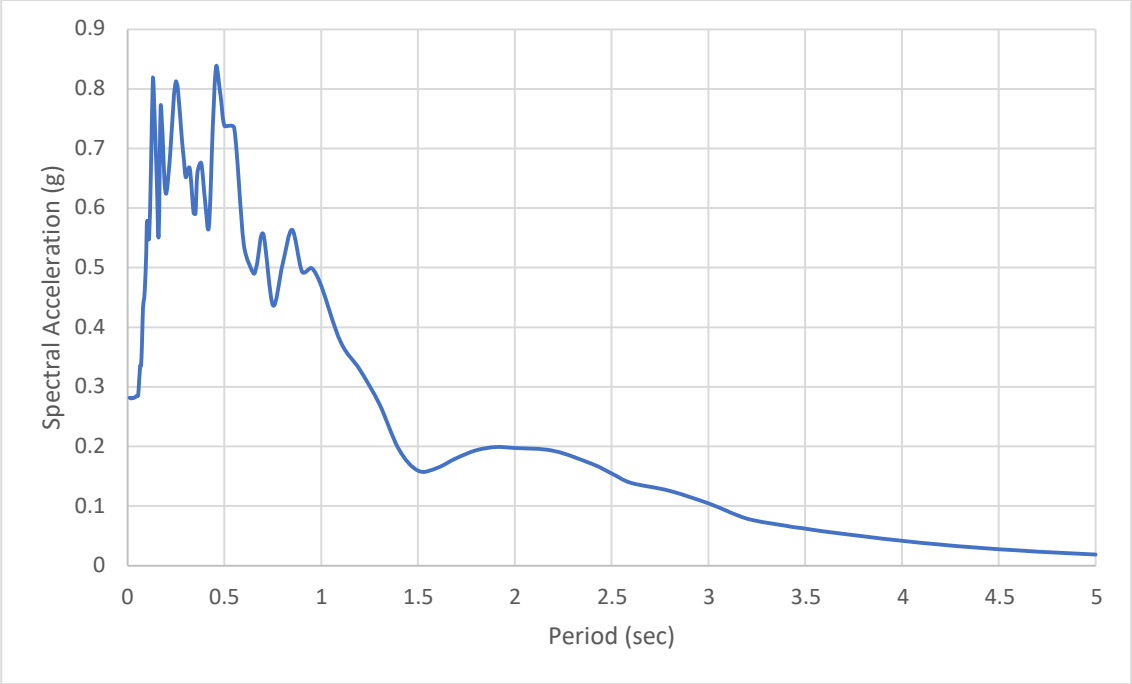

Figure 3.9 Imperial Valley-02 El Centro H1 response spectrum

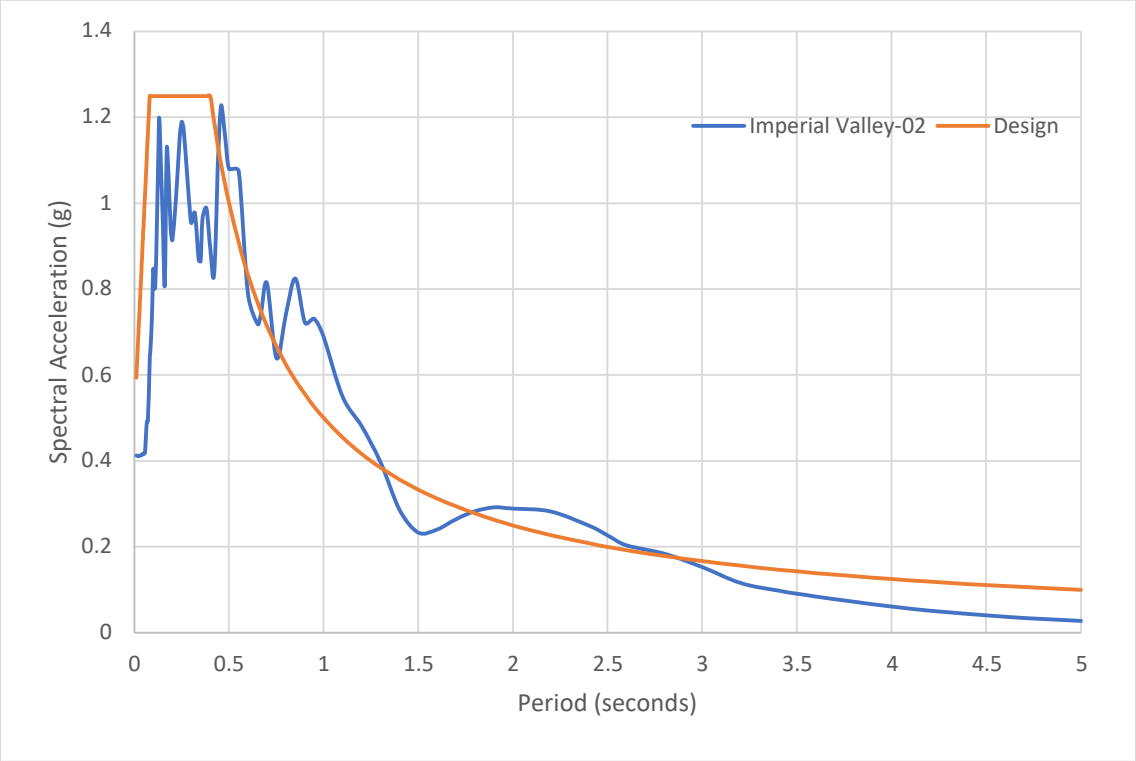

Figure 3.10 Comparison of scaled Imperial Valley-02 H1 and design response spectra

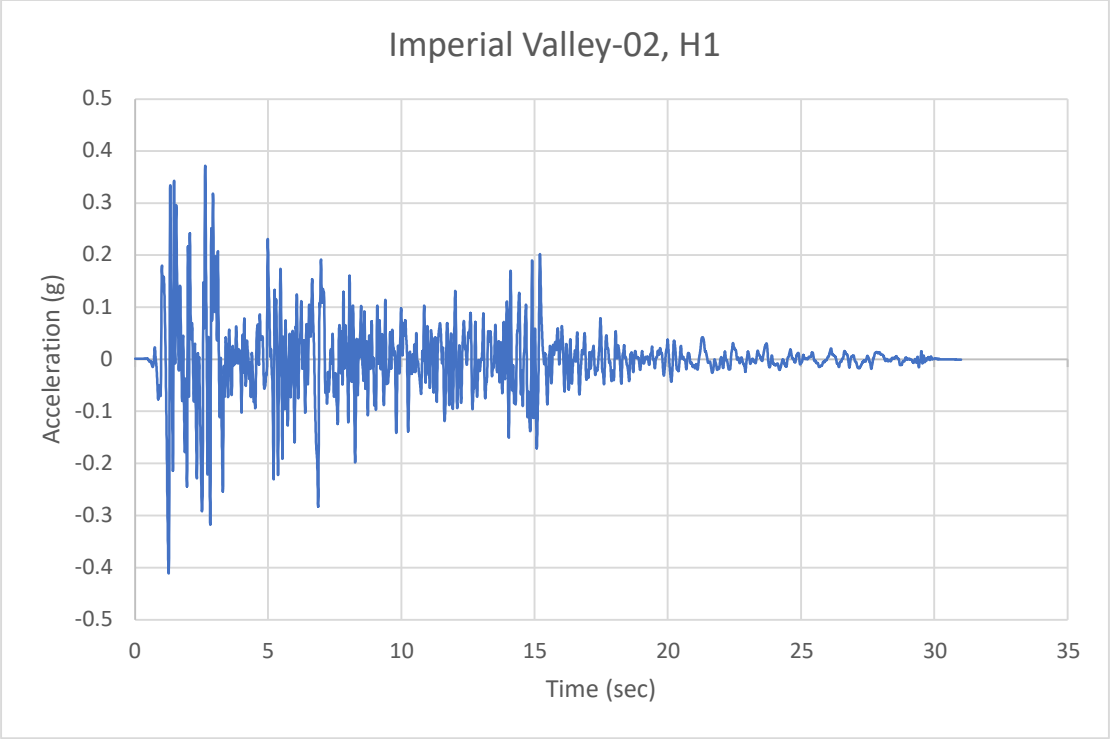

Figure 3.11 Imperial Valley-02 El Centro H1 acceleration history, scaled and compressed

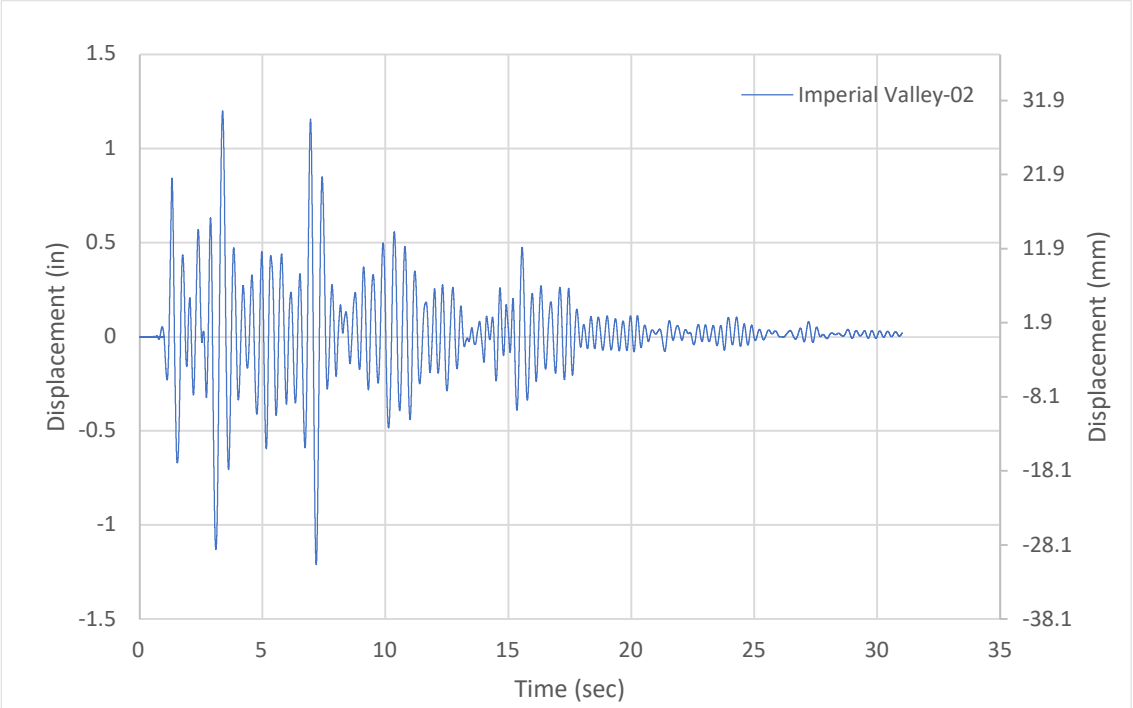

Figure 3.12 Displacement history for Imperial Valley-02 El Centro H1 dynamic analysis

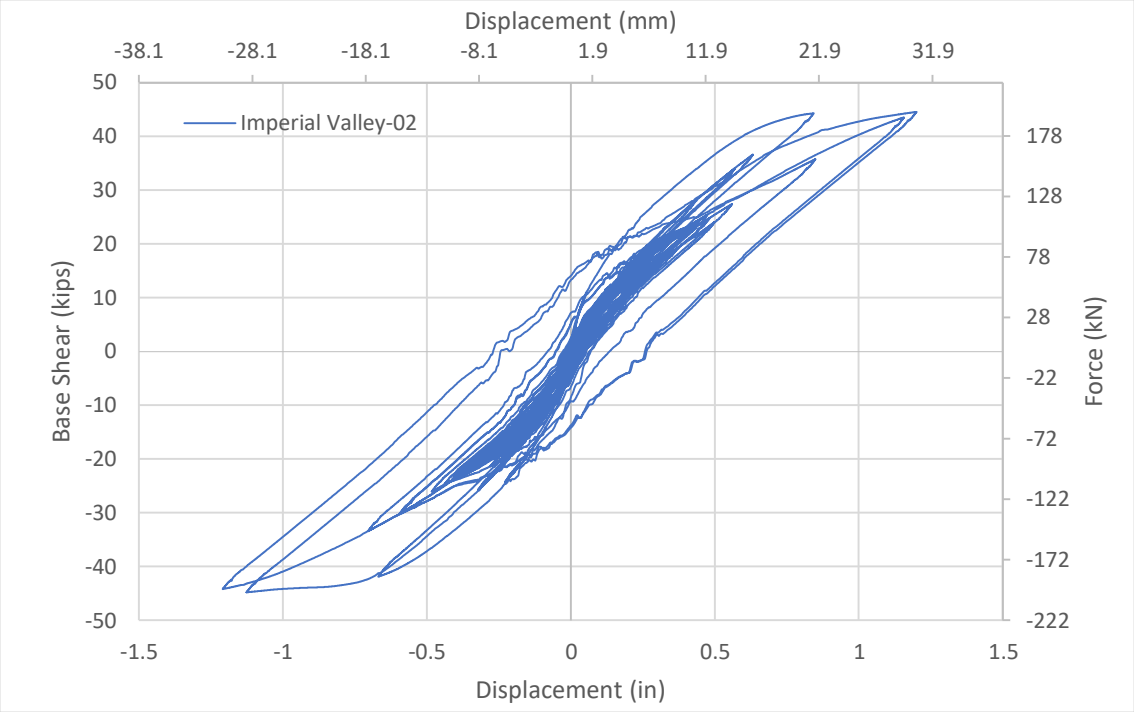

Figure 3.13 Force-displacement relationship for Imperial Valley-02 H1 dynamic analysis

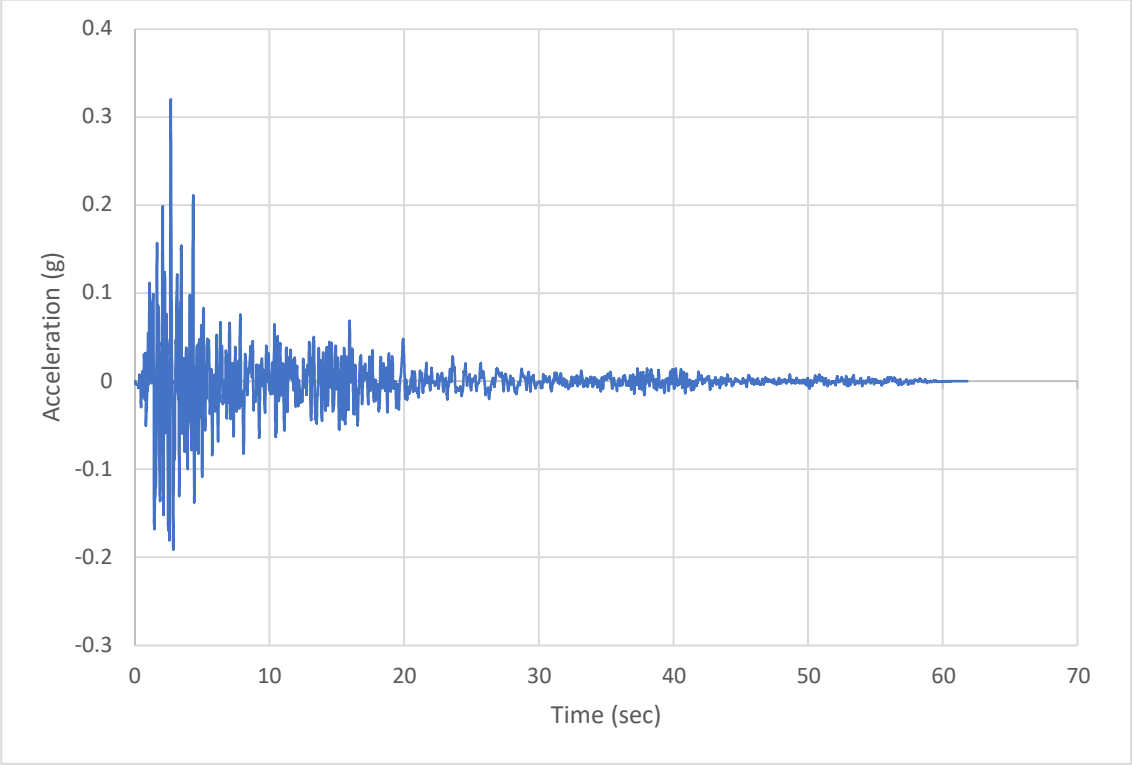

Figure 3.14 San Fernando H1 acceleration history, unscaled and uncompressed

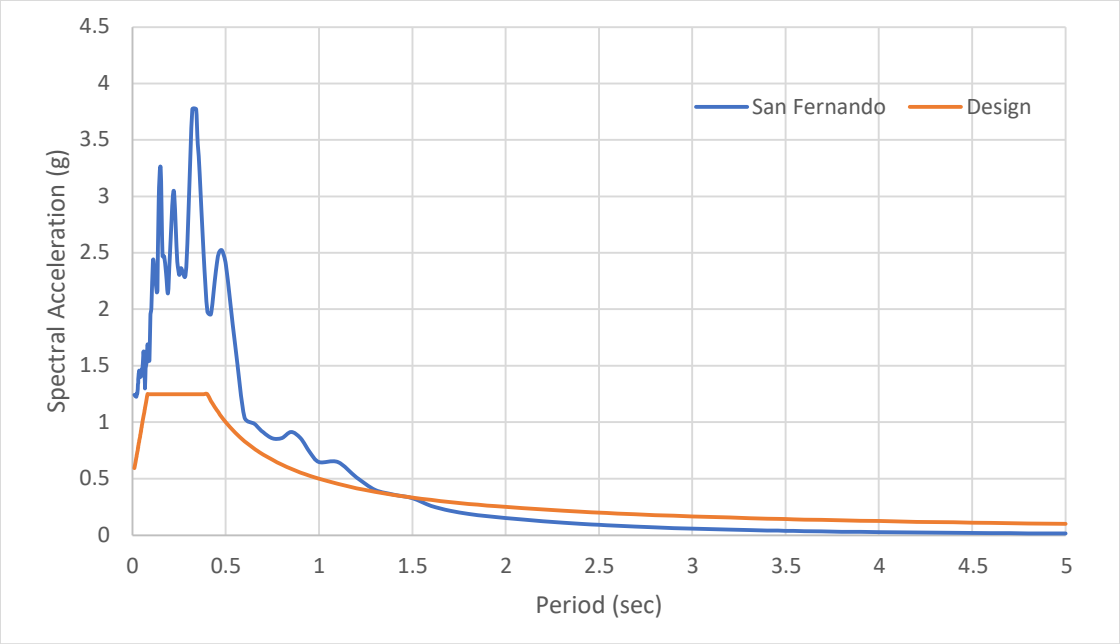

Figure 3.15 Comparison of scaled San Fernando H1 and design response spectra

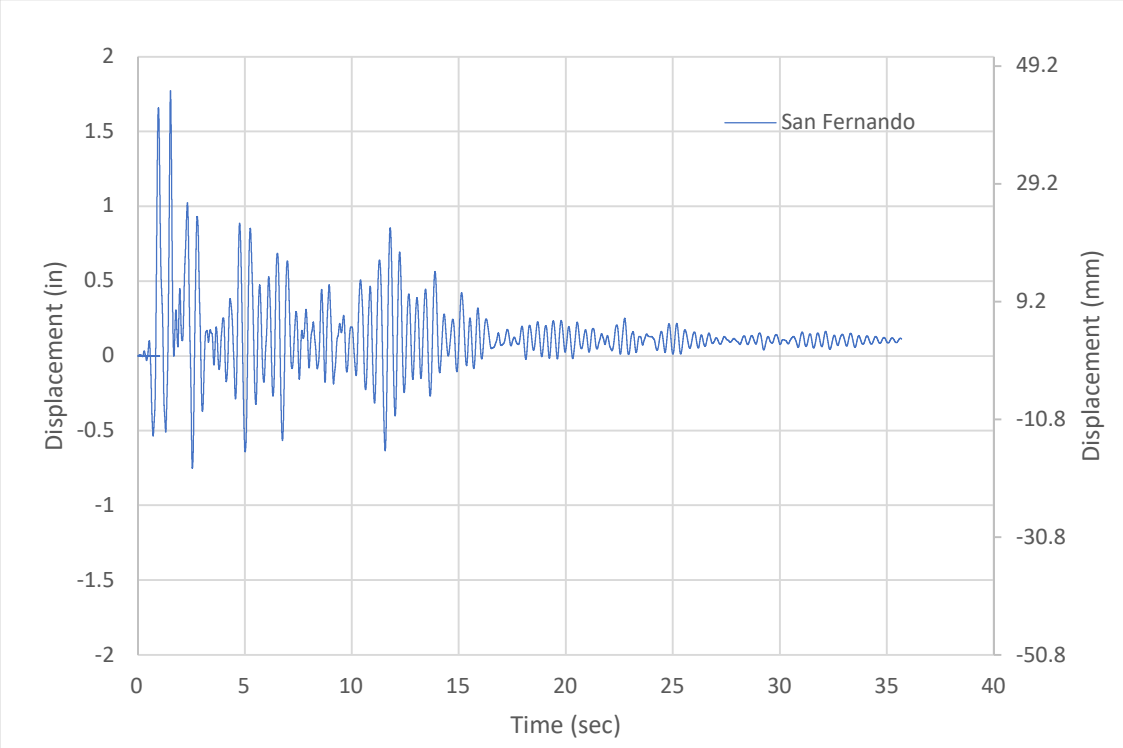

Figure 3.16 Displacement history for San Fernando H1 dynamic analysis

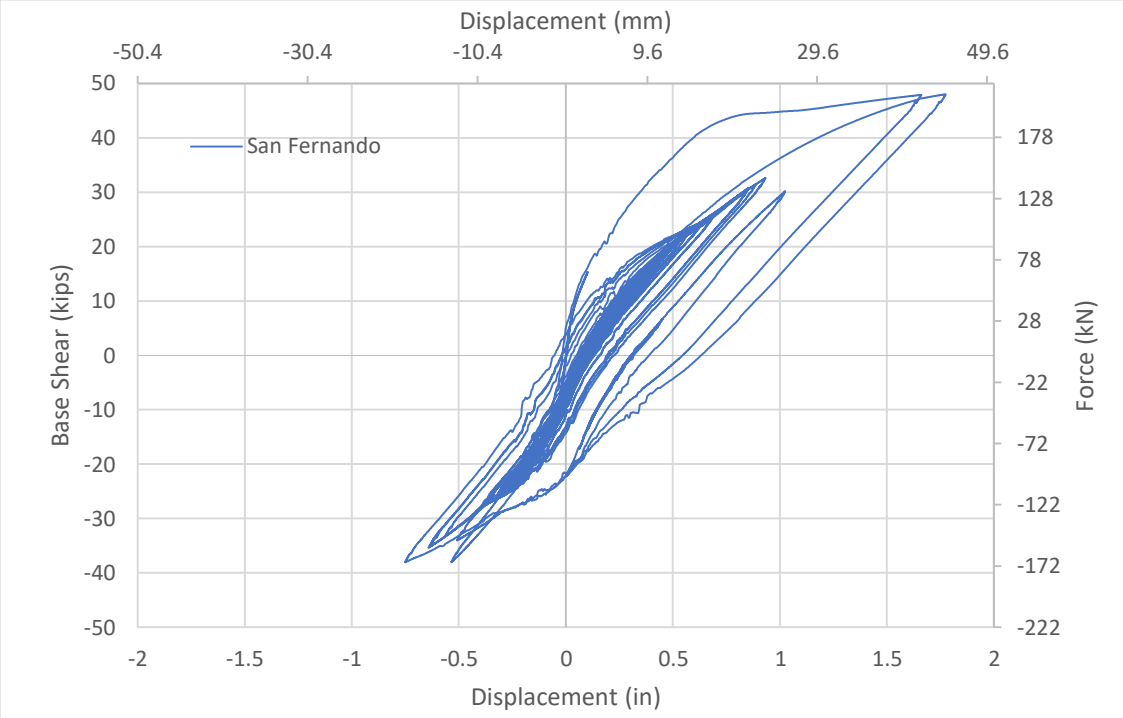

Figure 3.17 Force-displacement relationship for San Fernando H1 dynamic analysis

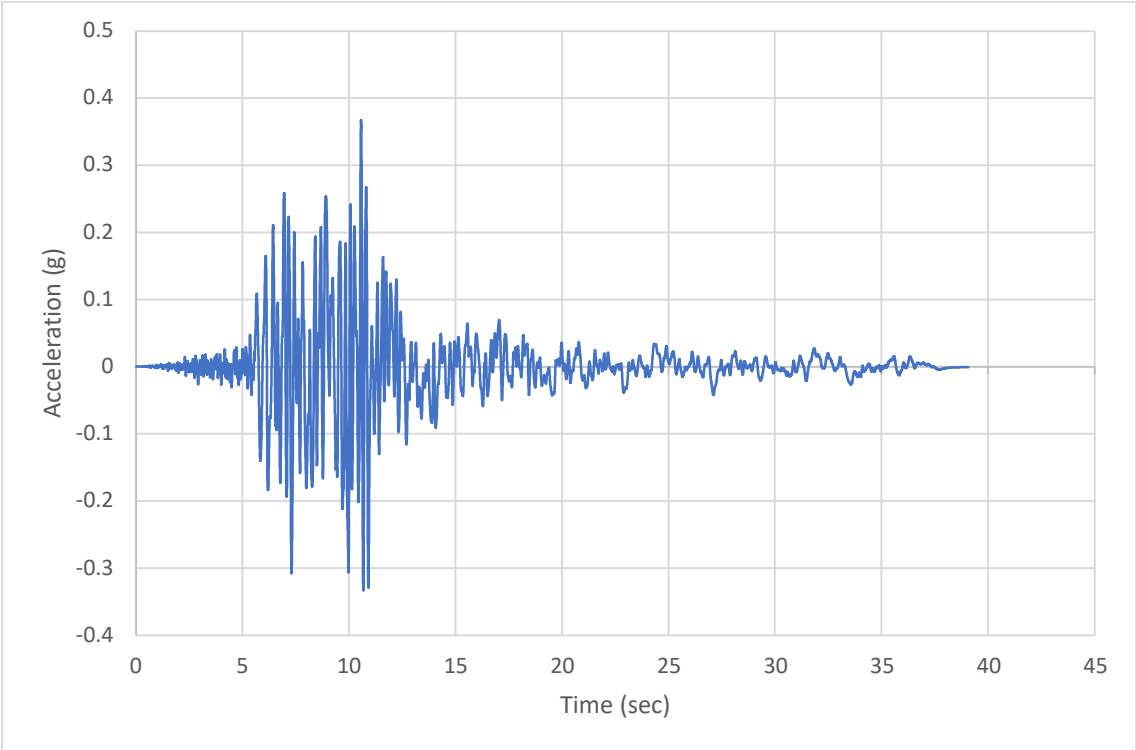

Figure 3.18 Imperial Valley-06 H1 acceleration history, unscaled and uncompressed

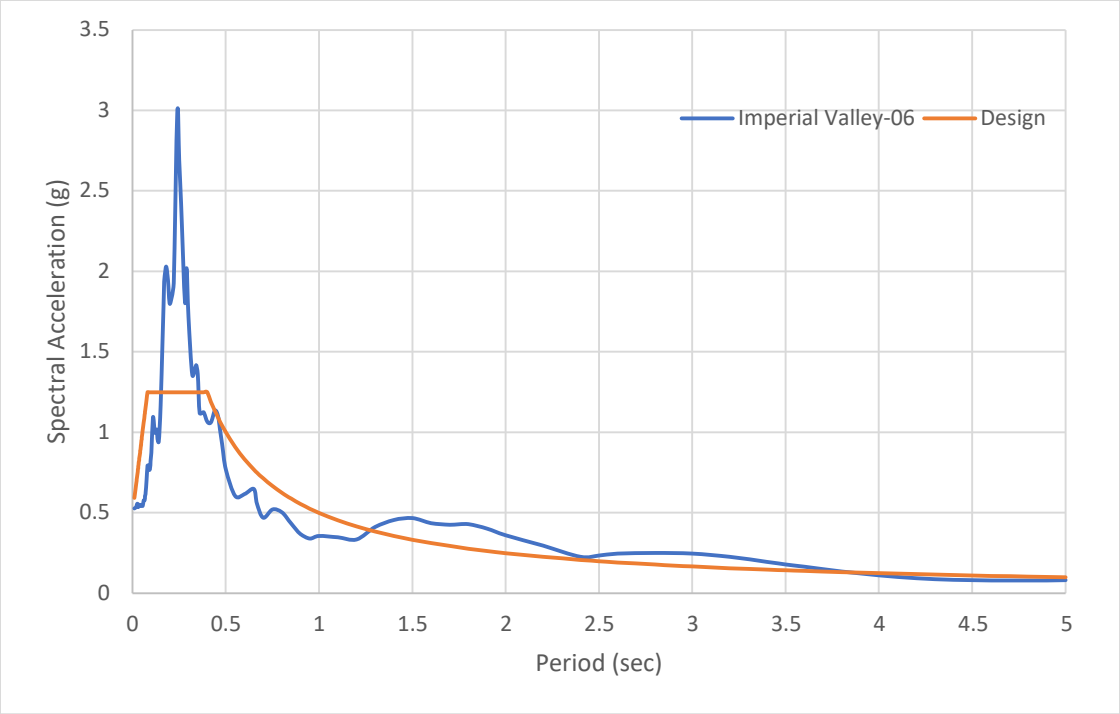

Figure 3.19 Comparison of scaled Imperial Valley-06 H1 and design response spectra

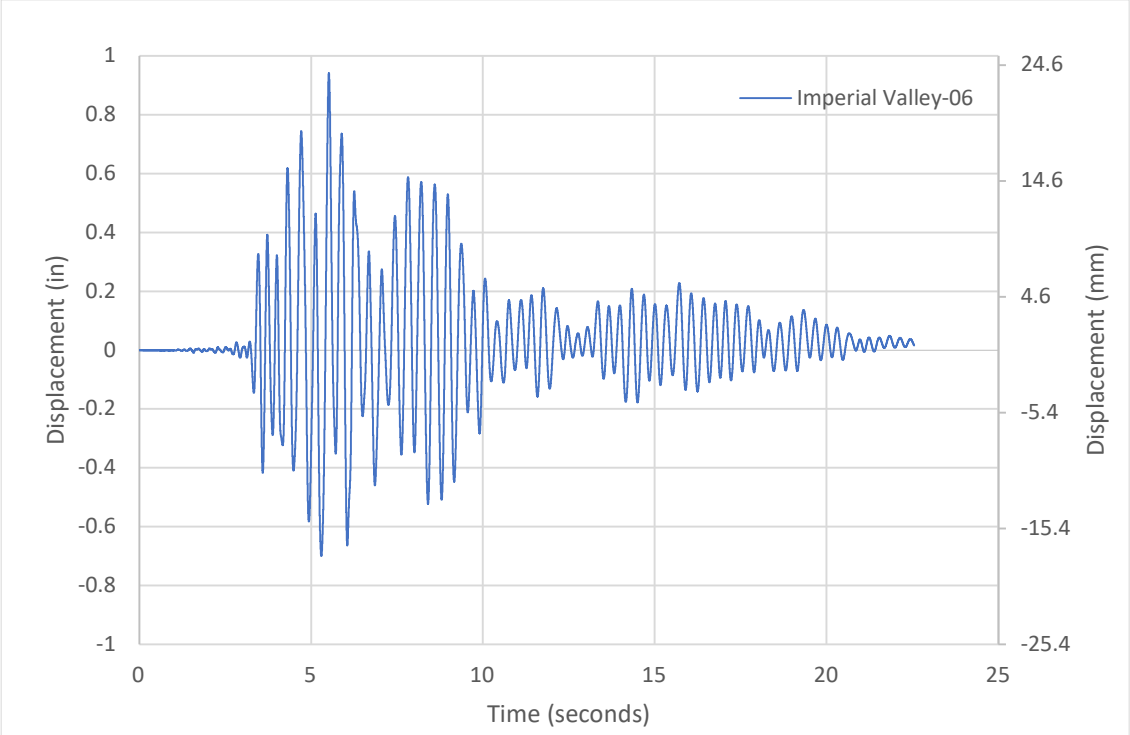

Figure 3.20 Displacement history for Imperial Valley-06 H1 dynamic analysis

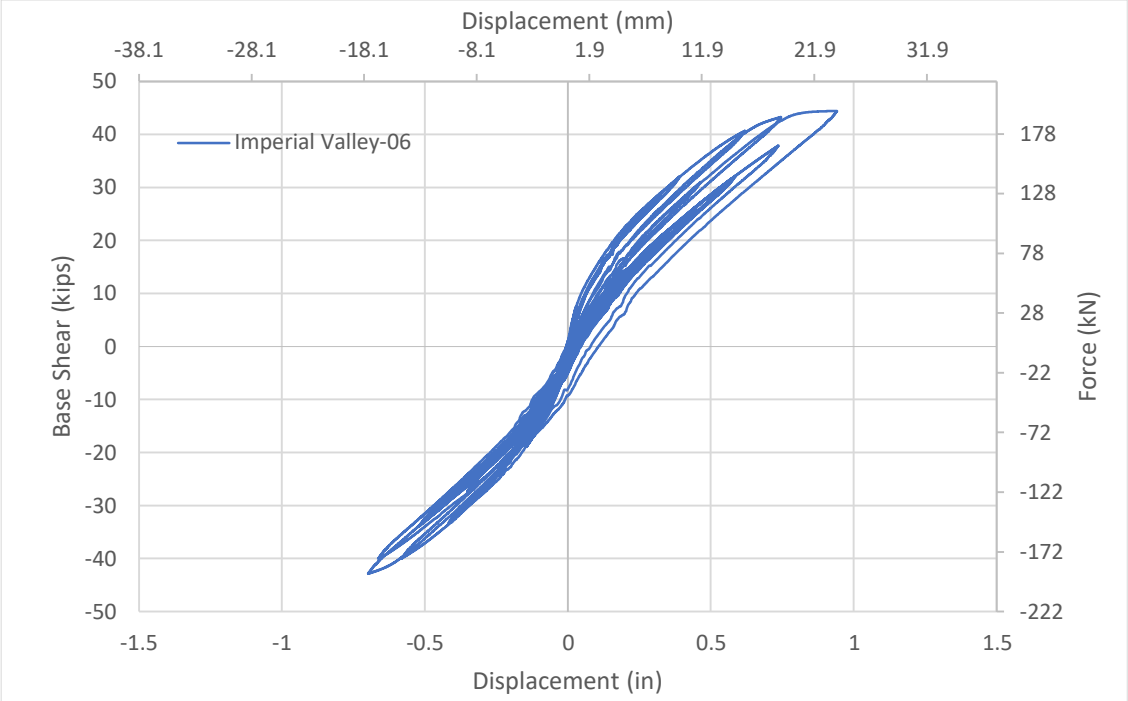

Figure 3.21 Force-displacement relationship for Imperial Valley-06 H1 dynamic analysis

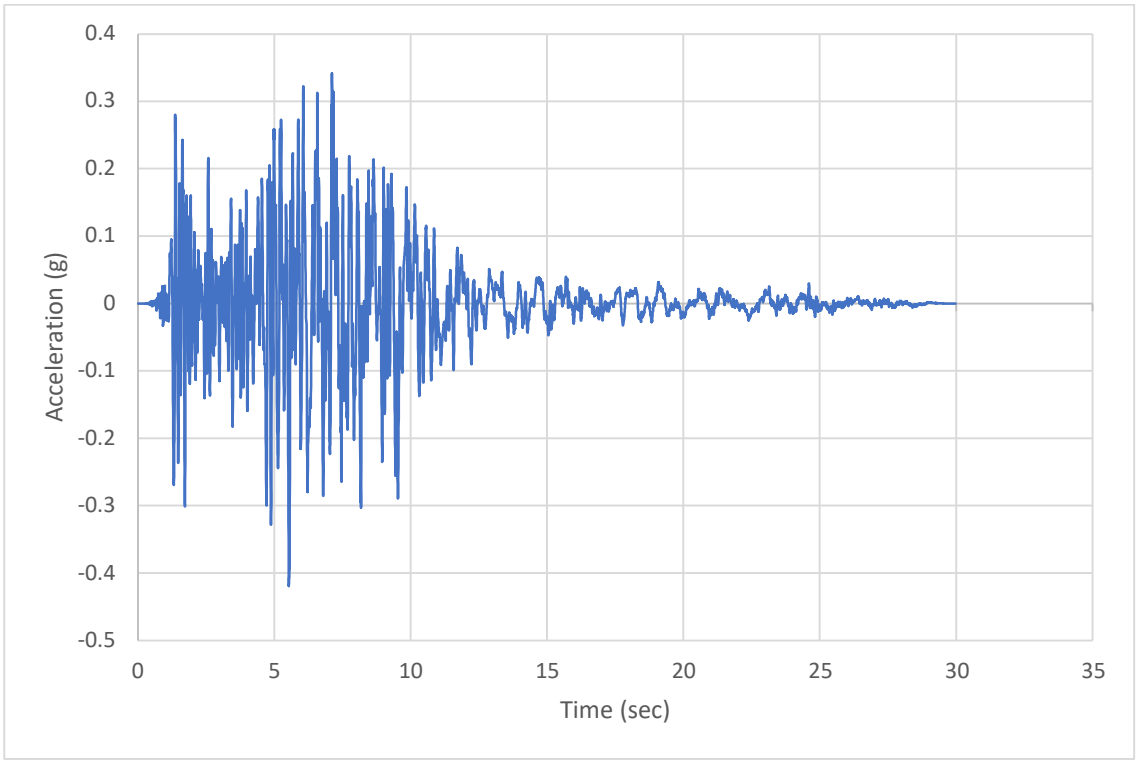

Figure 3.22 Mammoth Lakes-01 H1 acceleration history, unscaled and uncompressed

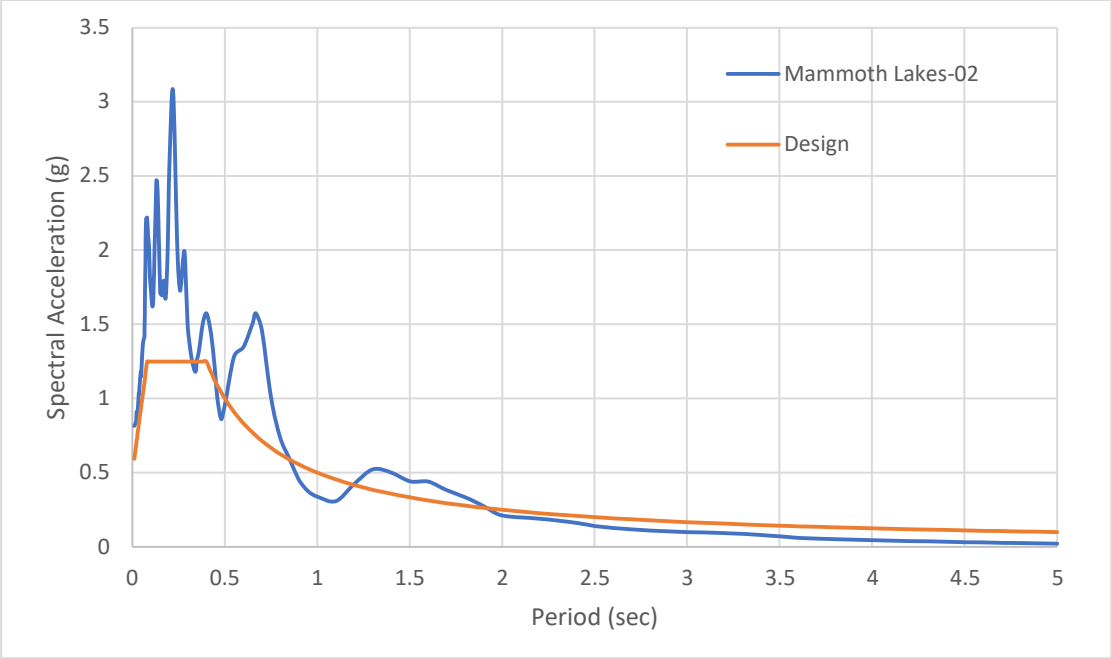

Figure 3.23 Comparison of scaled Mammoth Lakes-01 H1 and design response spectra

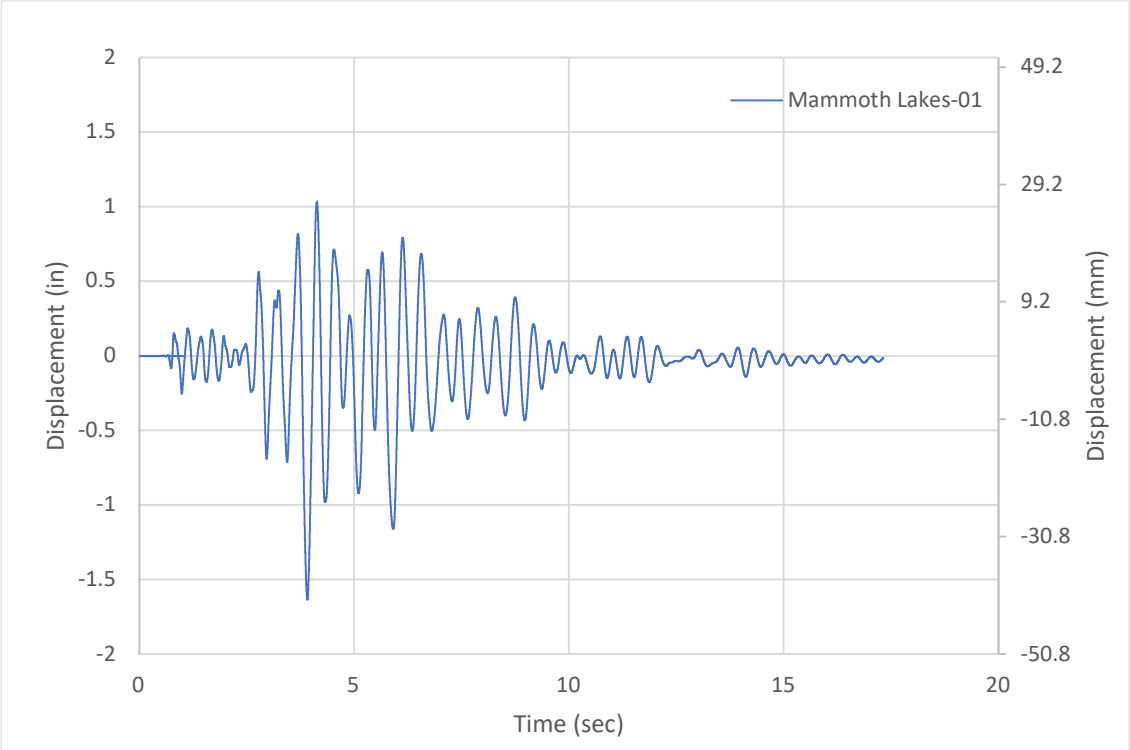

Figure 3.24 Displacement history for Mammoth Lakes-01 H1 dynamic analysis

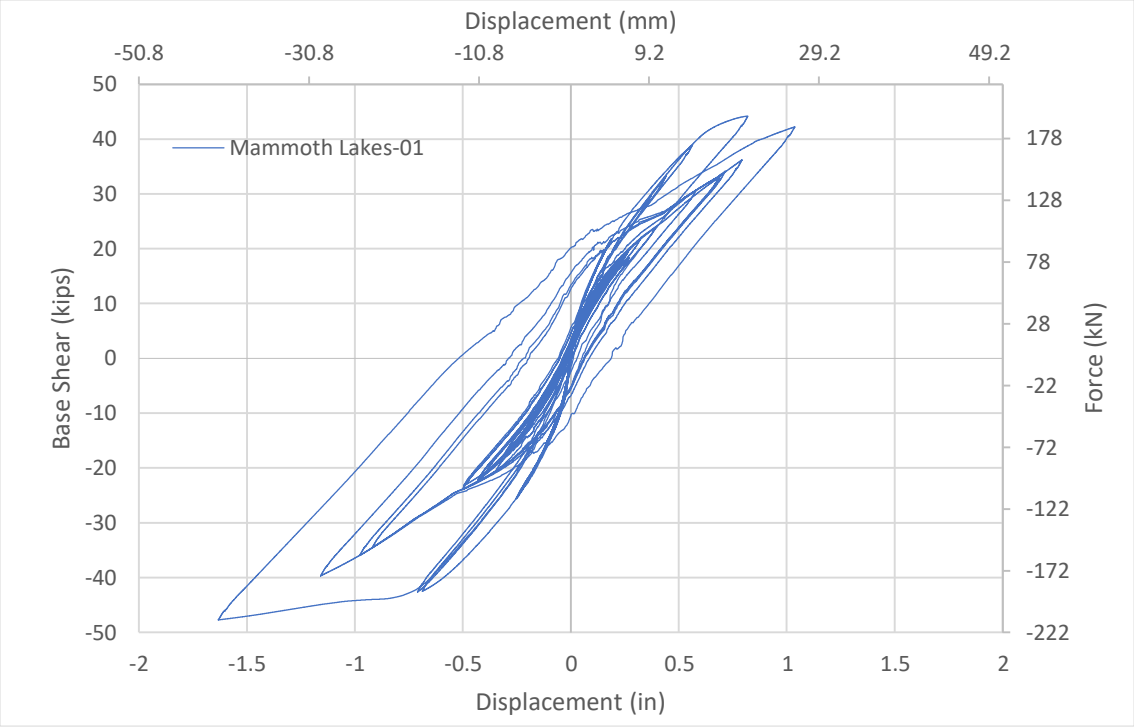

Figure 3.25 Force-displacement relationship for Mammoth Lakes-01 H1 dynamic analysis

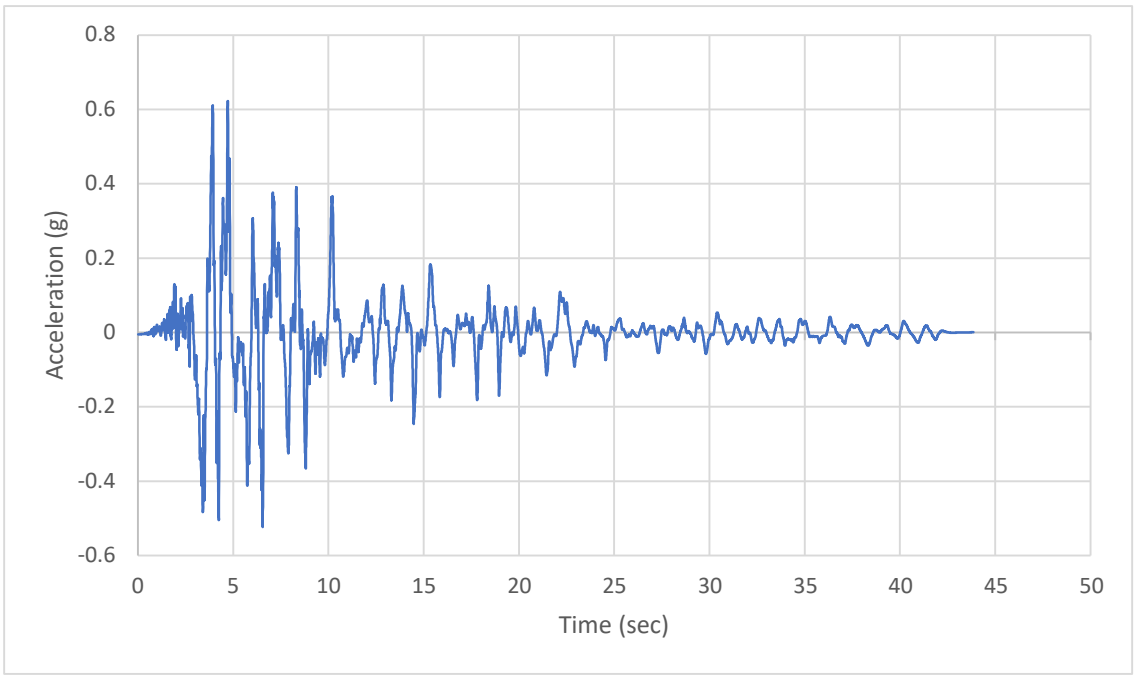

Figure 3.26 Northridge-01 H1 acceleration history, unscaled and uncompressed

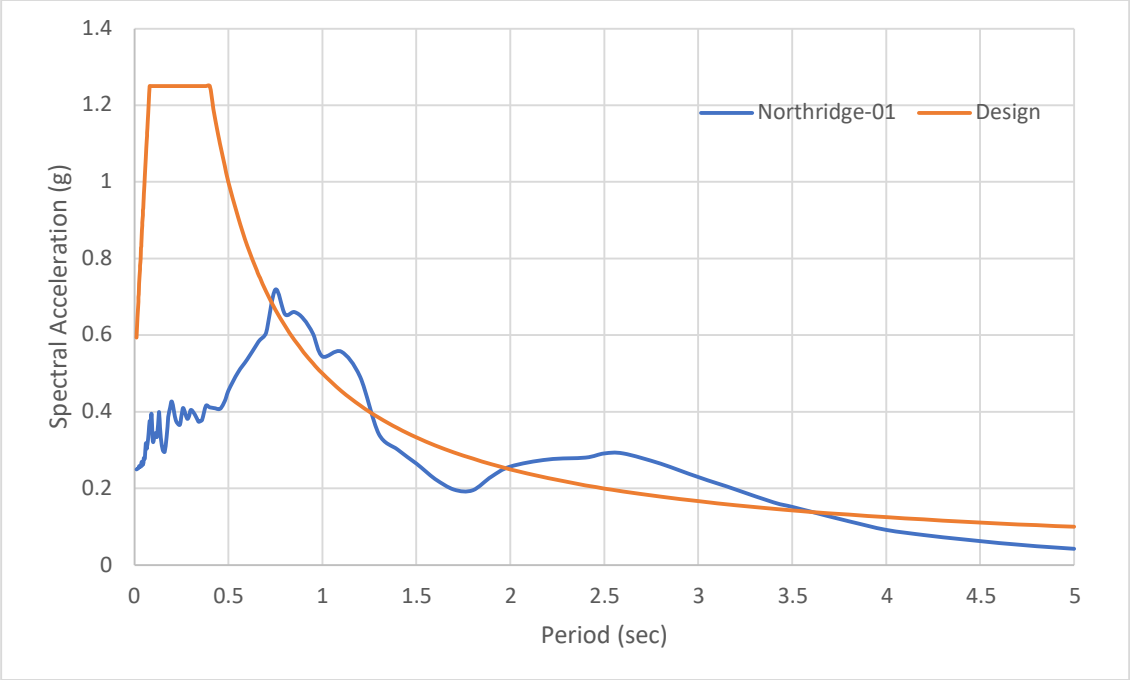

Figure 3.27 Comparison of scaled Northridge-01 H1 and design response spectra

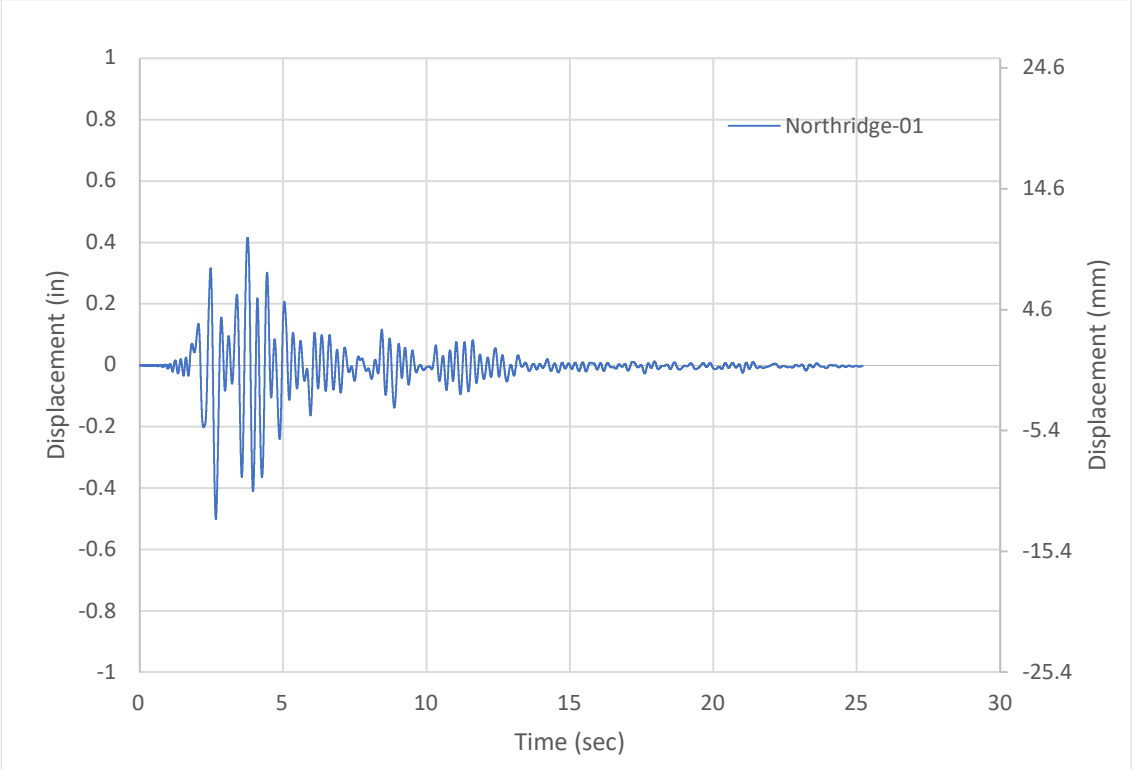

Figure 3.28 Displacement history for Northridge-01 H1 dynamic analysis

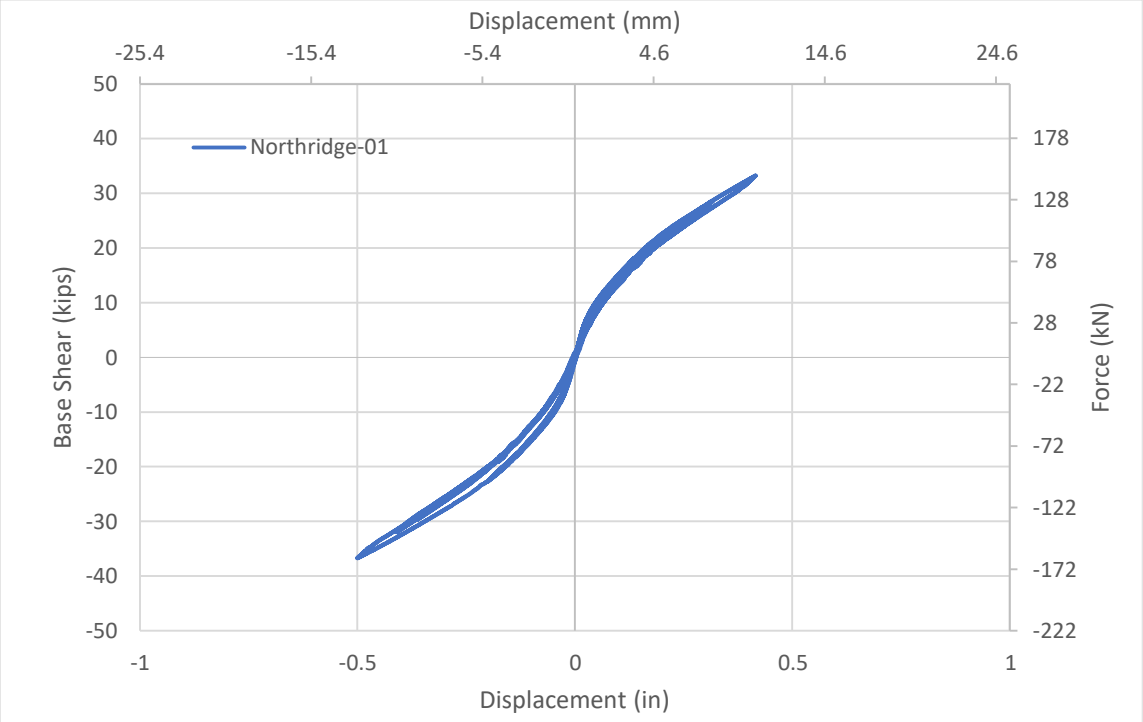

Figure 3.29 Force-displacement relationship for Northridge-01 H1 dynamic analysis

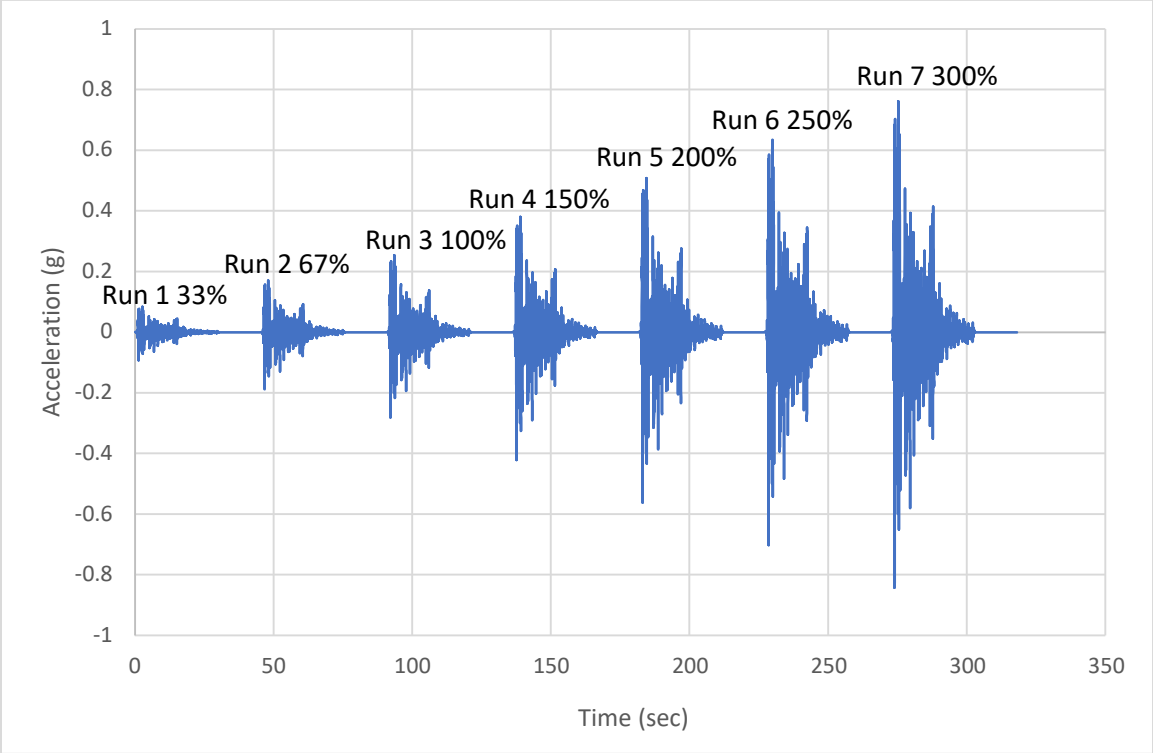

Figure 3.30 Loading protocol acceleration history

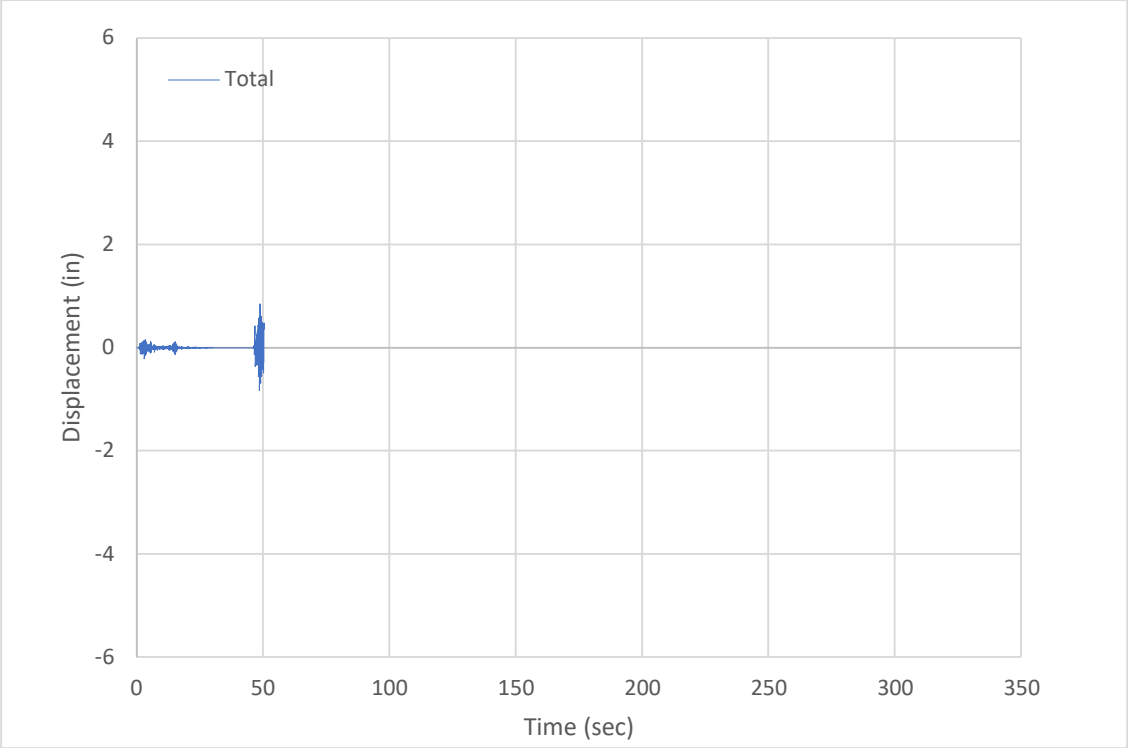

Figure 3.31 Predicted displacement history for all runs

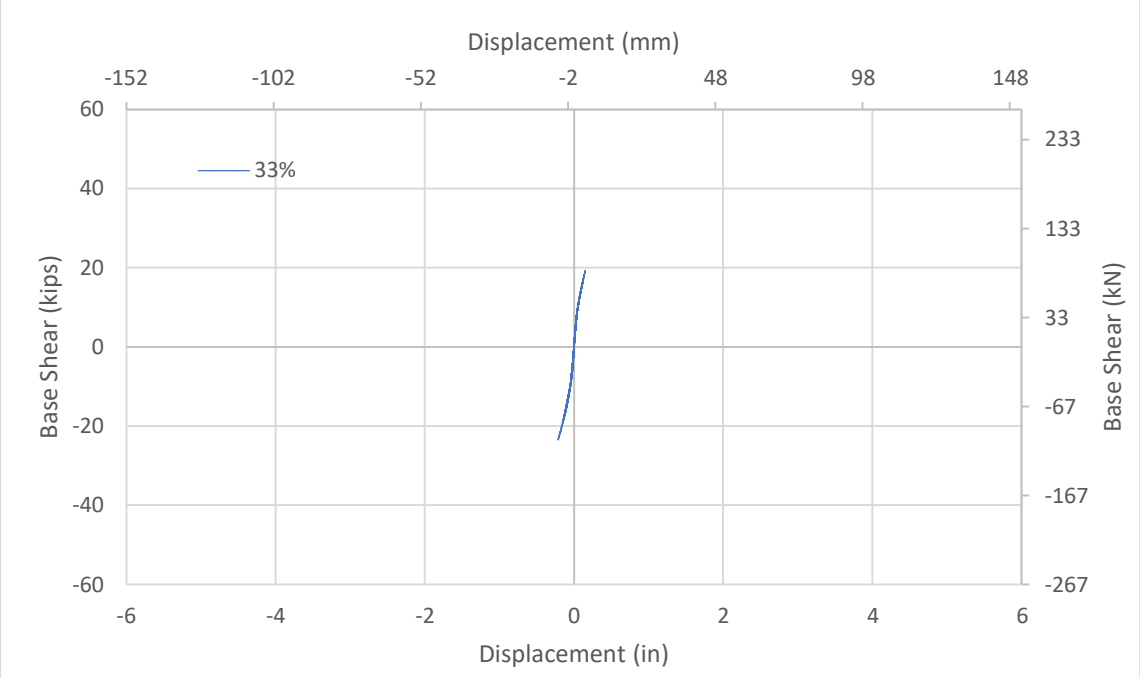

Figure 3.32 Force-displacement relationship for run 1 (33% design earthquake)

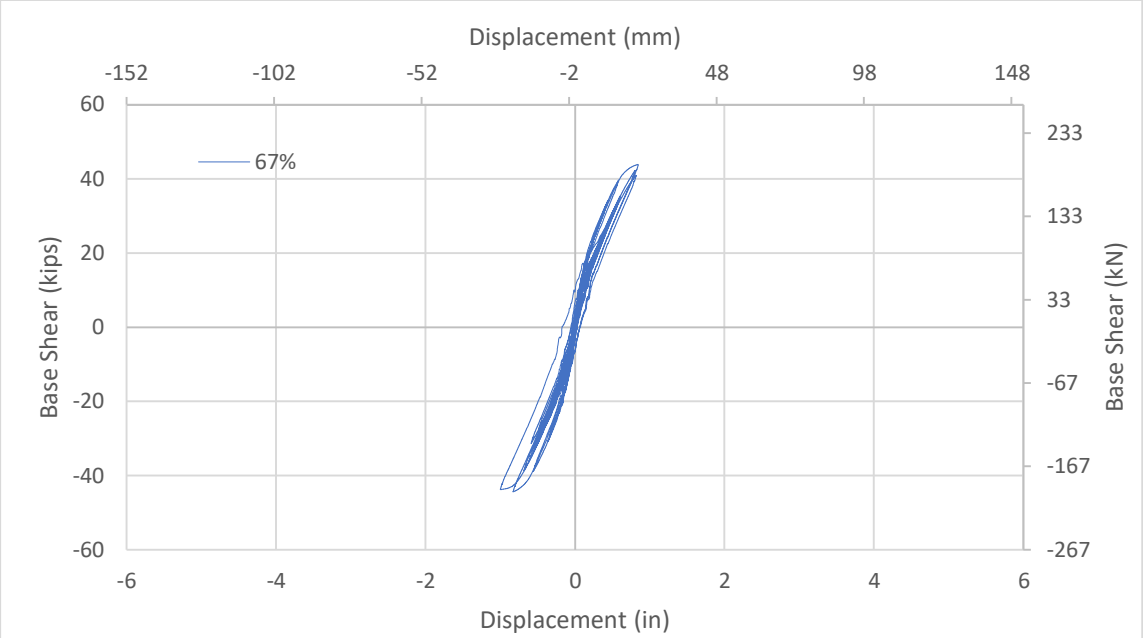

Figure 3.33 Force-displacement relationship for run 2 (67% design earthquake)

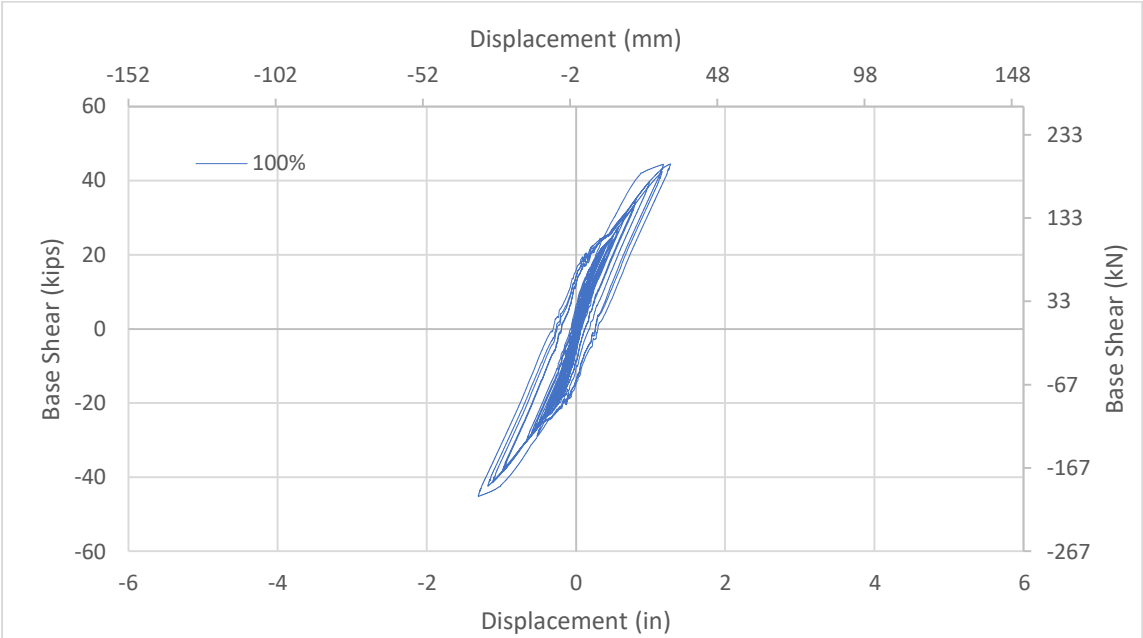

Figure 3.34 Force-displacement relationship for run 3 (100% design earthquake)

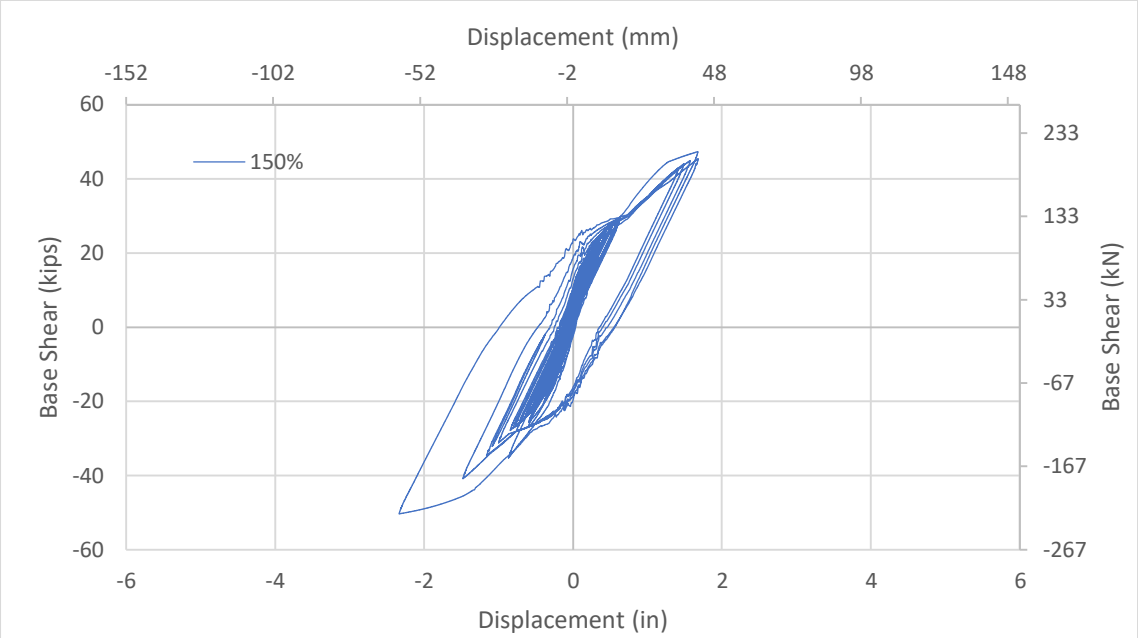

Figure 3.35 Force-displacement relationship for run 4 (150% design earthquake)

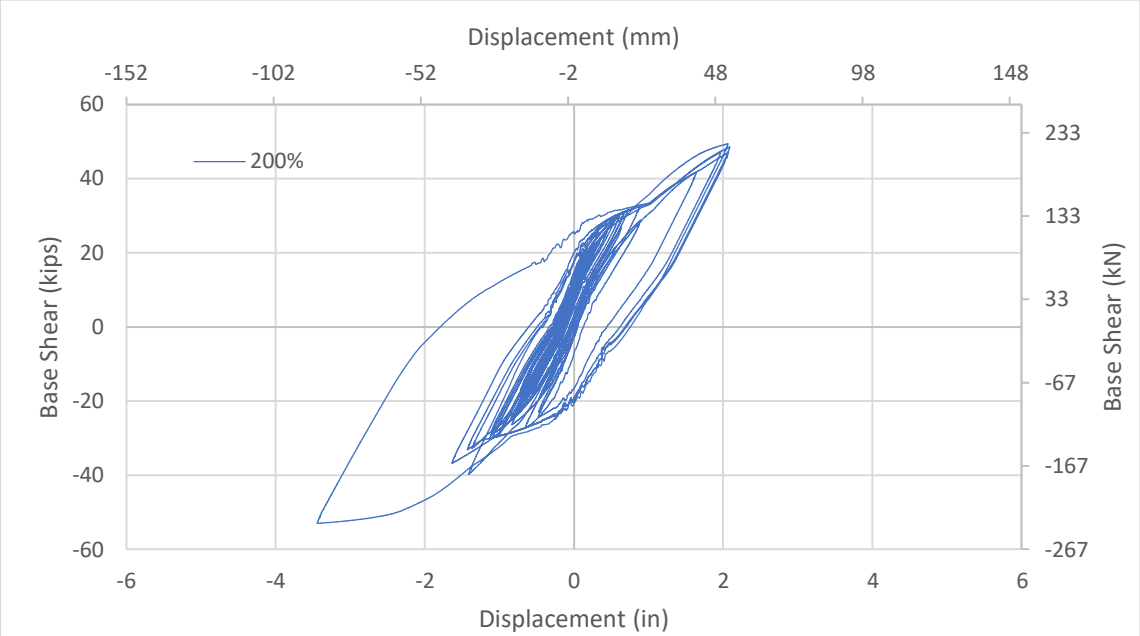

Figure 3.36 Force-displacement relationship for run 5 (200% design earthquake)

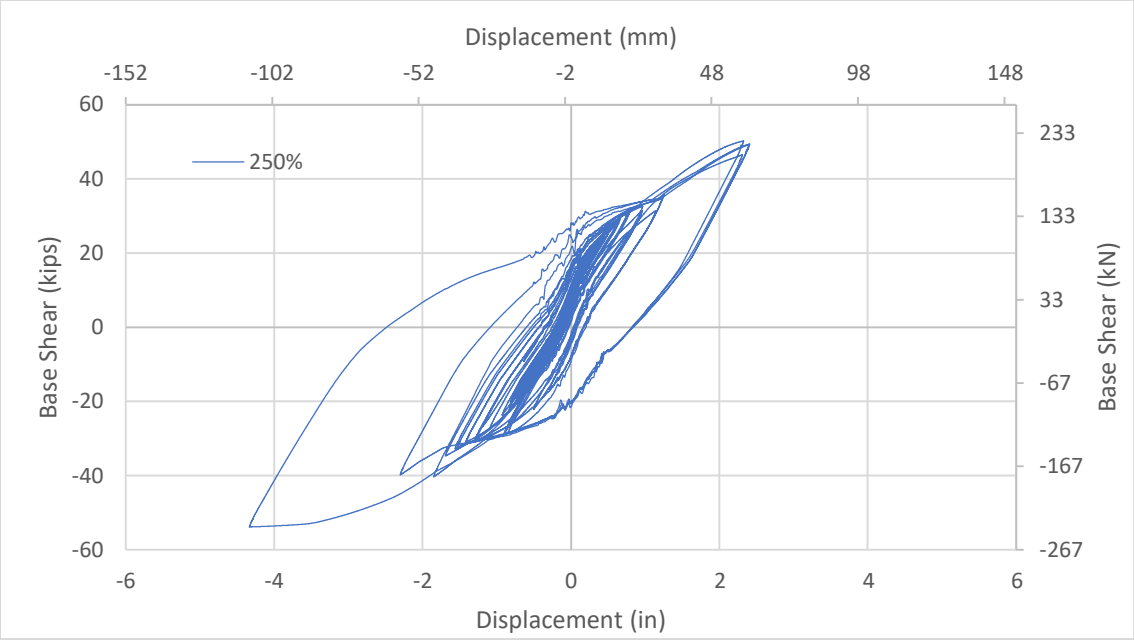

Figure 3.37 Force-displacement relationship for run 6 (250% design earthquake)

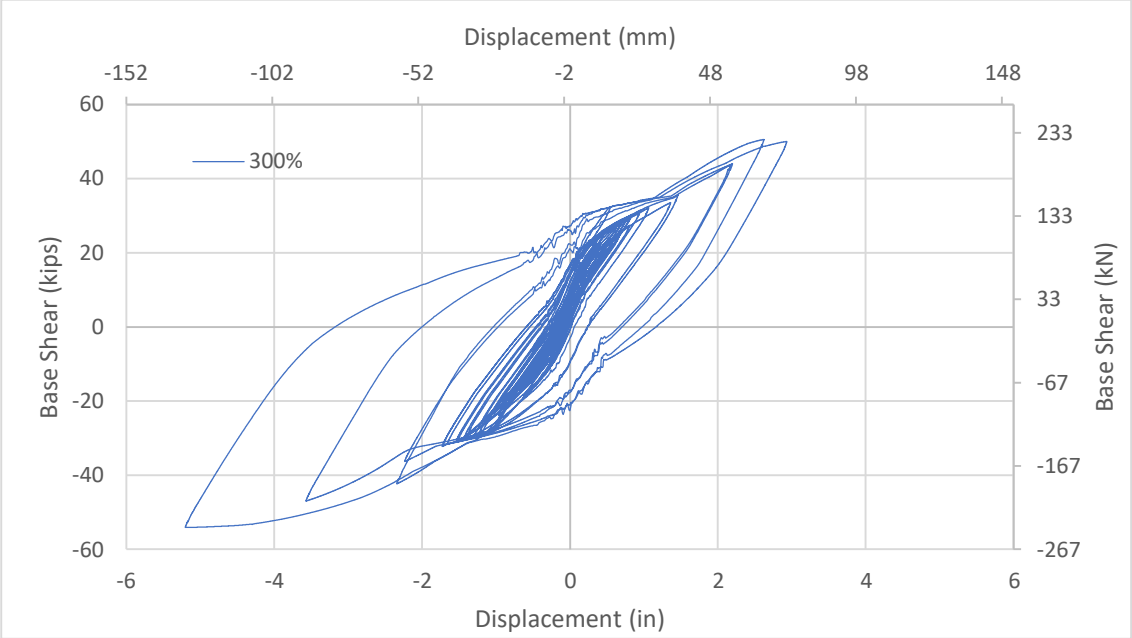

Figure 3.38 Force-displacement relationship for run 7 (300% design earthquake)

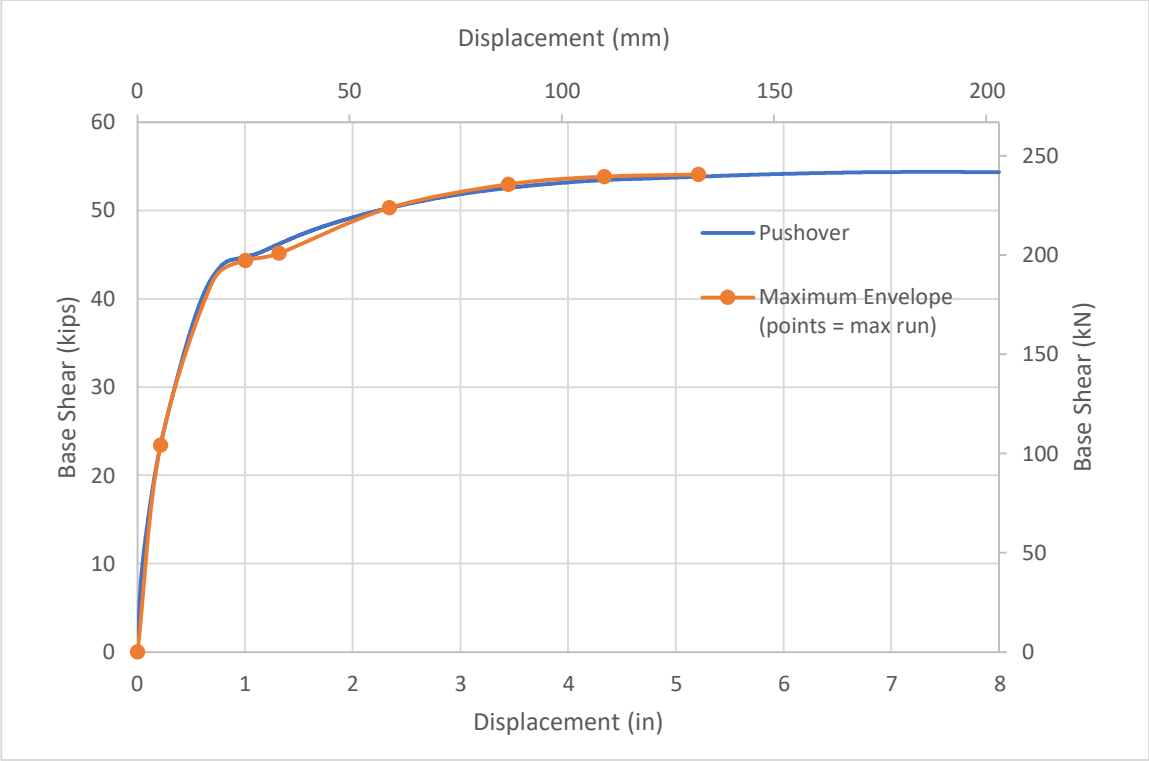

Figure 3.39 Hysteresis envelope compared to pushover curve

Chapter 4 Tables

Table 4.1 Concrete compressive strength test results

	7-day, ksi (MPa)	14-day, ksi (MPa)	28-day, ksi (MPa)	Test day, ksi (MPa)	Test day age, days
Footing	3603 (24842)	- -	4421 (30482)	4406 (30378)	72
Columns	- -	3932 (27110)	4401 (30344)	4457 (30730)	56
Cap Beam	3551 (24483)	3912 (26972)	4339 (29916)	4364 (30089)	41

Table 4.2 Steel reinforcement material properties test results

Bar Size	fy, yield stress, ksi (MPa)	fu, ultimate stress, ksi (MPa)	Ɛsh, strain at hardening, in/in	Ɛu, ultimate strain, in/in
#3	60 (414)	98 (676)	0.0025	0.1043
#4	65.5 (452)	95 (655)	0.0083	0.1202
#5	61 (421)	96.5 (665)	0.0028	0.1213

Table 4.3 CAM bar material properties test results

CAM Bar Sample #	fy, yield Stress, ksi (Mpa)	fu, ultimate stress, ksi (MPa)	Elastic Modulus, ksi (MPa)	Post-yield Modulus, ksi (MPa)	Ɛy, yield strain, in/in	Ɛr, rupture strain, in/in
1	20 (138)	52.5 (362)	5000 (34474)	250 (1724)	0.004	0.134
2	25 (172)	> 60 > (414)	4167 (28728)	147.5 (1017)	0.006	> .10
3	26 (179)	59 (407)	4401 (30344)	227.5 (1569)	0.008	0.12
Average	23.67 (163)	55.75 (384)	4522.56 (31182)	208.33 (1436)	0.006	0.127

Chapter 4 Figures

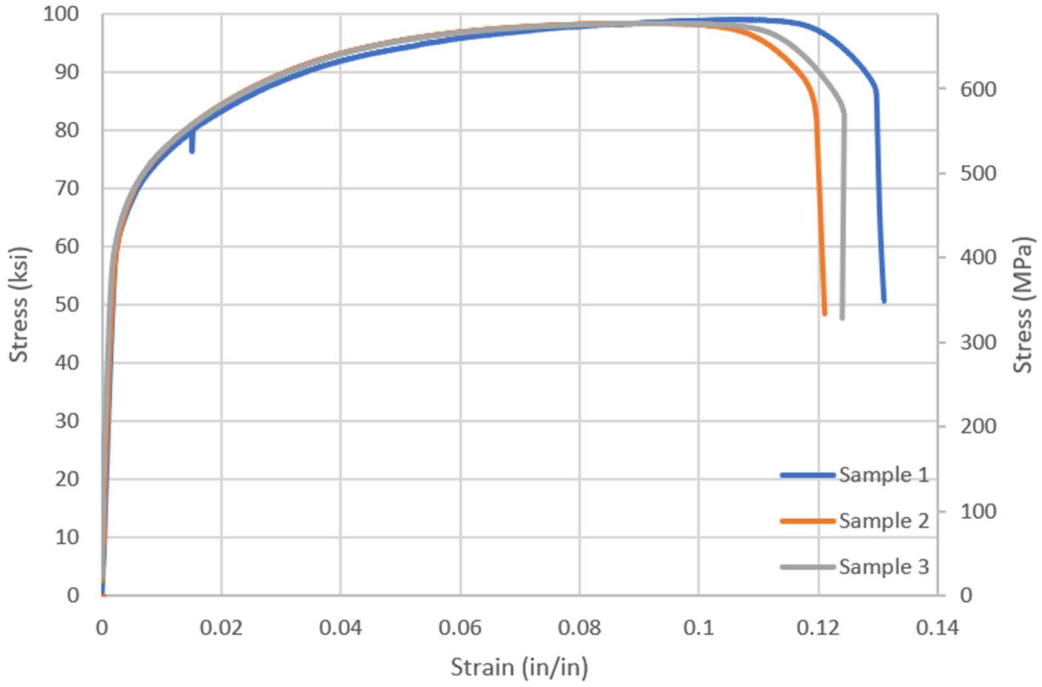

Figure 4.1 Measured stress-strain relationships for #3 bars

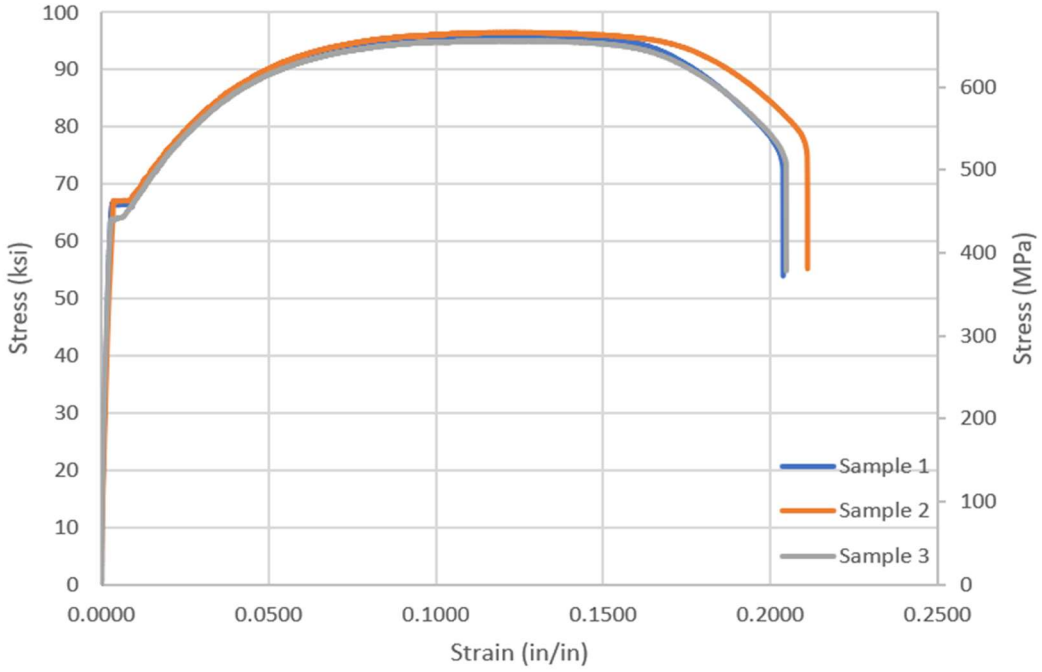

Figure 4.2 Measured stress-strain relationships for #4 bars

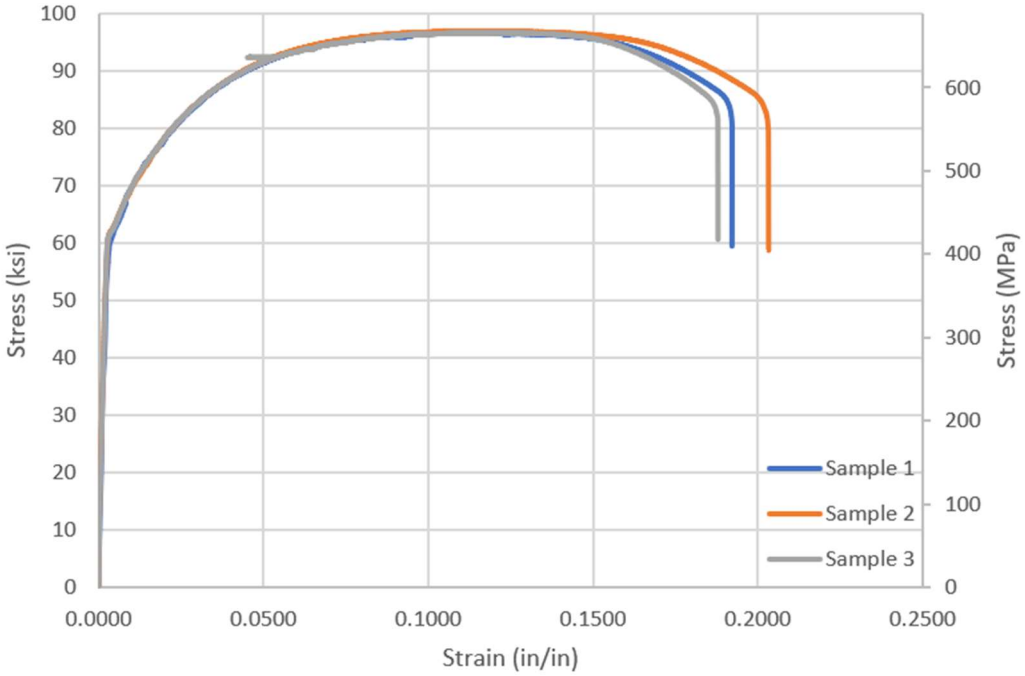

Figure 4.3 Measured stress-strain relationships for #5 bars

Figure 4.4 CAM bar test setup

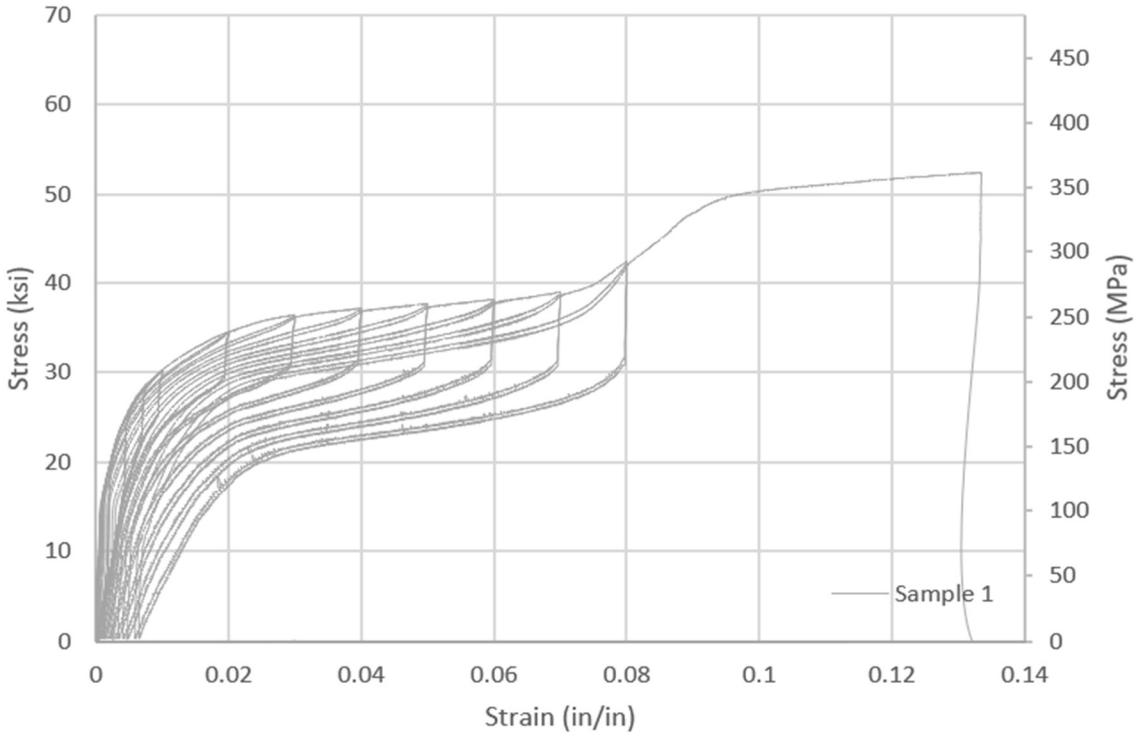

Figure 4.5 Measured stress-strain relationships for CAM sample 1

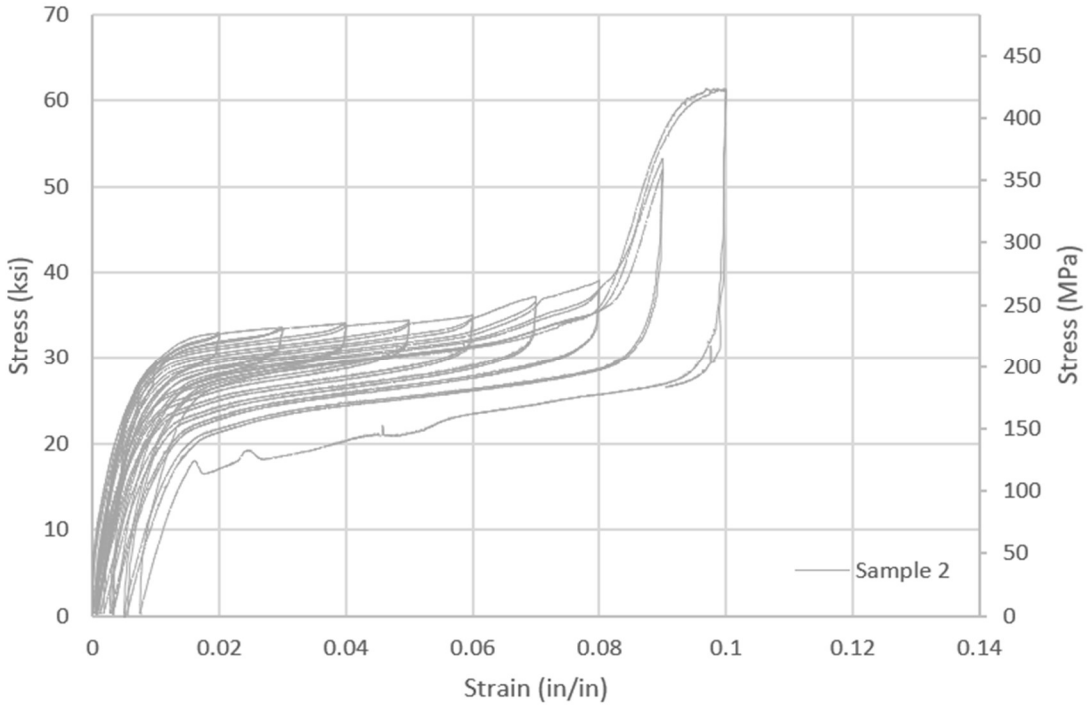

Figure 4.6 Measured stress-strain relationships for CAM sample 2

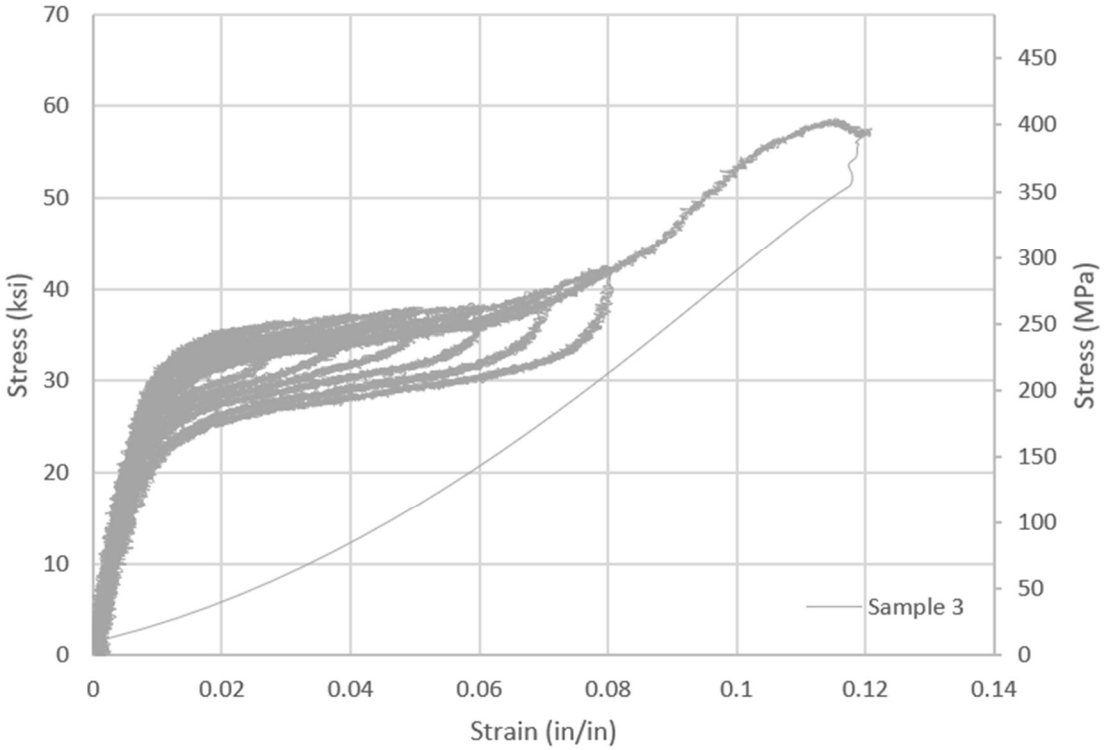

Figure 4.7 Measured stress-strain relationships for CAM sample 3

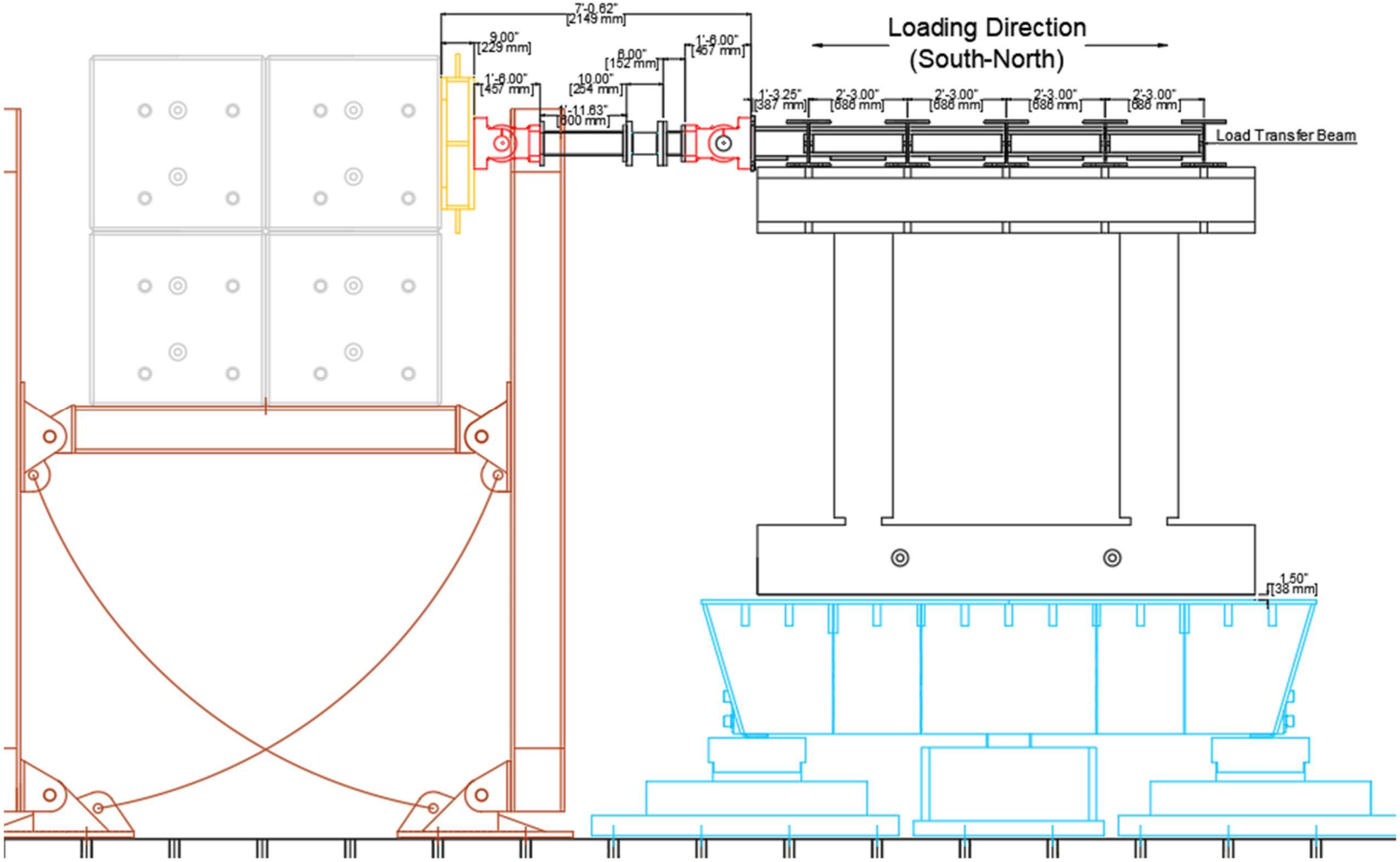

Figure 4.8 Elevation view of test setup

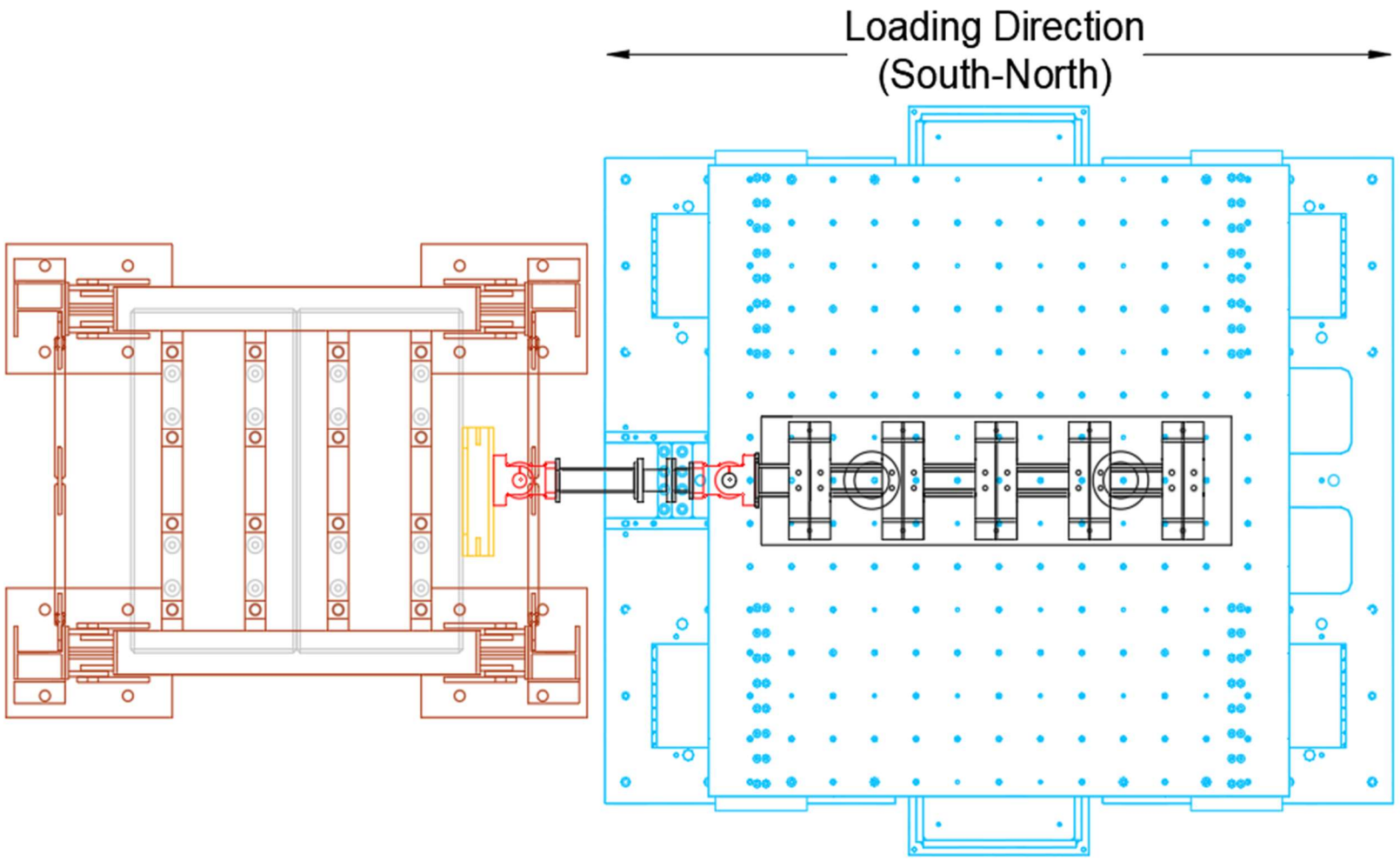

Figure 4.9 Plan view of test setup

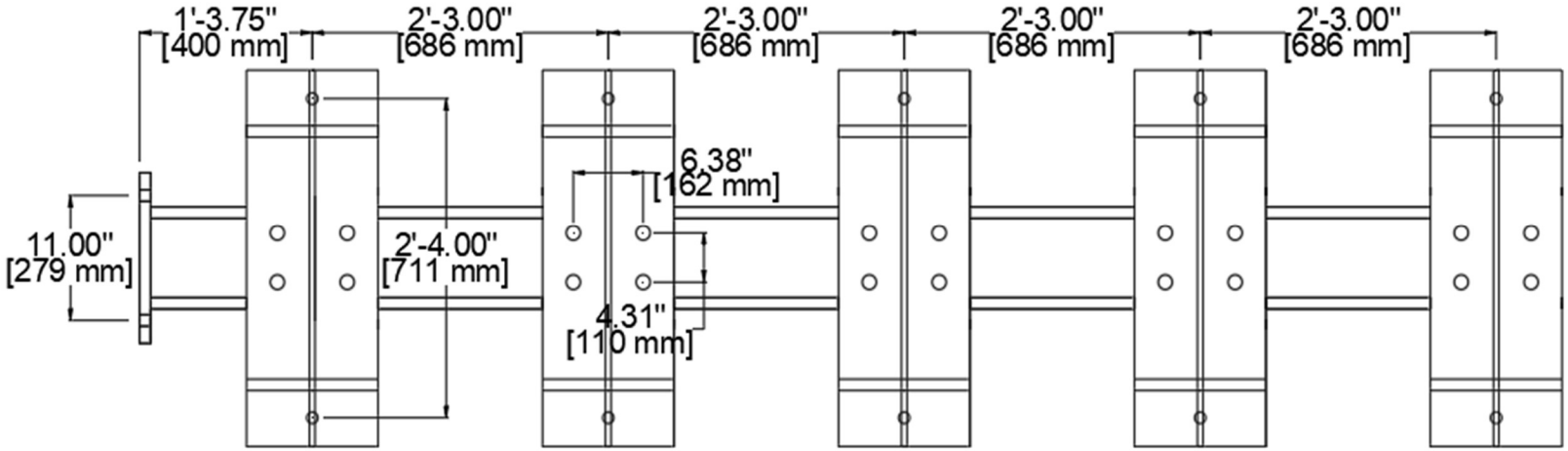

Figure 4.10 Plan view of load transfer beam

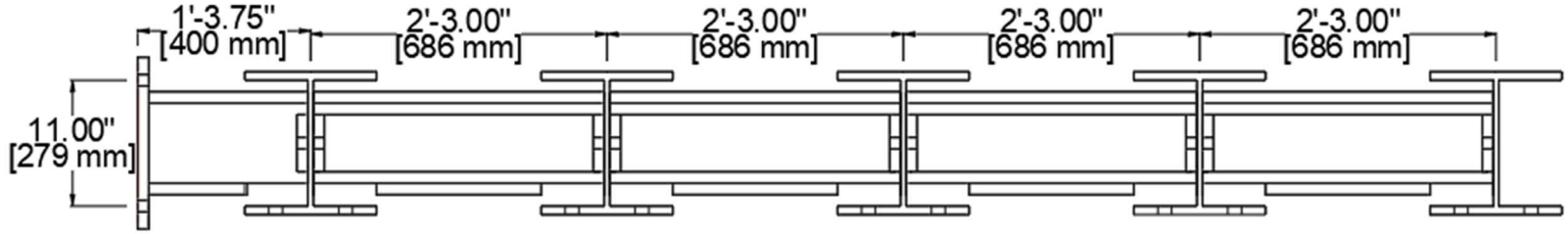

Figure 4.11 Elevation view of load transfer beam

Figure 4.12 Placement of load transfer beam onto specimen cap beam

Figure 4.13 Connection of a steel column to load transfer beam using a compression rod

Figure 4.14 Photo of completed test setup

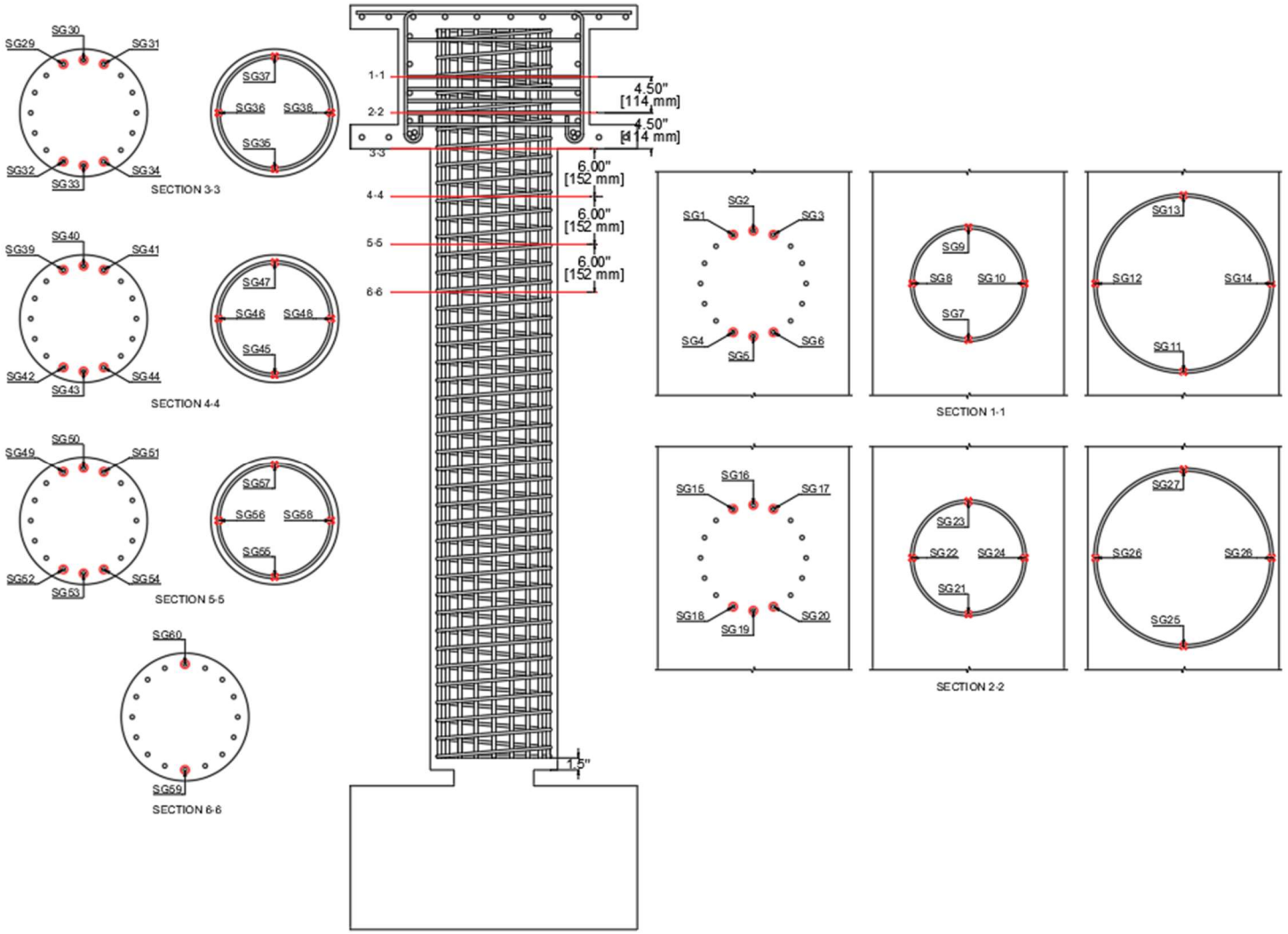

Figure 4.15 Strain gauge locations of columns and hoops

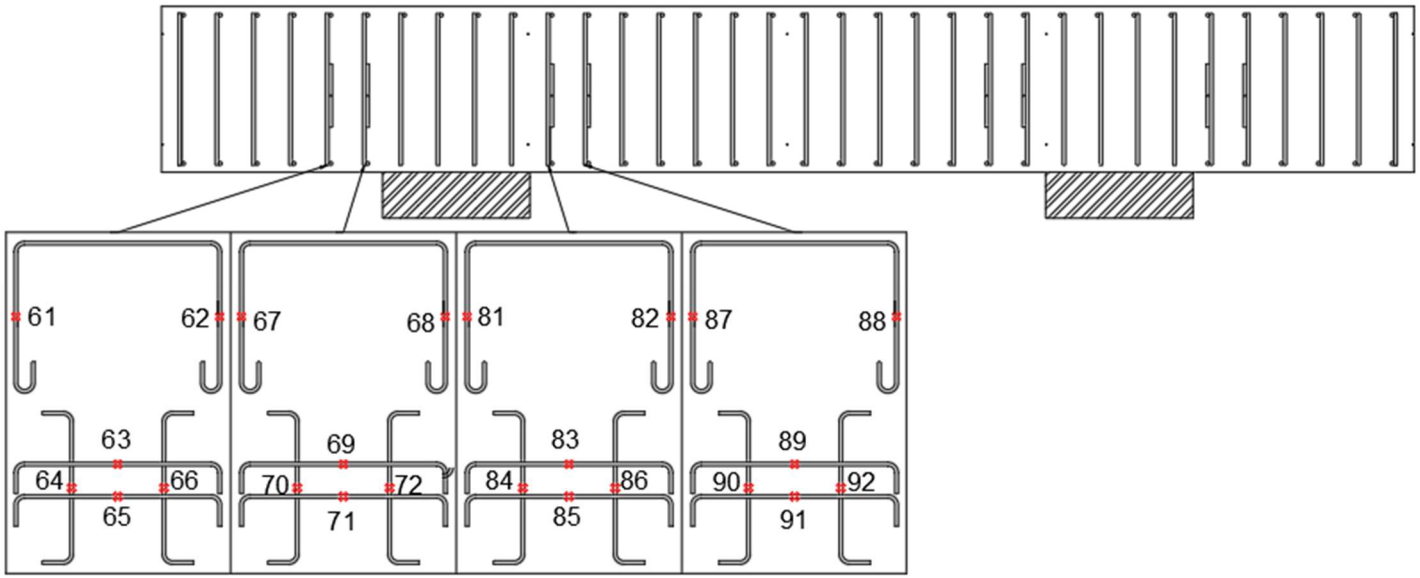

Figure 4.16 Strain Gauge locations adjacent to cap-column pocket connections

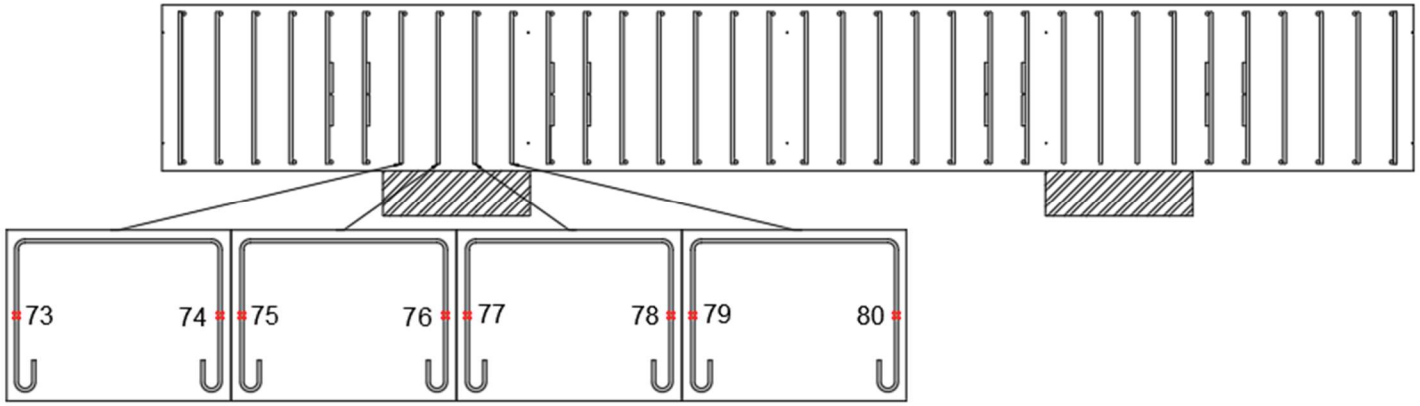

Figure 4.17 Strain gauge locations at cap-column pocket connections

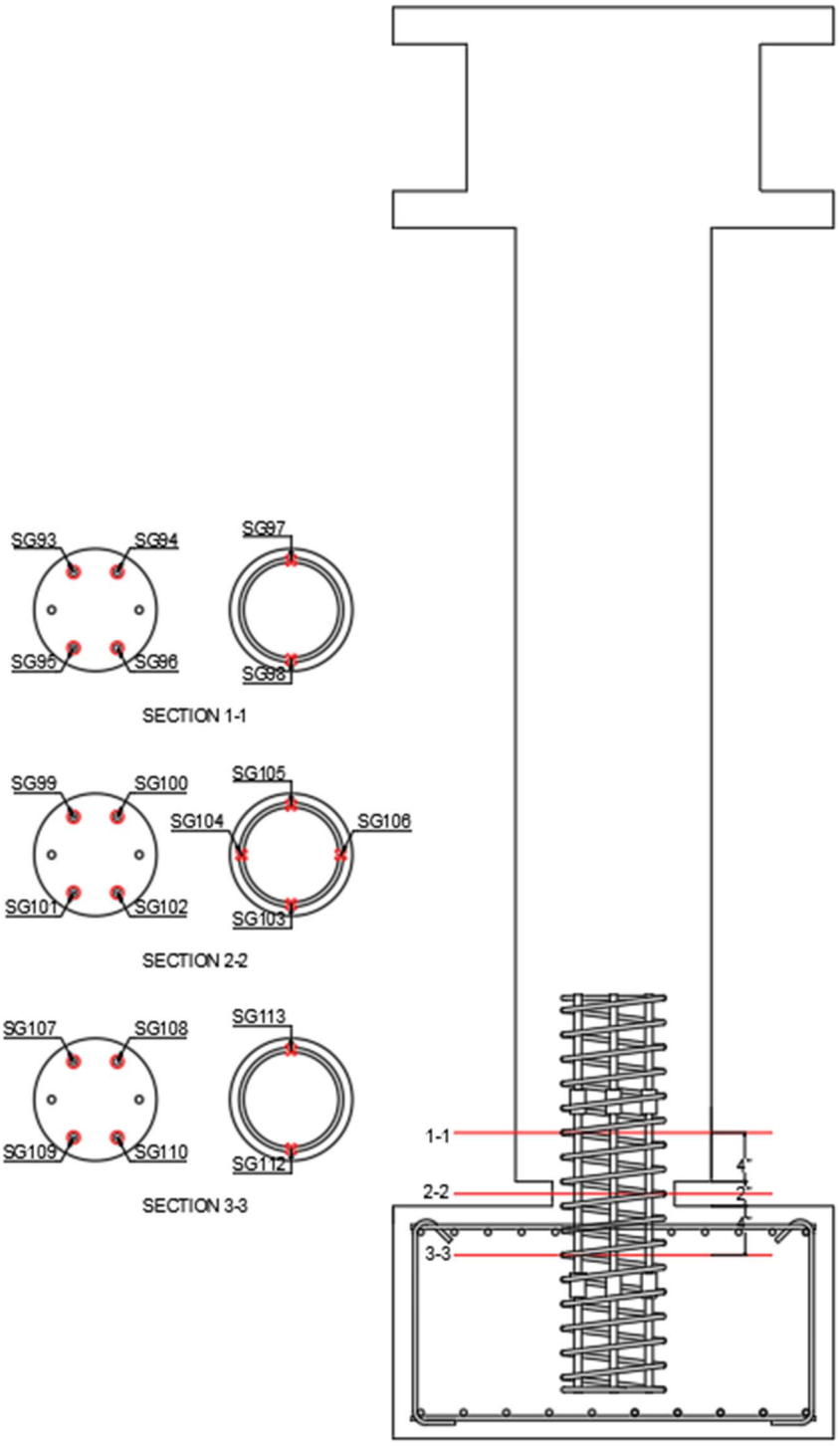

Figure 4.18 Strain gauge locations of two-way hinges

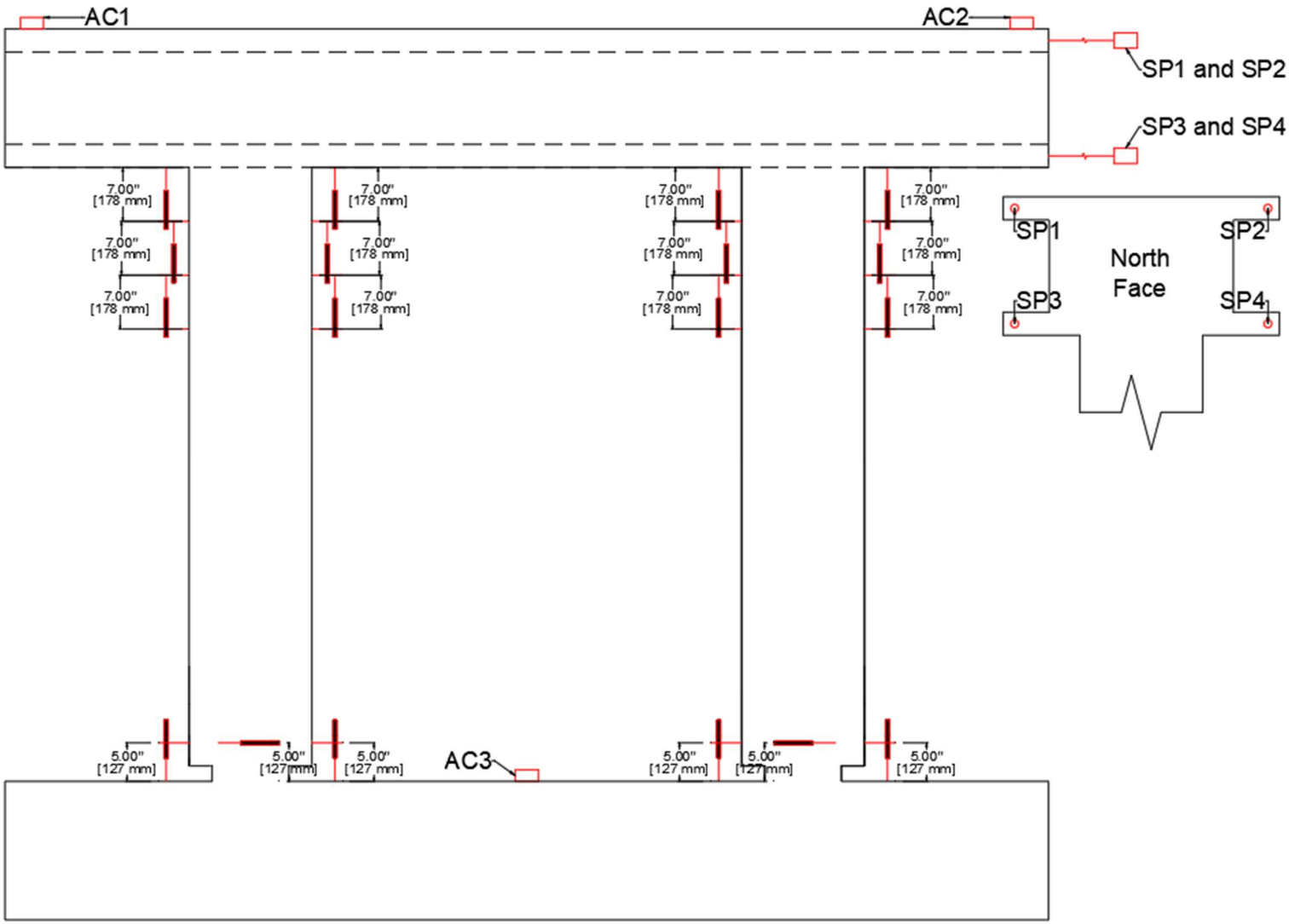

Figure 4.19 Locations of displacement transducers, accelerometers, and string potentiometers

Chapter 5 Tables

Table 5.1 Alterations of pretest loading protocol

Run #	Pretest Protocol Design Level (%)	Pretest PGA (g)	Test Protocol Design Level (%)	Test PGA (g)
1	33	0.136	14	0.058
2	66	0.271	27	0.111
3	100	0.411	41	0.169
4	150	0.617	62	0.255
5	200	0.822	100	0.411
6	250	1.028	150	0.617
7	300	1.233	225	0.925
8	~	~	300	1.233
9	~	~	375	1.541

Table 5.2 Target and achieved peak ground accelerations

Run #	% Design	PGA Achieved (g)	PGA Target (g)	% Difference
1	14	0.062	0.058	6.82
2	27	0.114	0.111	2.34
3	41	0.181	0.169	7.15
4	62	0.232	0.255	9.38
5	100	0.323	0.411	23.98
6	150	0.543	0.617	12.68
7	225	0.723	0.925	24.49
8	300	0.957	1.233	25.21
9	375	1.234	1.541	22.14

Table 5.3 Target and achieved spectral accelerations

Run #	% Design	Initial Period (sec)	Target Spectral Accel. (g)	Achieved Spectral Accel. (g)	% Difference
1	14	0.400	0.1175	0.0904	26.07
2	27	0.444	0.258	0.24	7.23
3	41	0.471	0.325	0.29	11.38
4	62	0.533	0.4532	0.434	4.33
5	100	0.533	0.745	0.51	37.45
6	150	0.667	0.7155	0.55	26.16
7	225	0.800	0.68	0.56	19.35
8	300	0.889	0.697	0.614	12.66
9	375	1.000	1.035	0.899	14.06

Table 5.4 Maximum displacement, maximum force, and drift ratio for each run.

Run #	Max Displacement, in (mm)	Max Force, kip (kN)	Drift Ratio
1	0.09 (2.36)	-6.81 (-30.29)	0.10
2	0.29 (7.24)	15.48 (68.86)	0.32
3	0.57 (14.48)	24.10 (107.20)	0.64
4	1.25 (31.75)	35.24 (156.76)	1.40
5	2.04 (51.82)	40.47 (180.02)	2.29
6	2.32 (58.93)	41.05 (182.60)	2.61
7	3.40 (86.36)	42.59 (189.45)	3.82
8	6.33 (160.78)	44.05 (195.94)	7.11
9	11.20 (284.48)	40.87 (181.80)	12.58

Table 5.5 Maximum shear displacement of each run

Run #	Max Displacement, in. (mm)	Max Shear Disp, in (mm)		Max Disp due to Shear %		% Difference
		ABC	CIP	ABC	CIP	
1	0.09 (2.36)	0.01 (0.14)	0.00 (0.11)	5.81	4.62	22.68
2	0.29 (7.24)	0.02 (0.38)	0.01 (0.33)	5.30	4.60	14.18
3	0.57 (14.48)	0.03 (0.86)	0.03 (0.76)	5.95	5.26	12.21
4	1.25 (31.75)	0.08 (2.04)	0.07 (1.70)	6.42	5.35	18.08
5	2.04 (51.82)	0.13 (3.40)	0.11 (2.76)	6.57	5.33	20.85
6	2.32 (58.93)	0.15 (3.82)	0.13 (3.22)	6.48	5.47	16.96
7	3.40 (86.36)	0.22 (5.50)	0.20 (4.97)	6.37	5.75	10.19
8	6.33 (160.78)	0.37 (9.42)	0.37 (9.42)	5.86	5.86	0.05
9	11.20 (284.48)	0.66 (16.83)	0.64 (16.23)	5.92	5.71	3.63

Table 5.6 Peak strains of column longitudinal reinforcement 9 in (229 mm) above column-cap interface (Section 1-1)

Longitudinal Strain Guages Section 1-1 (9 inches above Column-Cap Interface)													
Run no.		**N SG 1**	**N SG 2**	**N SG 3**	**N SG 4**	**N SG 5**	**N SG 6**	**S SG 1**	**S SG 2**	**S SG 3**	**S SG 4**	**S SG 5**	**S SG 6**
1	Min.	6.8	0	6.8	-6.8	-20.3	-13.5	32.1	-	19.3	0	-6.4	6.4
	Max	88.1	96.3	101.6	61	61	54.2	173.3	-	134.8	83.4	83.4	102.7
2	Min.	-47.4	-109.1	-176.2	-54.2	-101.6	-81.2	-57.8	-	-44.9	-70.6	-83.4	-51.3
	Max	128.7	166.9	189.7	115.2	101.6	94.8	340.2	-	243.9	141.1	147.6	160.5
3	Min.	-467.4	-789.4	-758.9	-433.8	-650.4	-494.3	-680.4	-	-487.8	-436.3	-410.6	-320.9
	Max	176.1	320.9	345.6	162.7	196.5	142.2	455.8	-	346.6	243.8	301.6	237.5
4	Min.	-1022.9	-1488.9	-1226.5	-928.5	-1571.7	-1266.1	-1136.2	-	-1059.1	-1578.2	-1559.2	-1039.8
	Max	304.8	487.7	745.4	338.9	365.8	223.4	693.3	-	513.5	346.4	429.9	365.9
5	Min.	-	**-2278.2**	-1938	-1260.6	-2066.3	-1685.9	-1758.9	-	-1694.5	-1931.1	-1873.6	-1213.1
	Max	-	1020.4	1206.1	901.4	1056.9	832.8	898.7	-	654.7	673.6	750.7	590.5
6	Min.	-	-	-	-1613	**-2256**	-1882.3	-1996.4	-	-1861.4	-1988.8	-1918.5	-1238.8
	Max	-	-	-	1186.1	1327.9	1083.3	1033.5	-	763.8	801.9	924	789.5
7	Min.	-	-	-	-	**-2594.7**	-2241.1	-2169.7	-	-2098.9	-2136.4	-2066.1	-1405.7
	Max	-	-	-	-	1619.2	1523.4	1360.9	-	1007.7	1116.3	1058.7	1071.9
8	Min.	-	-	-	-	-	**-2694.8**	-	-	**-2490.4**	-	**-2393.3**	-
	Max	-	-	-	-	-	1848.4	-	-	1707.3	-	1302.5	-
9	Min.	-	-	-	-	-	**-2478.1**	-	-	-	-	-	-
	Max	-	-	-	-	-	2092.2	-	-	-	-	-	-

Table 5.7 Peak strains of column longitudinal reinforcement 4.5 in (114 mm) above column-cap interface (Section 2-2)

Longitudinal Strain Guages Section 2-2 (4.5 inches above Column-Cap Interface)													
Run no.		**N SG 15**	**N SG 16**	**N SG 17**	**N SG 18**	**N SG 19**	**N SG 20**	**S SG 15**	**S SG 16**	**S SG 17**	**S SG 18**	**S SG 19**	**S SG 20**
1	Min.	-20.3	-32	-32.1	-13.5	-33.8	-33.9	-32.1	-32.1	-32.1	-32.1	-6.4	-12.8
	Max	101.7	153.4	218.3	121.9	115.1	101.6	160.5	179.7	147.6	134.8	192.8	160.5
2	Min.	-257.7	-460.3	-475.2	-237.1	-440	-392.9	-231.1	-308	-198.9	-282.4	-308.5	-231.1
	Max	210.2	345.2	462.4	223.5	264	230.3	378.7	404.2	314.4	243.9	411.3	314.5
3	Min.	-901.9	-1214.7	-1175.2	-955	-1225.4	-1110.9	-994.9	-1090.8	-866.2	-860.1	-1002.6	-949.9
	Max	345.9	588.2	789.9	359	460.4	379.3	564.9	583.9	449.2	391.5	617	564.8
4	Min.	-1519	-1962.7	-1843	-1828.8	**-2525.2**	**-2391.1**	-1547	-1738.9	-1405.2	-2163.1	**-2468**	**-2310.6**
	Max	535.7	901.4	1380.6	521.6	589	521.6	873	924	686.6	545.6	835.5	757.4
5	Min.	-	**-3171**	**-3808**	-2174.3	-	**-3183.6**	**-2259.5**	**-2406.2**	-2034	**-2927**	**-3123.5**	**-2811.2**
	Max	-	1227.5	1939.3	1171.8	-	1361.5	1142.6	1212.7	898.3	917.9	1253.3	1078.3
6	Min.	-	-	**-7378.4**	**-2411.3**	-	**-6834.5**	**-2464.9**	**-2560.2**	**-2367.7**	**-3273.6**	**-3907.6**	**-2978.1**
	Max	-	-	1637.5	1469.8	-	1449.5	1348	1437.3	1135.7	1084.8	1426.8	1283.7
7	Min.	-	-	-	**-11487.7**	-	**-15098.2**	**-2817.9**	**-2996.6**	**-3772.9**	**-10623**	**-11992.7**	**-8388.8**
	Max	-	-	-	1679.8	-	799.3	1855.1	1912.2	1341	1078.4	1478.2	1283.7
8	Min.	-	-	-	-	-	-	**-15456.7**	**-17523.8**	**-15694.7**	**-12869.6**	**-17057.2**	-
	Max	-	-	-	-	-	-	1816.5	1944.2	1052.3	-2086.1	-861.2	-
9	Min.	-	-	-	-	-	-	-	-	-	-	-	-
	Max	-	-	-	-	-	-	-	-	-	-	-	-

Table 5.8 Peak strains of column longitudinal reinforcement at column-cap interface (Section 3-3)

Longitudinal Strain Guages Section 3-3 (Column-Cap Interface)													
Run no.		N SG 29	N SG 30	N SG 31	N SG 32	N SG 33	N SG 34	S SG 29	S SG 30	S SG 31	S SG 32	S SG 33	S SG 34
1	Min.	-155.8	-186.2	-	-128.8	-108.3	-67.8	-147.7	-121.4	-102.7	-32.1	-64.2	-19.3
	Max	433.6	423.8	-	271.2	291.2	237.1	218.3	191.7	166.9	282.4	282.4	327.3
2	Min.	-921.4	-982.5	-	-976.2	-487.6	-609.8	-821.8	-658.2	-738.1	-667.6	-718.8	-789.3
	Max	968.8	976	-	583	623	474.3	552.2	498.4	417.2	545.6	558.4	584
3	Min.	-1761.5	-1708.1	-	-1830.3	-1124.1	-1185.7	-1521.6	-1367.5	-1437.6	-1335.2	-1508.2	-1597.9
	Max	1612.4	1643.8	-	908.4	961.6	711.4	873.2	862.7	603.3	763.9	872.8	853.5
4	Min.	**-2439**	**-2472.2**	-	**-9178.8**	-2112.8	**-2520.4**	-2163.7	-2025.7	-2111.5	**-2484.2**	**-2984.3**	**-3009.7**
	Max	2913.2	3769.3	-	1125.3	1158	853.7	1592.3	1533.7	898.5	943.6	1161.6	1103.8
5	Min.	**-9322.3**	**-9407.2**	-	**-11341.3**	**-8139.7**	**-9261.7**	**-9990.2**	**-9425.6**	**-9658.9**	**-8916**	**-9665.4**	**-10556.6**
	Max	4810.2	5201.2	-	488.1	1848.7	948.5	2157.3	1425	815.1	1277.4	1957.5	1700.6
6	Min.	**-11408.9**	**-12155.5**	-	-	**-9460.2**	**-10217**	**-11871.4**	**-12441.8**	**-12758.7**	**-9878.8**	**-10904**	**-11788.7**
	Max	4112.4	4154.6	-	-	2404	-664	1117.2	-63.9	-2034.5	853.7	2259.1	1758.4
7	Min.	-	-	-	-	-	-	**-19832.7**	**-20742.7**	**-20755.4**	**-19507.4**	**-19375.7**	**-20439.3**
	Max	-	-	-	-	-	-	1001.6	-338.7	-2862.4	1476.4	3497.8	2605.5
8	Min.	-	-	-	-	-	-	**-38586.8**	**-33433.7**	**-41286.2**	**-24334.4**	**-25607.5**	**-21203**
	Max	-	-	-	-	-	-	-353.1	-2153.5	-6026.4	1450.7	4511.8	1758.4
9	Min.	-	-	-	-	-	-	-	-	-	**-15193.8**	-	**-11949.1**
	Max	-	-	-	-	-	-	-	-	-	-8736.3	-	-9029.2

Table 5.9 Peak strains of column longitudinal reinforcement 6 in (152 mm) below column-cap interface (Section 4-4)

Longitudinal Strain Guages Section 4-4 (6 inches below Column-Cap Interface)													
Run no.		N SG 39	N SG 40	N SG 41	N SG 42	N SG 43	N SG 44	S SG 39	S SG 40	S SG 41	S SG 42	S SG 43	S SG 44
1	Min.	-94.9	-340.3	-101.6	-142.3	-128.9	-81.3	-166.8	-173.3	-147.7	-12.8	-25.7	-25.7
	Max	332	301.8	325.2	325.2	284.9	244	205.3	224.6	192.6	282.4	372.3	340.2
2	Min.	-772.4	-2061.3	-677.5	-887.5	-759.7	-657.3	-769.9	-802.3	-616.3	-378.6	-744.5	-815.1
	Max	792.7	353.2	792.7	677.5	590.1	487.9	532.5	571.2	475.1	532.7	751	699.6
3	Min.	-1829.3	**-25737.9**	-1578.6	-1775	-1560.1	-1429.9	-1552.6	-1668.7	-1335.4	-1264.3	-1643.1	-1777.9
	Max	1355.1	1001.8	1294.1	1097.5	942.8	731.9	840.4	866.5	706.2	860	1225.9	1116.8
4	Min.	**-2689.8**	-	**-2344.2**	**-6686.9**	**-4571.8**	**-3232.5**	-2251.9	**-2471**	-2067.2	**-2579.9**	**-6655.9**	**-7477.5**
	Max	2452.7	-	2235.8	1463.4	1261.6	935.2	1475.6	1482.6	1142.8	1168	1694.5	1534
5	Min.	**-11612.9**	-	**-8814.6**	**-12764.1**	**-13505**	**-11615.3**	**-11131**	**-11116.2**	**-9668.5**	**-3356.4**	**-11290**	**-12573.8**
	Max	3360.6	-	3082.8	2208.6	1858.6	1192.7	1360.1	1373.5	1052.9	1700.7	3786.9	3145.1
6	Min.	**-12636**	-	**-10962.4**	**-13543.2**	**-14346.1**	-	**-12106.1**	**-13266.3**	**-11864.1**	**-3702.9**	**-12432.5**	**-13658.6**
	Max	2215.5	-	2987.9	1388.9	13.6	-	782.7	-295.2	-667.7	1912.4	4249	3543
7	Min.	**-13394.9**	-	**-10799.8**	-	-	-	**-18675.7**	**-19909.1**	**-17160.6**	**-6655**	**-18189.8**	**-19505.8**
	Max	2161.3	-	3401.2	-	-	-	1302.4	-288.8	-288.9	2182	7066.7	5532.7
8	Min.	-	-	-	-	-	-	-	-	-	**-**	**-19839.4**	-
	Max	-	-	-	-	-	-	-	-	-	-	14903.6	-
9	Min.	-	-	-	-	-	-	-	-	-	-	**-11938.3**	-
	Max	-	-	-	-	-	-	-	-	-	-	5558.4	-

Table 5.10 Peak strains of column longitudinal reinforcement 12 in (114 mm) below column-cap interface (Section 5-5)

Longitudinal Strain Guages Section 5-5 (12 inches below Column-Cap Interface)													
Run no.		**N SG 49**	**N SG 50**	**N SG 51**	**N SG 52**	**N SG 53**	**N SG 54**	**S SG 49**	**S SG 50**	**S SG 51**	**S SG 52**	**S SG 53**	**S SG 54**
1	Min.	-54.2	-89.9	-	-57.8	-67.7	-40.7	-	-121.9	-96.2	-38.5	-32.1	-12.8
	Max	257.4	295.3	-	282.6	230.2	216.8	-	192.6	160.4	141.3	314.7	314.6
2	Min.	-555.5	-654.8	-	-642.3	-595.7	-494.7	-	-539.1	-410.6	-288.9	-635.9	-635.6
	Max	575.9	706.2	-	629.4	480.6	413.4	-	481.4	327.2	250.4	616.6	616.3
3	Min.	-1443	-1560	-	-1560.7	-1286.2	-1185.8	-	-1264.4	-930.4	-712.7	-1470.8	-1521.6
	Max	962	1200.5	-	1053.3	792	650.5	-	783	468.4	391.7	995.5	995.1
4	Min.	-2188.3	**-2362.5**	-	**-2337.8**	**-2369.3**	**-2378.5**	-	-1964	-1424.4	-1348.3	**-3397.7**	**-3370.5**
	Max	1653.1	2060.8	-	1804.8	1049.2	826.7	-	1264.4	712.2	520.1	1323.1	1322.5
5	Min.	**-3224.8**	**-3704.3**	-	**-4926.1**	**-6667.8**	**-3245.8**	-	**-3119.3**	-2117.4	**-3878**	**-9955.4**	**-9553.1**
	Max	2046	2657.8	-	2427.8	1475.7	1192.6	-	1816.4	988.1	680.6	1888.3	1887.5
6	Min.	**-4166.5**	**-5476.1**	-	**-7071.3**	**-7392.1**	**-3760.8**	-	**-7445.3**	**-2739.7**	**-3916.5**	**-10064.6**	**-9771.4**
	Max	2289.9	2972.4	-	2010.3	792	1341.7	-	2066.7	1174.2	455.9	1117.6	1624.3
7	Min.	-	**-6233.7**	-	**-7707.1**	-	**-8375.4**	-	**-12143.6**	**-7410.7**	**-5881.2**	**-13552.2**	**-13552.8**
	Max	-	3120.1	-	1939.6	-	1355.2	-	2220.8	1187	520.1	1387.3	1720.6
8	Min.	-	-	-	**-5440**	**-**	-	-	-	-	-	-	**-16576.6**
	Max	-	-	-	1445.1	-	-	-	-	-	-	-	2465.3
9	Min.	-	-	-	**-4637.1**	-	**-**	-	-	-	-	-	-
	Max	-	-	-	899.2	-	-	-	-	-	-	-	-

Table 5.11 Peak strains of column spiral reinforcement 9 in (229 mm) above column-cap interface (Section 1-1)

Column Spiral Strain Guages Section 1-1 (9 inches above Column-Cap Interface)									
Run no.		**N SG 7**	**N SG 8**	**N SG 9**	**N SG 10**	**S SG 7**	**S SG 8**	**S SG 9**	**S SG 10**
1	Min.	-20.3	-27.1	6.8	-27.1	-25.7	-25.7	-57.8	-19.3
	Max	27.1	27.1	61	27.1	25.7	25.7	-6.4	32.1
2	Min.	-20.3	-27.1	20.3	-20.3	-51.4	-32.1	-64.2	-19.3
	Max	27.1	20.3	74.5	27.1	32.1	32.1	-12.8	32.1
3	Min.	-20.3	-33.9	20.3	-33.9	-57.8	-38.5	-64.2	-19.3
	Max	33.9	20.3	74.5	20.3	51.4	38.5	-6.4	32.1
4	Min.	-40.7	-115.3	13.5	-47.4	-64.2	-89.8	-64.2	-25.7
	Max	33.9	13.6	101.6	20.3	57.8	44.9	-6.4	38.5
5	Min.	-54.2	-217	13.5	-284.5	-288.9	-211.7	-83.4	-70.6
	Max	27.1	-6.8	142.3	13.5	12.8	44.9	12.8	115.6
6	Min.	-54.2	-203.4	-	-338.6	-166.9	-243.8	-109.1	-32.1
	Max	27.1	0	-	61	12.8	25.7	0	141.2
7	Min.	-	-244.1	-	-250.6	-179.8	-256.7	-121.9	-19.3
	Max	-	0	-	88	6.4	32.1	6.4	199
8	Min.	-	-	-	-203.2	-179.8	-314.4	-121.9	19.3
	Max	-	-	-	128.7	-12.8	38.5	38.5	269.6
9	Min.	-	-	-	-243.8	-205.5	-295.1	-564.8	32.1
	Max	-	-	-	169.3	-25.7	32.1	44.9	276

Table 5.12 Peak strains of column spiral reinforcement 4.5 in (114 mm) above column-cap interface (Section 2-2)

Column Spiral Strain Guages Section 2-2 (4.5 inches above Column-Cap Interface)									
Run no.		N SG 21	N SG 22	N SG 23	N SG 24	S SG 21	S SG 22	S SG 23	S SG 24
1	Min.	-33.9	-27	-47.4	-	-25.7	-	-38.5	12.8
	Max	20.3	20.2	20.3	-	25.7	-	19.3	64.2
2	Min.	-27.1	-67.5	-149.1	-	-25.7	-	-44.9	-6.4
	Max	27.1	27	94.9	-	25.7	-	12.8	64.2
3	Min.	-74.5	-209.2	-67.8	-	-32.1	-	-44.9	-6.4
	Max	33.9	20.2	162.7	-	25.7	-	32.1	64.2
4	Min.	-94.9	-350.9	-54.2	-	-51.3	-	-57.8	-38.5
	Max	47.4	20.2	216.9	-	12.8	-	51.4	44.9
5	Min.	-122	-323.9	-74.6	-	-64.2	-	-64.2	-6.4
	Max	47.4	6.7	277.9	-	6.4	-	109.2	122
6	Min.	-135.5	-229.5	-142.3	-	-57.8	-	-64.2	57.8
	Max	33.9	27	277.9	-	-6.4	-	134.8	160.5
7	Min.	-	-479.2	-569.3	-	-64.2	-	-57.8	102.7
	Max	-	114.7	189.8	-	32.1	-	122	231.1
8	Min.	-	-1086.5	-1823.1	-	-64.2	-	-57.8	115.5
	Max	-	162	-54.2	-	57.8	-	109.2	282.4
9	Min.	-	-	-1945.1	-	-115.5	-	-38.5	83.4
	Max	-	-	833.6	-	44.9	-	96.3	353

Table 5.13 Peak strains of column spiral reinforcement at column-cap interface (Section 3-3)

Column Spiral Strain Guages Section 3-3 (Column-Cap Interface)									
Run no.		N SG 35	N SG 36	N SG 37	N SG 38	S SG 35	S SG 36	S SG 37	S SG 38
1	Min.	-13.6	-47.4	-47.5	-27.1	-38.5	-32.1	-44.9	-38.5
	Max	33.9	6.8	13.6	20.3	19.3	32.1	12.8	12.8
2	Min.	-6.8	-47.4	-67.8	-33.9	-38.5	-32.1	-109.1	-38.5
	Max	47.4	13.6	13.6	20.3	12.8	25.7	-25.7	12.8
3	Min.	0	-54.2	-94.9	-33.9	-147.6	-64.2	-147.6	-51.3
	Max	81.3	47.4	13.6	20.3	12.8	19.3	-32.1	25.7
4	Min.	6.8	-88.1	-88.1	-33.9	-256.7	-96.3	-147.6	-115.5
	Max	142.3	61	33.9	27.1	89.8	6.4	-51.3	32.1
5	Min.	13.6	-101.7	-33.9	-74.5	-121.9	-96.3	-141.2	-89.9
	Max	210.1	81.3	183.1	47.4	147.6	25.7	25.7	25.7
6	Min.	-413.5	-244	-20.3	-54.2	-128.3	-77	-109.1	-77
	Max	264.4	54.2	203.4	74.5	166.8	12.8	70.6	25.7
7	Min.	-1057.5	-643.9	-47.5	-210	-96.3	-128.4	-70.6	-64.2
	Max	596.5	61	210.2	81.3	173.3	64.2	96.2	19.3
8	Min.	-1694.6	-1247.2	-223.7	-494.6	-102.7	-224.7	-	-147.6
	Max	657.5	318.6	230.5	88.1	333.7	51.4	-	25.7
9	Min.	-1172.7	-	-393.3	-603	-455.6	-442.9	-	-128.4
	Max	454.2	-	203.4	393	288.8	134.8	-	192.6

Table 5.14 Peak strains of column spiral reinforcement 6 in (152 mm) below column-cap interface (Section 4-4)

Column Spiral Strain Guages Section 4-4 (6 inches below Column-Cap Interface)									
Run no.		N SG 45	N SG 46	N SG 47	N SG 48	S SG 45	S SG 46	S SG 47	S SG 48
1	Min.	-38.5	-13.6	-38.5	-20.3	-32.1	-25.7	-32.1	-
	Max	12.8	33.9	12.8	33.9	19.3	25.7	25.7	-
2	Min.	-38.5	-40.7	-44.9	-27.1	-83.4	-51.3	-64.2	-
	Max	12.8	27.1	12.8	27.1	19.3	12.8	19.3	-
3	Min.	-77	-74.5	-57.7	-54.2	-141.2	-173.3	-83.5	-
	Max	6.4	13.6	12.8	13.6	12.8	6.4	12.8	-
4	Min.	-109.1	-61	-102.7	-47.5	-231	-256.7	-83.5	-
	Max	-19.3	6.8	-12.8	27.1	19.3	6.4	-6.4	-
5	Min.	-121.9	-176.2	-154	-108.5	-231	-442.9	-109.2	-
	Max	-44.9	54.2	-19.2	61	38.5	-32.1	32.1	-
6	Min.	-179.7	-101.6	-154	-54.2	-757.2	-199	-109.2	-
	Max	-38.5	128.7	-38.5	74.6	32.1	-25.7	44.9	-
7	Min.	-173.3	-67.8	-218.2	-54.2	-	-205.4	-	-
	Max	44.9	135.5	-44.9	149.1	-	77	-	-
8	Min.	-	-223.6	-	0	-	-	-	-
	Max	-	135.5	-	250.8	-	-	-	-
9	Min.	-	-318.4	-	40.7	-	-	-	-
	Max	-	128.7	-	277.9	-	-	-	-

Table 5.15 Peak strains of column spiral reinforcement 12 in (114 mm) below column-cap interface (Section 5-5)

Column Spiral Strain Guages Section 5-5 (12 inches below Column-Cap Interface)									
Run no.		N SG 55	N SG 56	N SG 57	N SG 58	S SG 55	S SG 56	S SG 57	S SG 58
1	Min.	-	-47.4	0	-33.9	-57.8	25.7	-32.1	-
	Max	-	6.8	217	20.3	-6.4	160.5	25.7	-
2	Min.	-	-88	0	-47.4	-64.2	-109.1	-64.2	-
	Max	-	0	244.1	6.8	0	308.1	25.7	-
3	Min.	-	-155.8	**-2542.7**	-115.2	-77	-738.1	-83.5	-
	Max	-	-13.5	318.7	-20.3	-6.4	468.5	25.7	-
4	Min.	-	-426.7	-623.8	-183	-102.7	-1251.6	-102.8	-
	Max	-	-33.9	420.4	-81.3	-25.7	699.6	32.1	-
5	Min.	-	-562.1	176.3	-250.7	-154.1	-1688	-141.3	-
	Max	-	-40.6	556	-122	-32.1	917.8	57.8	-
6	Min.	-	-399.6	67.8	-305	-173.3	-1713.7	-134.9	-
	Max	-	-27.1	556	-108.4	-32.1	1071.9	70.7	-
7	Min.	-	-311.5	101.7	-298.2	-282.4	-1797.2	-	-
	Max	-	-33.9	488.2	-94.9	32.1	1347.9	-	-
8	Min.	-	-237	-20.3	-264.3	-590.5	-	-	-
	Max	-	-47.4	474.6	-74.5	96.3	-	-	-
9	Min.	-	-203.2	305.1	-264.3	-288.8	-	-	-
	Max	-	-54.2	495	-61	109.1	-	-	-

Table 5.16 Peak strains of hoops 9 in (229 mm) above column-cap interface (Section 1-1)

Hoop Strain Guages Section 1-1 (9 inches above Column-Cap Interface)									
Run no.		N SG 11	N SG 12	N SG 13	N SG 14	S SG 11	S SG 12	S SG 13	S SG 14
1	Min.	-33.9	-33.9	-33.9	-33.9	-32.1	38.5	-12.8	-25.7
	Max	13.5	20.3	13.6	13.5	19.3	89.8	32.1	32.1
2	Min.	-33.9	-33.9	-33.9	-27.1	-38.5	211.7	-19.3	-25.7
	Max	13.5	20.3	13.6	13.5	25.7	269.5	38.5	32.1
3	Min.	-40.6	-47.4	-40.7	-27.1	-57.8	198.9	-19.3	-25.7
	Max	13.5	20.3	13.6	20.3	19.3	256.7	32.1	25.7
4	Min.	-40.6	-67.7	-115.2	-27.1	-64.2	198.9	-25.7	-45
	Max	13.5	6.8	6.8	13.5	12.8	256.7	32.1	19.3
5	Min.	-47.4	-54.2	-135.5	-40.6	-205.4	237.4	-44.9	-147.7
	Max	13.5	33.9	0	13.5	6.4	320.8	25.7	6.4
6	Min.	-47.4	-33.9	-88.1	-40.6	-263.1	-250.2	-44.9	-173.4
	Max	13.5	40.6	6.8	13.5	-12.8	-77	19.3	-32.1
7	Min.	-54.2	-20.3	-88.1	-60.9	-327.3	-211.7	-51.3	-211.9
	Max	13.5	40.6	13.6	6.8	-6.4	96.2	19.3	-32.1
8	Min.	-54.2	-27.1	-81.3	-101.6	-372.2	-263.1	-57.8	-301.8
	Max	13.5	47.4	13.6	0	-6.4	160.4	12.8	-32.1
9	Min.	-61	-47.4	-67.8	-108.3	-353	-295.2	-57.8	-282.6
	Max	6.8	47.4	13.6	-20.3	-12.8	340.1	6.4	-38.5

Table 5.17 Peak strains of hoops 4.5 in (114 mm) above column-cap interface (Section 2-2)

Hoop Strain Guages Section 2-2 (4.5 inches above Column-Cap Interface)									
Run no.		N SG 25	N SG 26	N SG 27	N SG 28	S SG 25	S SG 26	S SG 27	S SG 28
1	Min.	-40.5	-20.3	-20.3	-20.3	-32.1	-12.8	-19.3	-38.5
	Max	6.7	27.1	27.1	27.1	19.3	44.9	38.5	12.8
2	Min.	-47.2	-33.9	-20.3	-27.1	-32.1	-64.2	-19.3	-44.9
	Max	6.7	20.3	27.1	27.1	19.3	57.8	32.1	12.8
3	Min.	-47.2	-61	-27.1	-40.7	-44.9	-122	-25.7	-70.6
	Max	0	20.3	20.3	27.1	19.3	70.6	32.1	12.8
4	Min.	-60.7	-176.3	-40.6	-54.2	-57.8	-224.7	-25.7	-192.6
	Max	0	6.8	13.5	27.1	12.8	89.9	32.1	6.4
5	Min.	-87.7	-271.2	-108.4	-169.4	-121.9	-256.8	-51.4	-250.4
	Max	-6.7	-27.1	13.5	13.6	0	70.6	25.7	-19.3
6	Min.	-94.4	-291.5	-115.1	-223.6	-147.6	-256.8	-64.2	-269.6
	Max	-13.5	-33.9	6.8	-20.3	-12.8	44.9	19.3	-19.3
7	Min.	-101.2	-311.8	-121.9	-250.8	-192.5	-276.1	-70.6	-301.7
	Max	-13.5	-47.5	6.8	-27.1	-12.8	38.5	19.3	-19.3
8	Min.	-114.7	-318.6	-94.8	-277.9	-205.4	-250.4	-89.9	-333.8
	Max	-20.2	-61	0	-40.7	-19.3	38.5	19.3	-38.5
9	Min.	-114.7	-332.2	-94.8	-284.6	-160.4	-231.1	-83.5	-301.7
	Max	-27	-67.8	6.8	-40.7	-12.8	32.1	12.8	-51.4

Table 5.18 Peak strains of cap beam transverse reinforcement 14 in (357 mm) out from column center

Cap Beam Transverse Reinforcement Strain Guages (14 inches Out from Center of Column)													
Run no.		N SG 61	N SG 62	N SG 63	N SG 64	N SG 65	N SG 66	S SG 61	S SG 62	S SG 63	S SG 64	S SG 65	S SG 66
1	Min.	0	6.8	-40.7	-20.3	-33.9	-13.6	-19.3	6.8	-32.1	-25.7	-	-25.7
	Max	40.6	54.2	6.8	33.9	20.3	33.9	32.1	54.2	19.3	32.1	-	25.7
2	Min.	0	6.8	-40.7	-13.5	-33.9	-13.6	-19.3	6.8	-32.1	-19.3	-	-25.7
	Max	47.4	54.2	13.6	33.9	20.3	40.7	38.5	54.2	25.7	32.1	-	25.7
3	Min.	-6.8	6.8	-33.9	-13.5	-40.7	-6.8	-19.3	-33.9	-32.1	-25.7	-	-25.7
	Max	54.2	54.2	13.6	40.6	20.3	40.7	38.5	13.6	19.3	25.7	-	25.7
4	Min.	0	6.8	-40.7	-6.8	-61	-6.8	-12.8	-40.7	-32.1	-25.7	-	-25.7
	Max	61	54.2	20.3	40.6	13.6	40.7	38.5	20.3	19.3	32.1	-	32.1
5	Min.	-20.3	-6.8	-61	-13.5	-74.5	-33.9	-19.3	-33.9	-51.4	-32.1	-	-32.1
	Max	61	60.9	13.6	40.6	6.8	40.7	38.5	13.6	19.3	38.5	-	44.9
6	Min.	-20.3	-33.8	-74.6	-13.5	-88.1	-61	-19.3	-40.7	-51.4	-32.1	-	-32.1
	Max	54.2	47.4	6.8	47.4	6.8	33.9	32.1	20.3	12.9	38.5	-	38.5
7	Min.	-33.9	-67.7	-122	-13.5	-94.9	-94.9	-19.3	-94.9	-57.8	-45	-	-38.5
	Max	54.2	33.8	6.8	47.4	0	27.1	38.5	0	12.9	38.5	-	51.4
8	Min.	-33.9	-67.7	-122	-13.5	-94.9	-108.4	-19.3	-94.9	-64.3	-51.4	-	-44.9
	Max	40.6	27.1	-6.8	40.6	0	33.9	38.5	0	6.4	25.7	-	38.5
9	Min.	-33.9	-67.7	-128.8	-13.5	-81.3	-108.4	-19.3	-81.3	-57.8	-45	-	-38.5
	Max	47.4	27.1	-6.8	40.6	0	33.9	38.5	0	6.4	25.7	-	32.1

Table 5.19 Peak strains of cap beam transverse reinforcement 10 in (254 mm) out from column center

Cap Beam Transverse Reinforcement Strain Guages (10 inches Out from Center of Column)													
Run no.		N SG 67	N SG 68	N SG 69	N SG 70	N SG 71	N SG 72	S SG 67	S SG 68	S SG 69	S SG 70	S SG 71	S SG 72
1	Min.	-	0	-40.7	-20.3	-40.6	-6.8	-19.3	-19.3	-44.9	-32.1	-38.5	-32.1
	Max	-	40.6	6.8	27.1	6.8	47.4	32.1	32.1	12.8	25.7	12.8	19.3
2	Min.	-	0	-47.4	-27.1	-47.4	-6.8	-19.3	-19.3	-44.9	-32.1	-38.5	-32.1
	Max	-	47.4	6.8	40.6	6.8	67.7	38.5	38.5	6.4	25.7	12.8	19.3
3	Min.	-	6.8	-47.4	-27.1	-67.7	-13.5	-19.3	-12.8	-44.9	-32.1	-38.5	-32.1
	Max	-	60.9	6.8	47.4	13.5	88.1	38.5	38.5	12.8	32.1	12.8	25.7
4	Min.	-	6.8	-67.8	-13.5	-115.2	-13.5	-19.3	-19.3	-44.9	-38.5	-45	-32.1
	Max	-	74.5	0	94.8	0	121.9	45	32.1	6.4	25.7	12.8	38.5
5	Min.	-	-13.5	-94.9	-20.3	-135.5	-20.3	-51.4	-25.7	-57.8	-64.2	-57.8	-44.9
	Max	-	74.5	-20.3	115.2	-20.3	162.6	45	32.1	19.3	32.1	6.4	51.4
6	Min.	-	-27.1	-115.2	-27.1	-142.3	-27.1	-70.7	-38.5	-77	-70.6	-83.5	-51.4
	Max	-	67.7	-33.9	115.2	-20.3	155.8	12.8	25.7	0	32.1	-12.8	38.5
7	Min.	-	-27.1	-135.6	-33.9	-155.8	-47.4	-96.4	-44.9	-83.4	-83.5	-89.9	-70.6
	Max	-	54.2	-40.7	115.2	-27.1	169.3	-6.4	19.3	-12.8	25.7	-12.8	38.5
8	Min.	-	-47.4	-149.1	-40.6	-149	-47.4	-134.9	-64.2	-89.9	-89.9	-102.7	-83.4
	Max	-	33.9	-61	94.8	-27.1	135.5	-32.1	12.8	-12.8	12.8	-19.3	25.7
9	Min.	-	-60.9	-155.9	-47.4	-142.3	-61	-154.2	-70.6	-89.9	-89.9	-115.6	-77
	Max	-	13.5	-67.8	81.3	-33.9	128.7	-45	0	-25.7	0	-25.7	19.3

Table 5.20 Peak strains of cap beam transverse reinforcement adjacent to north (CIP) column

Cap Beam Transverse Reinforcement Strain Guages (Adjacent to Column)									
Run no.		N SG 73	N SG 74	N SG 75	N SG 76	N SG 77	N SG 78	N SG 79	N SG 80
1	Min.	-10.2	-13.5	-6.8	-27.1	-27.1	-20.3	-27.1	-33.9
	Max	40.6	33.9	40.6	20.3	27.1	27.1	27.1	20.3
2	Min.	0	-13.5	0	-27.1	-20.3	-20.3	-27.1	-33.9
	Max	47.4	33.9	47.4	20.3	20.3	20.3	20.3	20.3
3	Min.	-13.5	-20.3	-13.5	-27.1	-27.1	-27.1	-33.9	-33.9
	Max	54.2	33.9	54.2	20.3	27.1	27.1	33.9	27.1
4	Min.	-13.5	-20.3	-13.5	-94.8	-13.5	-33.9	-27.1	-33.9
	Max	67.7	74.5	67.7	13.5	33.9	27.1	47.4	40.6
5	Min.	-20.3	-13.5	-291.3	-149	-20.3	-183	-27.1	-33.9
	Max	74.5	88	420	-13.5	40.6	20.3	47.4	40.6
6	Min.	-74.5	-47.4	-331.9	-169.3	-40.6	-325.3	-33.9	-40.6
	Max	20.3	33.9	189.7	-60.9	27.1	-6.8	40.6	40.6
7	Min.	-121.9	-74.5	-1219.3	-277.6	-684.2	-643.8	-176.1	-155.8
	Max	-20.3	20.3	1090.6	-81.3	13.5	13.6	47.4	33.9
8	Min.	-121.9	-121.9	1178.7	-345.4	-948.5	-969.1	-250.6	-
	Max	-20.3	-20.3	2770.6	-115.1	-81.3	-257.5	0	-
9	Min.	-155.2	-142.2	2804.5	-325	-955.2	-975.9	-264.1	-
	Max	33.9	-47.4	3461.6	13.5	-108.4	-345.6	-20.3	-

Table 5.21 Peak strains of cap beam transverse reinforcement adjacent to south (ABC) column

Cap Beam Transverse Reinforcement Strain Guages (Adjacent to Column)									
Run no.		S SG 73	S SG 74	S SG 75	S SG 76	S SG 77	S SG 78	S SG 79	S SG 80
1	Min.	-12.8	-25.7	-25.7	-25.7	25.7	-44.9	0	-19.3
	Max	44.9	25.7	32.1	32.1	77	6.4	57.8	32.1
2	Min.	-6.4	-25.7	-19.3	-19.3	25.7	-44.9	6.4	-25.7
	Max	38.5	25.7	32.1	32.1	83.5	12.8	57.8	32.1
3	Min.	-12.8	-32.1	-44.9	-19.3	6.4	-38.5	12.8	-44.9
	Max	51.4	25.7	32.1	32.1	83.5	32.1	102.7	25.7
4	Min.	-38.5	-70.6	-205.4	-44.9	6.4	-96.3	0	-57.8
	Max	51.4	25.7	19.3	32.1	122	25.7	115.5	51.4
5	Min.	-237.5	-231.1	-526.5	-481.4	-134.8	-205.4	-12.8	-70.6
	Max	64.2	19.3	-12.8	12.8	128.4	-6.4	115.5	51.4
6	Min.	-340.3	-327.4	-609.9	-686.8	-186.2	-288.9	-51.3	-89.9
	Max	-38.5	-83.5	-160.5	-199	102.7	-141.2	83.4	19.3
7	Min.	-462.2	-436.5	-725.5	-853.7	-173.3	-391.6	-83.4	-109.1
	Max	-102.7	-141.2	-211.9	-263.2	577.8	-192.6	64.2	-19.3
8	Min.	-539.3	-532.8	-821.8	-1097.6	-430.1	-500.7	-109.1	-122
	Max	-154.1	-186.2	-231.1	-320.9	-19.3	-243.9	32.1	-32.1
9	Min.	-571.4	-545.7	-841	-1046.3	-378.8	-520	-109.1	-128.4
	Max	-179.8	-250.4	-224.7	-340.2	12.8	-295.3	32.1	-51.4

Table 5.22 Peak strains of cap beam transverse reinforcement 10 in (254 mm) in from column center

Cap Beam Transverse Reinforcement Strain Guages (10 inches In from Center of Column)													
Run no.		N SG 81	N SG 82	N SG 83	N SG 84	N SG 85	N SG 86	S SG 81	S SG 82	S SG 83	S SG 84	S SG 85	S SG 86
1	Min.	-20.3	-13.6	-27.1	-13.5	-33.9	0	-64.2	-25.7	-25.7	0	-32.1	-12.8
	Max	27.1	40.7	20.3	33.9	13.5	54.2	-6.4	32.1	25.7	57.8	19.3	38.5
2	Min.	-20.3	-13.6	-27.1	-20.3	-33.9	-6.8	-57.8	-25.7	-32.1	0	-32.1	-19.3
	Max	33.9	40.7	20.3	47.4	13.5	67.7	-6.4	25.7	25.7	64.2	25.7	57.8
3	Min.	-13.5	-6.8	-27.1	-27.1	-54.2	-13.5	-57.8	-32.1	-44.9	6.4	-51.4	-6.4
	Max	33.9	40.7	27.1	54.2	20.3	74.5	6.4	19.3	25.7	89.8	19.3	102.7
4	Min.	-13.5	-6.8	-40.7	-40.6	-67.7	-27.1	-83.4	-44.9	-44.9	0	-70.6	-6.4
	Max	54.2	47.4	27.1	74.5	13.5	94.8	25.7	19.3	25.7	115.5	12.8	109.1
5	Min.	-13.5	-6.8	-54.2	-47.4	-74.5	-33.9	-83.4	-64.2	-89.9	-19.3	-109.2	-6.4
	Max	67.7	61	27.1	88.1	13.5	121.9	44.9	6.4	19.3	134.8	6.4	147.6
6	Min.	0	-6.8	-47.4	-61	-74.5	-40.6	-83.4	-89.9	-109.2	-38.5	-115.6	-12.8
	Max	60.9	61	27.1	74.5	13.5	108.4	51.3	0	0	96.3	-6.4	141.2
7	Min.	6.8	-6.8	-54.2	-81.3	-88.1	-74.5	-89.8	-102.7	-134.8	-38.5	-134.8	-25.7
	Max	67.7	54.2	27.1	67.7	6.8	115.2	38.5	0	0	70.6	-6.4	122
8	Min.	0	-6.8	-74.5	-94.8	-94.8	-67.7	-51.3	-141.2	-186.2	-57.8	-160.5	-44.9
	Max	74.5	61	6.8	67.7	6.8	115.2	44.9	-6.4	-12.8	70.6	-6.4	102.7
9	Min.	6.8	-13.6	-88.1	-101.6	-108.4	-54.2	-32.1	-128.4	-237.6	-57.8	-154.1	-44.9
	Max	81.3	94.9	0	54.2	-6.8	135.5	64.2	-6.4	-32.1	44.9	-19.3	70.6

Table 5.23 Peak strains of cap beam transverse reinforcement 14 in (357 mm) in from column center

Cap Beam Transverse Reinforcement Strain Guages (14 inches In from Center of Column)													
Run no.		N SG 87	N SG 88	N SG 89	N SG 90	N SG 91	N SG 92	S SG 87	S SG 88	S SG 89	S SG 90	S SG 91	S SG 92
1	Min.	-33.9	-20.3	-40.6	-6.8	-33.9	-13.5	**-4099.6**	-6.4	-	-6.4	-25.7	-25.7
	Max	13.5	27.1	6.8	40.7	13.5	33.9	-4035.4	44.9	-	44.9	25.7	25.7
2	Min.	-33.9	-20.3	-40.6	-13.6	-40.6	-13.5	**-4747.6**	-6.4	-	-6.4	-25.7	-25.7
	Max	20.3	33.9	13.5	33.9	6.8	33.9	-4683.4	51.4	-	44.9	32.1	25.7
3	Min.	-33.9	-13.5	-40.6	-13.6	-54.2	-13.5	**-5491.8**	-12.8	-	-6.4	-32.1	-25.7
	Max	20.3	33.9	13.5	40.7	0	33.9	-5414.8	44.9	-	44.9	38.5	25.7
4	Min.	-27.1	-13.5	-40.6	-13.6	-61	-13.5	**-103188.8**	-6.4	-	-12.8	-38.5	-32.1
	Max	27.1	40.6	13.5	40.7	-6.8	40.6	-6678.7	44.9	-	51.4	25.7	32.1
5	Min.	-27.1	-13.5	-54.2	-13.6	-81.3	-6.8	-	-122	-	-6.4	-57.7	-160.5
	Max	40.6	33.9	13.5	40.7	-6.8	40.6	-	51.4	-	64.2	25.7	25.7
6	Min.	-27.1	-13.5	-47.4	-20.3	-88.1	-13.5	-	-186.2	-	-134.8	-70.6	-282.4
	Max	40.6	40.6	20.3	33.9	-6.8	40.6	-	0	-	64.2	19.2	-57.8
7	Min.	-27.1	-13.5	-47.4	-27.1	-88.1	-13.5	-	-244	-	-243.9	-64.2	-327.4
	Max	40.6	40.6	20.3	40.7	-6.8	40.6	-	-6.4	-	19.3	19.2	-77
8	Min.	-27.1	-13.5	-54.2	-27.1	-94.8	-13.5	-	-333.9	-	-385.2	-57.7	-391.6
	Max	33.9	47.4	20.3	40.7	-13.5	40.6	-	-12.8	-	6.4	19.2	12.8
9	Min.	-81.3	-13.5	-54.2	-20.3	-101.6	-13.5	-	-340.3	-	-391.6	-70.6	-571.3
	Max	33.9	61	20.3	40.7	-13.5	47.4	-	-6.4	-	0	12.8	6.4

Table 5.24 Peak strains of hinge longitudinal reinforcement (CAM) 5 in above (127 mm) center of hinge (Section 1-1)

Longitudinal CAM Bar Strain Guages (Section 1-1 5 inches above Center of Hinge Gap)									
Run no.		N CAM	N CAM	N CAM	N CAM	S CAM	S CAM	S CAM	S CAM 93
1	Min.	32	-25.6	40.5	-70.4	47.3	33.7	-20.2	13.5
	Max	537.3	556.6	479.4	505.5	391.7	310.4	276.7	377.9
2	Min.	-710	-883	-580.6	-780.7	-587.6	-506.1	-323.9	-742.3
	Max	767.5	1004.5	600.9	991.9	499.8	391.4	364.4	600.6
3	Min.	-1976.4	-2604.1	-1701.4	-2265.3	-2208.4	-1727.6	-2247.3	-1950.3
	Max	876.3	1324.4	681.9	1465.4	587.6	411.7	377.9	722.1
4	Min.	-5298.1	-4536.3	-4557.3	-4031.5	-3937.3	-3259.5	-4521.5	-5230.1
	Max	1080.9	1977.1	837.2	2822.1	655.1	526.4	377.9	789.6
5	Min.	**-8775.3**	**-9904.5**	**-7413.2**	**-9106.2**	**-7867.9**	**-6276**	**-8928.3**	**-8948.5**
	Max	1541.4	2412.1	1330.1	3878	959	701.8	418.4	1194.5
6	Min.	**-9402.1**	**-17019.3**	-	-	**-10812.4**	**-7875.3**	**-10662.6**	**-9731.3**
	Max	1982.8	2360.9	-	-	959	742.3	310.4	1646.6
7	Min.	**-12996.7**	**-30839.5**	-	-	-	**-10540.9**	**-14219.1**	**-159608**
	Max	3332.3	1964.3	-	-	-	803.1	-67.5	-
8	Min.	**-13994.5**	**-51441.8**	-	-	-	**-14522.5**	-	-
	Max	7982.2	582.2	-	-	-	5817.1	-	-
9	Min.	**-12357.1**	-	-	-	-	**-32007.5**	-	-
	Max	21746.5	-	-	-	-	-	-	-

Table 5.25 Peak strains of hinge longitudinal reinforcement (CAM) at center height of hinge (Section 2-2)

Longitudinal CAM Bar Strain Guages (Section 2-2 Center of Hinge Gap)									
Run no.		N CAM	N CAM	N CAM	N CAM	S CAM	S CAM	S CAM	S CAM 102
1	Min.	-25.6	-172.8	-	-	0	20.2	-27	40.5
	Max	748.9	799.8	-	-	628.4	681.7	675.2	556.6
2	Min.	-1139.4	-1350.1	-	-	-898.7	-1012.4	-1046.1	-965.5
	Max	1305.8	1702	-	-	858.2	931.4	1012.4	652.3
3	Min.	-3565.5	-4005.5	-	-	-2378.6	-2692.9	-2024.8	-2808.7
	Max	1811.5	2572.2	-	-	1087.9	1181.1	3698.6	931.4
4	Min.	**-6439.6**	-	-	-	-	-3617.6	**-6222.7**	**-8419.5**
	Max	2906.1	-	-	-	-	10832.5	1545.5	1132.4
5	Min.	**-14639.5**	-	-	-	-	**-10312.6**	**-16900**	**-18817.2**
	Max	3443.8	-	-	-	-	2956.1	1883	1357.1
6	Min.	**-21207.2**	-	-	-	-	**-11392.5**	**-24135.1**	**-21463.9**
	Max	2771.7	-	-	-	-	3759.3	1356.6	1681.2
7	Min.	**-30367.3**	-	-	-	-	-	-	**-29194.7**
	Max	2118.8	-	-	-	-	-	-	1640.7
8	Min.	-	-	-	-	-	-	-	**-31861.7**
	Max	-	-	-	-	-	-	-	1802.7
9	Min.	-	-	-	-	-	-	-	**-29532.3**
	Max	-	-	-	-	-	-	-	1357.1

Table 5.26 Peak strains of hinge longitudinal reinforcement (CAM) 5 in below (127 mm) center of hinge (Section 3-3)

Longitudinal CAM Bar Strain Guages (Section 3-3 5 inches below Center of Hinge Gap)									
Run no.		N CAM	N CAM	N CAM	N CAM	S CAM	S CAM	S CAM	S CAM
1	Min.	-33.8	0	51.2	76.8	20.3	-6.8	-13.5	54
	Max	195.8	243.1	313.6	275.2	290.3	312.2	344.6	317.1
2	Min.	-236.4	-422.2	-416	-371.2	-668.5	-702.3	-331.1	-472.3
	Max	249.9	358.2	371.2	384	580.7	459.2	736.5	377.9
3	Min.	-830.6	-1471.3	-1235.3	-1286.4	-1991.9	-1695	-1209.4	-1376.5
	Max	249.9	537.3	396.8	435.2	553.7	439	1108.1	438.6
4	Min.	-2532.4	-2705.9	-2886.7	-4000.1	-3166.7	-	-2581	-2530.4
	Max	270.1	1074.7	403.2	409.6	526.7	-	1385.1	492.6
5	Min.	-4720.3	-4190	-4499.7	**-6822.5**	-4193	-	**-5398.4**	**-5971.7**
	Max	425.4	1784.8	524.9	492.8	452.4	-	2189.1	641
6	Min.	-4916.2	-	-4627.7	**-7212.9**	-4247	-	**-9601**	**-8475.1**
	Max	547	-	684.9	716.8	162	-	2472.9	5155.3
7	Min.	**-6408.6**	-	**-6144.7**	**-11174.6**	-	-	**-69044.3**	-
	Max	931.9	-	979.3	1190.4	-	-	217123.8	-
8	Min.	-	-	**-6145.9**	**-12006.6**	-	-	-	-
	Max	-	-	1670.6	2144	-	-	-	-
9	Min.	-	-	-5005.4	-	-	-	-	-
	Max	-	-	-	-	-	-	-	-

Table 5.27 Peak strains of hinge spiral reinforcement 5 in above (127 mm) center height of hinge (Section 1-1)

Hinge Spiral Strain Guages (Section 1-1 5 inches above Center of Hinge Gap)					
Run no.		N SG 97	N SG 98	S SG 97	S SG 98
1	Min.	-19.2	-32	-27	-33.7
	Max	32	25.6	13.5	13.5
2	Min.	-19.2	-38.4	-33.8	-40.5
	Max	44.8	19.2	20.3	13.5
3	Min.	-32	-44.8	-33.8	-47.2
	Max	32	12.8	13.5	6.7
4	Min.	-25.6	-51.2	-33.8	-60.7
	Max	38.4	6.4	13.5	0
5	Min.	-32	-57.6	-33.8	-74.2
	Max	44.8	0	20.3	6.7
6	Min.	-32	-57.6	-40.5	-60.7
	Max	44.8	6.4	13.5	-13.5
7	Min.	-32	-64	-101.3	-74.2
	Max	44.8	0	47.3	-13.5
8	Min.	-32	-70.4	-60.8	-81
	Max	32	0	40.5	-13.5
9	Min.	-44.8	-70.4	-47.3	-101.2
	Max	32	0	6.8	-20.2

Table 5.28 Peak strains of hinge spiral reinforcement at center height of hinge (Section 2-2)

Hinge Spiral Strain Guages (Section 2-2 Center of Hinge Gap)									
Run no.		**N SG 103**	**N SG 104**	**N SG105**	**N SG106**	**S SG 103**	**S SG 104**	**S SG 105**	**S SG 106**
1	Min.	-19.2	51.2	-19.2	-38.4	-	-67.5	0	-20.3
	Max	51.2	102.3	38.4	25.6	-	0	47.3	40.5
2	Min.	-12.8	19.2	-19.2	-25.6	-	-94.5	0	-33.8
	Max	63.9	115.1	44.8	51.2	-	6.8	60.8	33.8
3	Min.	-76.7	-76.7	-6.4	-19.2	-	-94.5	0	-54
	Max	76.7	102.3	121.6	115.2	-	6.8	108.1	67.5
4	Min.	-95.9	-70.3	-38.4	-6.4	-	-81	6.8	-60.8
	Max	166.3	217.4	211.1	179.2	-	54	182.5	108
5	Min.	-12.8	-140.7	-38.4	-364.8	-	-202.5	-6.8	-47.3
	Max	179.1	300.6	275.1	166.4	-	87.8	141.9	182.3
6	Min.	-6.4	-217.4	-51.2	-576	-	-405.1	-33.8	-87.8
	Max	179.1	332.5	275.1	166.4	-	27	81.1	175.5
7	Min.	-1317.3	-281.4	-217.5	-576	-	-	-87.9	-216
	Max	38.4	626.7	403.1	313.6	-	-	74.3	148.5
8	Min.	**-4195**	-402.9	-723	-96	-	-	-290.6	-438.8
	Max	-1080.7	1151.1	415.9	556.8	-	-	33.8	108
9	Min.	**-4233.3**	-	-851	140.8	-	-	-1696.5	-1154.4
	Max	-2129.5	-	166.4	864	-	-	-13.5	67.5

Table 5.29 Peak strains of hinge spiral reinforcement 5 in below (127 mm) center height of hinge (Section 1-1)

Hinge Spiral Strain Guages (Section 3-3 5 inches below Center of Hinge Gap)					
Run no.		**N SG112**	**N SG 113**	**S SG 112**	**S SG 113**
1	Min.	-38.4	-25.6	-47.3	-33.8
	Max	12.8	32	0	13.5
2	Min.	-38.4	-38.3	-54	-40.5
	Max	32	38.3	40.5	13.5
3	Min.	-38.4	-44.7	-60.8	-47.3
	Max	57.6	38.3	162.1	20.3
4	Min.	-38.4	-44.7	-54	-54
	Max	76.8	51.1	405.3	20.3
5	Min.	-32	-32	-47.3	-67.5
	Max	89.5	44.7	601.2	27
6	Min.	-	-25.6	-40.5	-81
	Max	-	57.5	513.4	27
7	Min.		-6.4	-6.8	-
	Max		63.9	493.1	-
8	Min.		0	-13.5	-
	Max		76.7	479.6	-
9	Min.		6.4	-	-
	Max		95.9	-	-

Table 5.30 Peak curvature of columns at various sections for runs 1-5

Minimum and Maximum Curvature at each section for runs 1-5 (rad/in)											
	In. (mm) below cap	Run 1		Run 2		Run 3		Run 4		Run 5	
		φ Min	φ Max	φ Min	φ Max	φ Min	φ Max	φ Min	φ Max	φ Min	φ Max
ABC	7 (152)	-0.00005	0.00004	-0.00020	0.00018	-0.00040	0.00036	-0.00090	0.00057	-0.00176	0.00121
	14 (356)	0.00000	0.00005	-0.00007	0.00010	-0.00014	0.00021	-0.00028	0.00032	-0.00048	0.00064
	21 (533)	-0.00003	0.00003	-0.00006	0.00008	-0.00015	0.00014	-0.00029	0.00021	-0.00037	0.00033
CIP	7 (152)	-0.00006	0.00005	-0.00023	0.00016	-0.00046	0.00034	-0.00104	0.00054	-0.00218	0.00124
	14 (356)	-0.00002	0.00002	-0.00008	0.00008	-0.00017	0.00017	-0.00032	0.00025	-0.00042	0.00047
	21 (533)	-0.00004	0.00001	-0.00008	0.00007	-0.00015	0.00022	-0.00027	0.00033	-0.00032	0.00048

Table 5.31 Peak curvature of columns at various sections for runs 6-9

Minimum and Maximum Curvature at each section for runs 6-9 (rad/in)									
	In. (mm) below cap	Run 6		Run 7		Run 8		Run 9	
		φ Min	φ Max	φ Min	φ Max	φ Min	φ Max	φ Min	φ Max
ABC	7 (152)	-0.00210	0.00185	-0.00328	0.00305	-0.00364	0.00655	-0.00355	0.01751
	14 (356)	-0.00047	0.00099	-0.00063	0.00160	-0.00081	0.00261	-0.00050	0.00139
	21 (533)	-0.00037	0.00037	-0.00044	0.00046	-0.00040	0.00098	-0.00027	0.00070
CIP	7 (152)	-0.00266	0.00176	-0.00424	0.00287	-0.00512	0.00782	-0.00413	0.01544
	14 (356)	-0.00042	0.00064	-0.00059	0.00066	-0.00054	0.00026	-0.00048	0.00012
	21 (533)	-0.00032	0.00054	-0.00032	0.00058	-0.00027	0.00054	-0.00024	0.00051

Table 5.32 Peak rotations at base of columns for runs 1-5

Minimum and Maximum Rotations at base for runs 1-5 (rad)											
	In. (mm) above foot.	Run 1		Run 2		Run 3		Run 4		Run 5	
		θ Min	θ Max	θ Min	θ Max	θ Min	θ Max	θ Min	θ Max	θ Min	θ Max
ABC	5 (127)	-0.00138	0.00066	-0.00355	0.00338	-0.00754	0.00749	-0.01205	0.01697	-0.02331	0.02785
CIP	5 (127)	-0.00106	0.00106	-0.00345	0.00375	-0.00770	0.00774	-0.01238	0.01699	-0.02329	0.02765

Table 5.33 Peak rotations at base of columns for runs 6-9

Minimum and Maximum Rotations at base for runs 6-9 (rad)									
	In. (mm) above foot.	Run 6		Run 7		Run 8		Run 9	
		θ Min	θ Max	θ Min	θ Max	θ Min	θ Max	θ Min	θ Max
ABC	5 (127)	-0.03204	0.03047	-0.04659	0.04190	-0.08501	0.04608	-0.13019	0.04066
CIP	5 (127)	-0.03153	0.03039	-0.04525	0.04190	-0.08098	0.04615	-0.13713	0.04106

Table 5.34 Initial period of each run and final period

Run #	Initial Period (s)
1	0.4
2	0.444
3	0.471
4	0.533
5	0.533
6	0.667
7	0.7272
8	0.889
9	1
Final	1.143

Chapter 5 Figures

Figure 5.1 Run 0 - Crack along Sonotube form spiral before start of testing (ABC - E face)

Figure 5.2 Run 0 - Voids on column before start of testing (ABC - N face)

Figure 5.3 Run 4 - Initiation of two-way hinge spalling (ABC - W face)

Figure 5.4 Run 5 – Progression of two-way hinge spalling (ABC - E face)

Figure 5.5 Run 5 – Appearance of flexural cracks in plastic hinge (ABC - N face)

Figure 5.6 Run 5 – Appearance of flexural cracks in plastic hinge (ABC - S face)

Figure 5.7 Run 6 – Extension of flexural cracks and grout crack (ABC - E face)

Figure 5.8 Run 6 – Appearance and extension of flexural cracks (ABC - N face)

Figure 5.9 Run 6 – Appearance and extension of flexural cracks (ABC - S face)

Figure 5.10 Run 7 – Spalling of column (ABC - N face)

Figure 5.11 Run 7 – Extension and widening of flexural cracks (ABC - S face)

Figure 5.12 Run 8 – Exposure of column reinforcement (ABC - N face)

Figure 5.13 Run 8 – Exposure of two-way hinge reinforcement (ABC - N face)

Figure 5.14 Run 8 – Appearance of shear cracks (ABC – W face)

Figure 5.15 Run 9 – Progression of spalling (ABC – N face)

Figure 5.16 Run 9 – Final damage of east face (ABC – E face)

Figure 5.17 Run 9 – Spalling of column, cracking of grout, and exposure of reinforcement (ABC – S face)

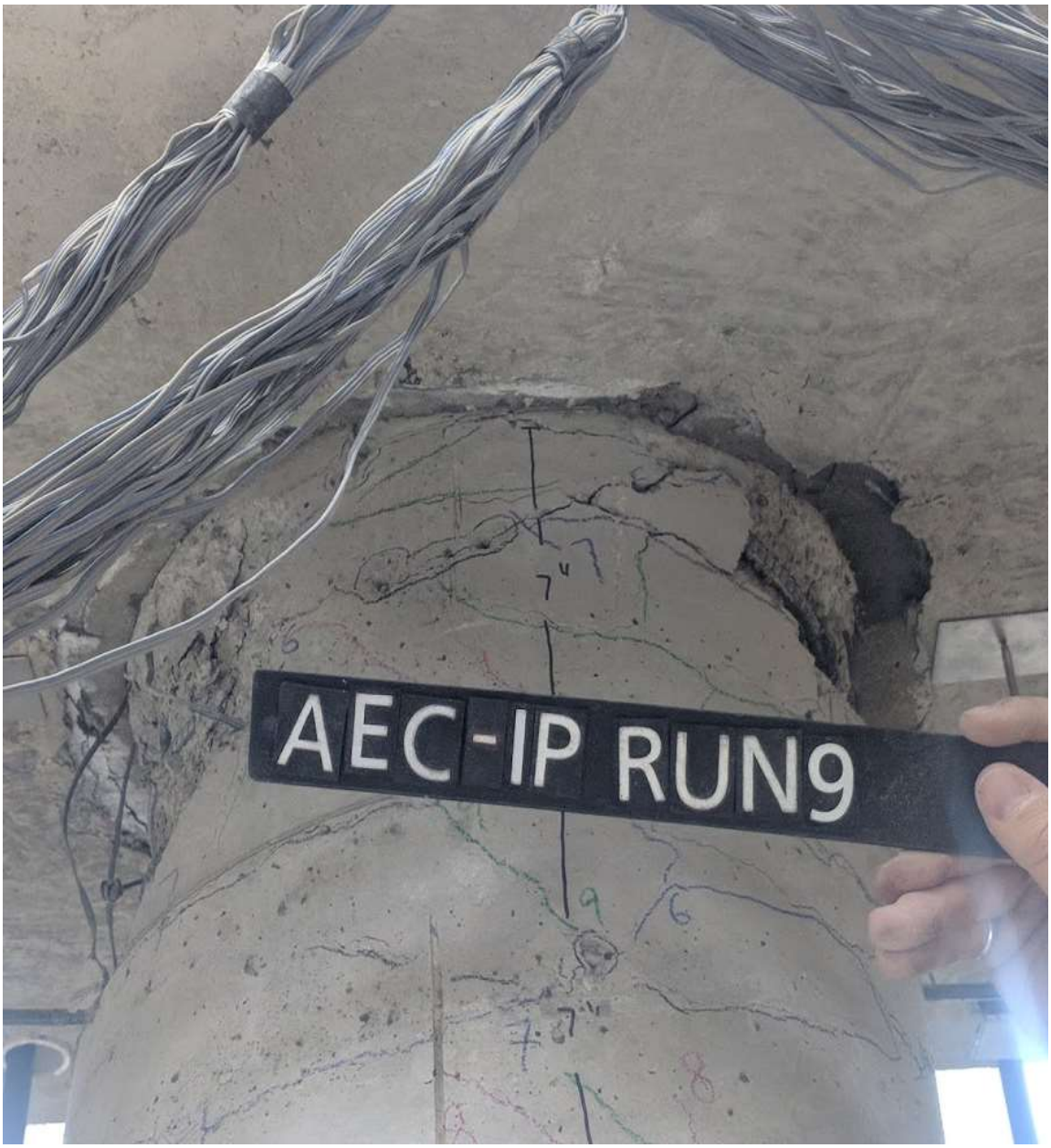

Figure 5.18 Run 9 – Final damage of west face (ABC – W face)

Figure 5.19 Run 9 – Severe spalling of two-way hinge (ABC – W face)

Figure 5.20 Run 9 – Overview of specimen after final ground motion (ABC – W face)

Figure 5.21 Run 9 – Absence of cracks on south column-cap joint (ABC – E face)

Figure 5.22 Run 9 – Absence of cracks on south column-cap joint (ABC – W face)

Figure 5.23 Run 0 – Cracks marked before testing (CIP – N face)

Figure 5.24 Run 0 – Cracks marked before testing (CIP – E face)

Figure 5.25 Run 0 – Cracks marked before testing (CIP – S face)

Figure 5.26 Run 0 – Voids marked before testing (CIP – W face)

Figure 5.27 Run 2 – Extension of pre-existing cracks (CIP – N face)

Figure 5.28 Run 4 – Appearance of flexural cracks (CIP – S face)

Figure 5.29 Run 5 – Major spalling of hinge (CIP – E face)

Figure 5.30 Run 5 – Major spalling of hinge concrete (CIP – S face)

Figure 5.31 Run 5 – Appearance of several flexural cracks (CIP – N face)

Figure 5.32 Run 5 – Appearance of several flexural cracks (CIP – S face)

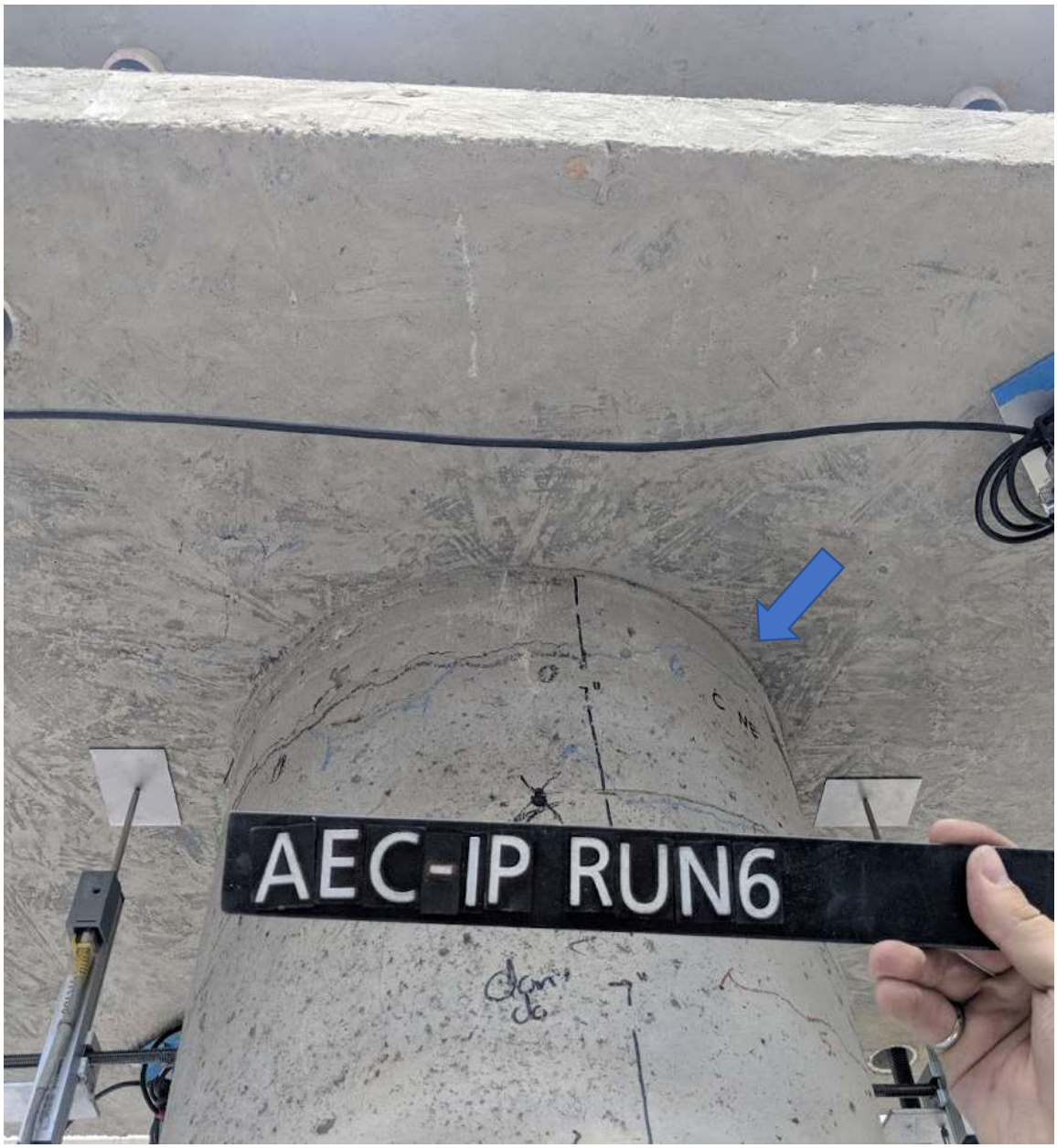

Figure 5.33 Run 6 – Cracks marked before testing (CIP – E face)

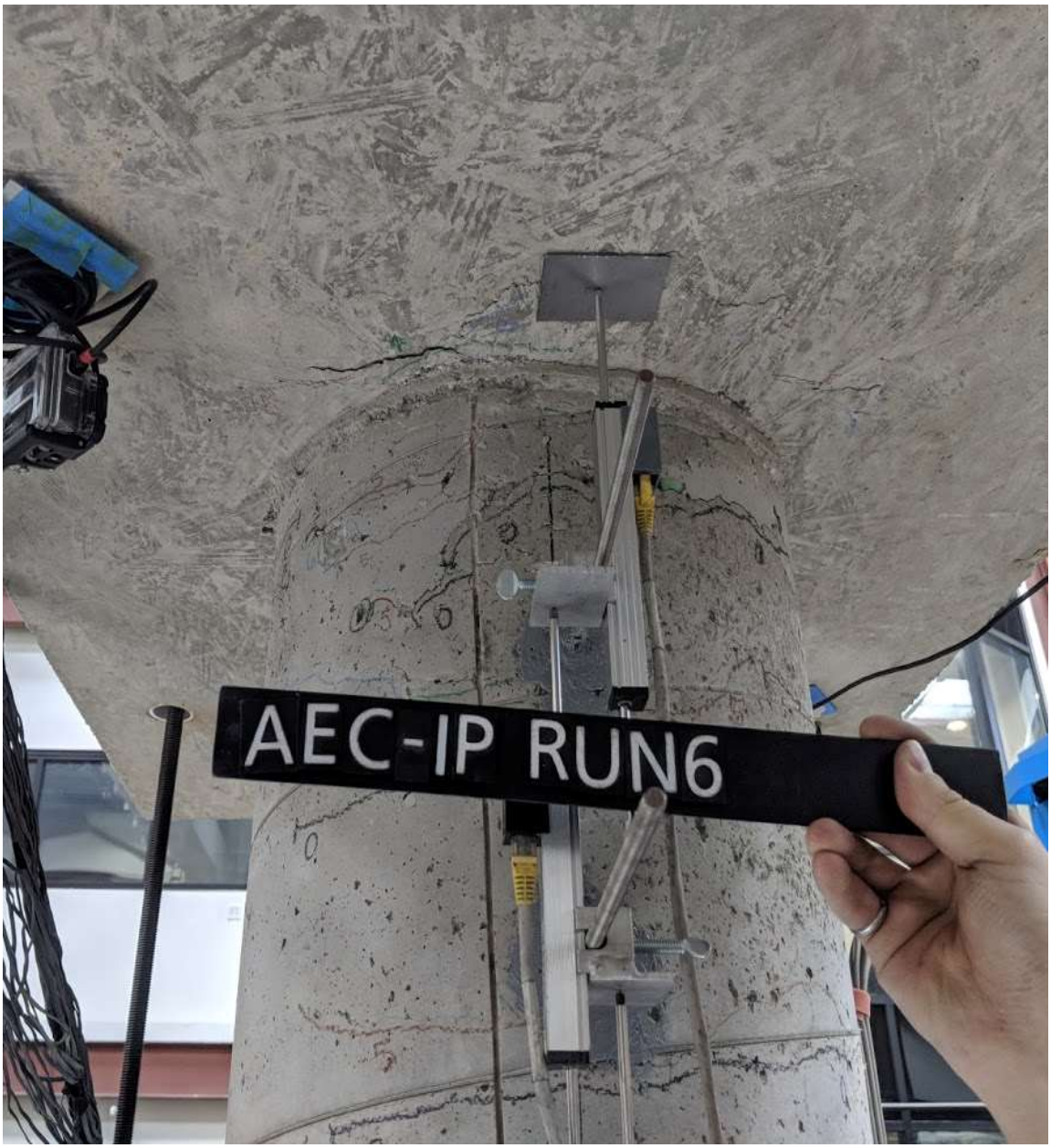

Figure 5.34 Run 6 – Cracks marked before testing (CIP – S face)

Figure 5.35 Run 6 – Progression of spalling in hinge (CIP – S face)

Figure 5.36 Run 7 – Spalling of column and formation of shear crack (CIP – N face)

Figure 5.37 Run 7 – Spalling of column and cap beam (CIP – S face)

Figure 5.38 Run 7 – Debris removed from hinge (CIP – W face)

Figure 5.39 Run 8 – Major spalling of column and cap beam and exposure of reinforcement (CIP – S face)

Figure 5.40 Run 8 – Progression of spalling, exposure of reinforcement, and appearance of new shear cracks (CIP – N face)

Figure 5.41 Run 9 – Progression of column and cap beam spalling (CIP – N face)

Figure 5.42 Run 9 – Progression of spalling into cap beam and column core (CIP – S face)

Figure 5.43 Run 9 – Progression of spalling into two-way hinge core (CIP – E face)

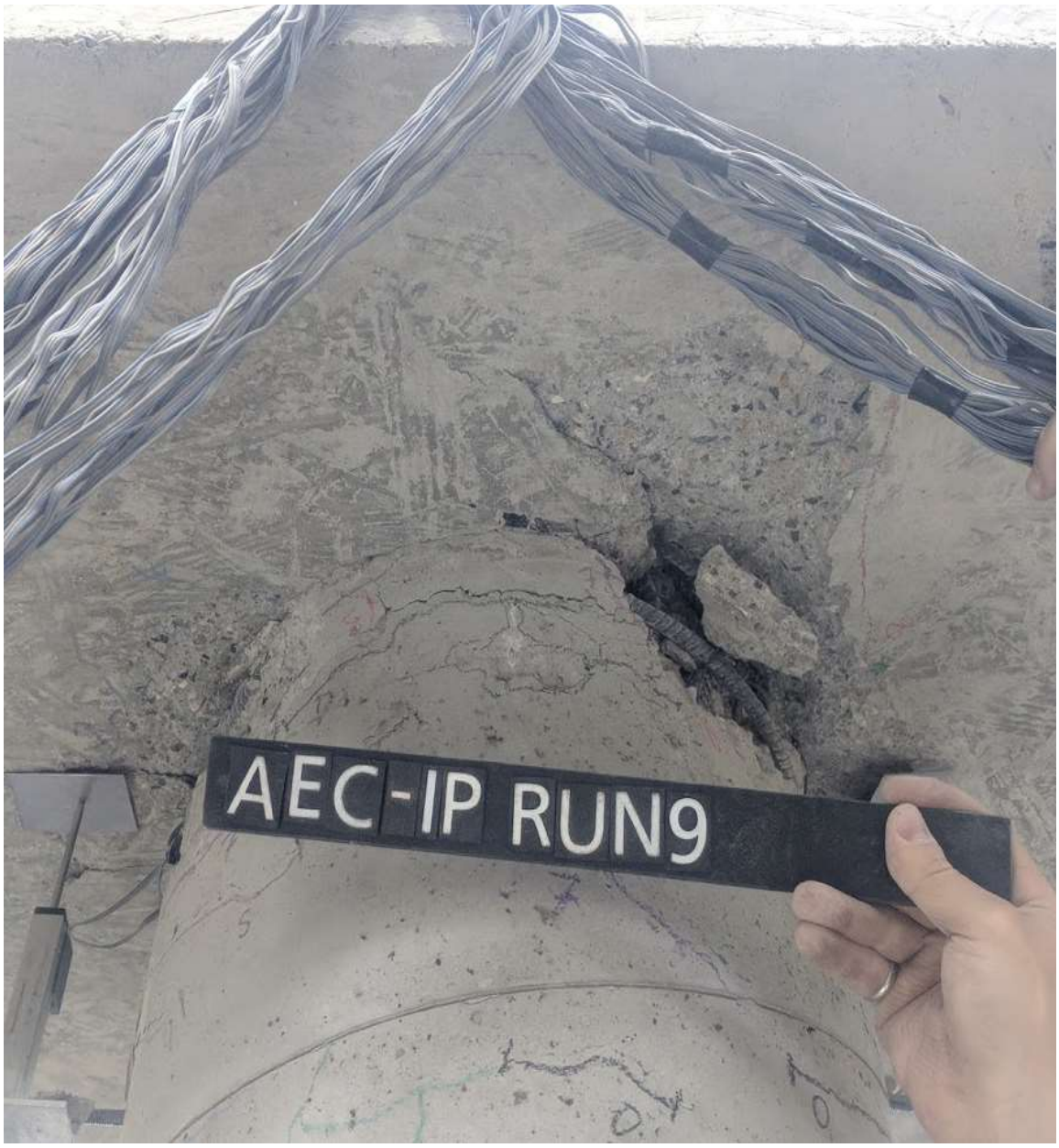

Figure 5.44 Run 9 – Column west face after final run (CIP – W face)

Figure 5.45 Run 9 – Close up of damage on southern face and deformed bars (CIP – S face)

Figure 5.46 Run 9 – Close up of damage on southern face and deformed bars (CIP – S face)

Figure 5.47 Run 9 – Absence of cracks on north column-cap joint (CIP – E face)

Figure 5.48 Run 9 – Absence of cracks on north column-cap joint (CIP – W face)

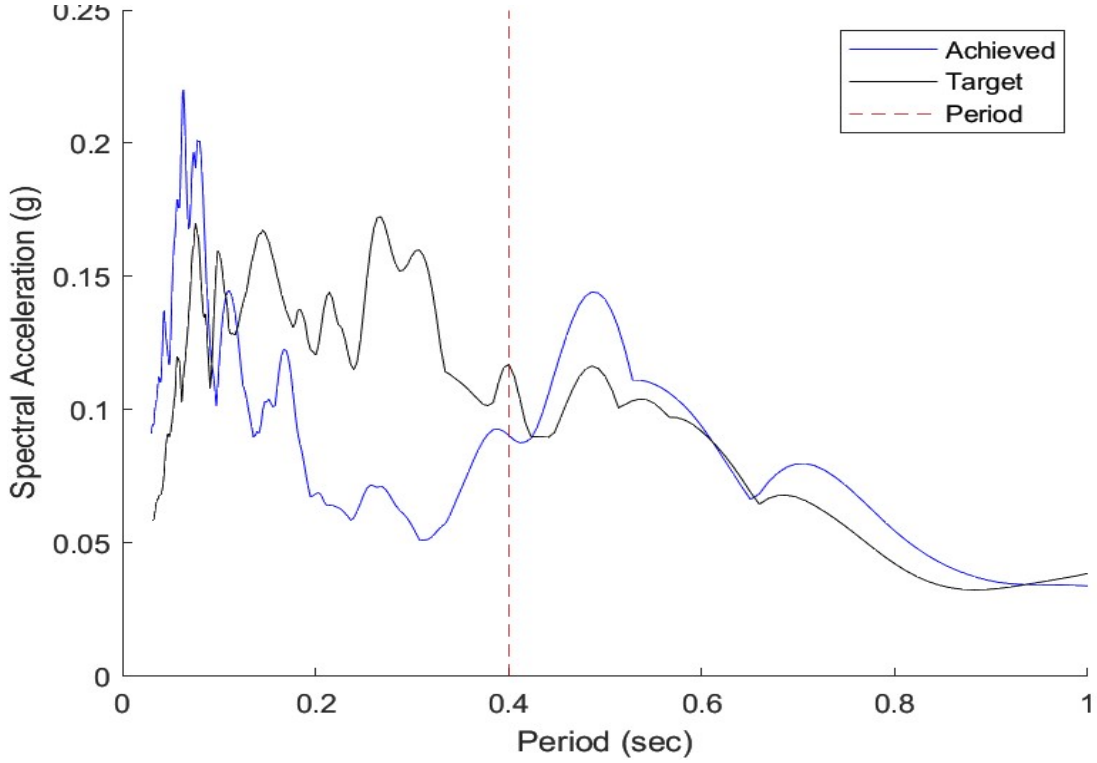

Figure 5.49 Run 1 - Target vs achieved response spectra and initial period

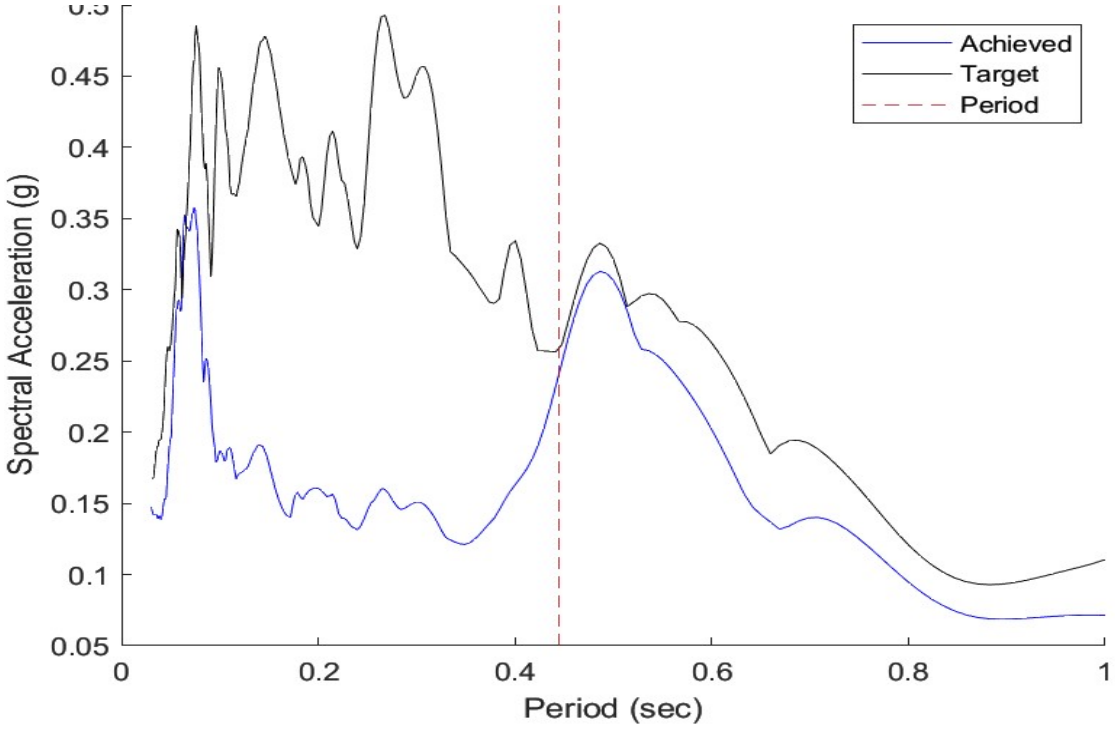

Figure 5.50 Run 2 - Target vs achieved response spectra and initial period

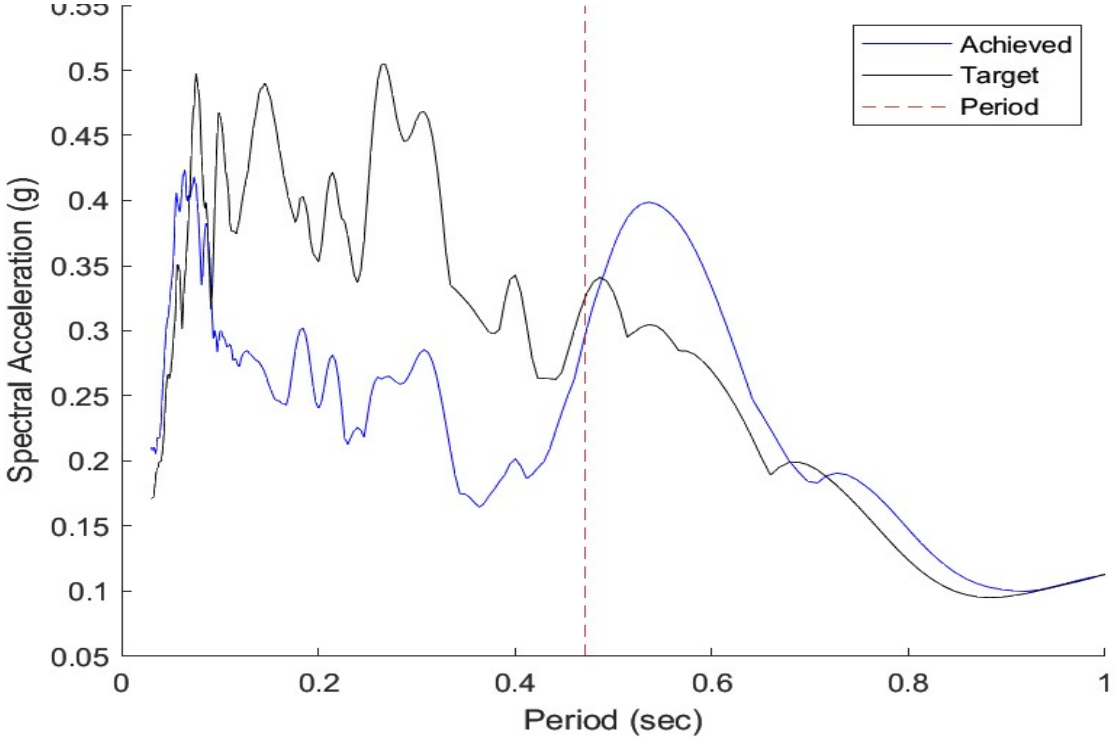

Figure 5.51 Run 3 - Target vs achieved response spectra and initial period

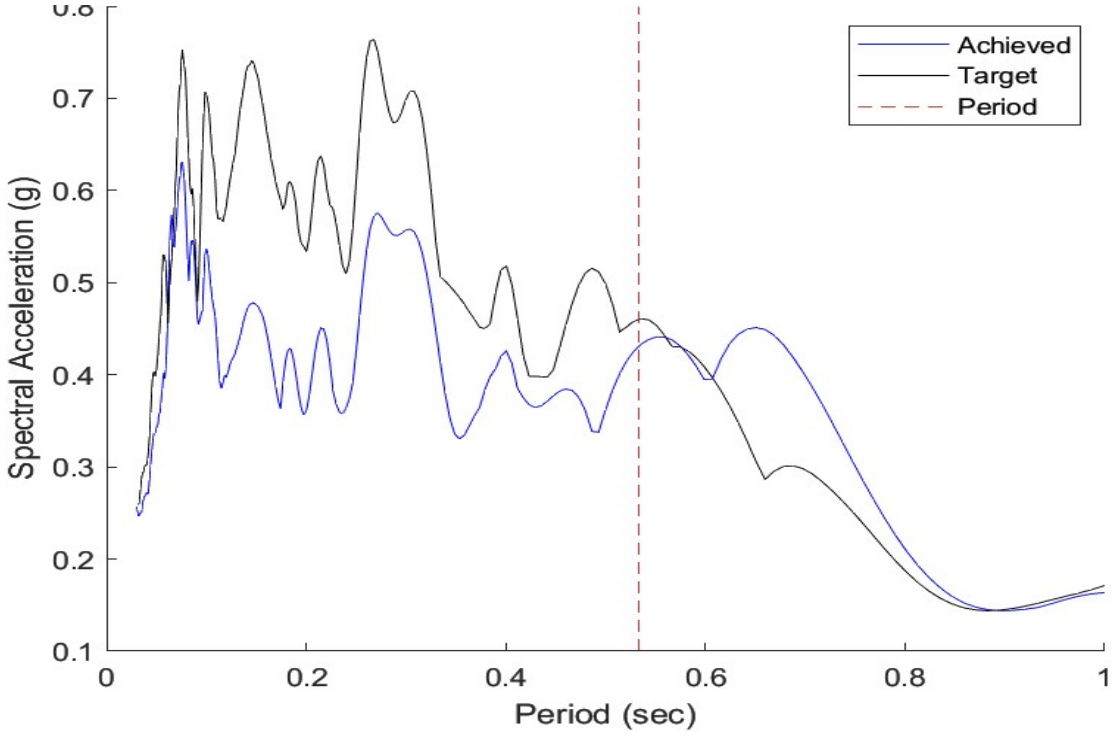

Figure 5.52 Run 4 - Target vs achieved response spectra and initial period

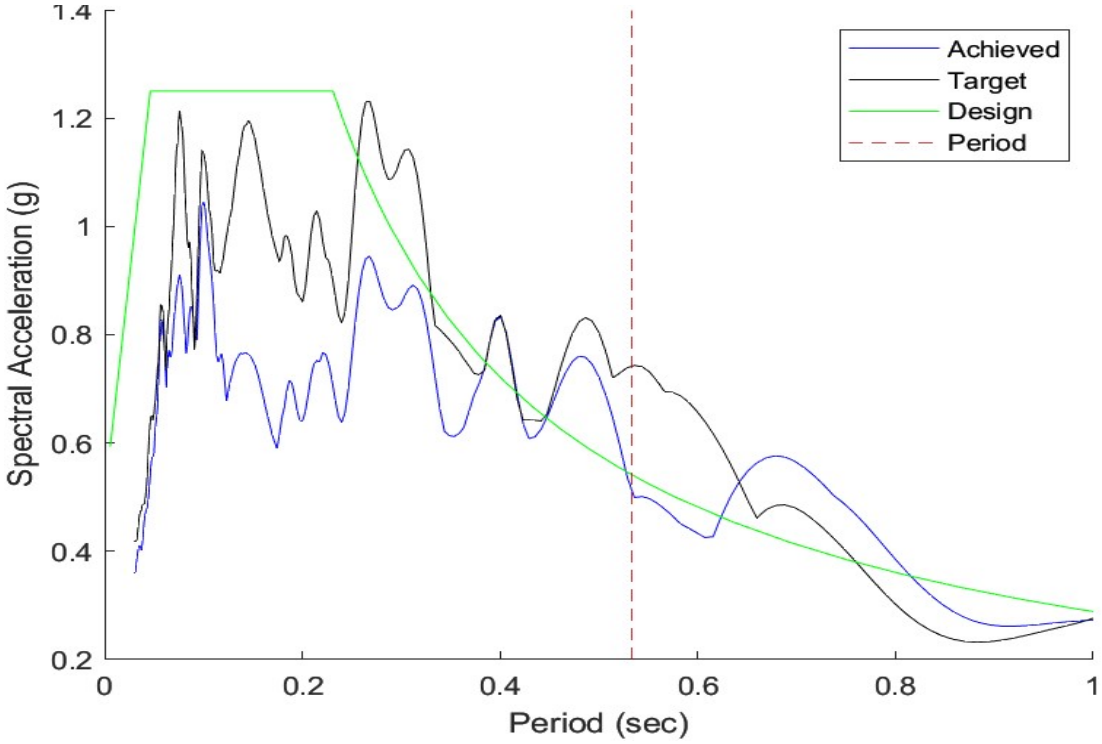

Figure 5.53 Run 5 - Target vs achieved vs design response spectra and initial period

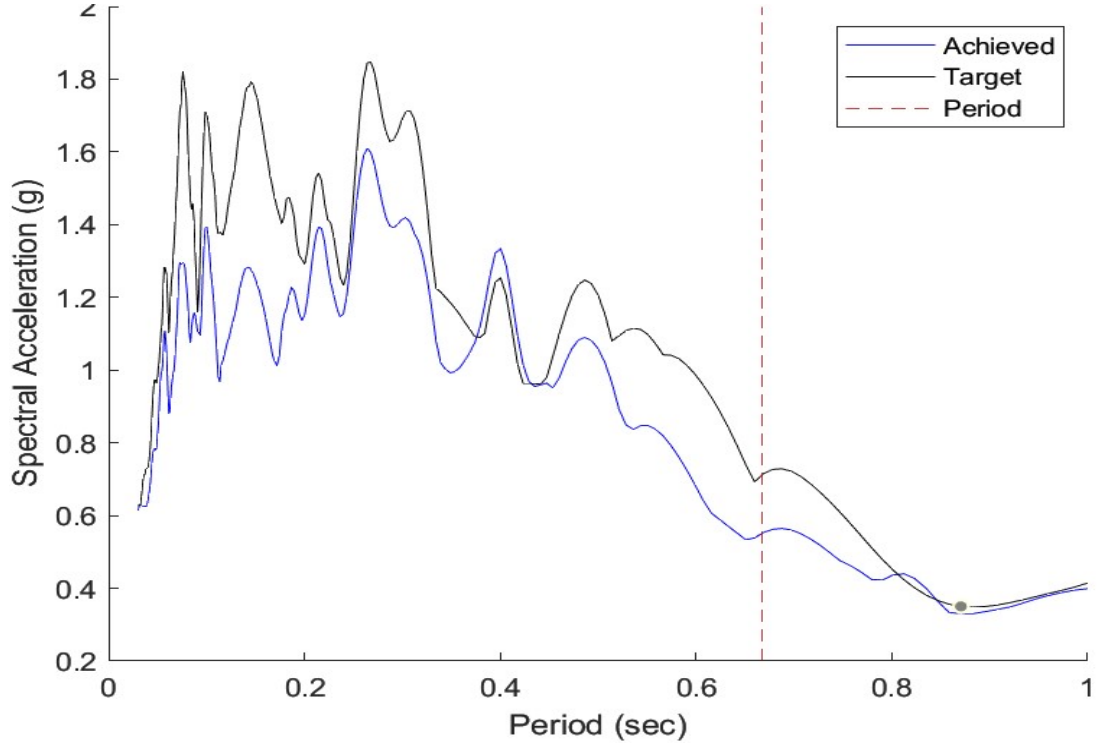

Figure 5.54 Run 6 - Target vs achieved response spectra and initial period

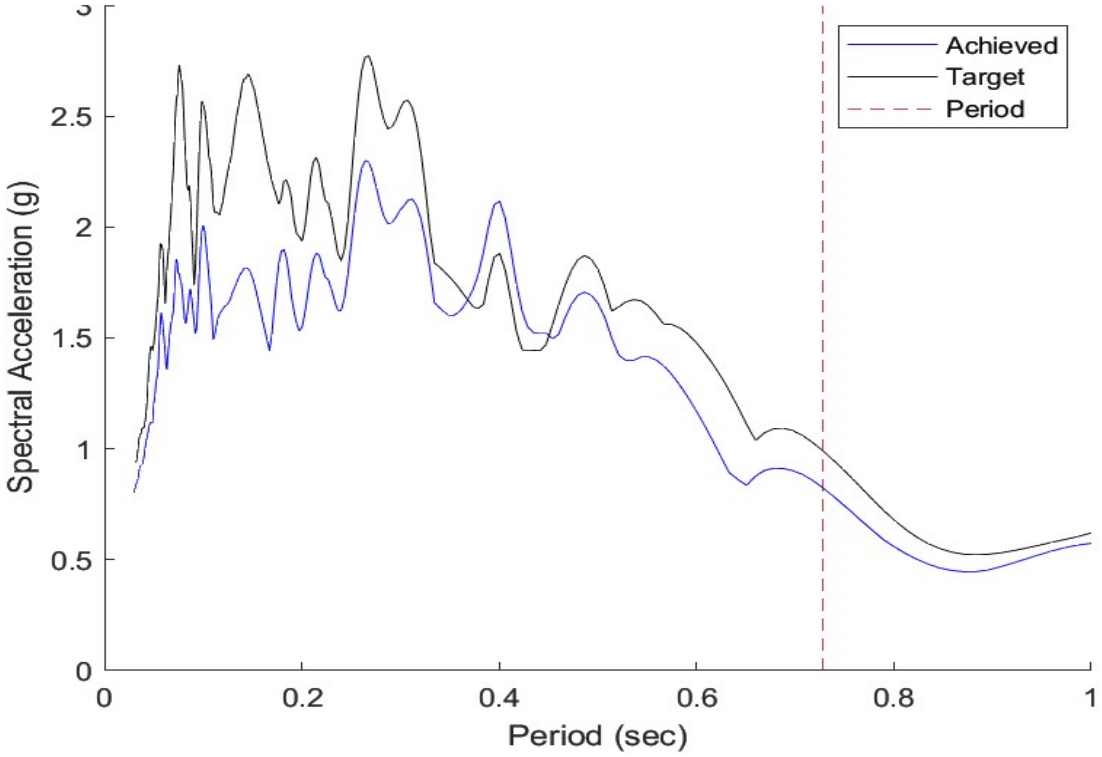

Figure 5.55 Run 7 - Target vs achieved response spectra and initial period

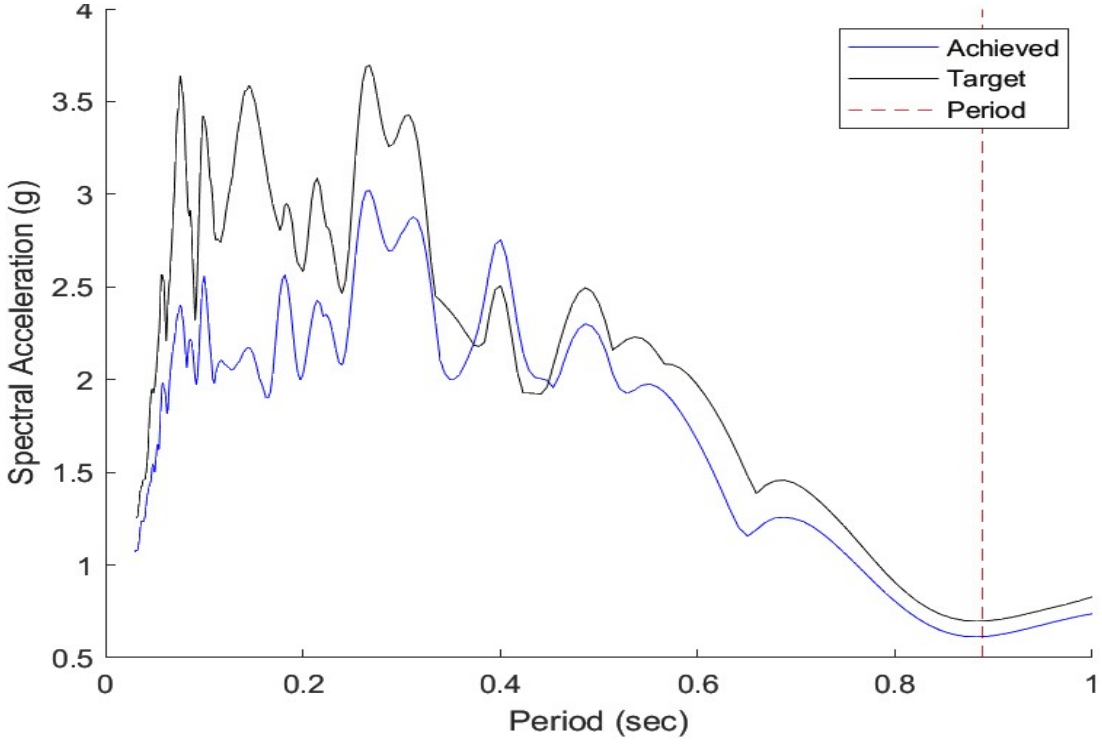

Figure 5.56 Run 8 - Target vs achieved response spectra and initial period

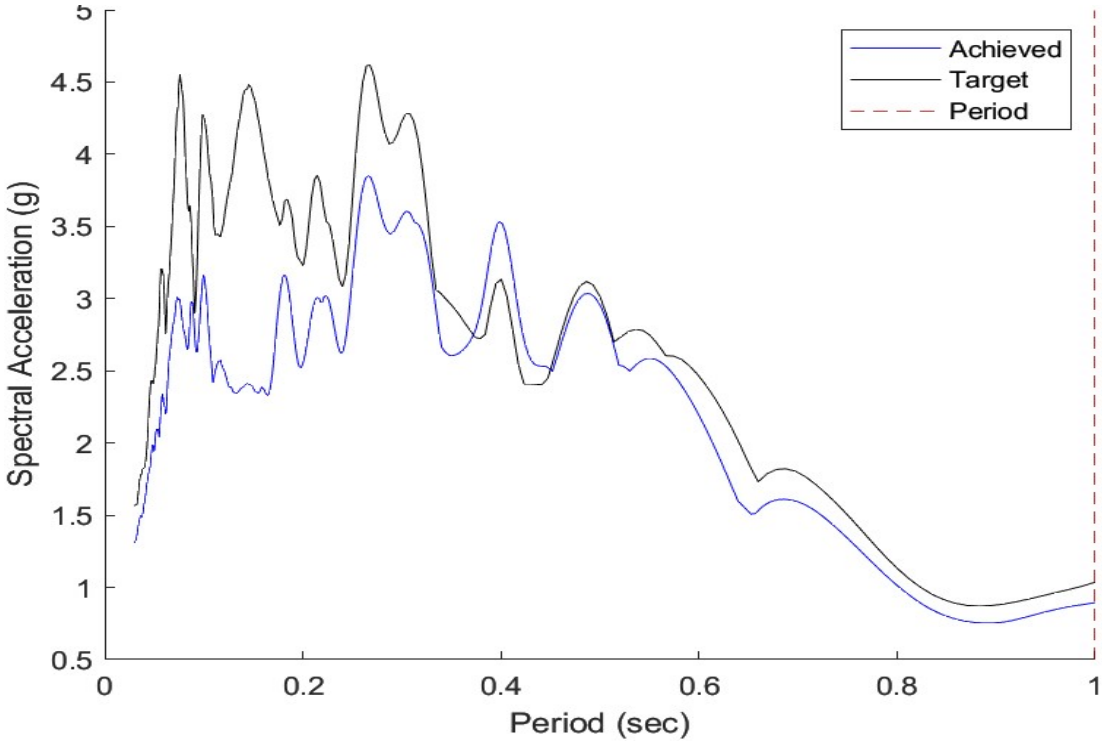

Figure 5.57 Run 9 - Target vs achieved response spectra and initial period

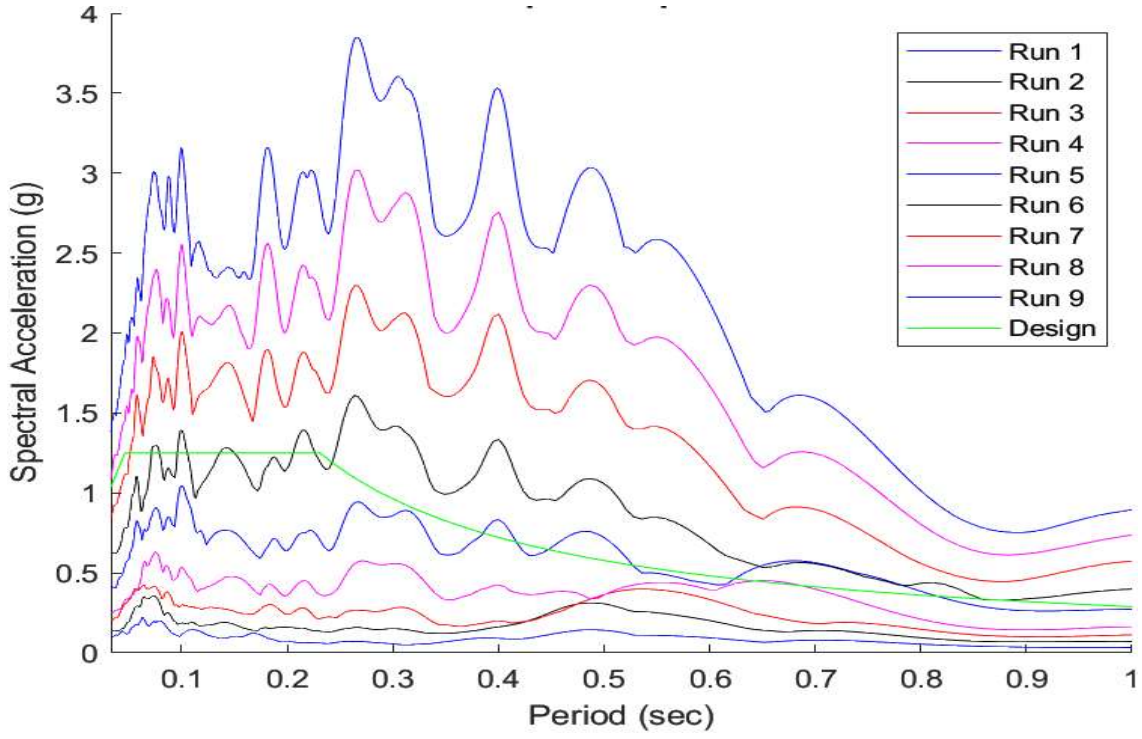

Figure 5.58 All runs – Achieved response spectra for all runs and design spectrum

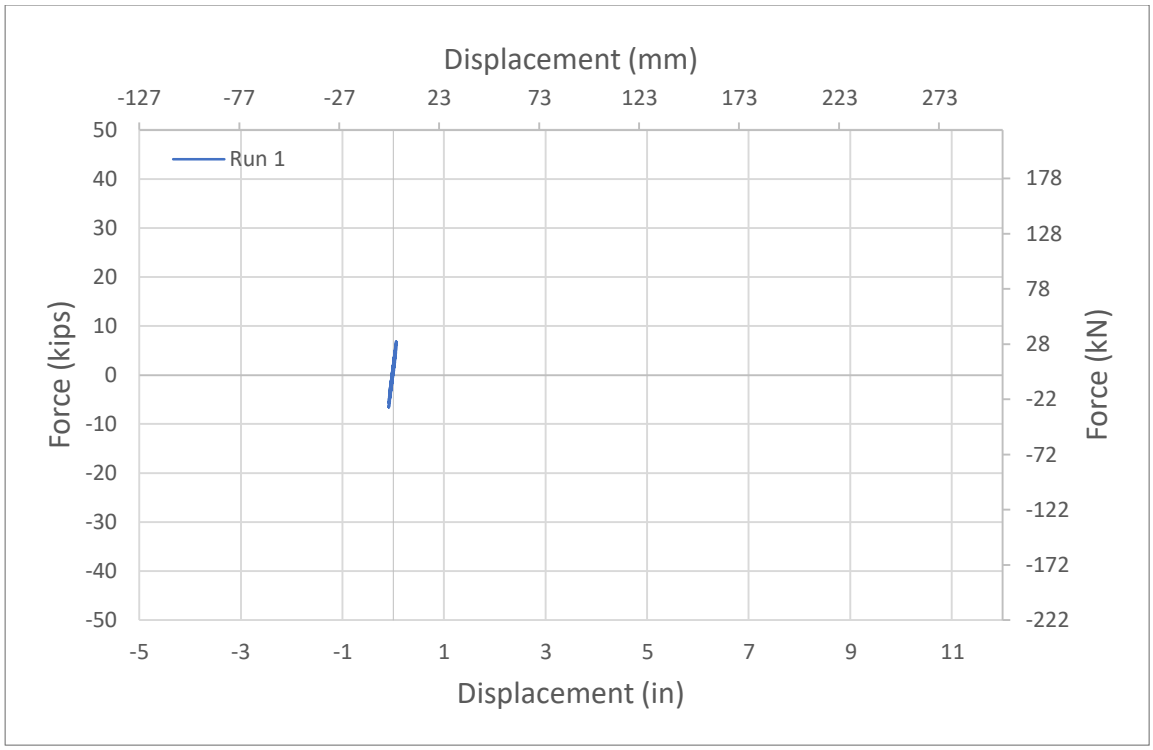

Figure 5.59 Run 1 – Force-displacement relationship

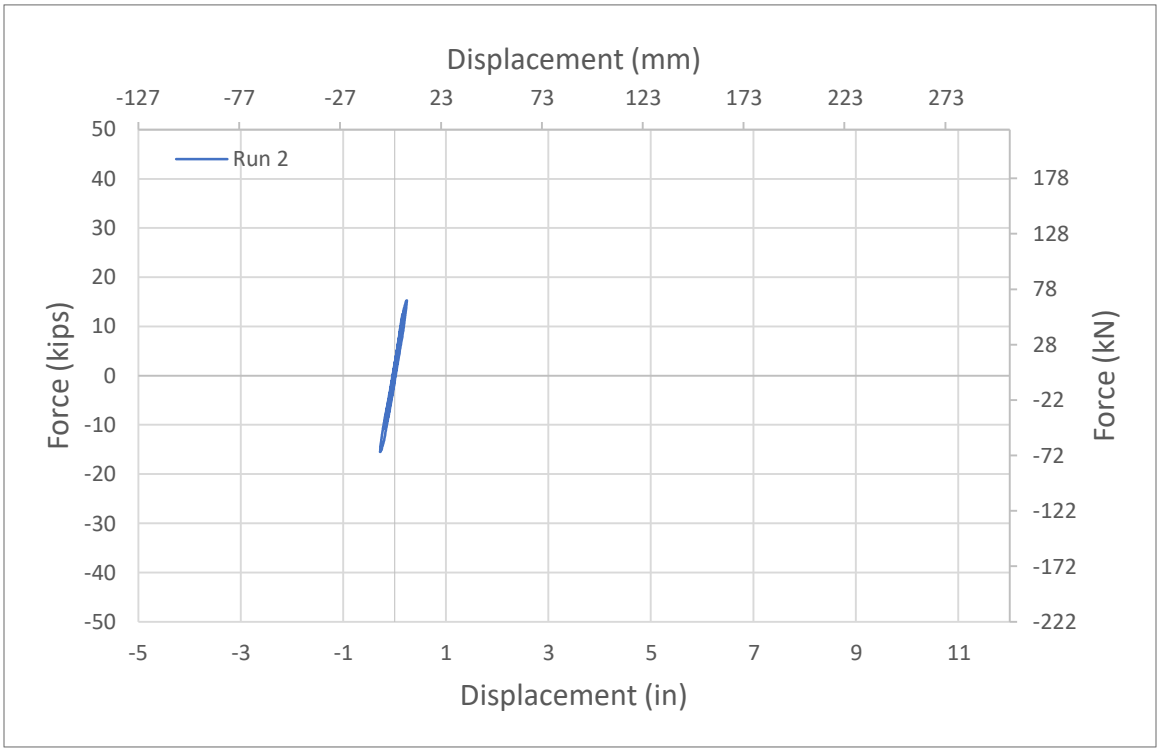

Figure 5.60 Run 2 – Force-displacement relationship

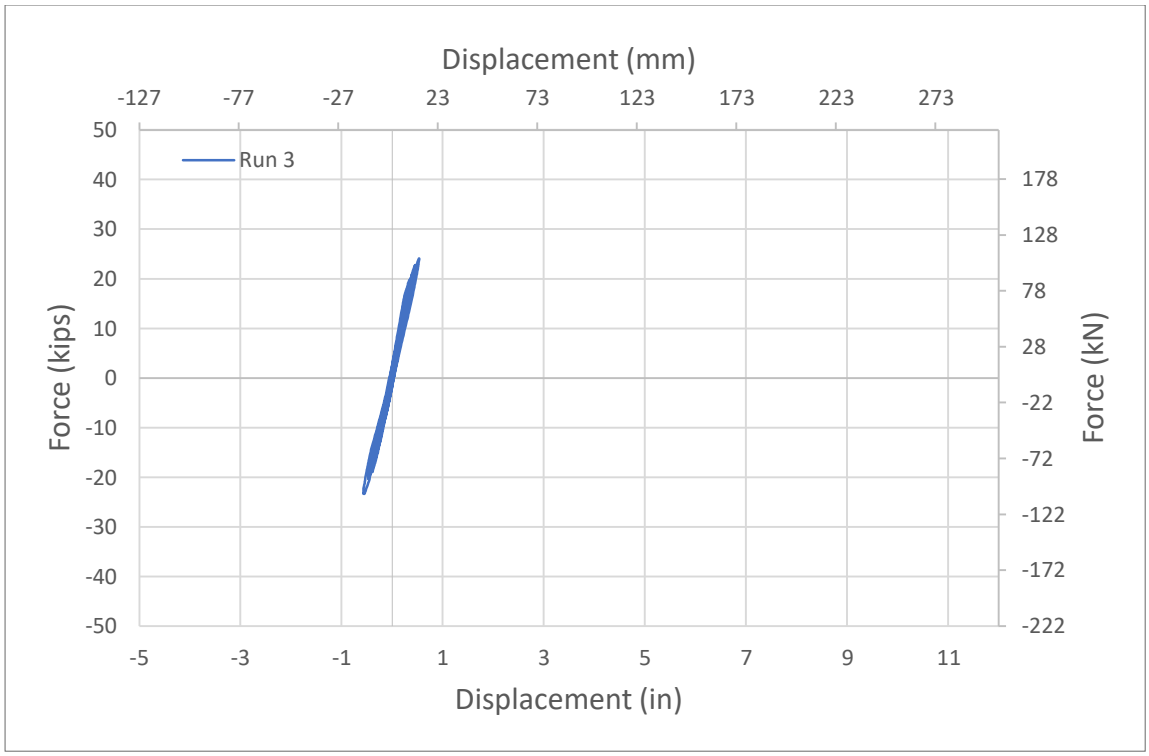

Figure 5.61 Run 3 – Force-displacement relationship

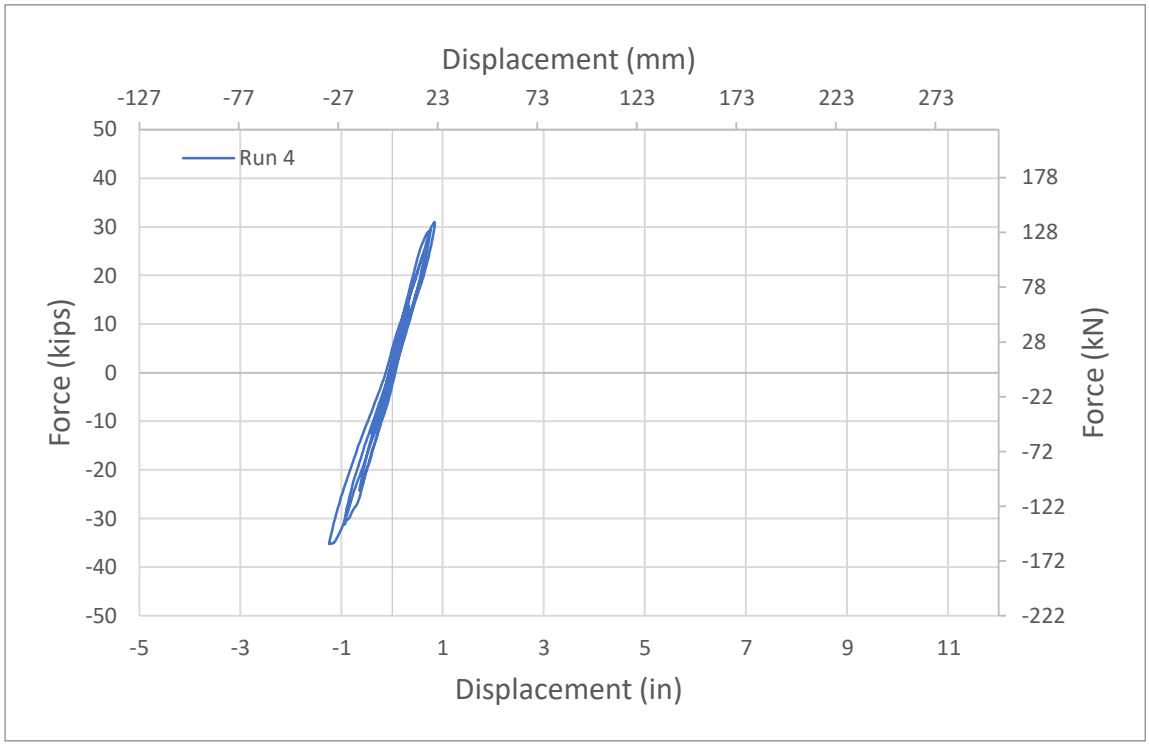

Figure 5.62 Run 4 – Force-displacement relationship

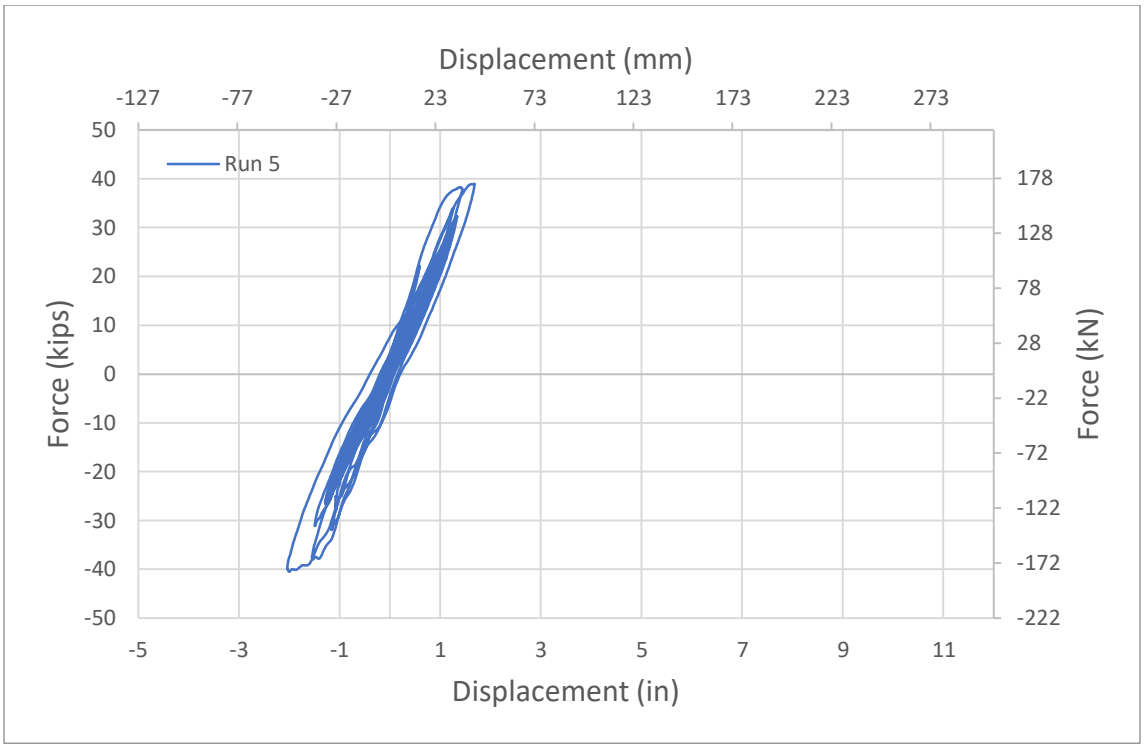

Figure 5.63 Run 5 – Force-displacement relationship

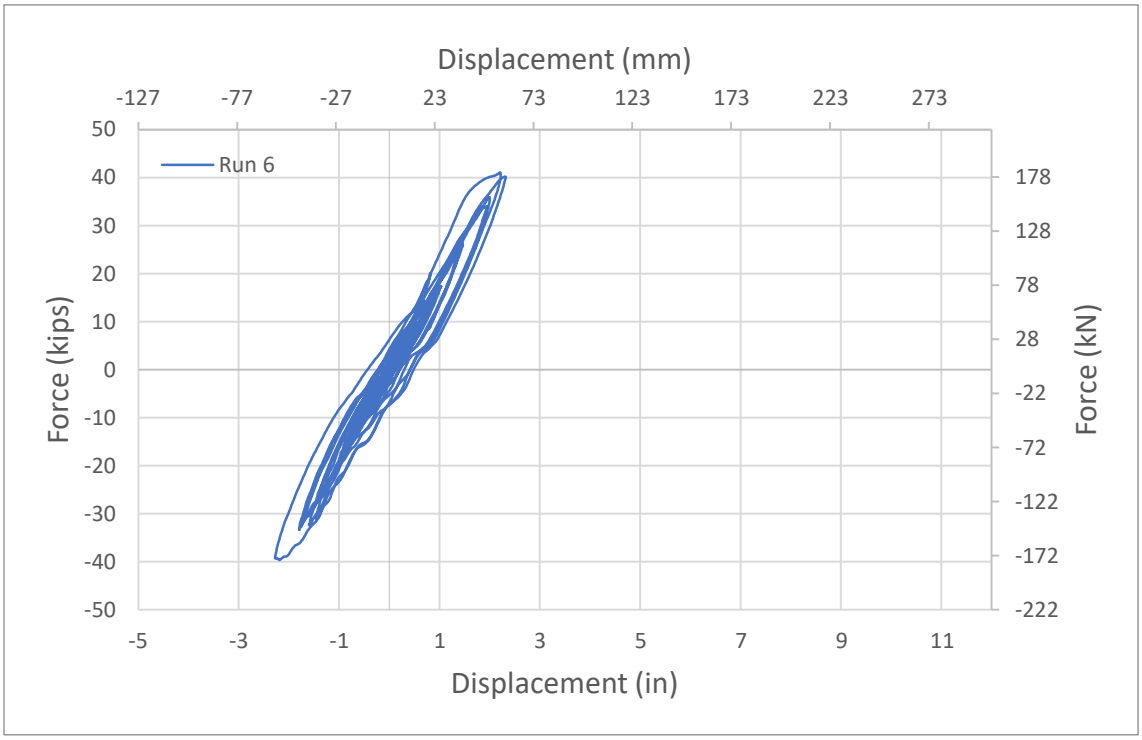

Figure 5.64 Run 6 – Force-displacement relationship

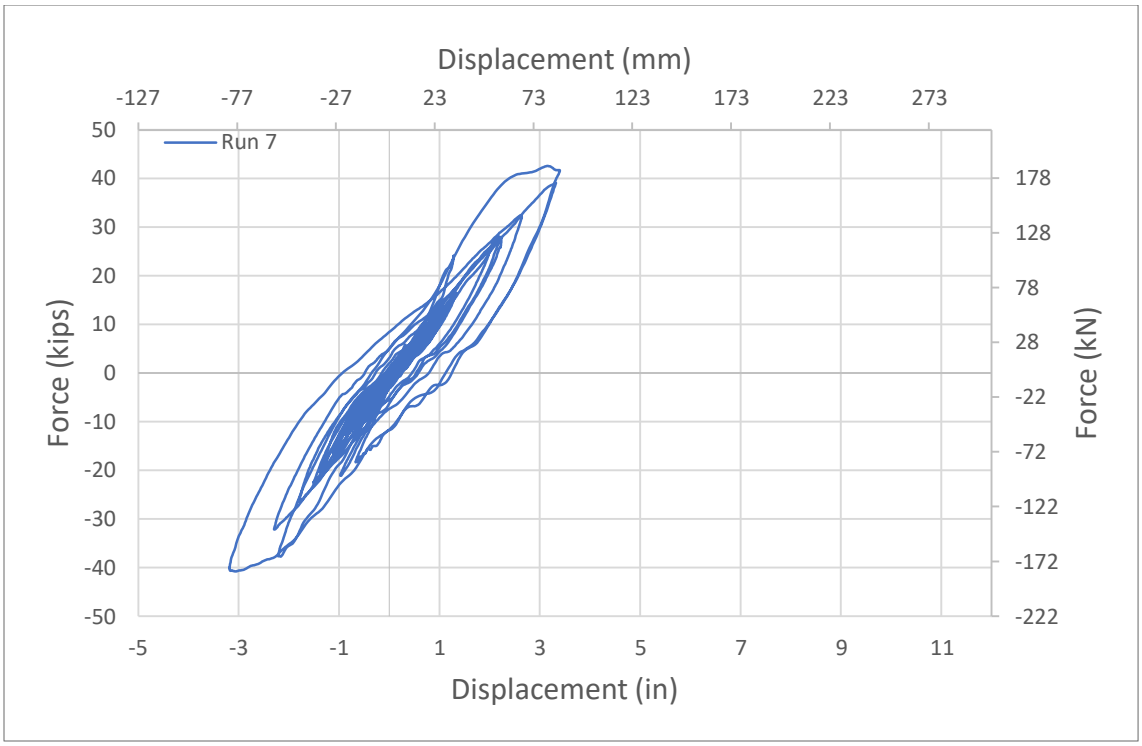

Figure 5.65 Run 7 – Force-displacement relationship

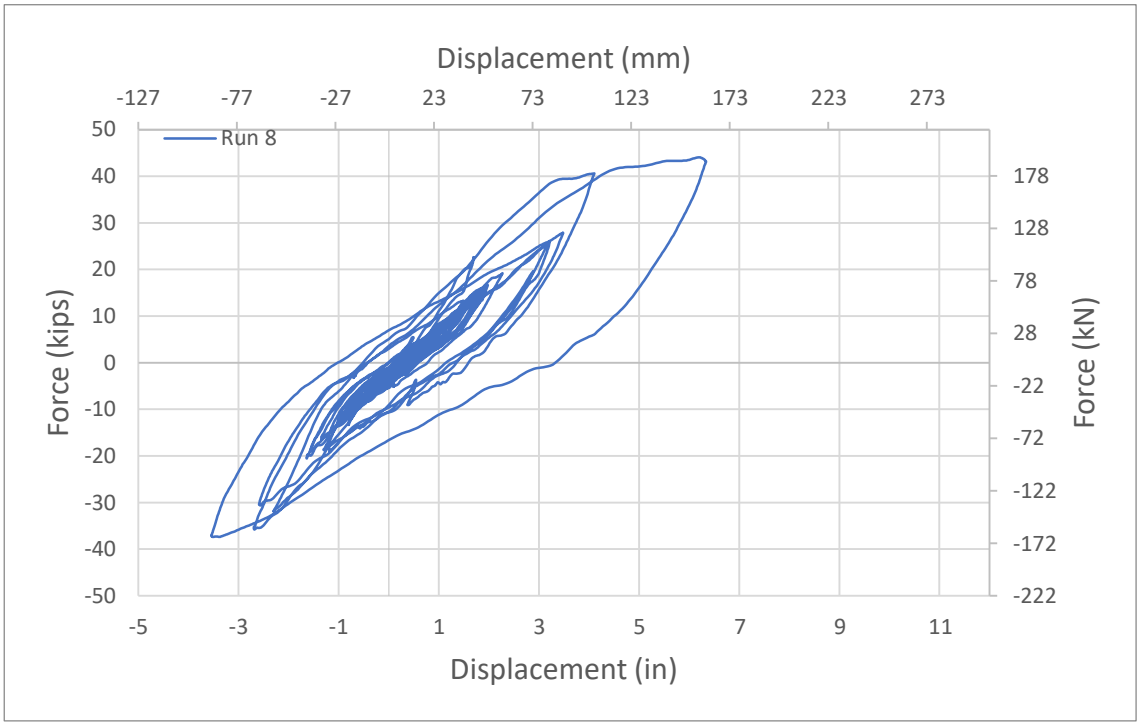

Figure 5.66 Run 8 – Force-displacement relationship

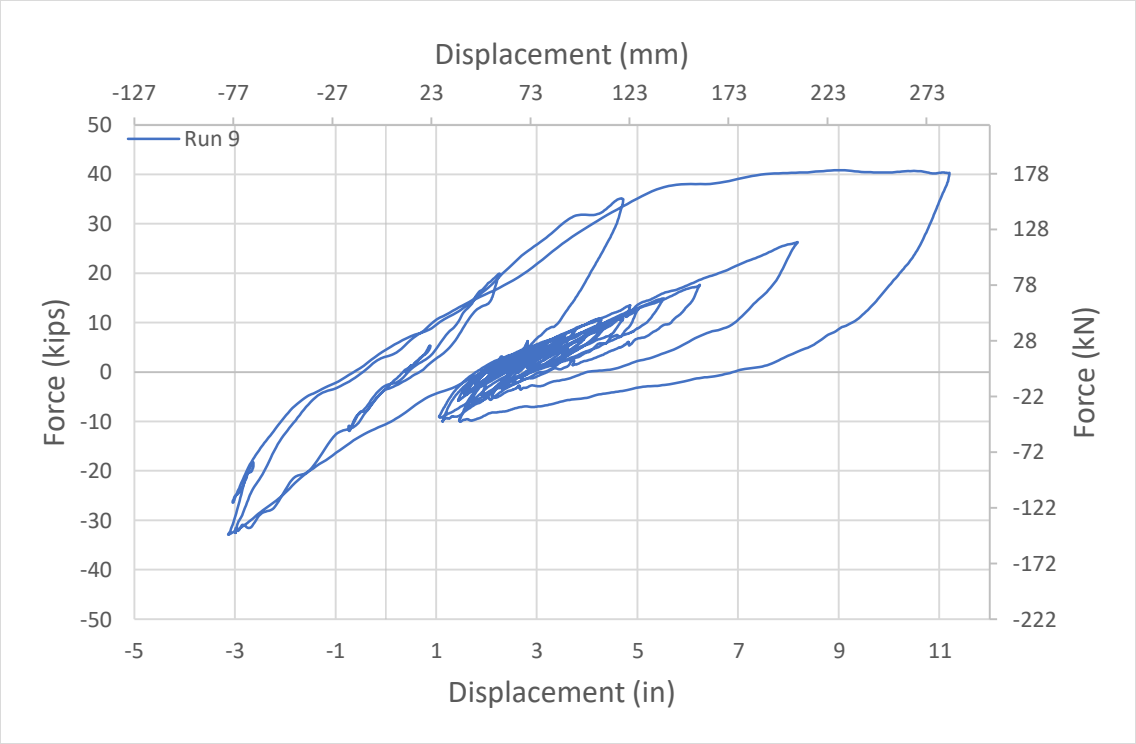

Figure 5.67 Run 9 – Force-displacement relationship

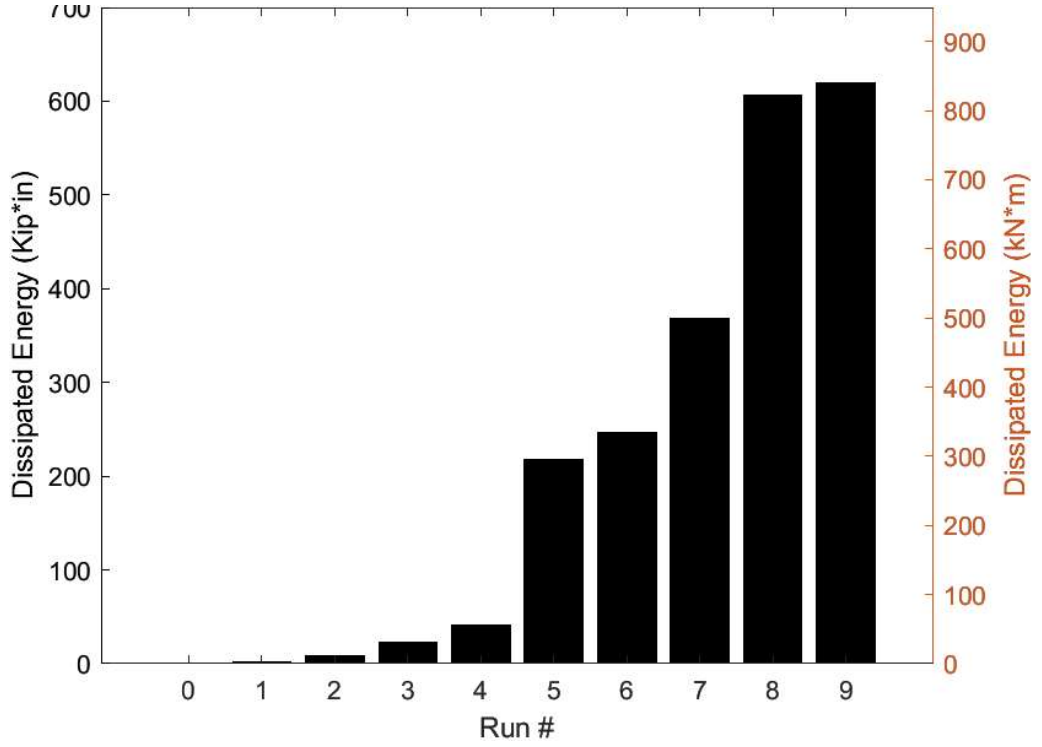

Figure 5.68 Energy dissipation of each run

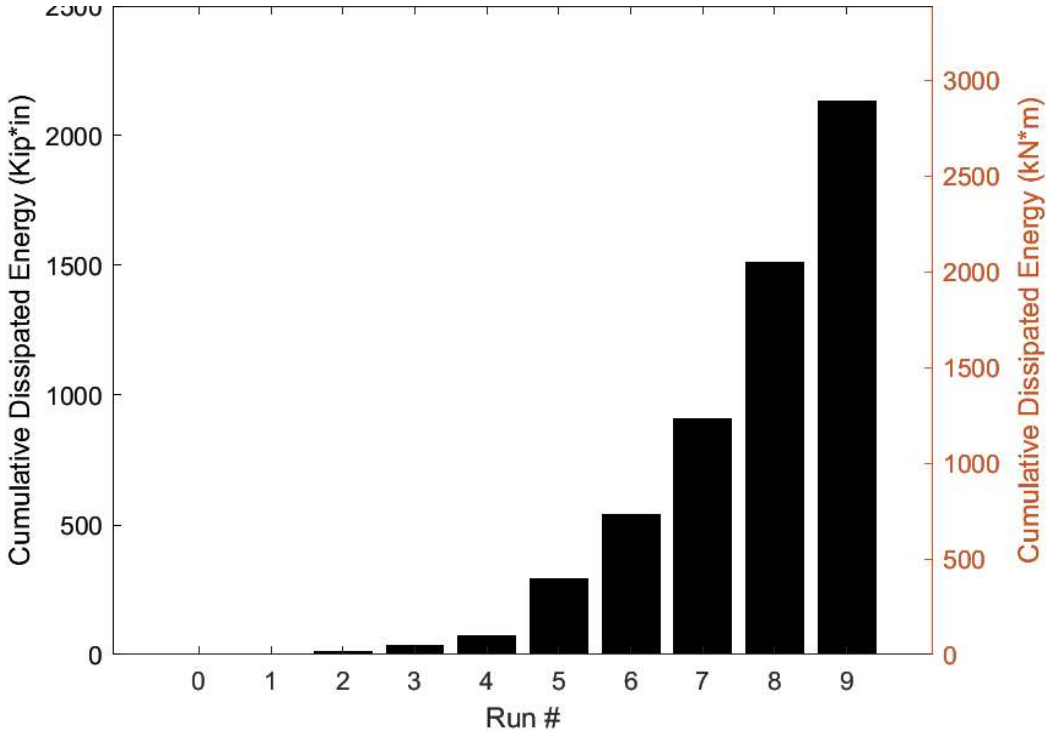

Figure 5.69 Cumulative energy dissipation of each run

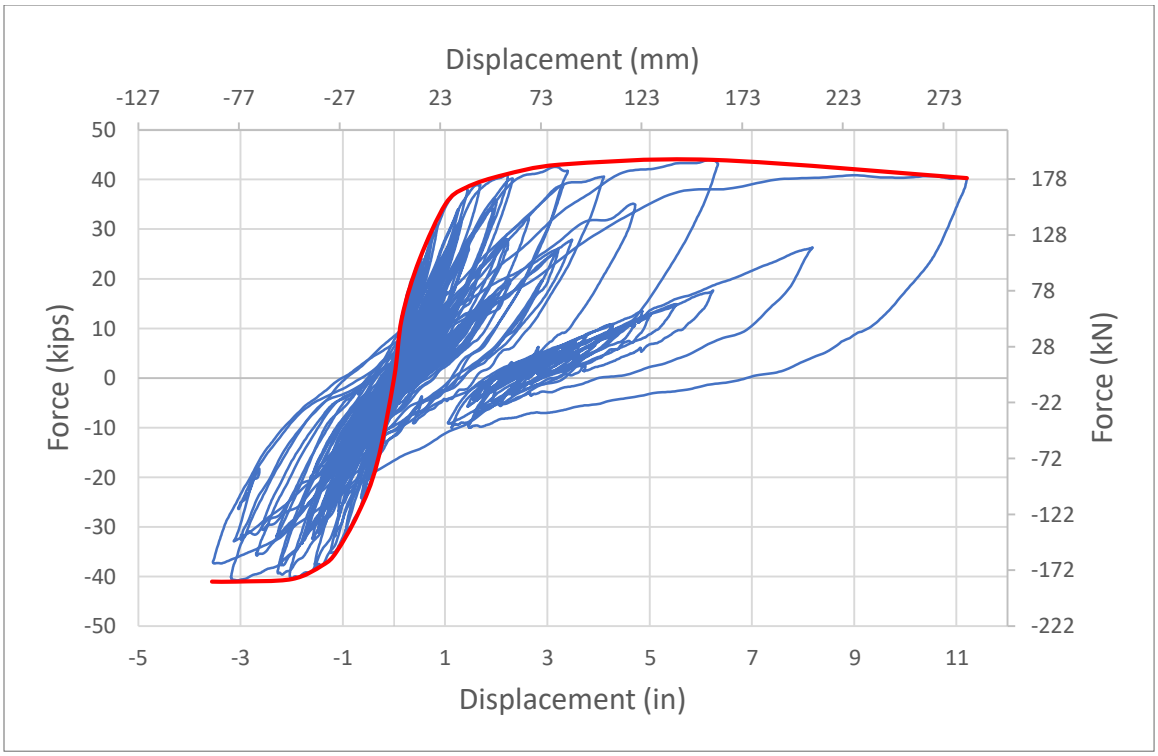

Figure 5.70 Hysteresis envelope for positive and negative sides

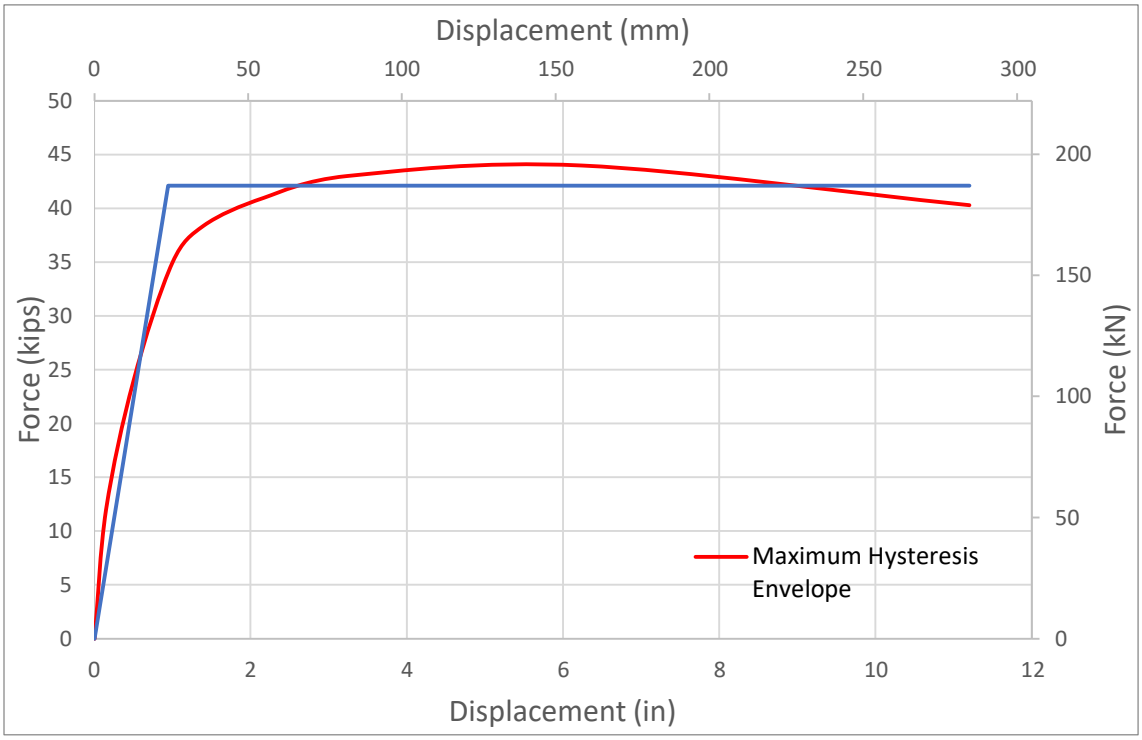

Figure 5.71 Actual and idealized pushover curves

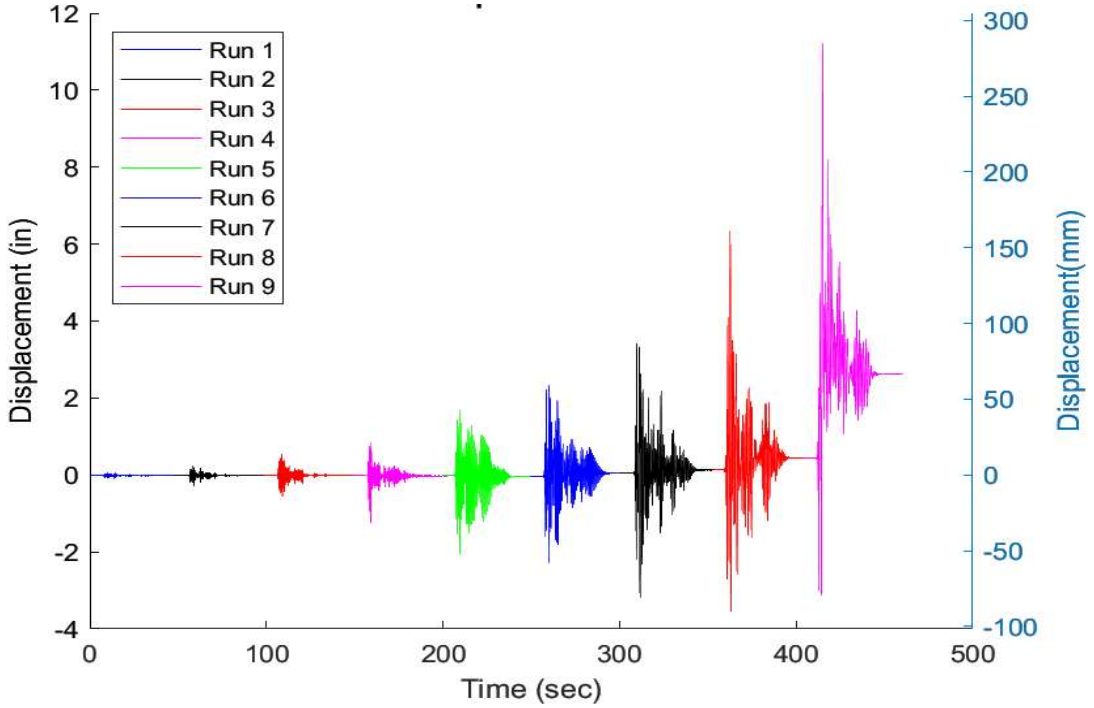

Figure 5.72 Displacement history of all runs

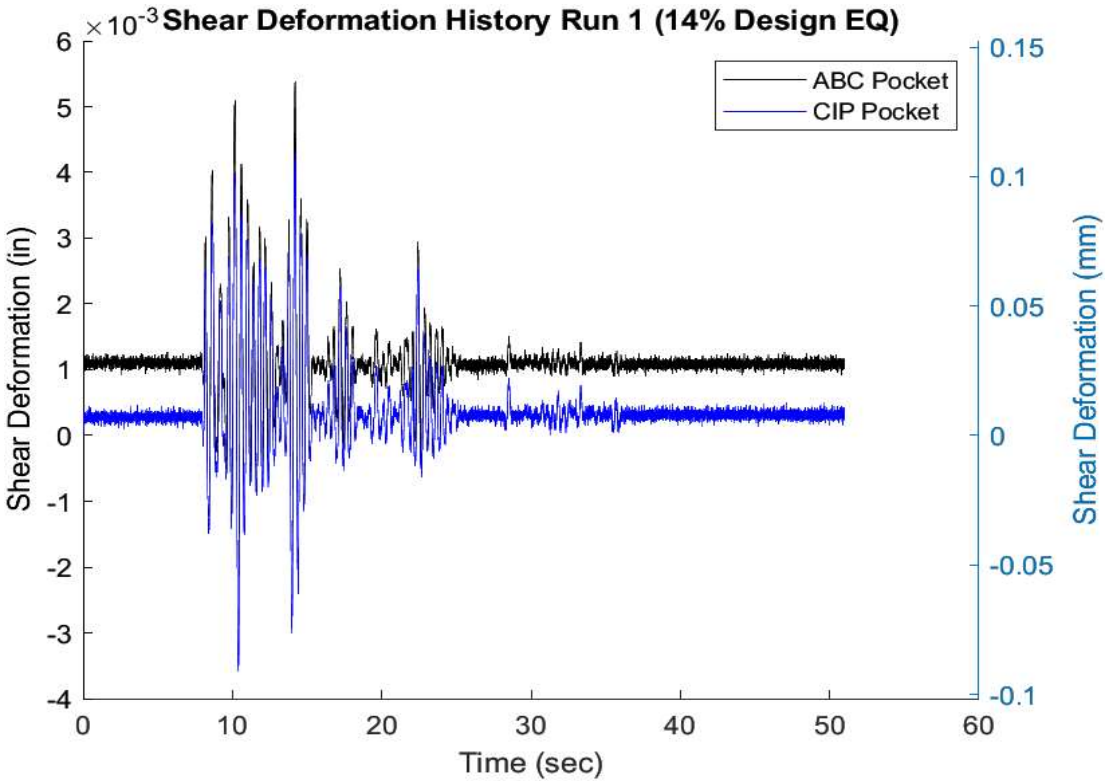

Figure 5.73 Run 1 – Shear deformation history

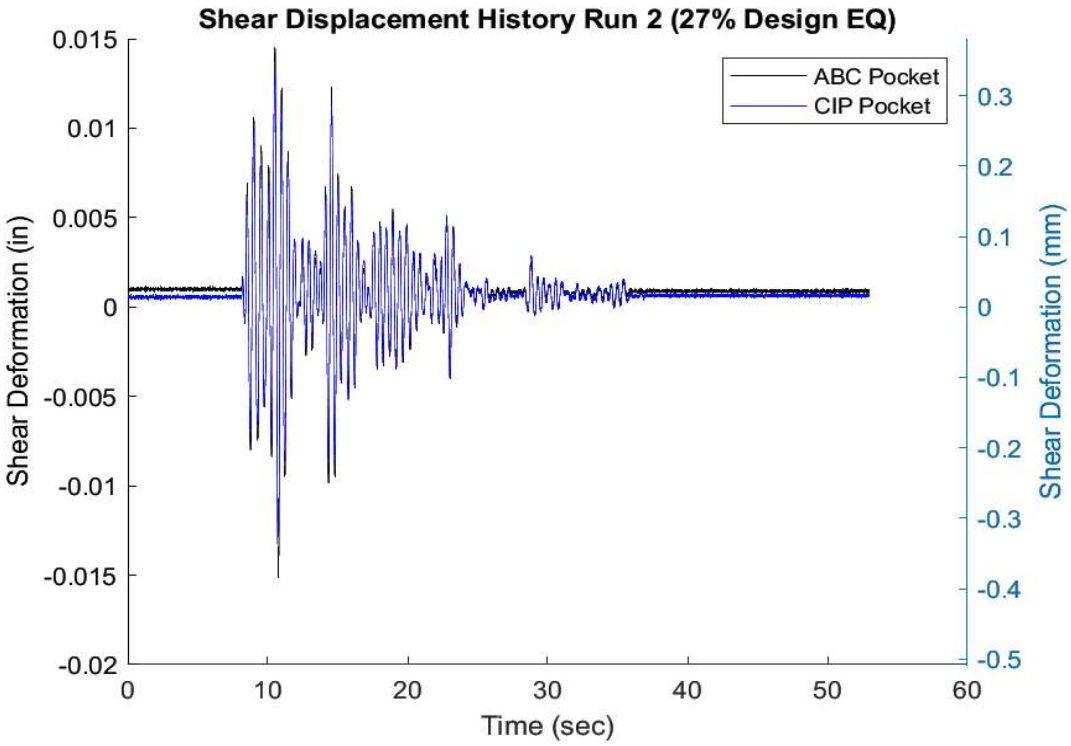

Figure 5.74 Run 2 – Shear deformation history

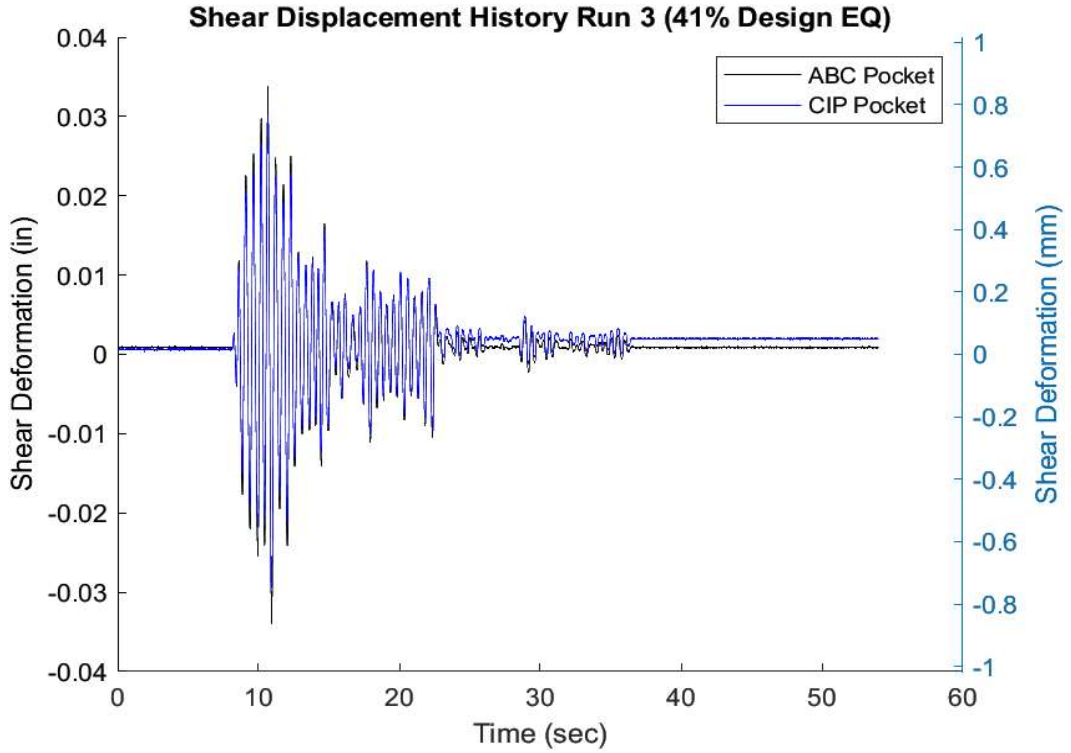

Figure 5.75 Run 3 – Shear deformation history

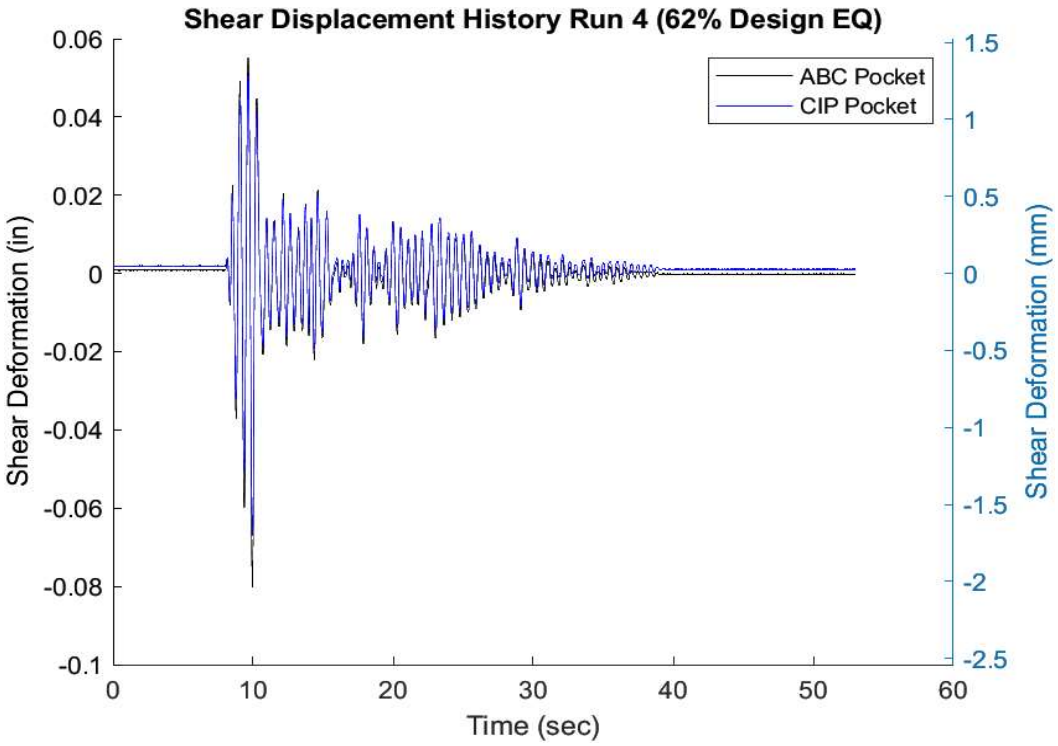

Figure 5.76 Run 4 – Shear deformation history

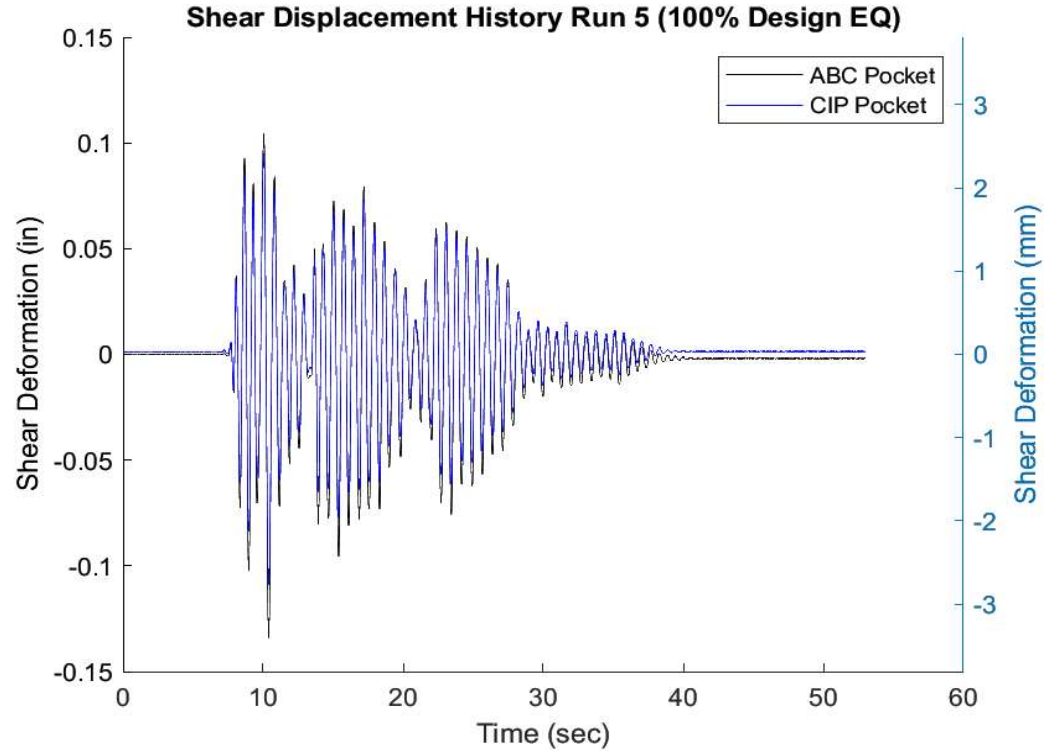

Figure 5.77 Run 5 – Shear deformation history

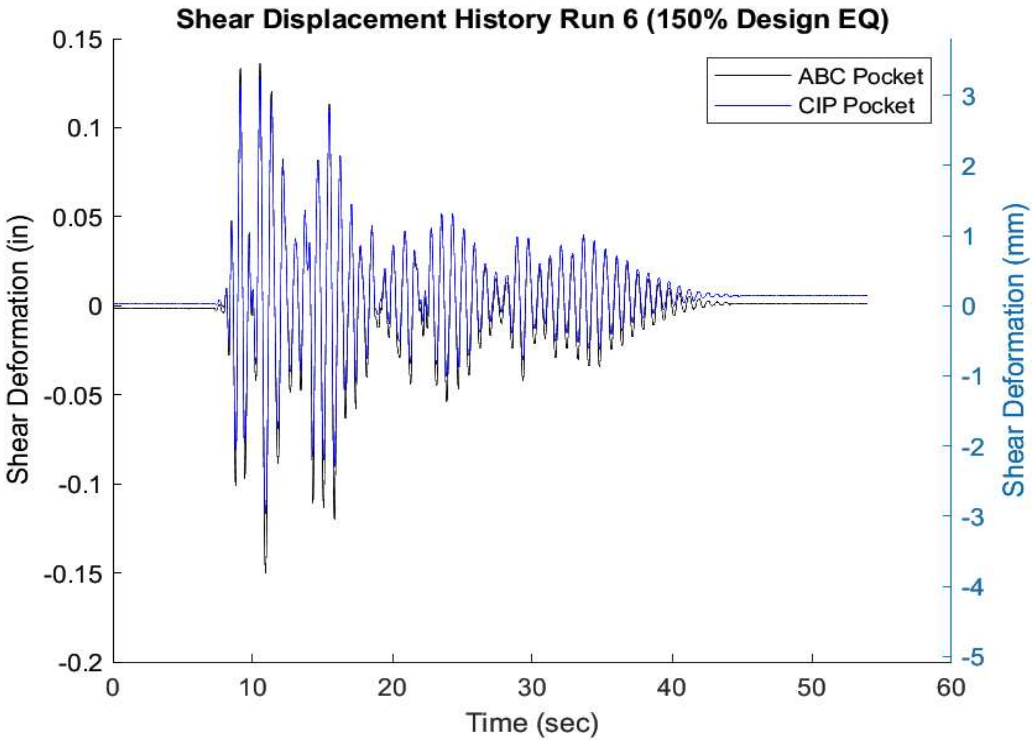

Figure 5.78 Run 6 – Shear deformation history

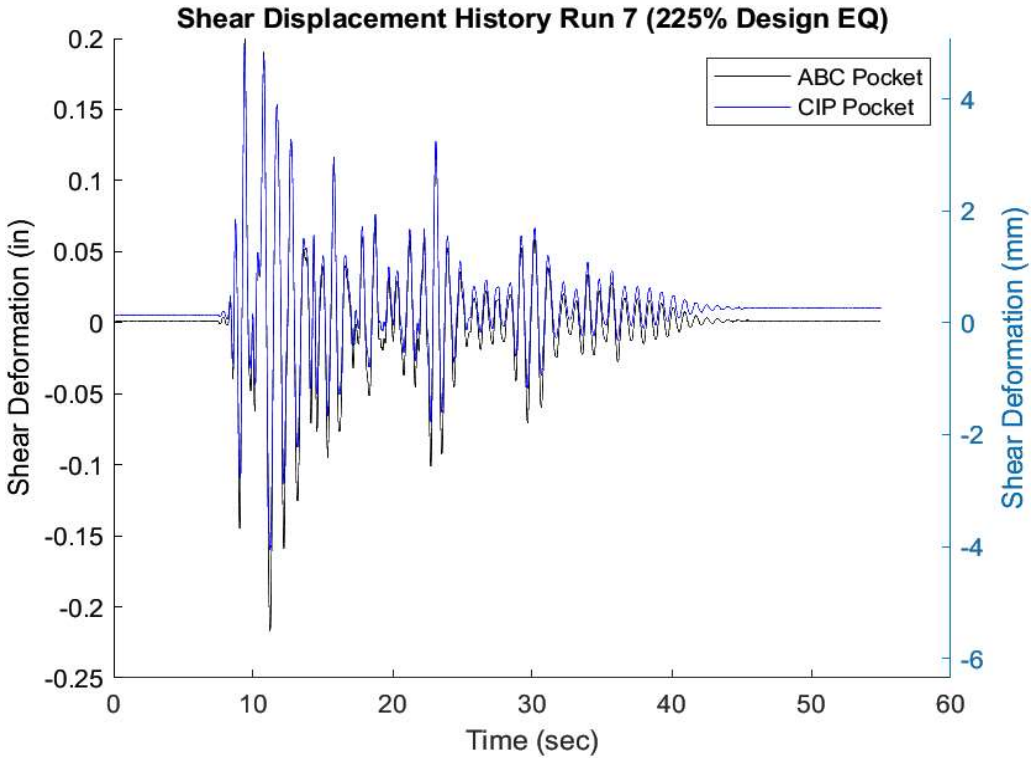

Figure 5.79 Run 7 – Shear deformation history

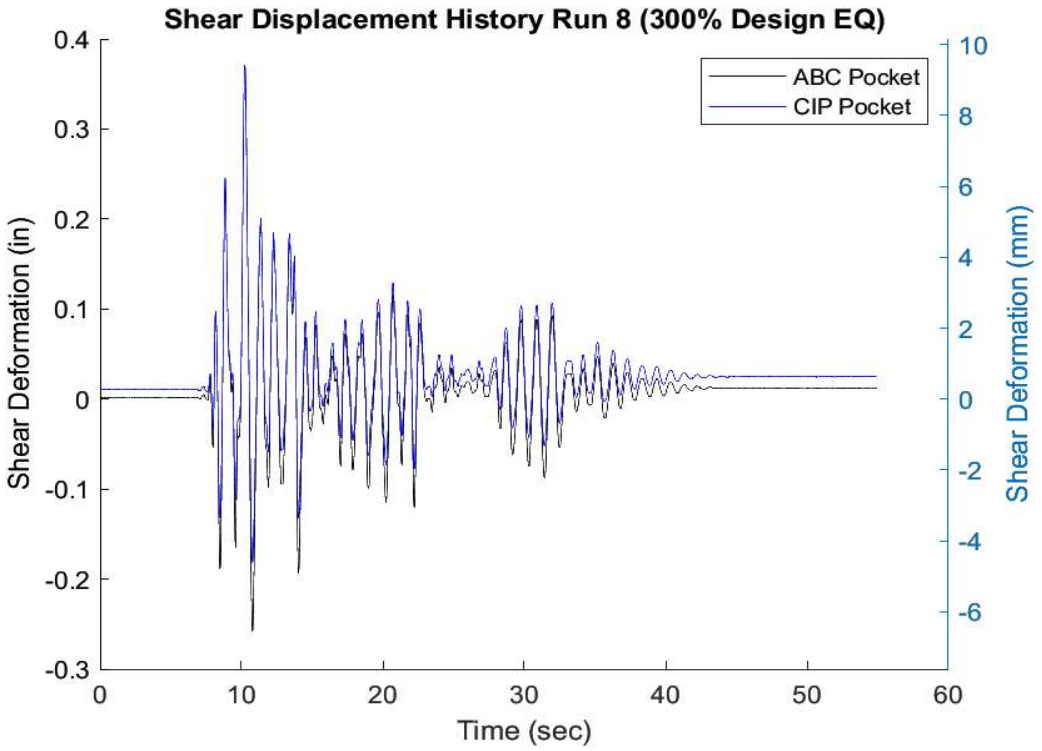

Figure 5.80 Run 8 – Shear deformation history

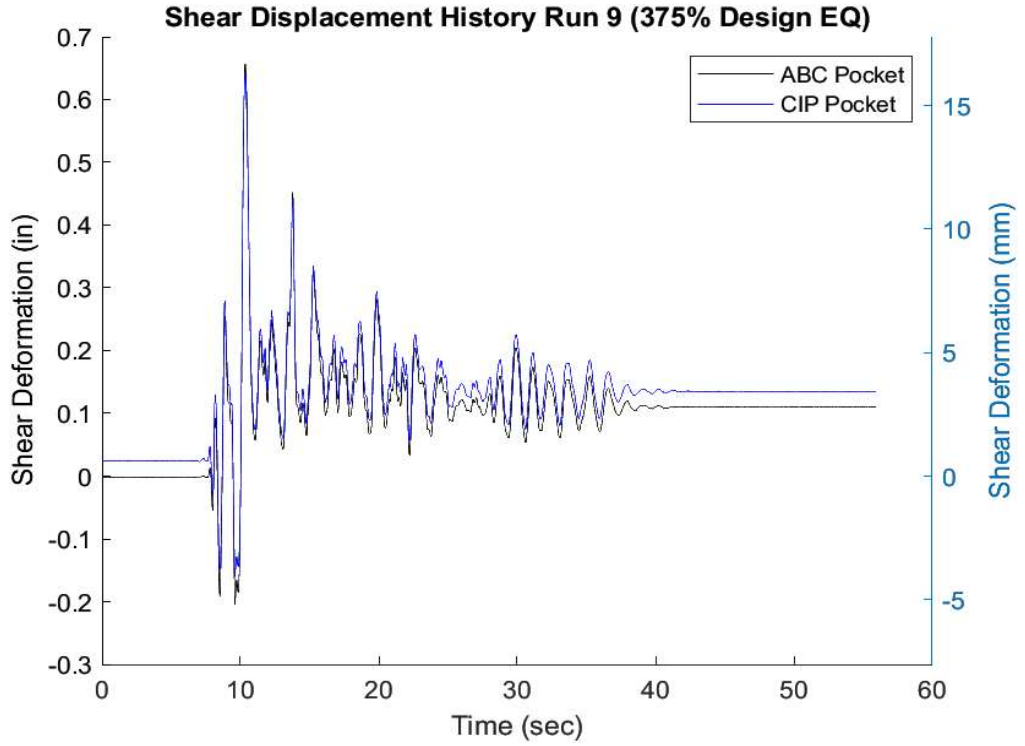

Figure 5.81 Run 9 – Shear deformation history

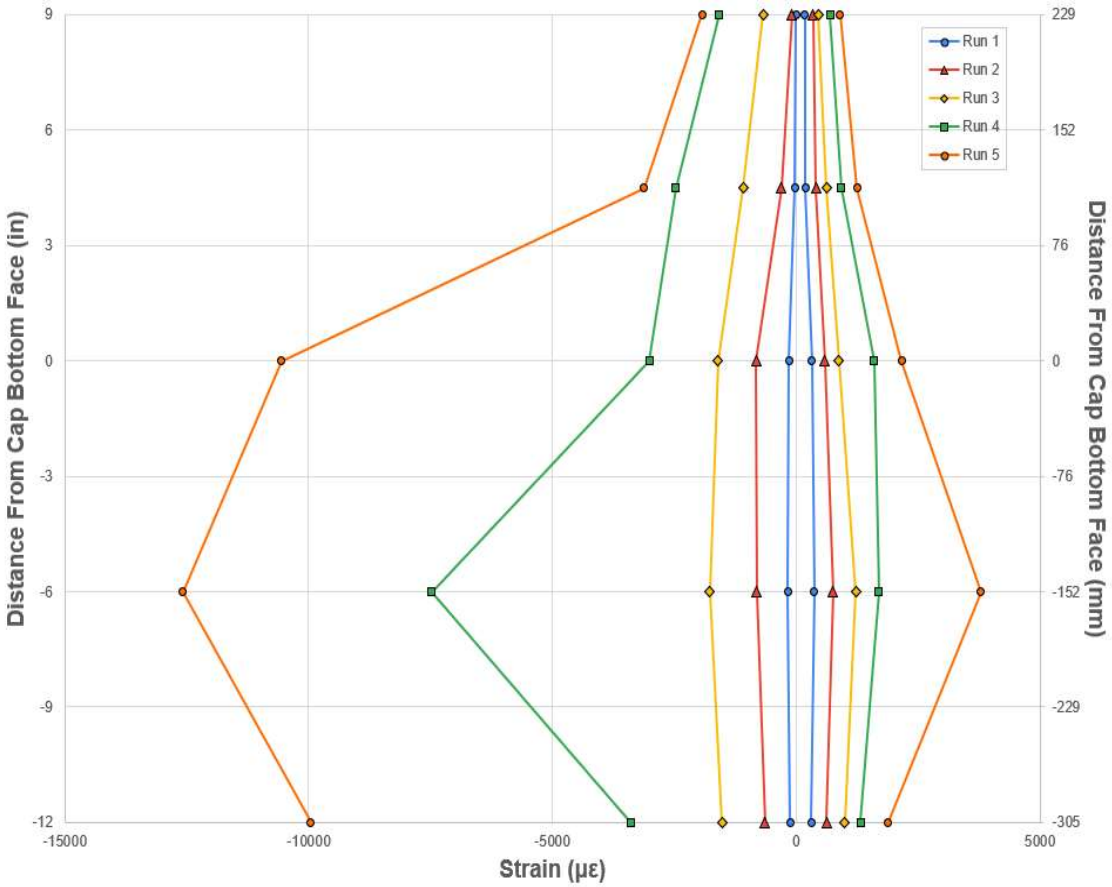

Figure 5.82 Top ABC (south) Column - Strain profile of column longitudinal reinforcement (run 1-5)

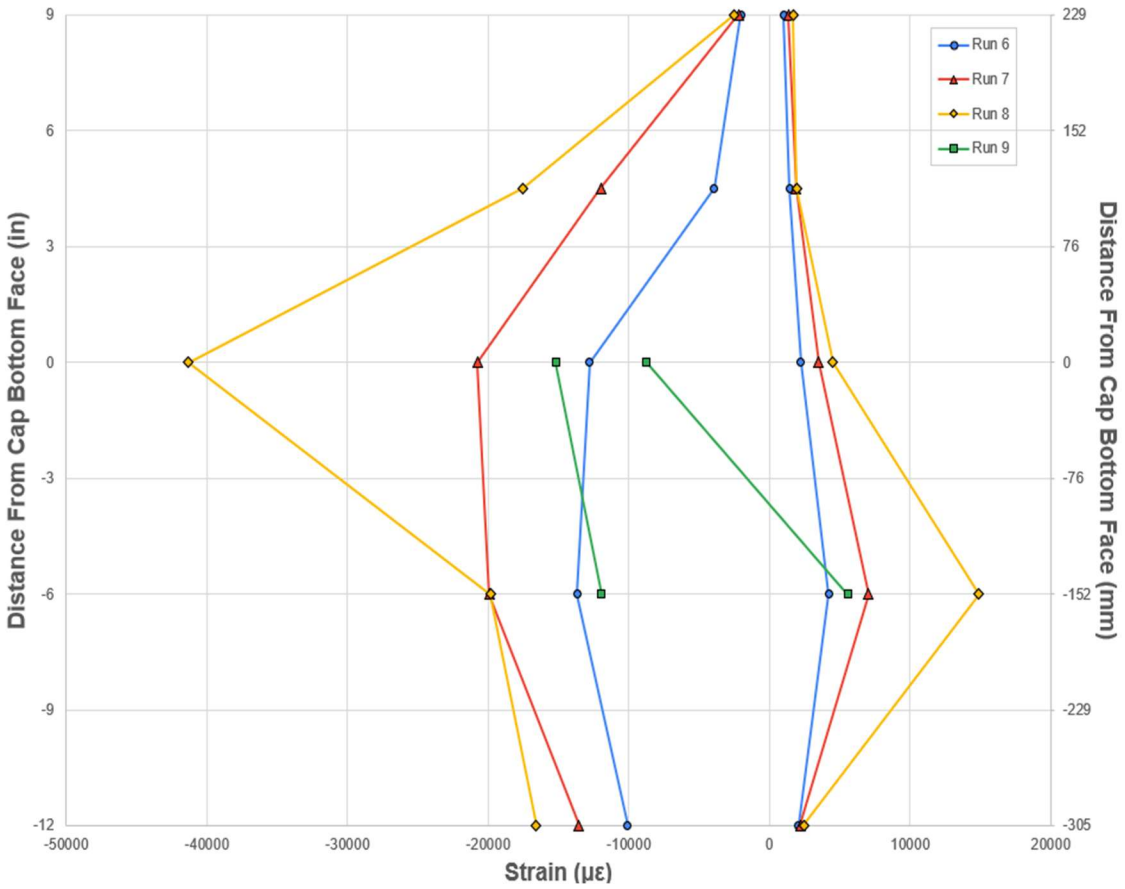

Figure 5.83 Top ABC (south) Column - Strain profile of column longitudinal reinforcement (run 6-9)

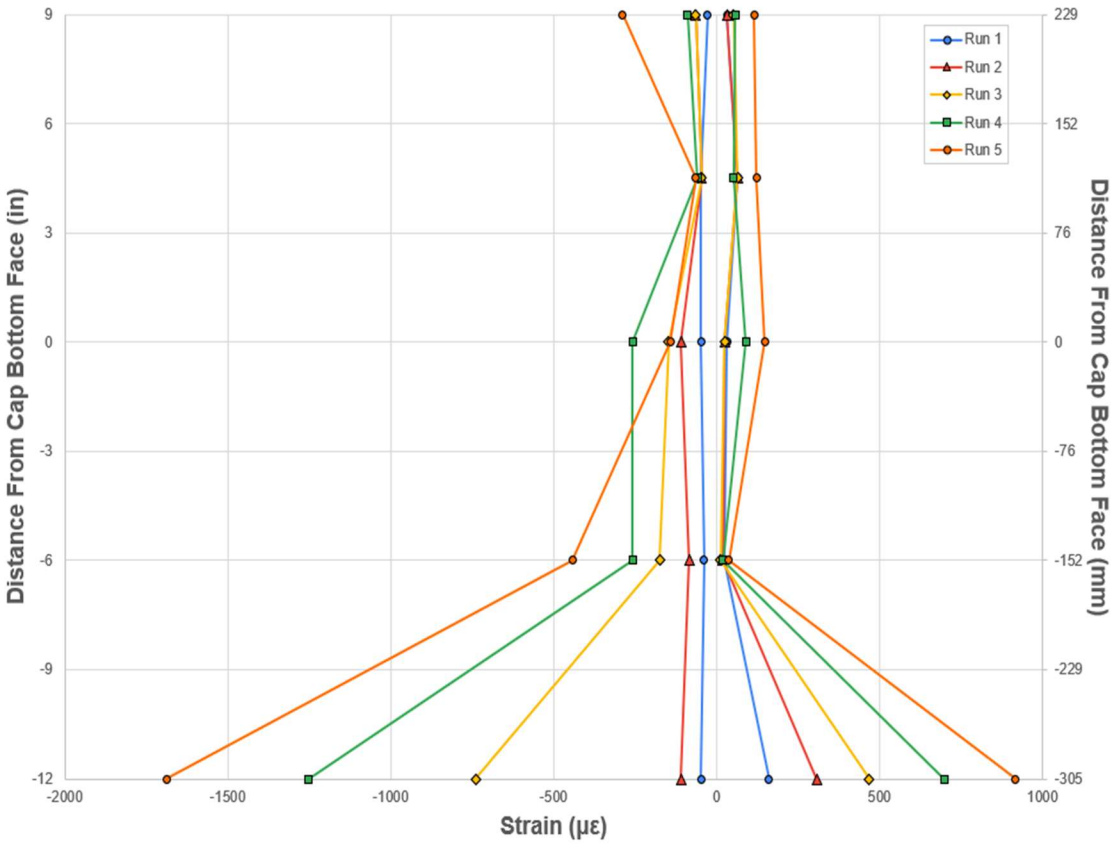

Figure 5.84 Top ABC (south) Column - Strain profile of column spiral reinforcement (run 1-5)

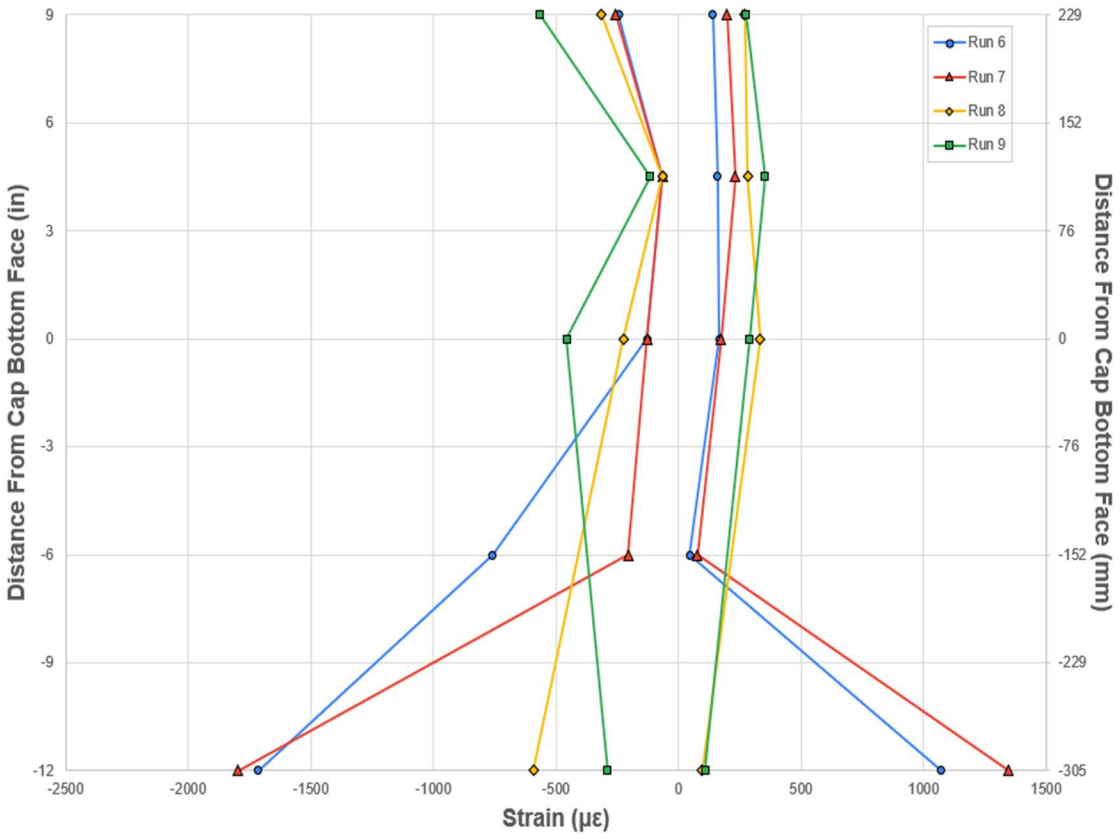

Figure 5.85 Top ABC (south) Column - Strain profile of column spiral reinforcement (run 6-9)

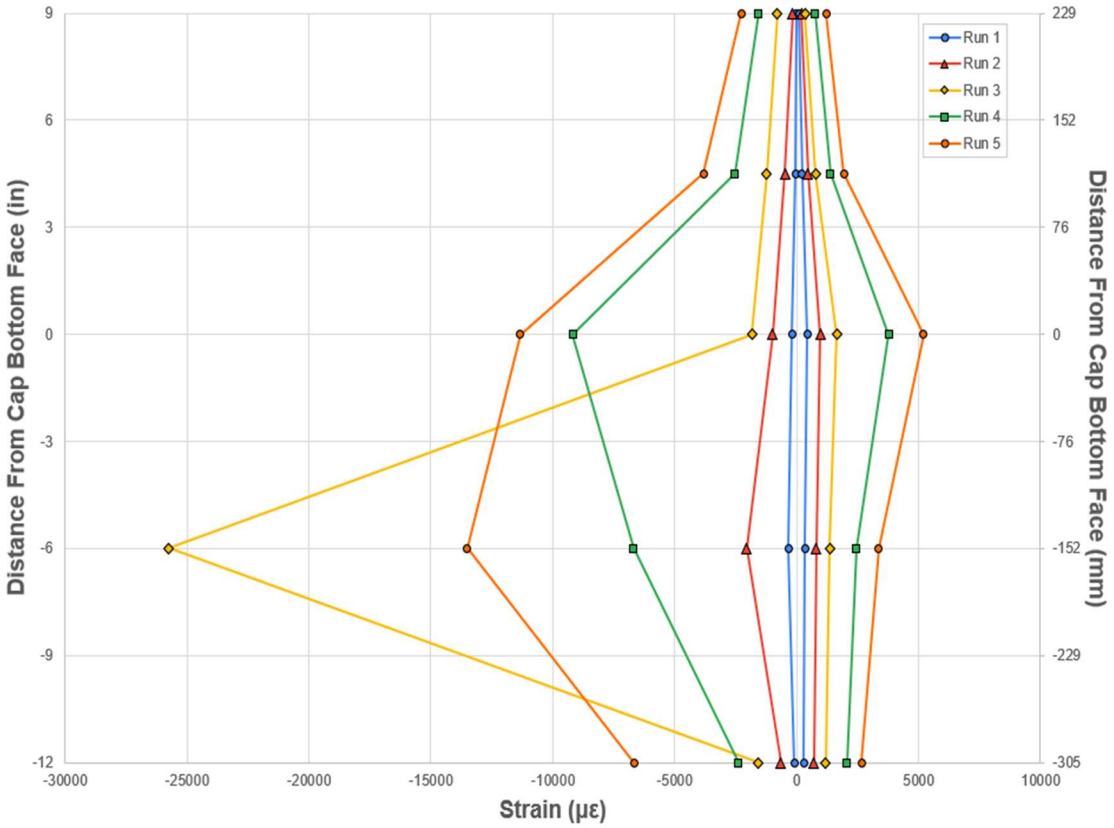

Figure 5.86 Top CIP (north) Column - Strain profile of column longitudinal reinforcement (run 1-5)

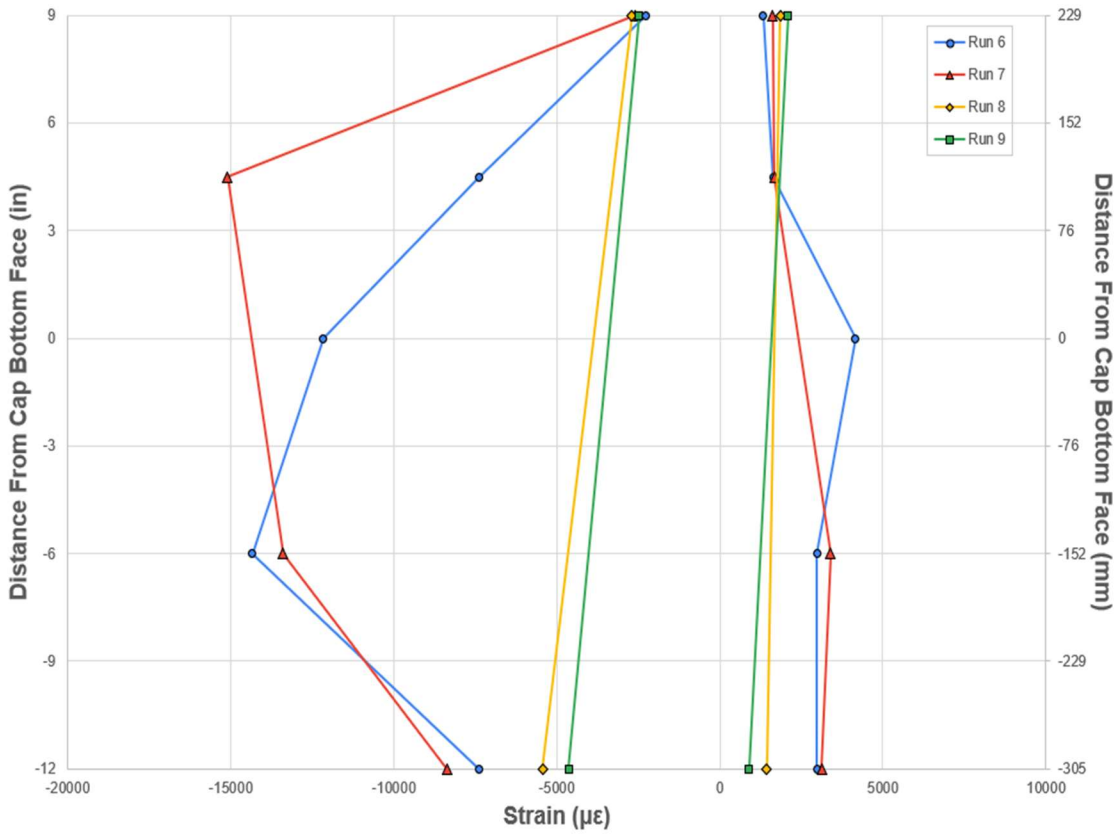

Figure 5.87 Top CIP (north) Column - Strain profile of column longitudinal reinforcement (run 6-9)

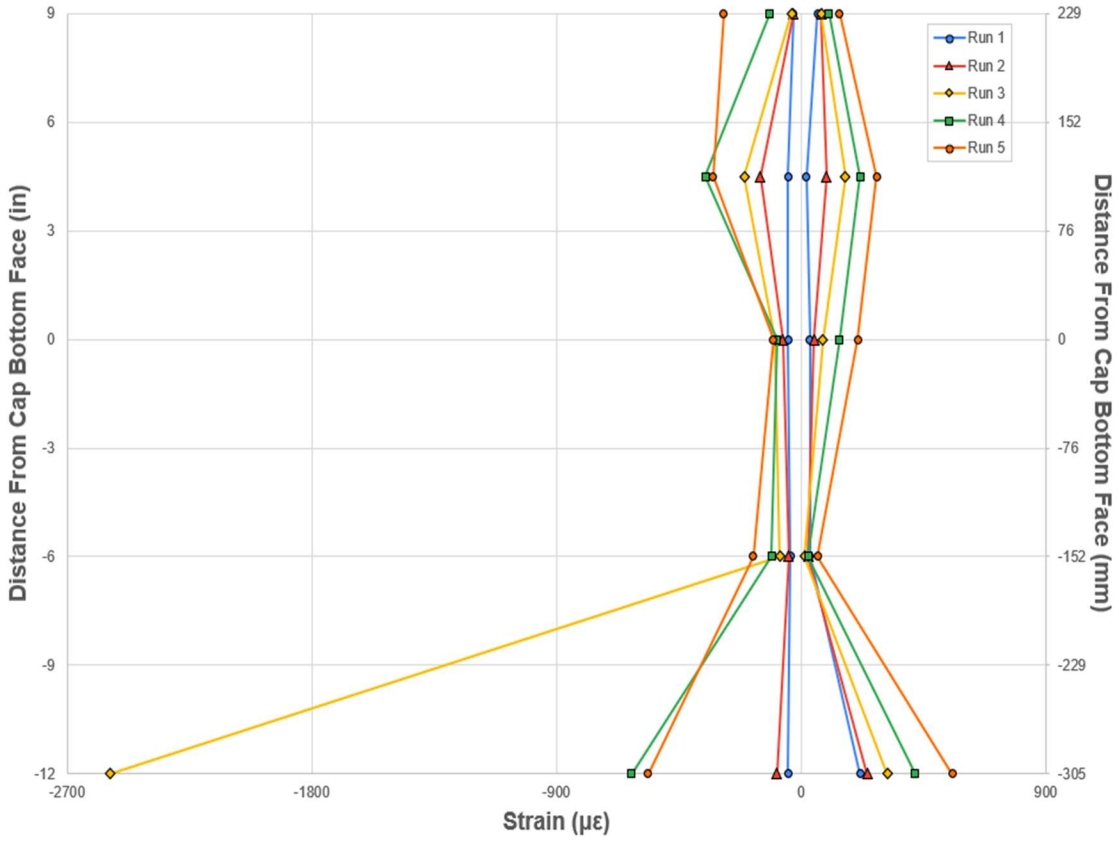

Figure 5.88 Top CIP (north) Column - Strain profile of column spiral reinforcement (run 1-5)

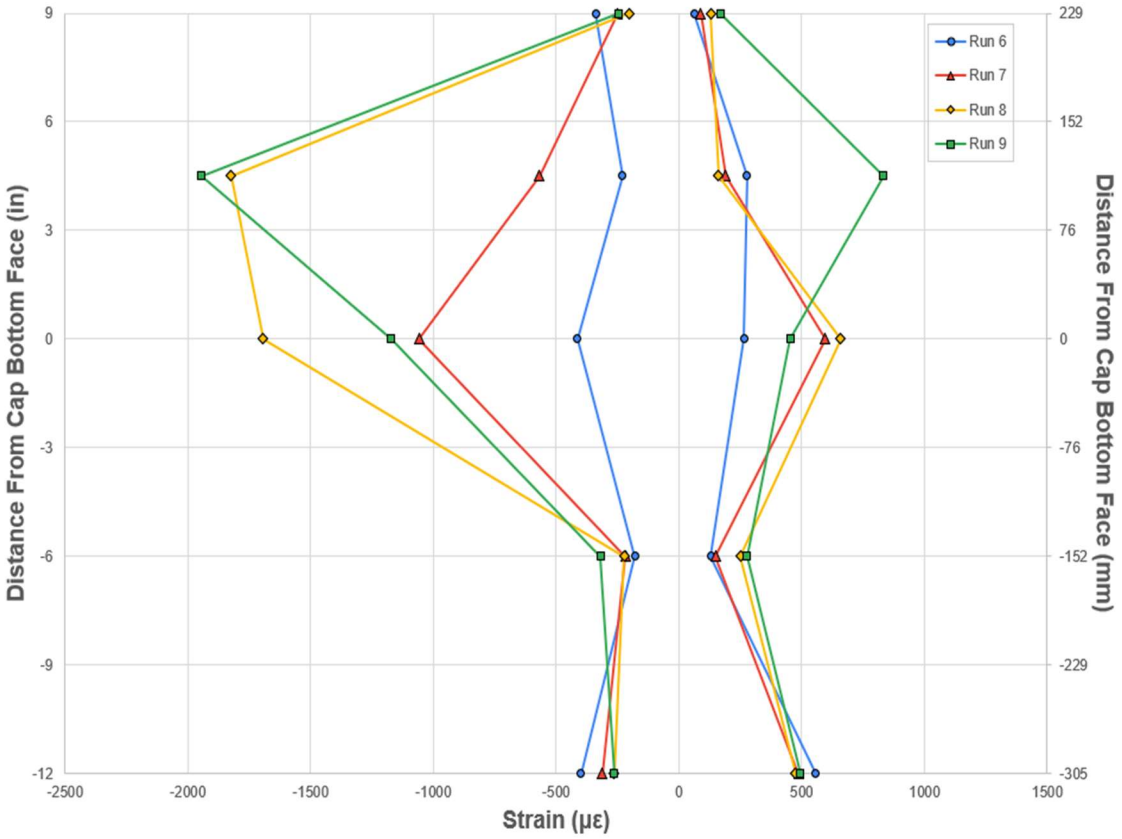

Figure 5.89 Top CIP (north) Column - Strain profile of column spiral reinforcement (run 6-9)

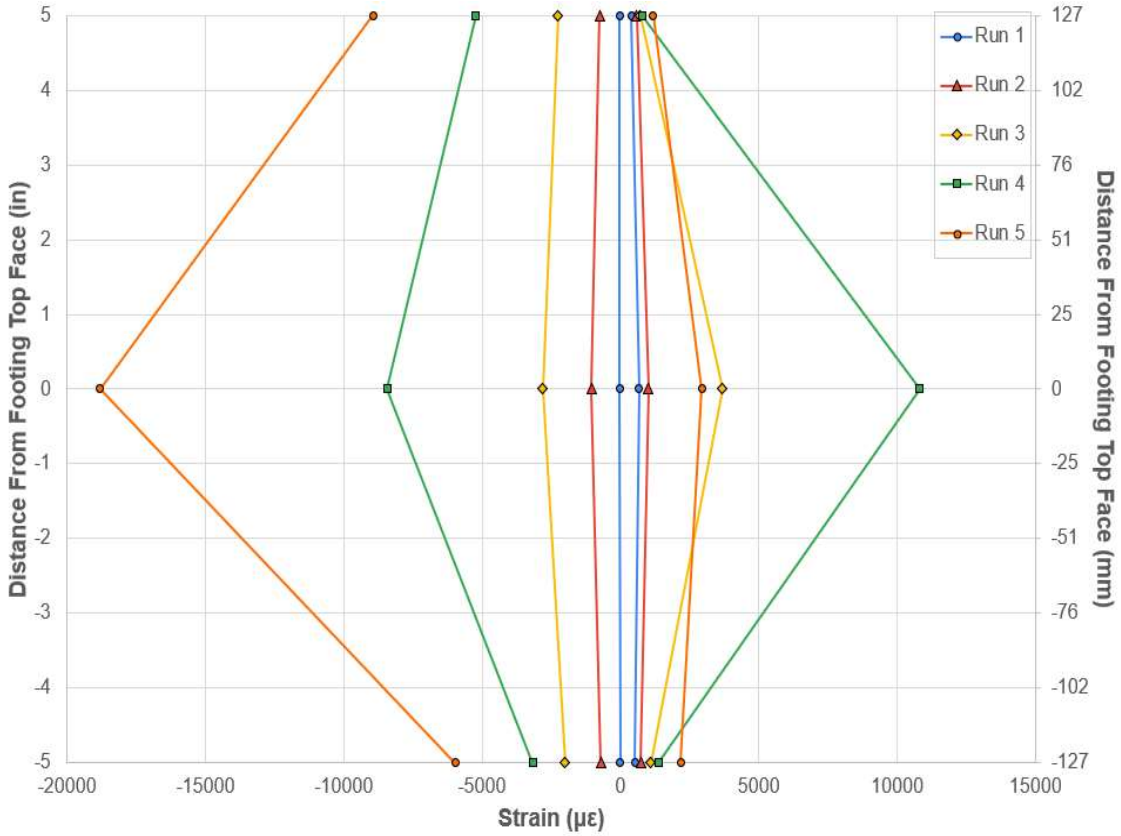

Figure 5.90 Bot ABC (south) Column - Strain profile of hinge longitudinal reinforcement (CAM) (run 1-5)

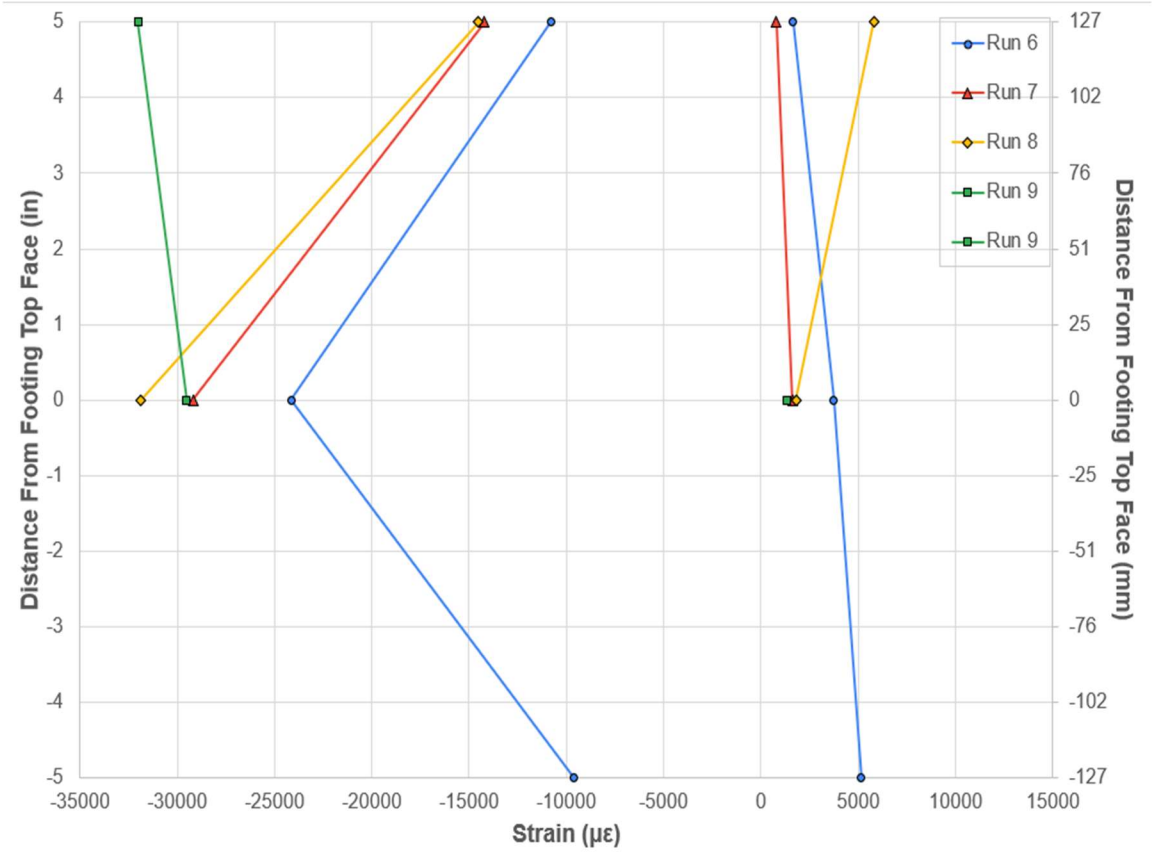

Figure 5.91 Bot ABC (south) Column - Strain profile of hinge longitudinal reinforcement (CAM) (run 6-9)

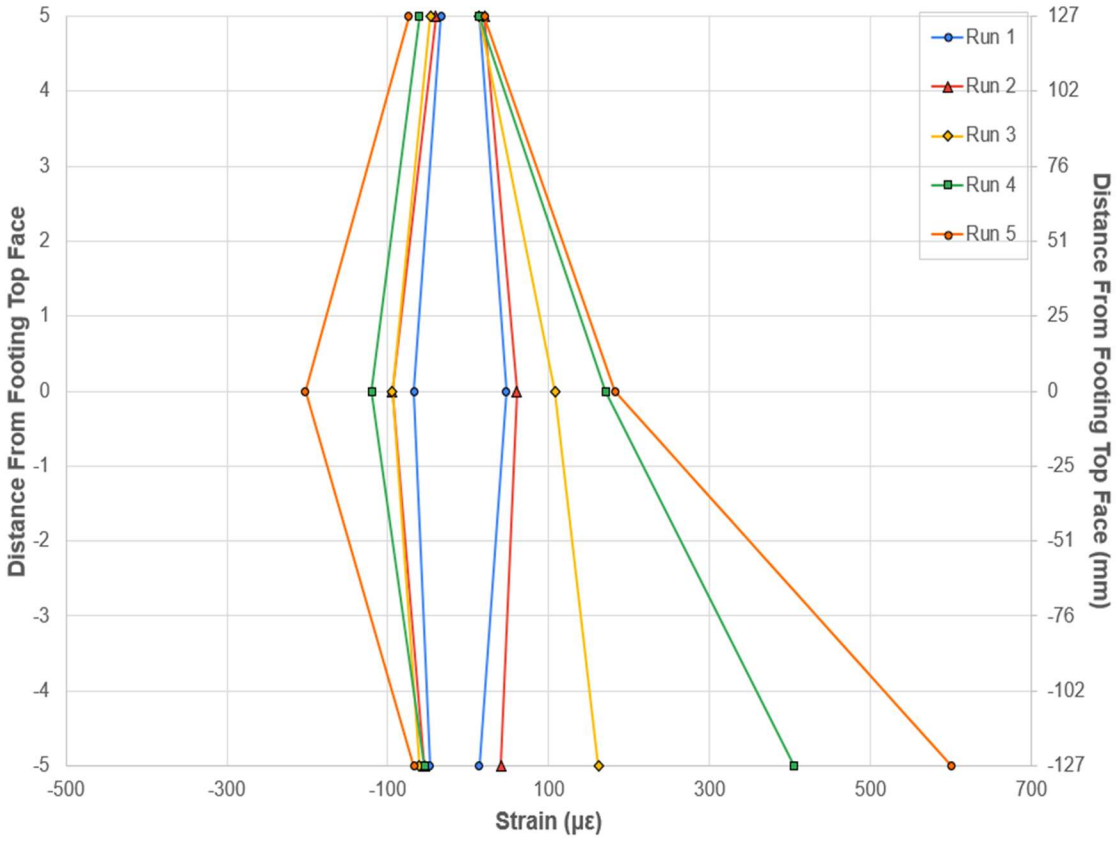

Figure 5.92 Bot ABC (south) Column - Strain profile of hinge spiral reinforcement (run 1-5)

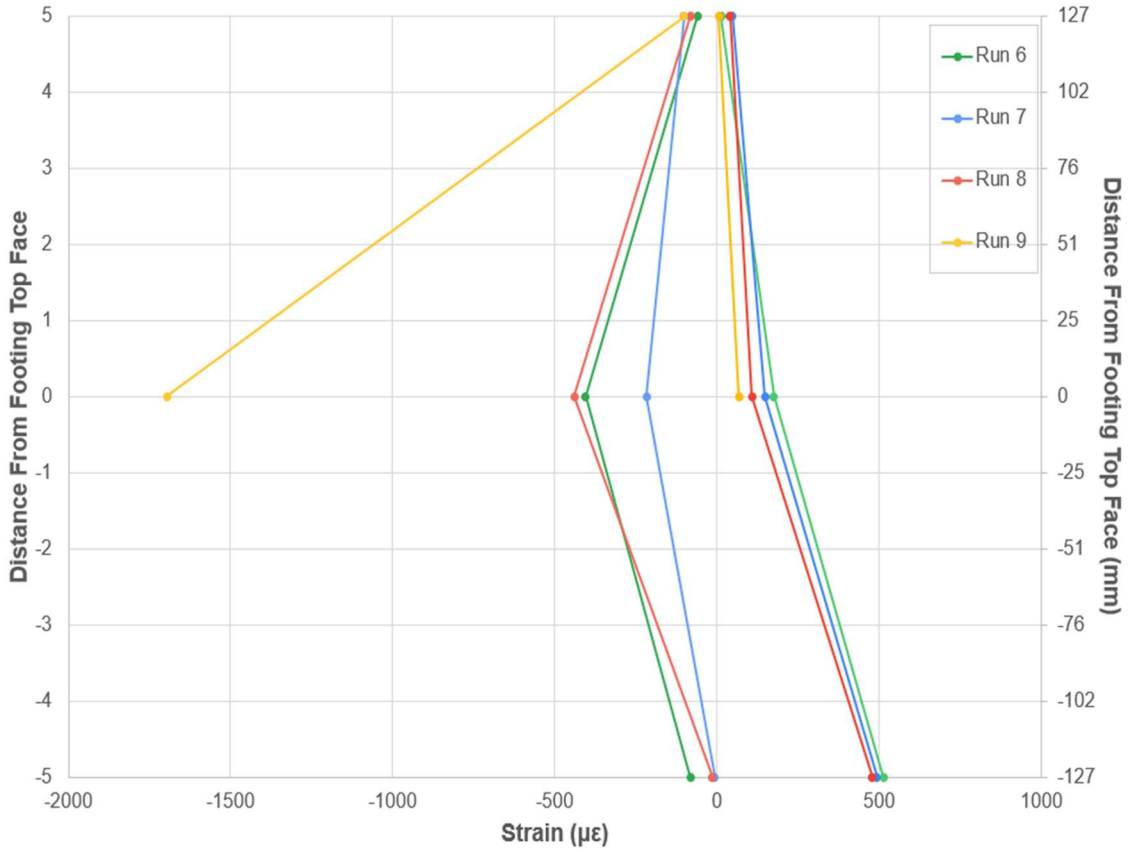

Figure 5.93 Bot ABC (south) Column - Strain profile of hinge spiral reinforcement (run 6-9)

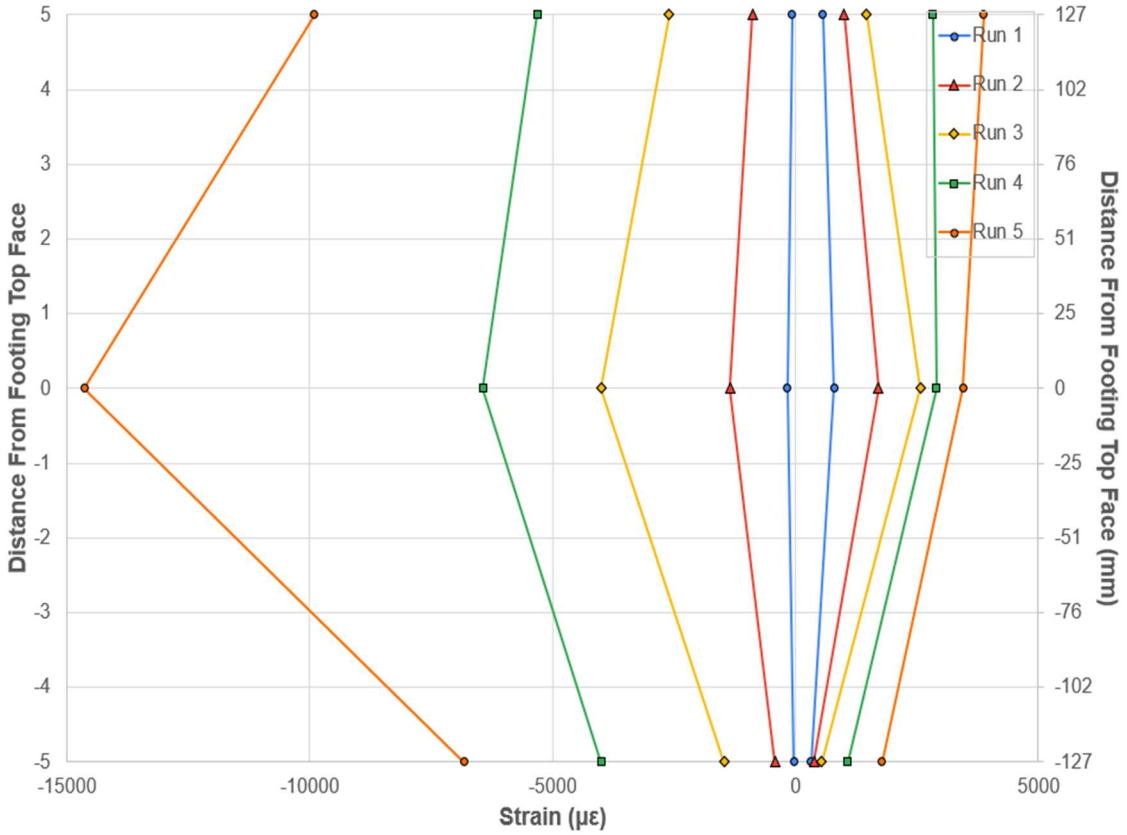

Figure 5.94 Bot CIP (north) Column - Strain profile of hinge longitudinal reinforcement (CAM) (run 1-5)

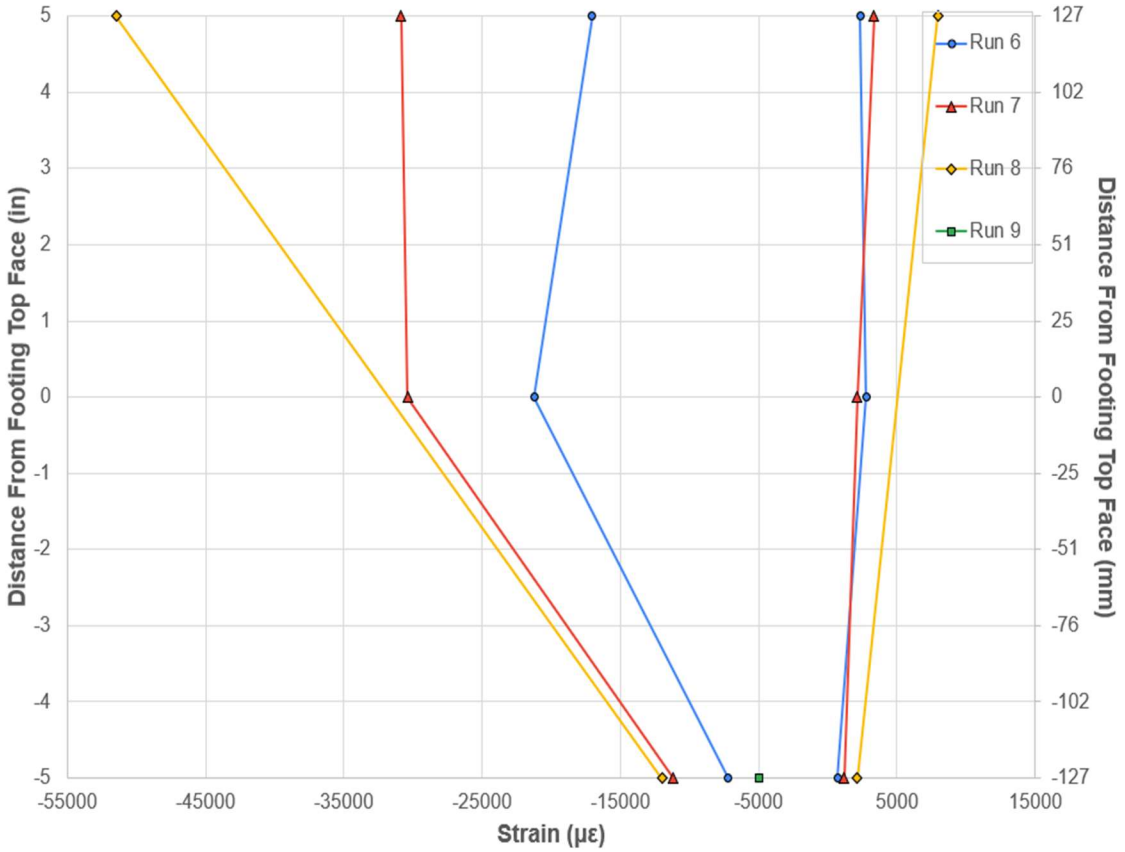

Figure 5.95 Bot CIP (north) Column - Strain profile of hinge longitudinal reinforcement (CAM) (run 6-9)

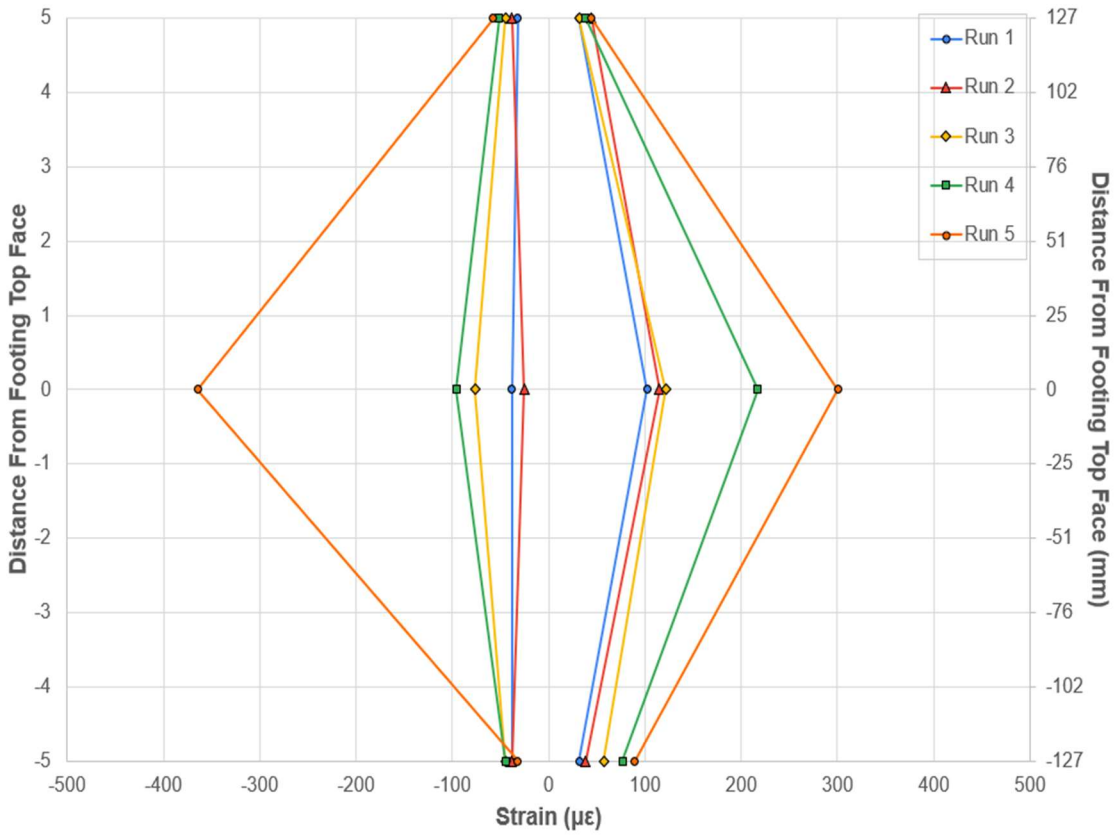

Figure 5.96 Bot CIP (north) Column - Strain profile of hinge spiral reinforcement (run 1-5)

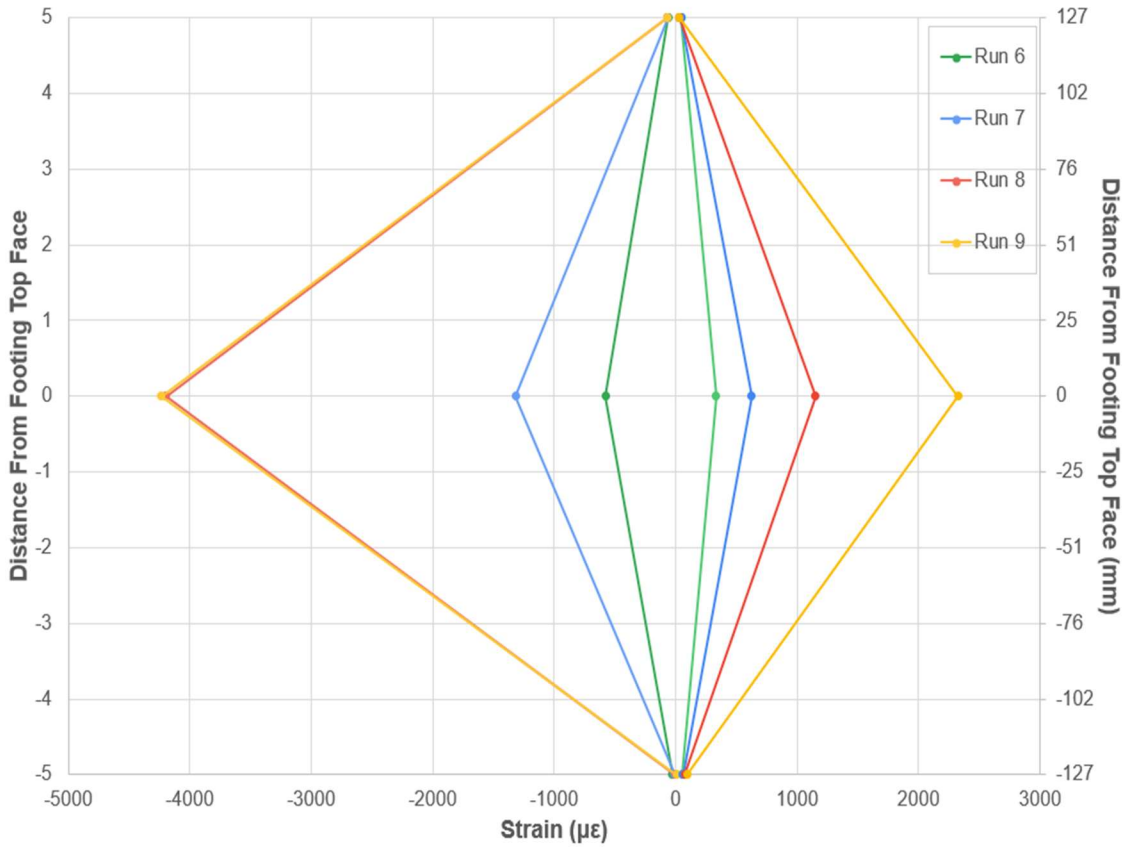

Figure 5.97 Bot CIP (north) Column - Strain profile of hinge spiral reinforcement (run 6-9)

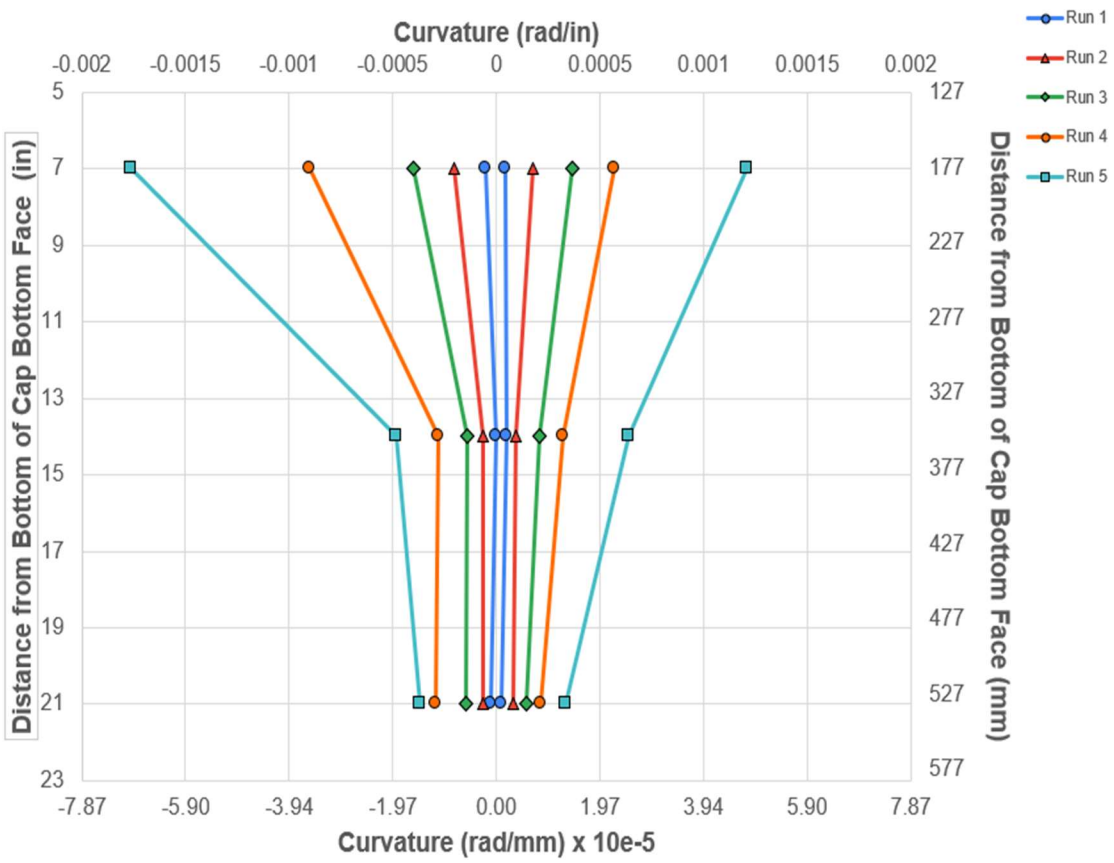

Figure 5.98 Top ABC (south) Column - Curvature profile (run 1-5)

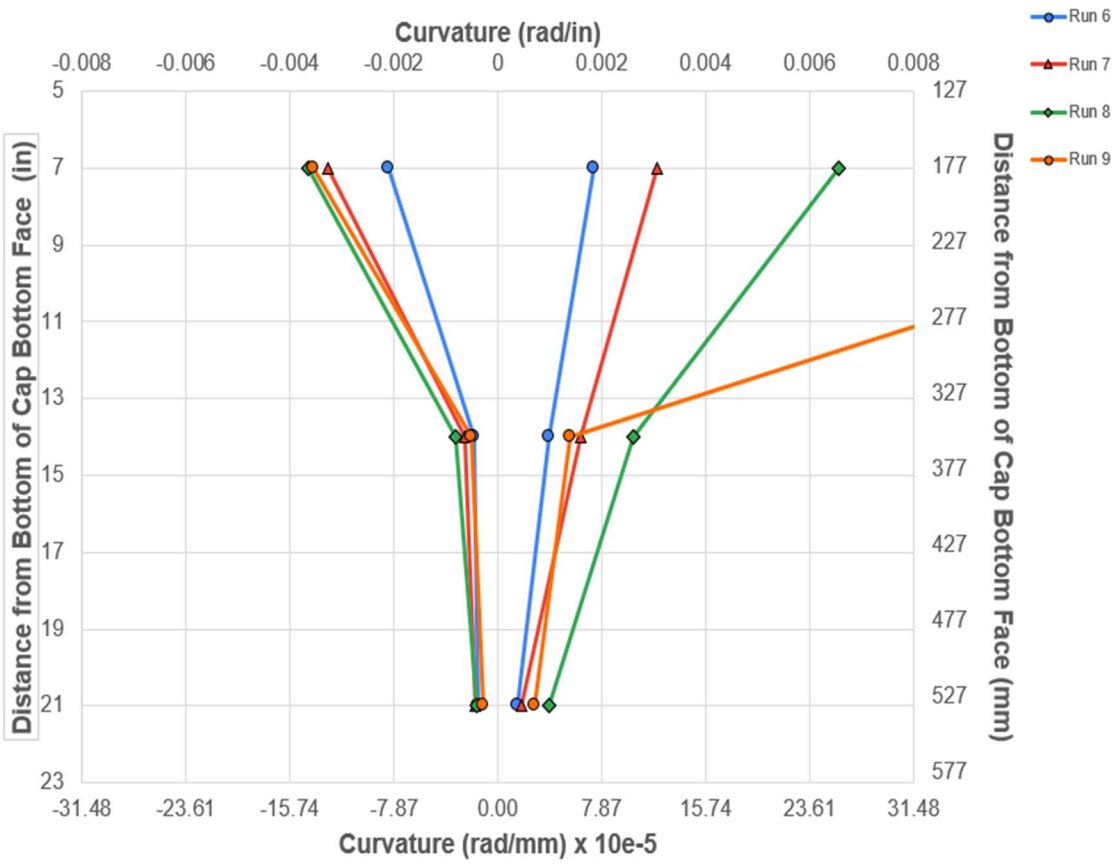

Figure 5.99 Top ABC (south) Column - Curvature profile (run 6-9)

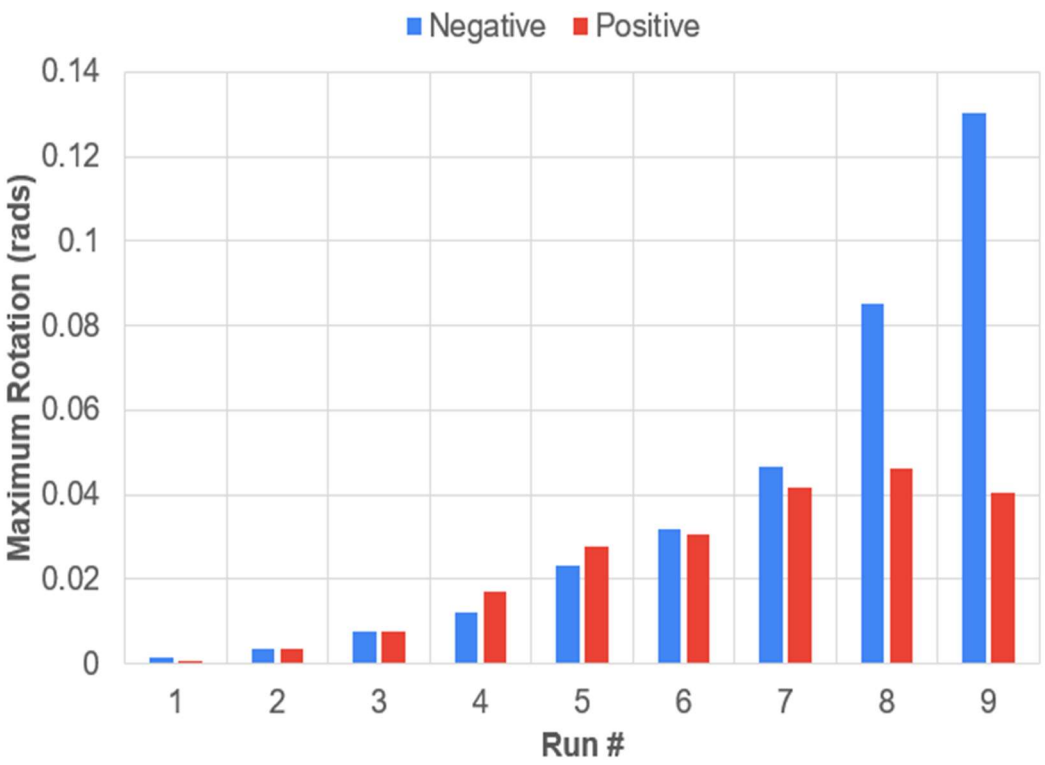

Figure 5.100 ABC (south) Column – Maximum and minimum rotations of the base (run 1-9)

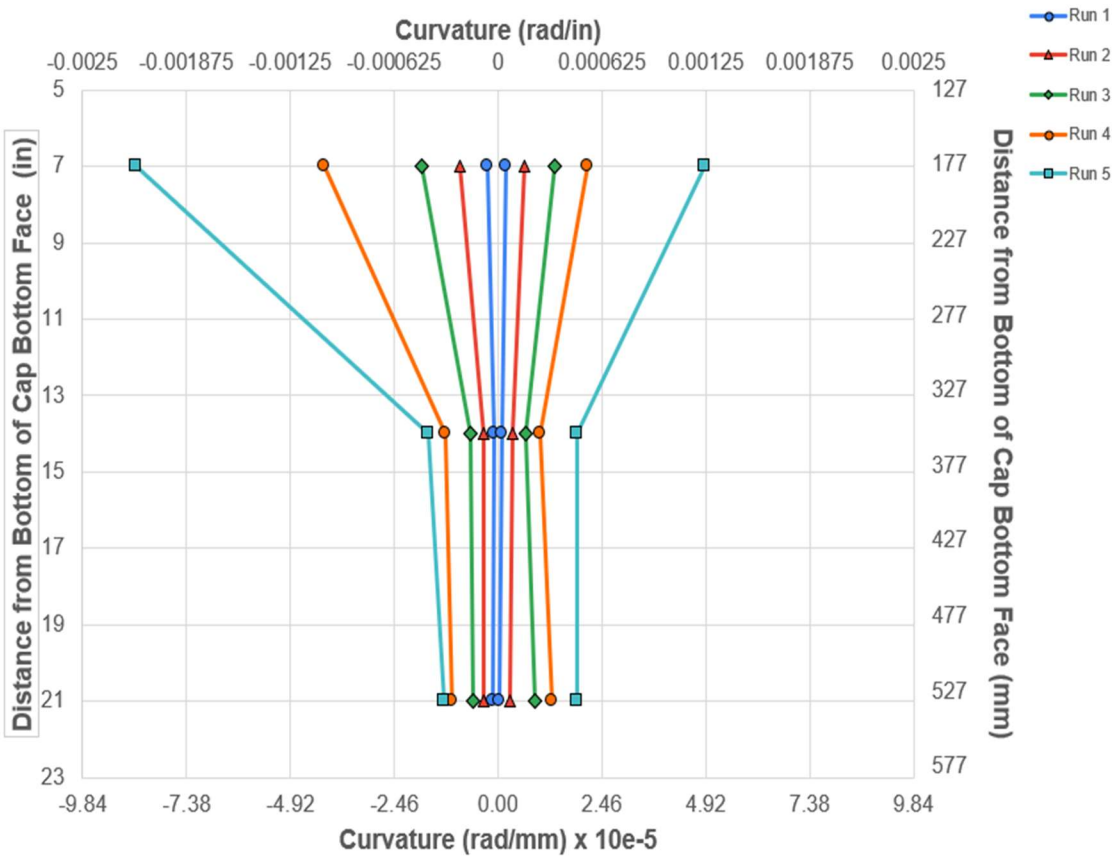

Figure 5.101 Top CIP (north) Column - Curvature profile (run 1-5)

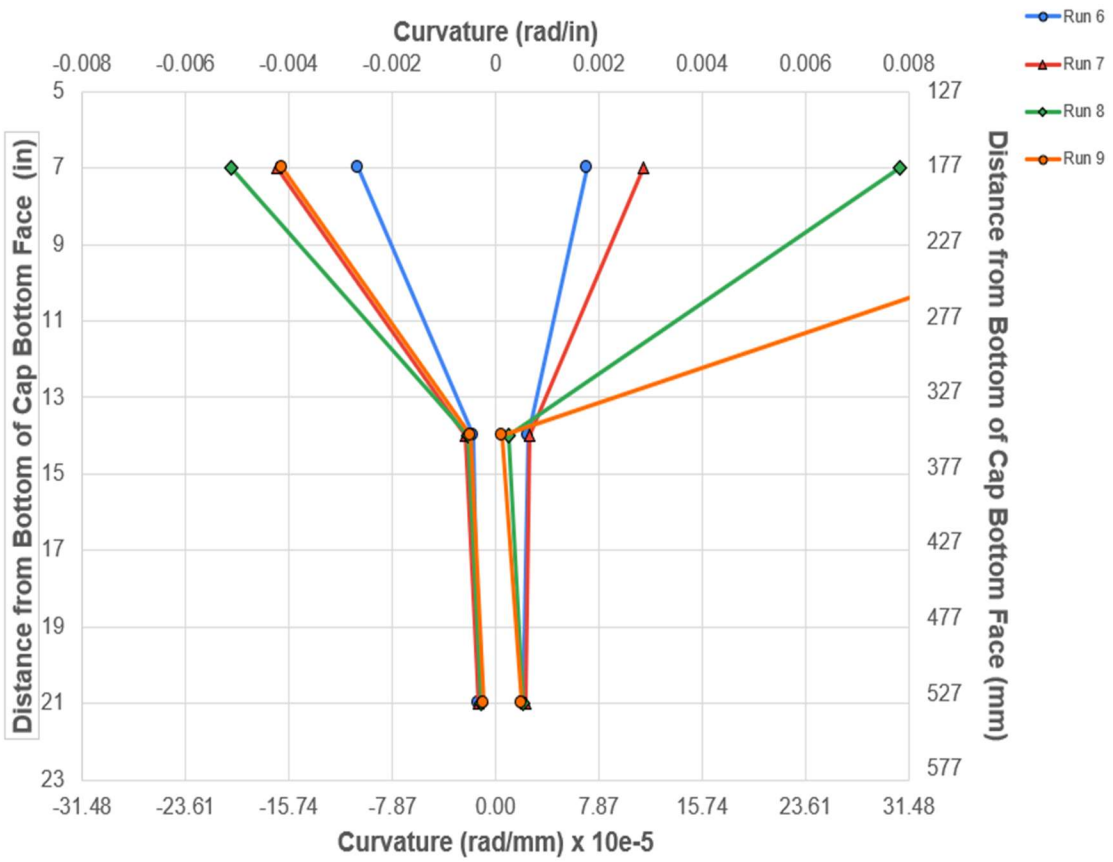

Figure 5.102 Top CIP (north) Column - Curvature profile (run 6-9)

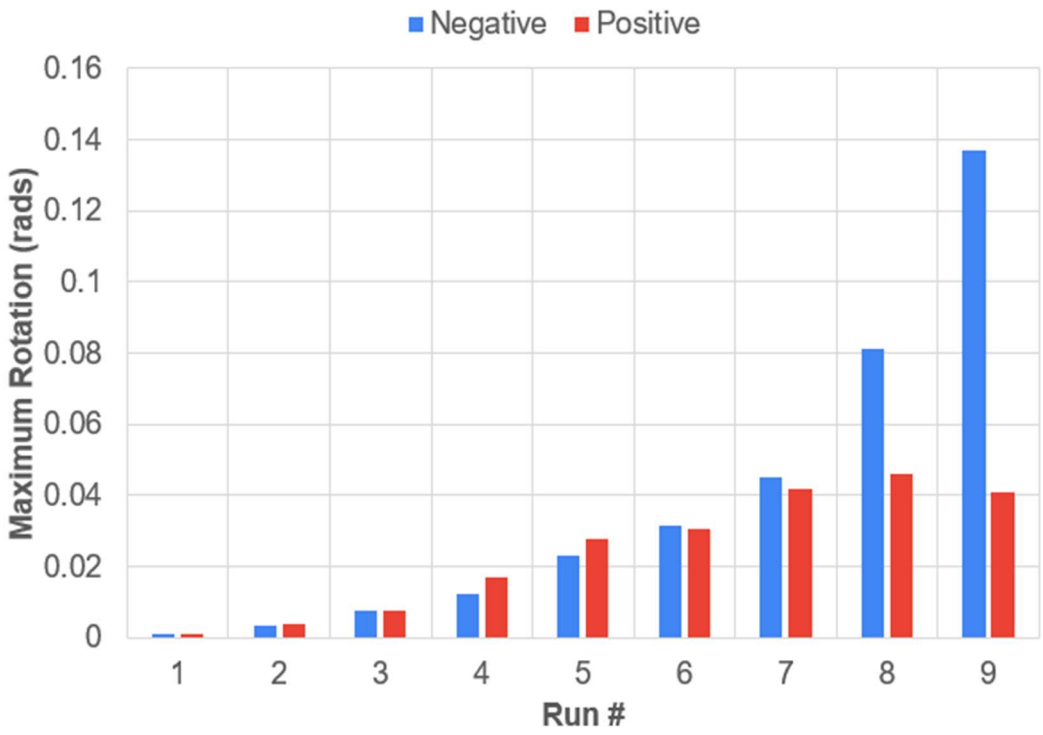

Figure 5.103 CIP (north) Column – Maximum and minimum rotations of the base (run 1-9)

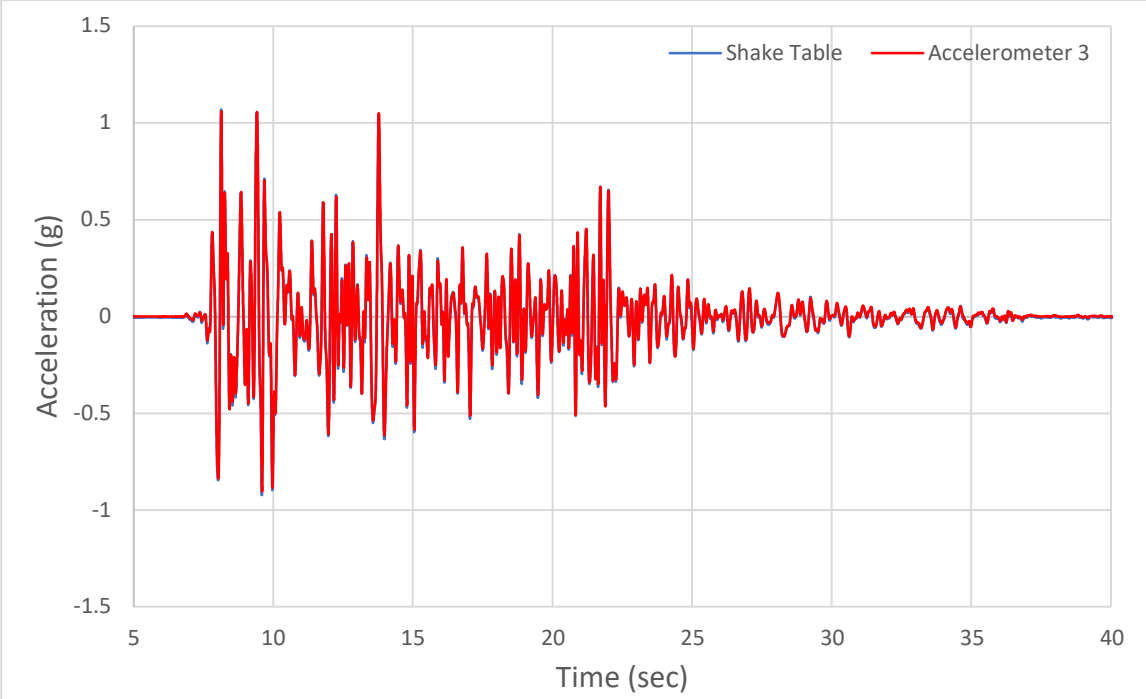

Figure 5.104 Comparison of accelerometer and shake table acceleration measurements (run 9)

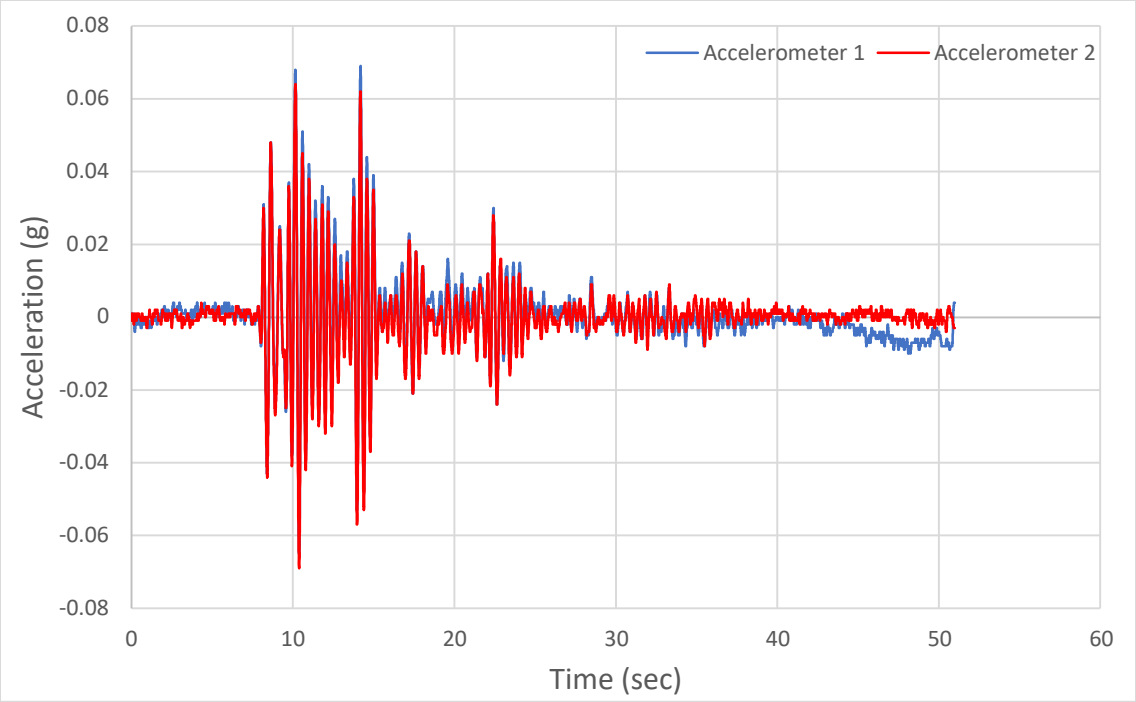

Figure 5.105 Acceleration history measured at the top of the specimen during run 1

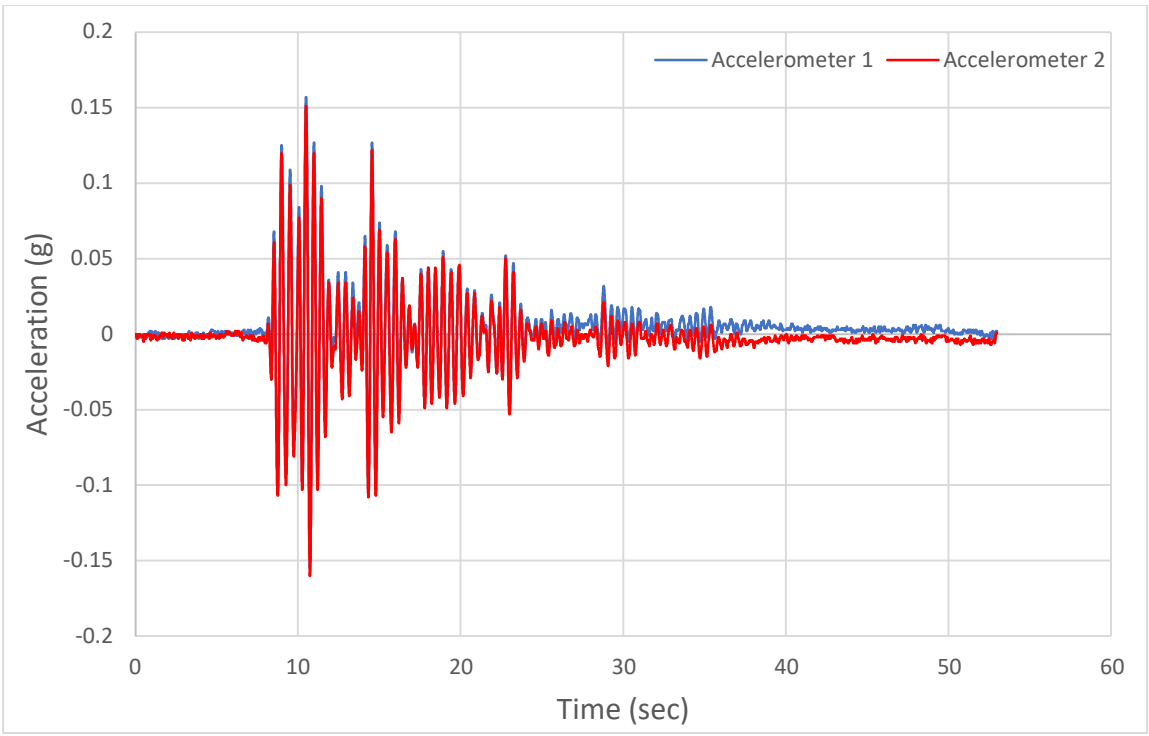

Figure 5.106 Acceleration history measured at the top of the specimen during run 2

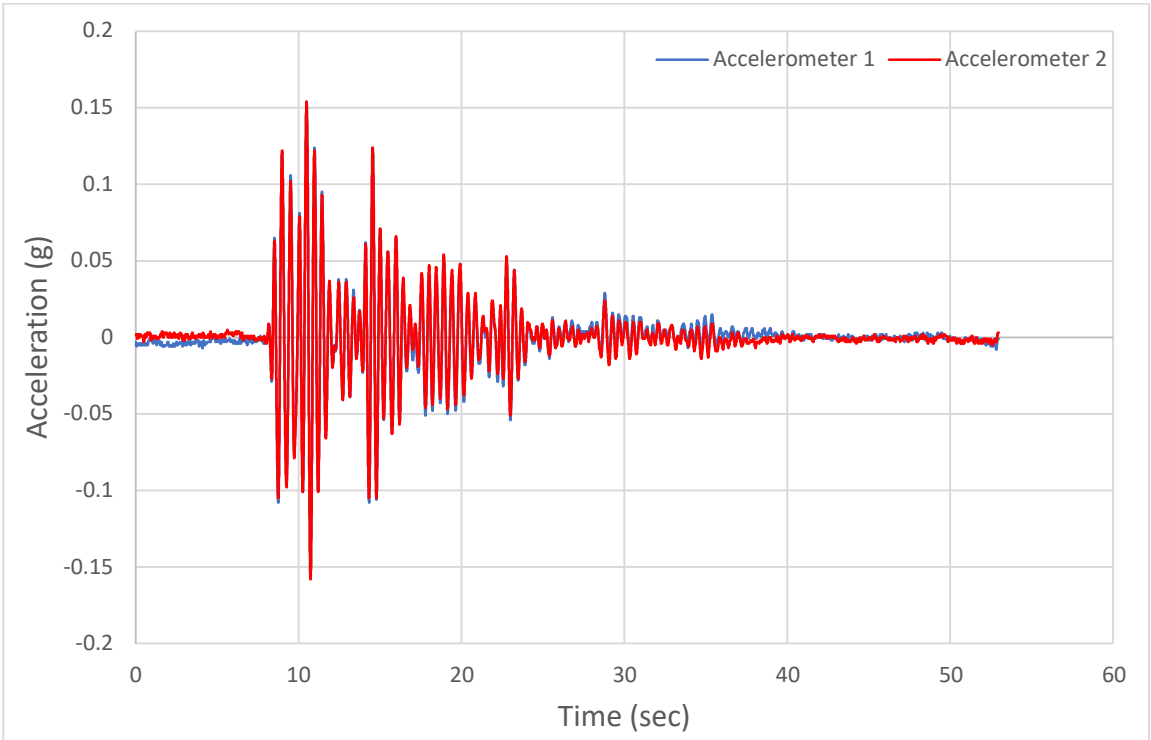

Figure 5.107 Acceleration history measured at the top of the specimen during run 3

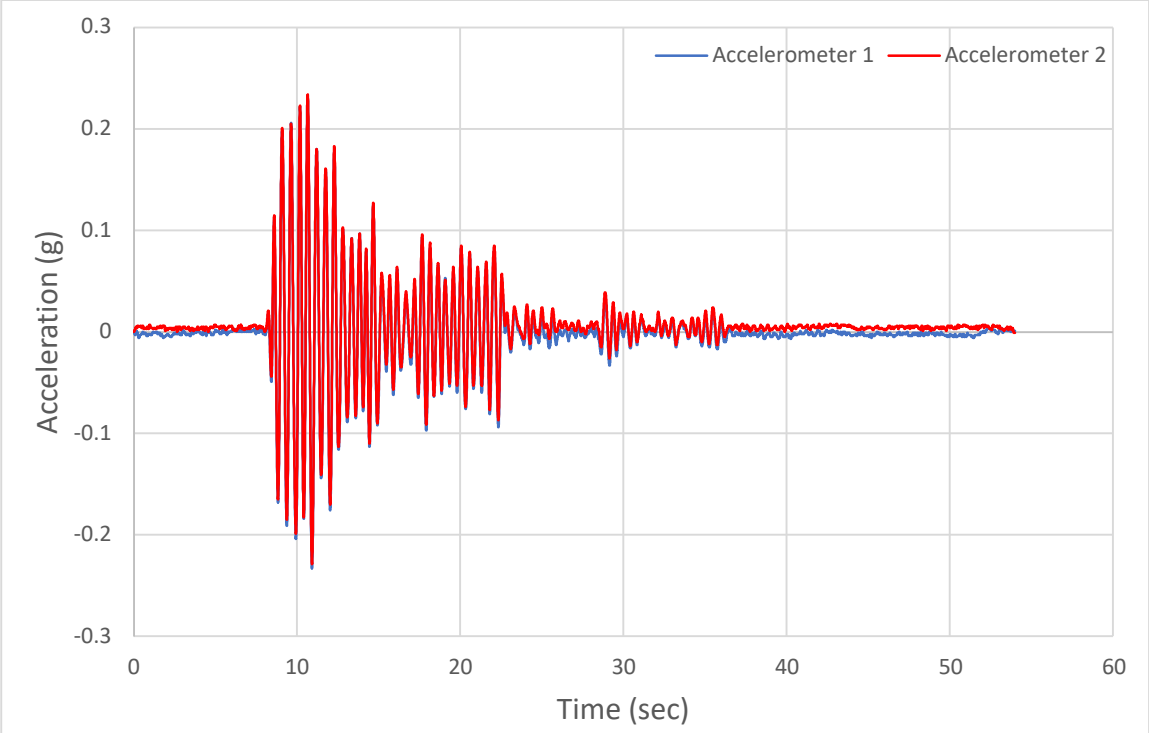

Figure 5.108 Acceleration history measured at the top of the specimen during run 4

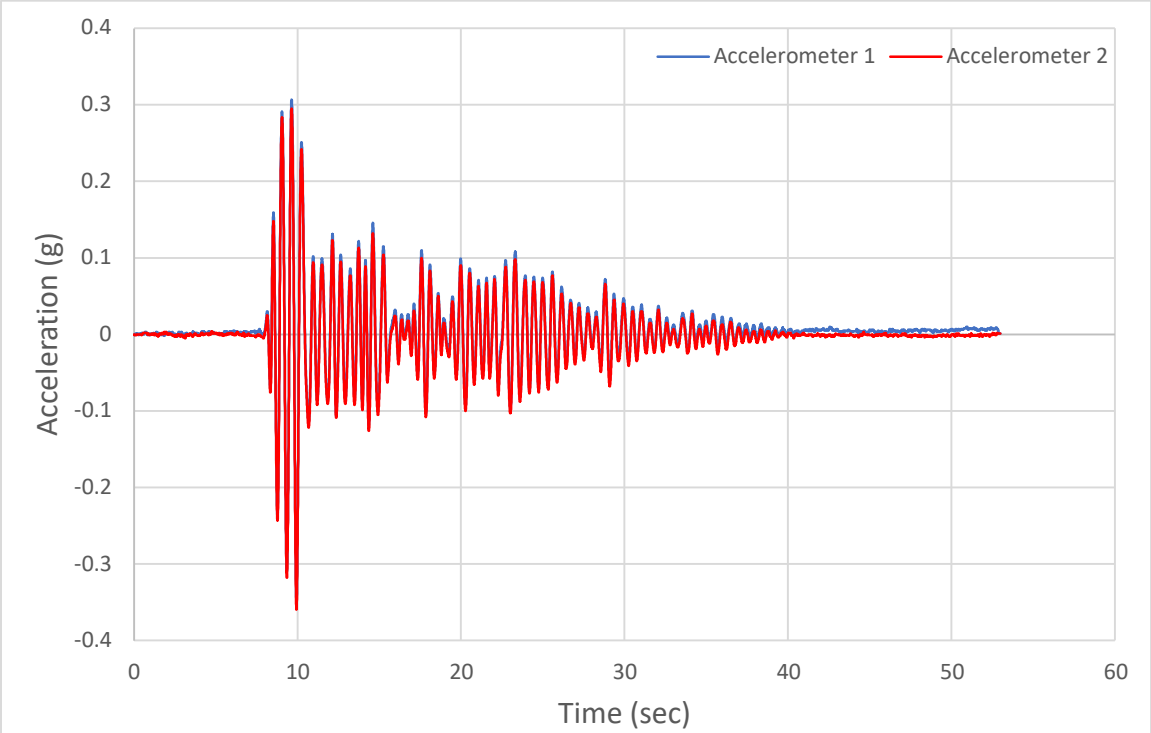

Figure 5.109 Acceleration history measured at the top of the specimen during run 5

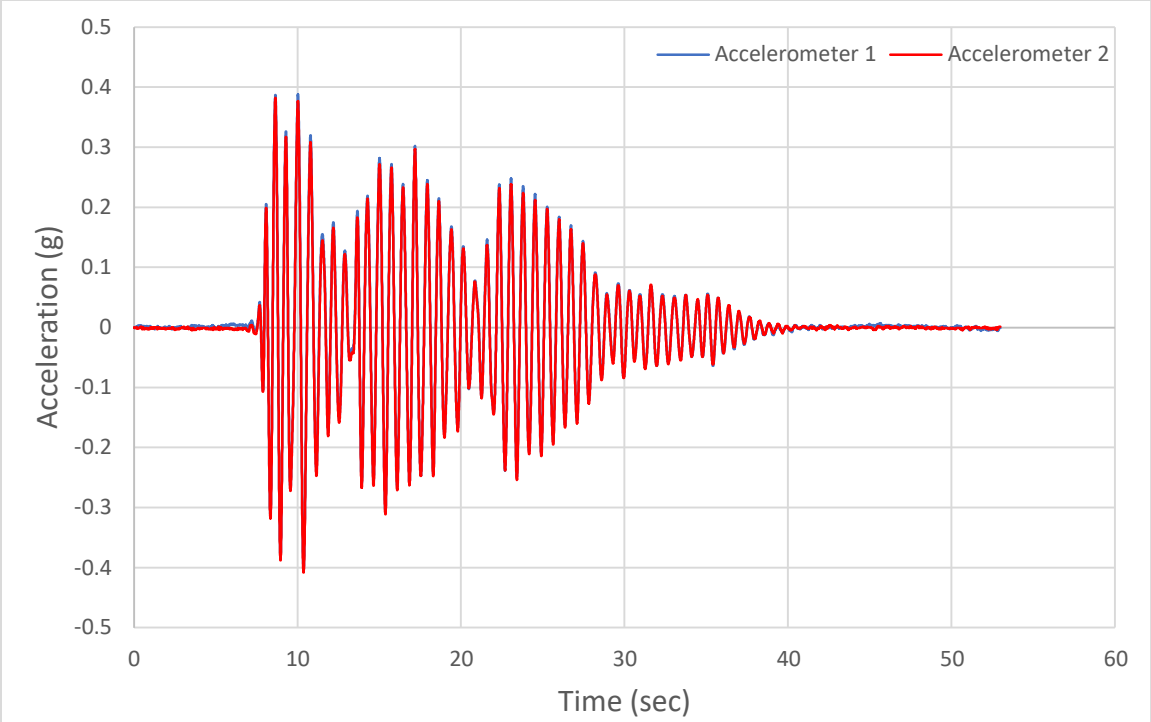

Figure 5.110 Acceleration history measured at the top of the specimen during run 6

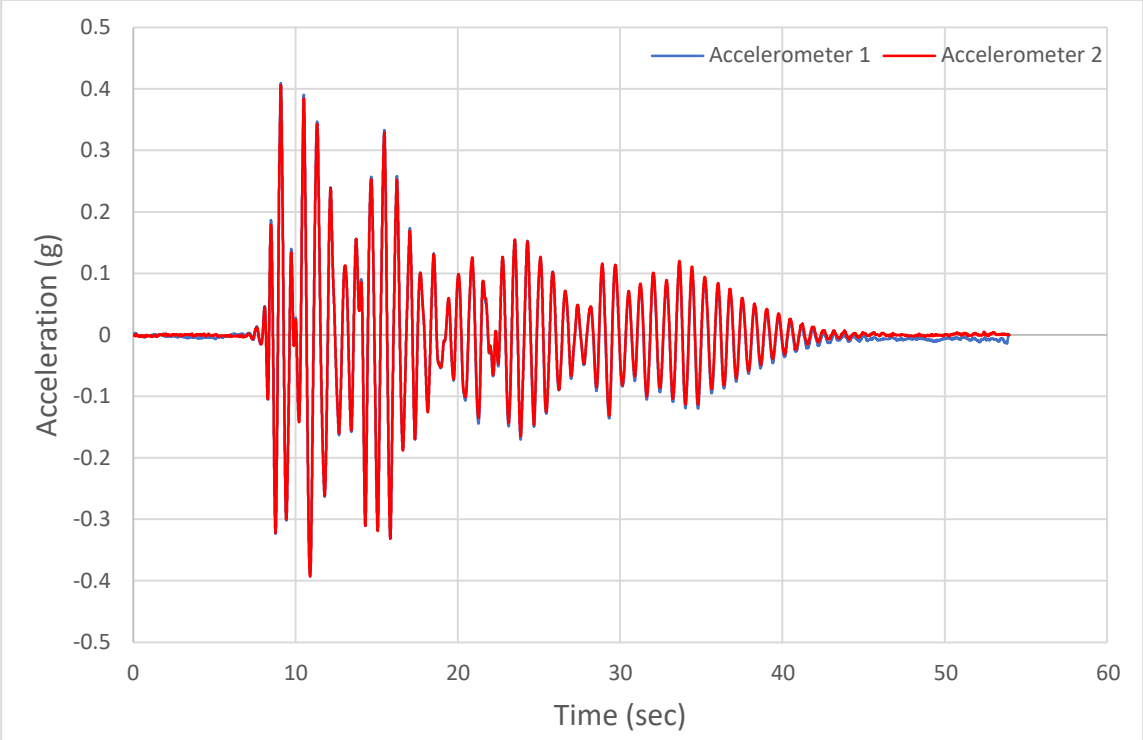

Figure 5.111 Acceleration history measured at the top of the specimen during run 7

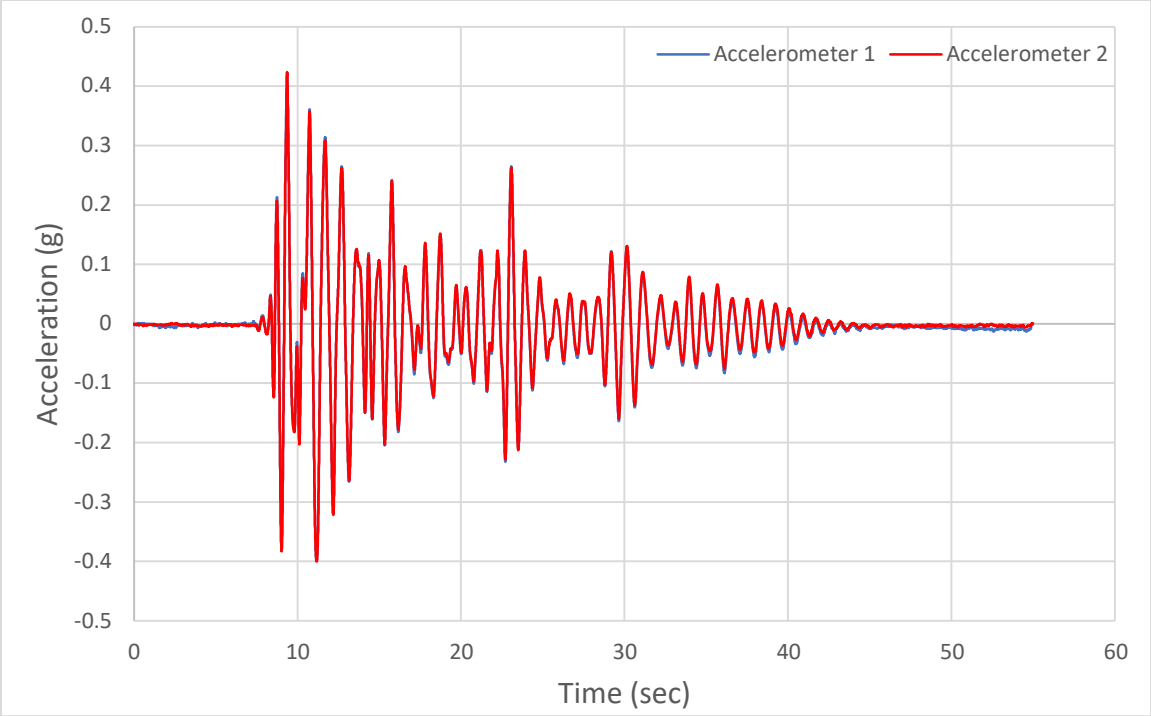

Figure 5.112 Acceleration history measured at the top of the specimen during run 8

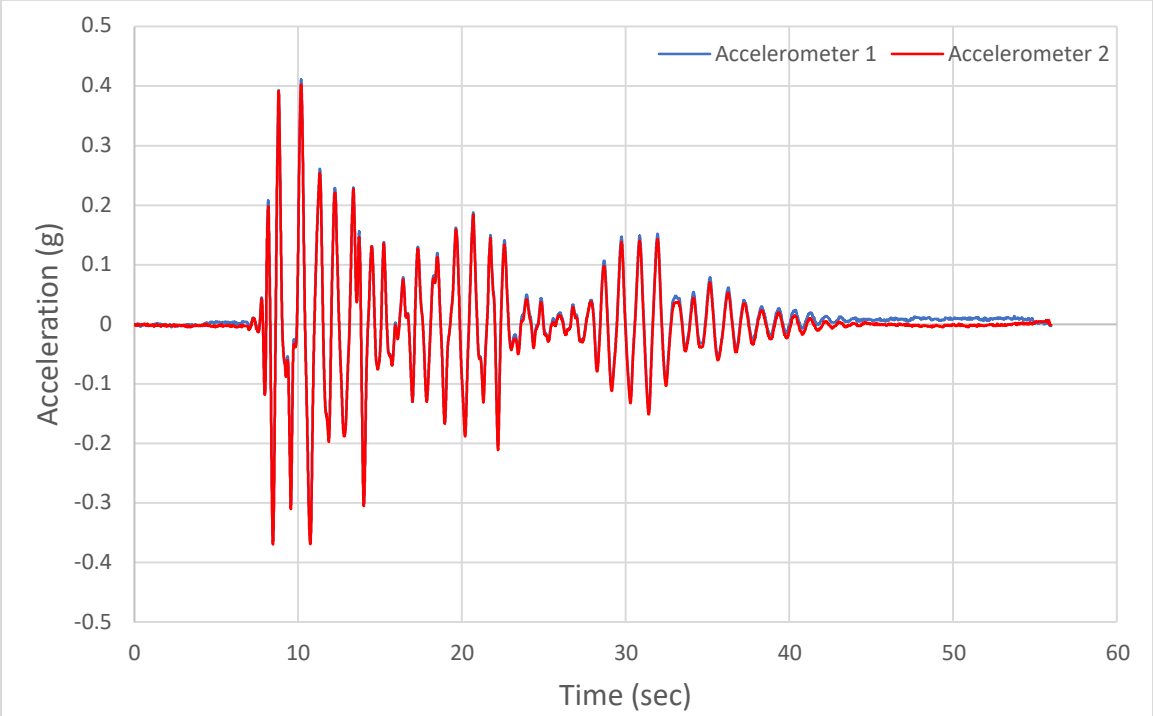

Figure 5.113 Acceleration history measured at the top of the specimen during run 9

Chapter 6 Tables

Table 6.1 Comparison of peak displacement of analytical model and measured results

	Measured	Calculated	
Run #	**Max Displacement, in (mm)**	**Max Displacement, in (mm)**	**% Difference**
1	0.09 (2.36)	0.20 (5.08)	73.0
2	0.29 (7.24)	0.90 (22.86)	103.8
3	0.57 (14.48)	1.37 (34.85)	82.6
4	1.25 (31.75)	1.61 (40.89)	25.2
5	2.04 (51.82)	2.20 (55.88)	7.5
6	2.32 (58.93)	2.23 (56.64)	4.0
7	3.40 (86.36)	3.07 (77.98)	10.2
8	6.33 (160.78)	4.87 (123.70)	26.1
9	11.20 (284.48)	7.50 (190.50)	39.6

Table 6.2 Comparison of peak lateral forces of analytical model and measured results

	Measured	Calculated	
Run #	**Max Force, kip (kN)**	**Max Force, kip (kN)**	**% Difference**
1	6.81 (30.29)	11.16 (49.64)	48.4
2	15.48 (68.86)	31.15 (138.56)	67.2
3	24.10 (107.20)	34.51 (153.51)	35.5
4	35.24 (156.76)	35.70 (158.80)	1.3
5	40.47 (180.02)	38.24 (170.10)	5.7
6	41.05 (182.60)	37.70 (167.70)	8.5
7	42.59 (189.45)	40.50 (180.15)	5.0
8	44.05 (195.94)	44.42 (197.59)	0.8
9	40.87 (181.80)	49.00 (217.96)	18.1

Chapter 6 Figures

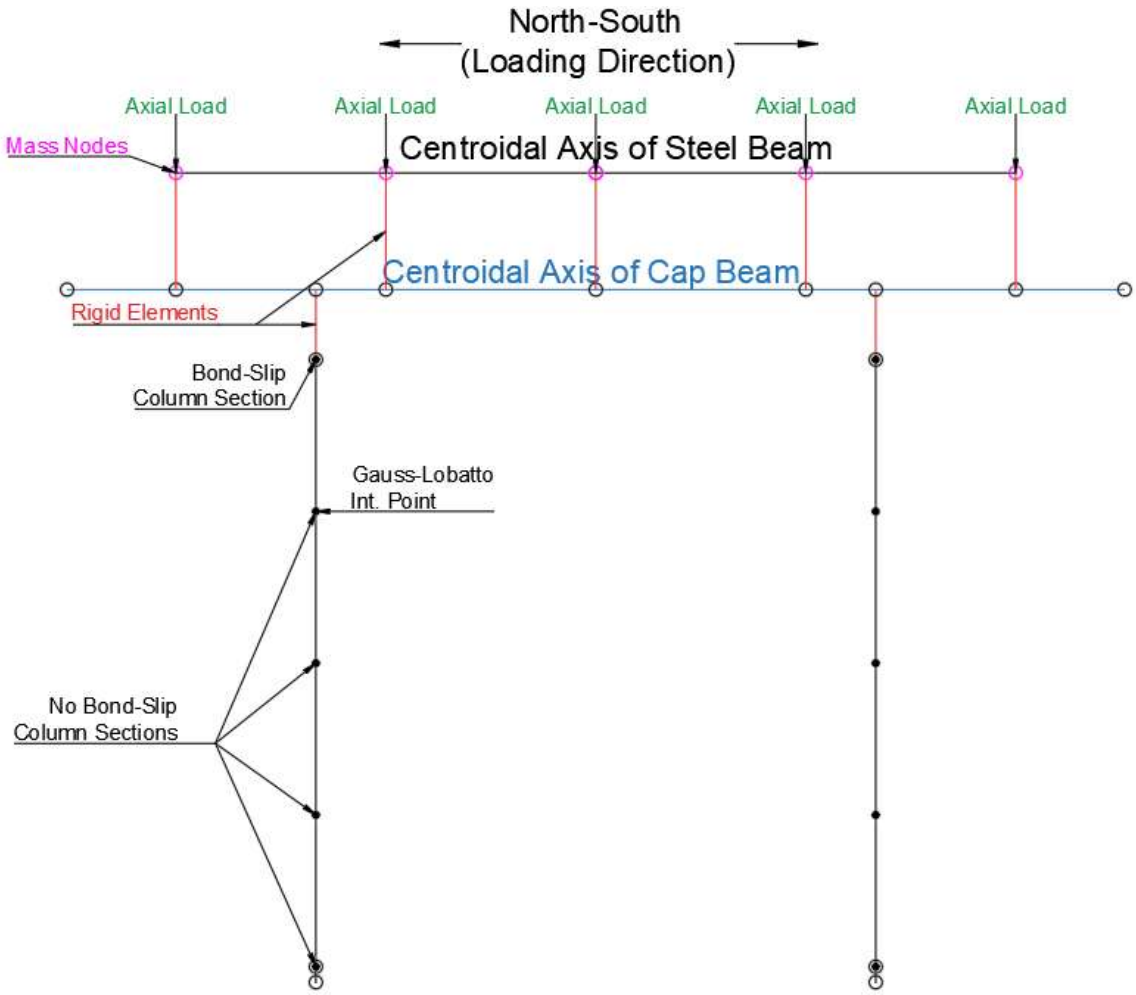

Figure 6.1 Post-test analytical model

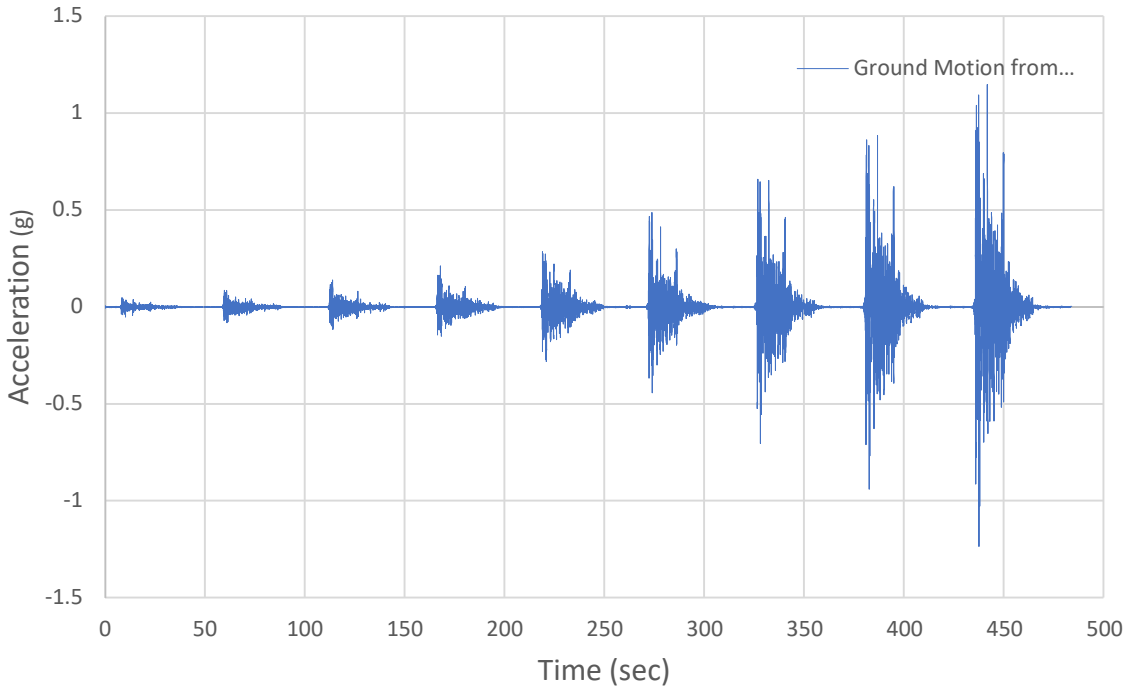

Figure 6.2 Filtered input acceleration history

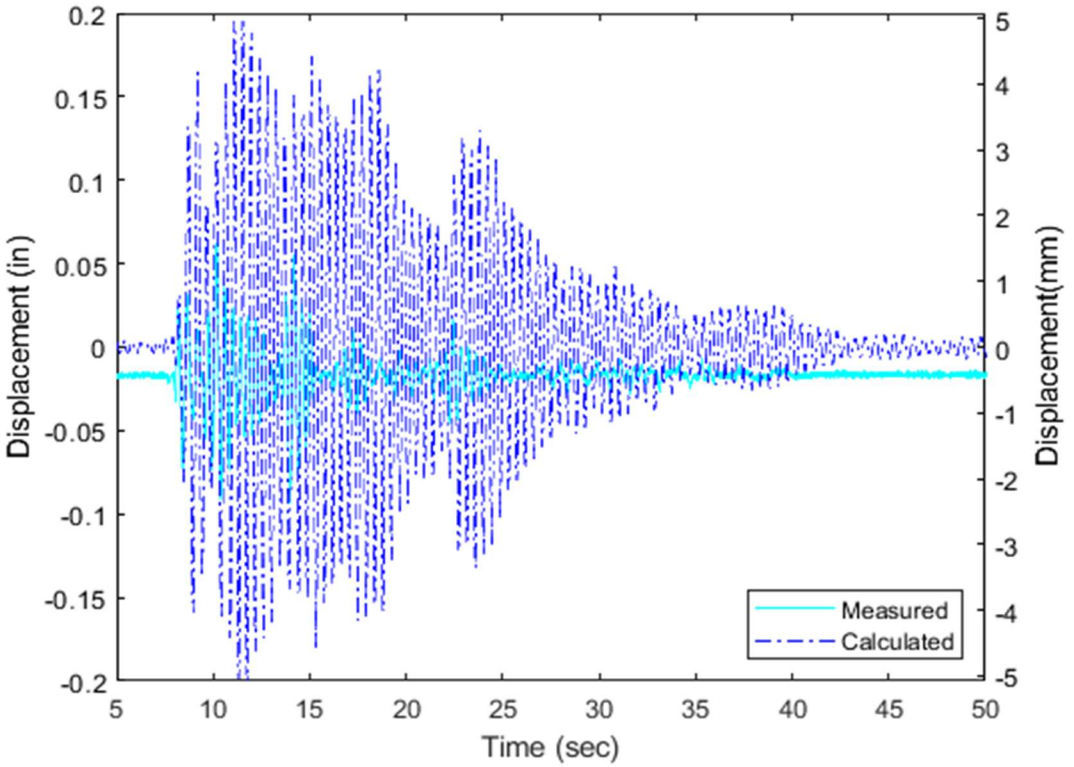

Figure 6.3 Comparison of displacement history for run 1

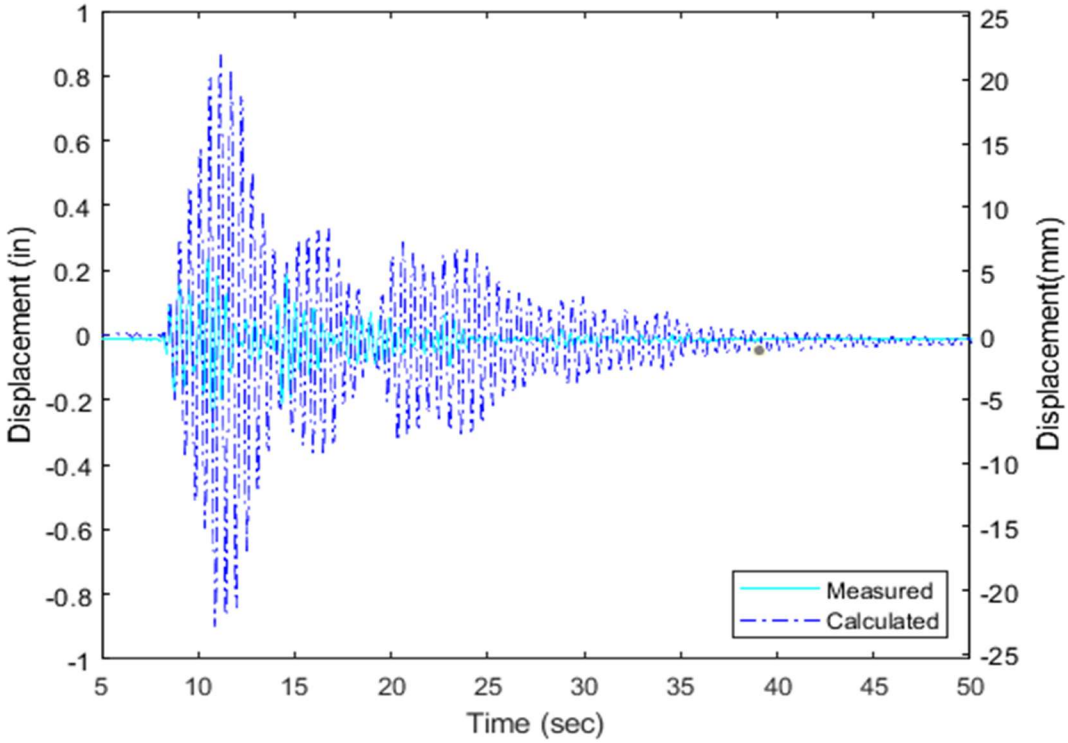

Figure 6.4 Comparison of displacement history for run 2

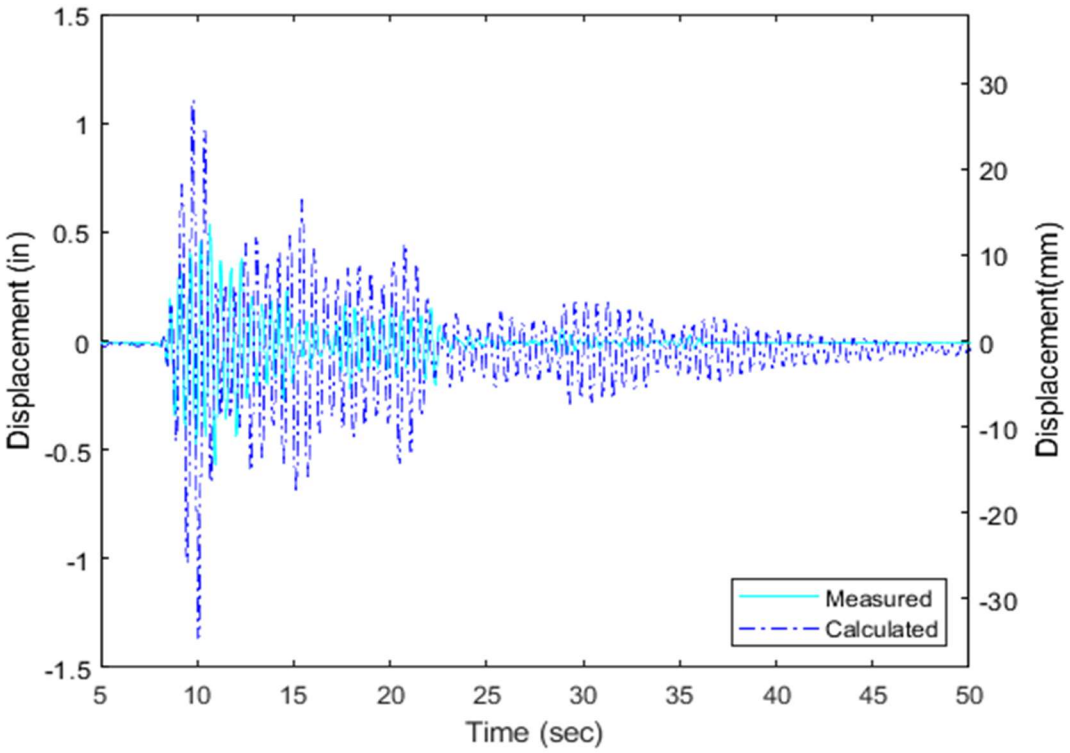

Figure 6.5 Comparison of displacement history for run 3

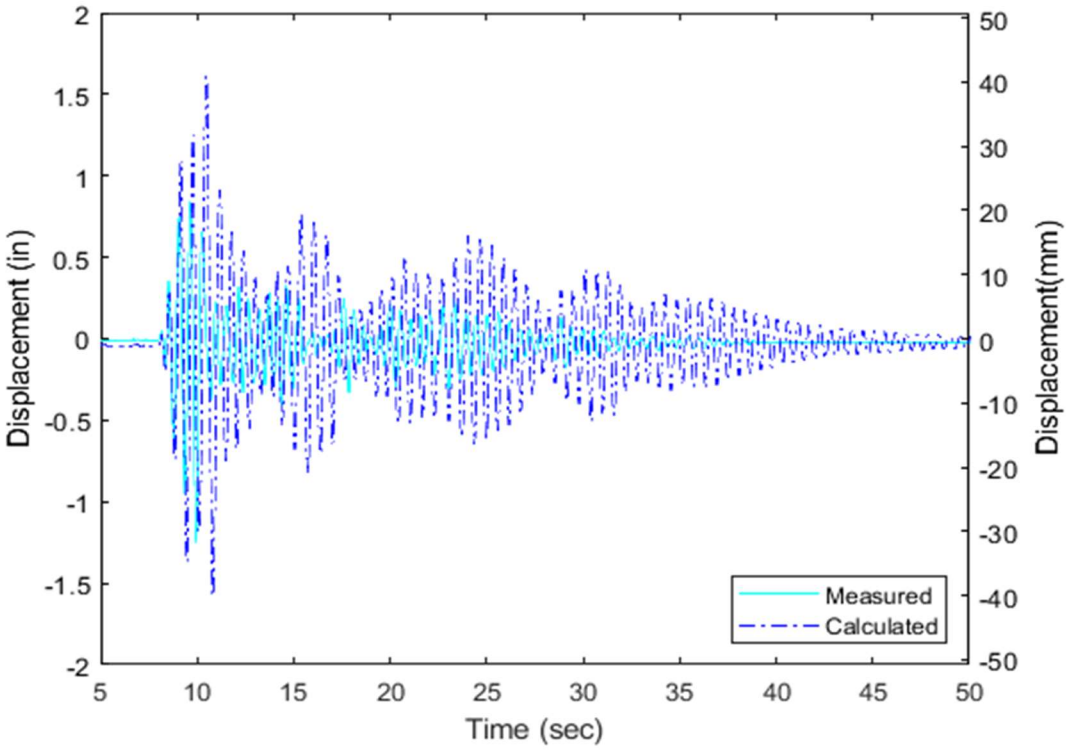

Figure 6.6 Comparison of displacement history for run 4

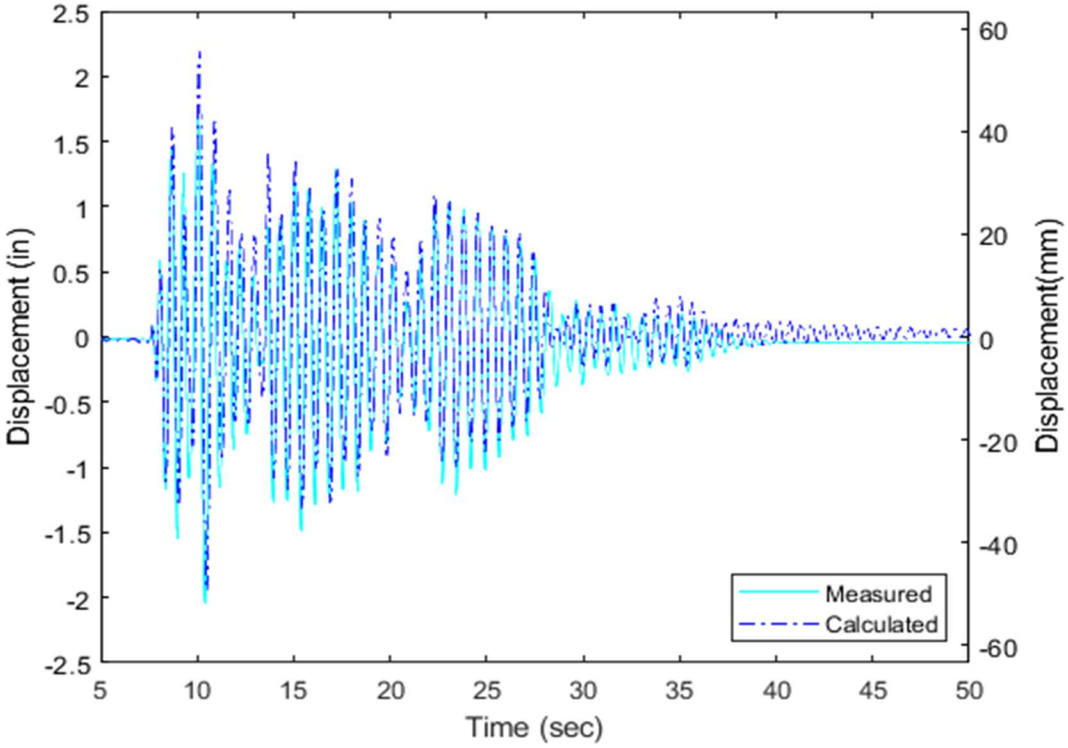

Figure 6.7 Comparison of displacement history for run 5

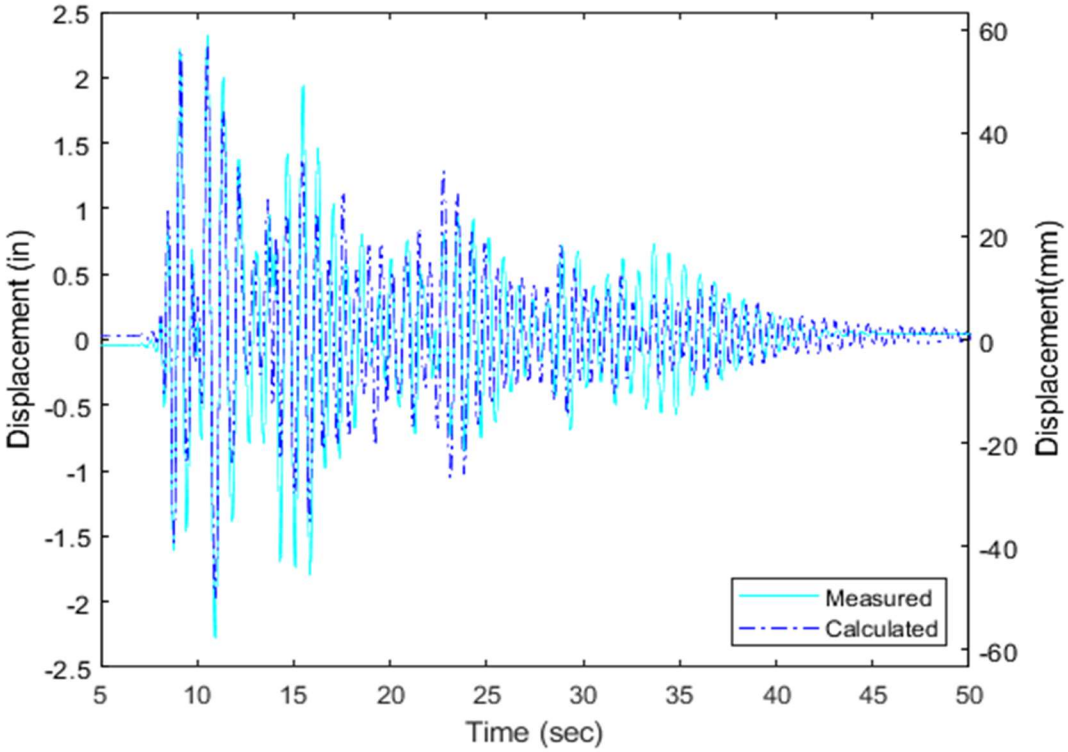

Figure 6.8 Comparison of displacement history for run 6

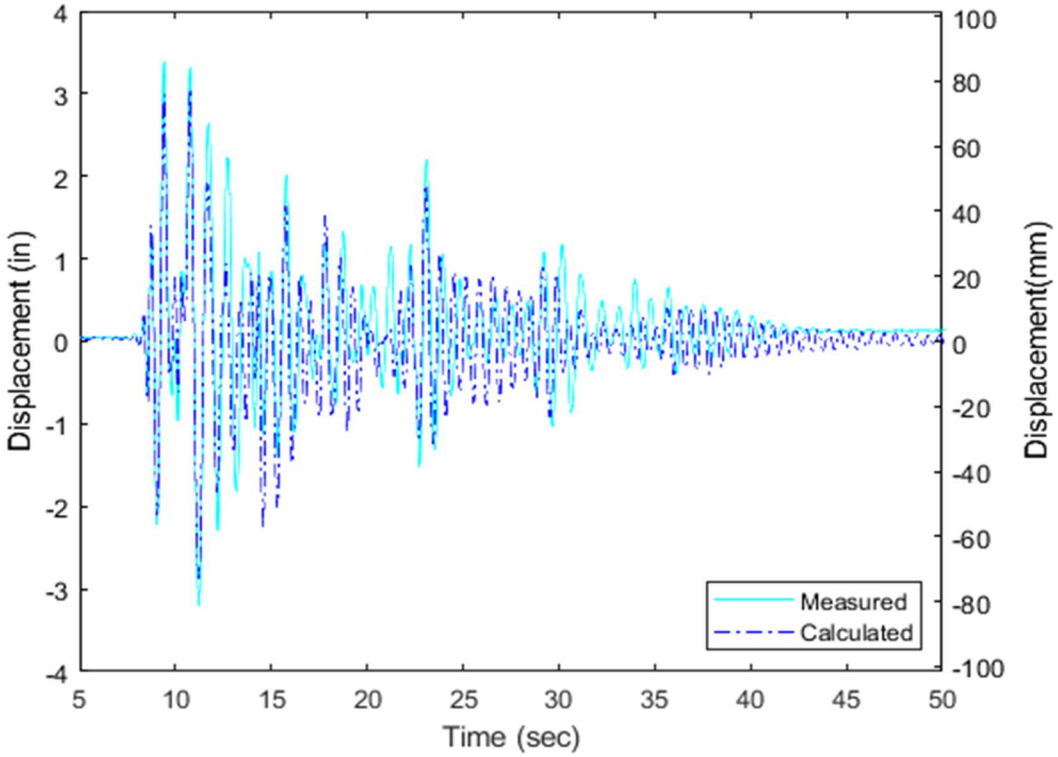

Figure 6.9 Comparison of displacement history for run 7

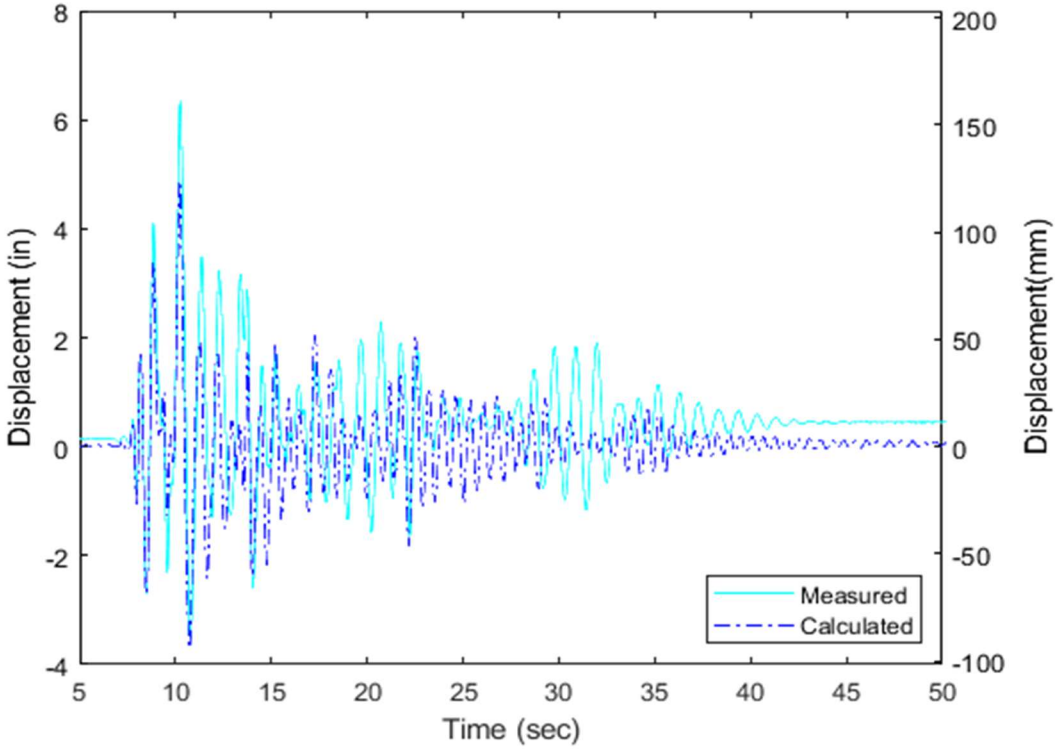

Figure 6.10 Comparison of displacement history for run 8

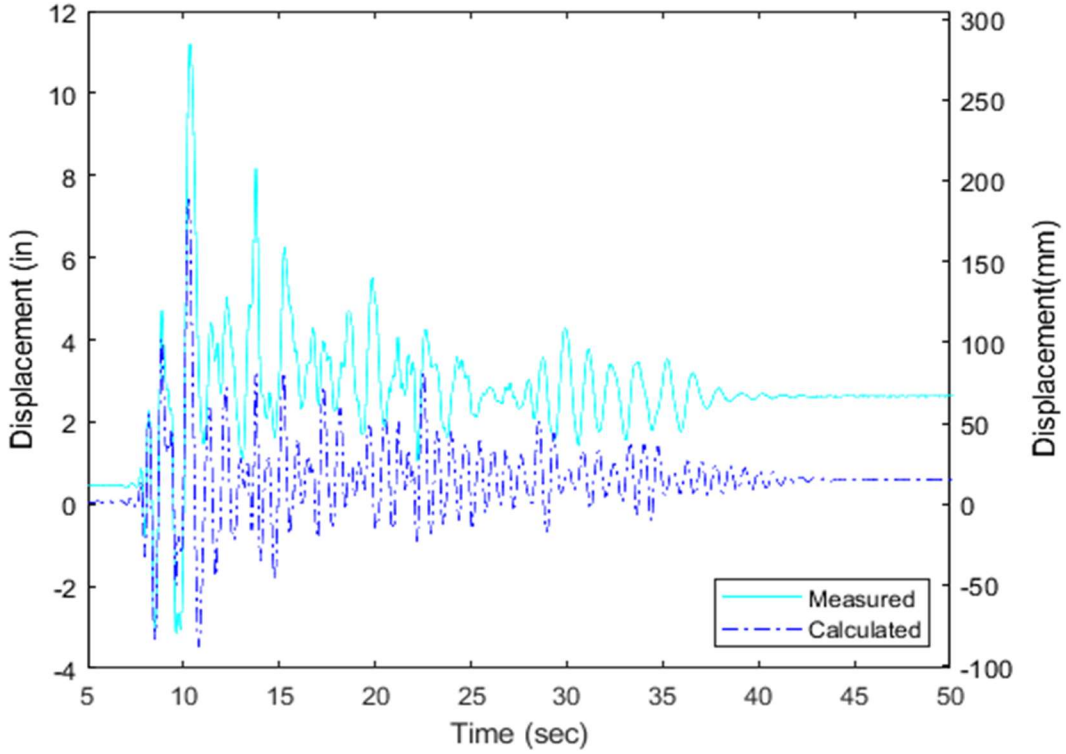

Figure 6.11 Comparison of displacement history for run 9

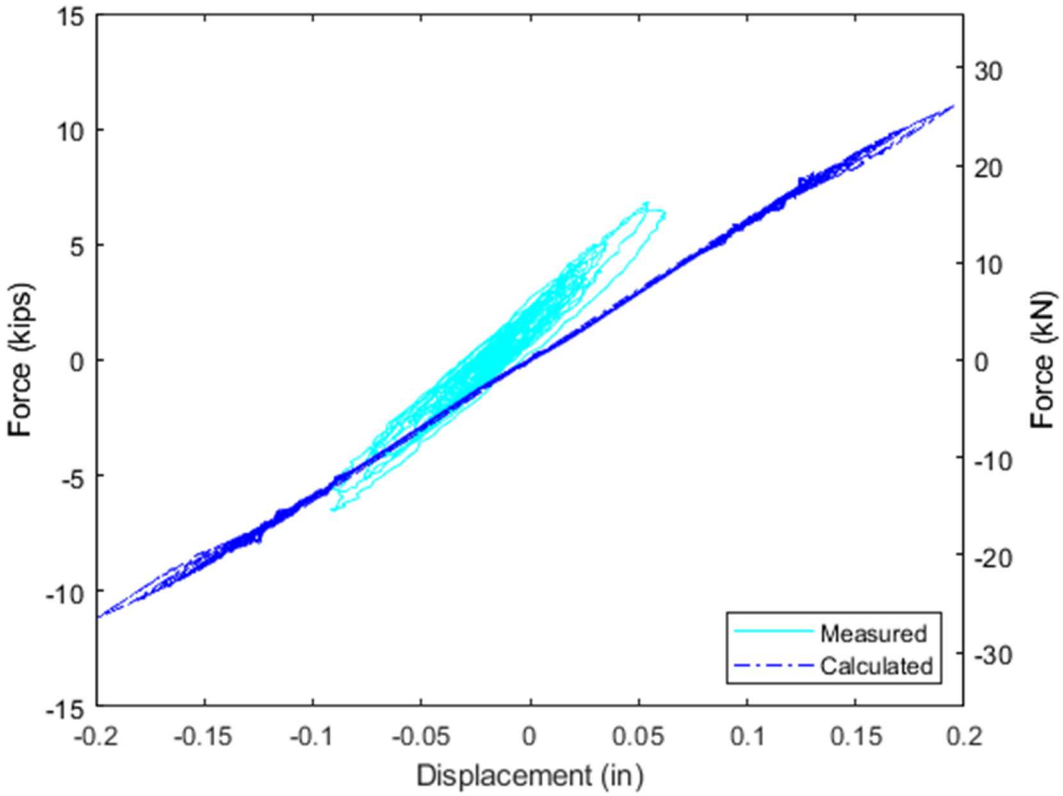

Figure 6.12 Comparison of force-displacement relationship for run 1

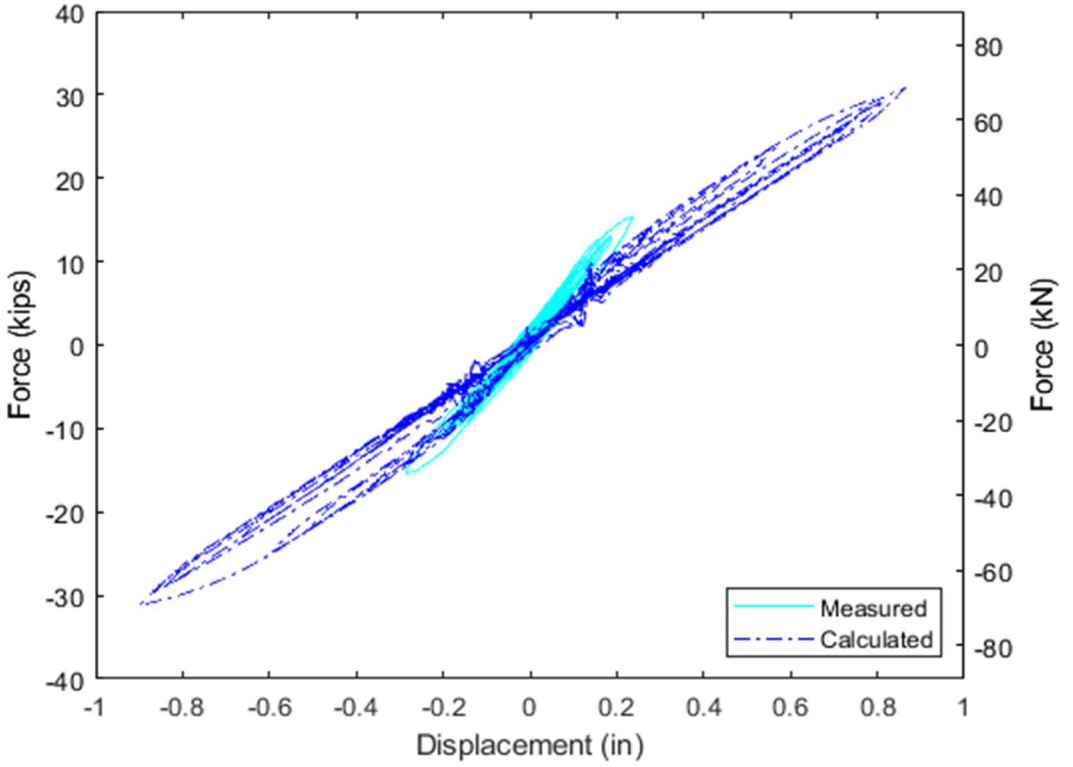

Figure 6.13 Comparison of force-displacement relationship for run 2

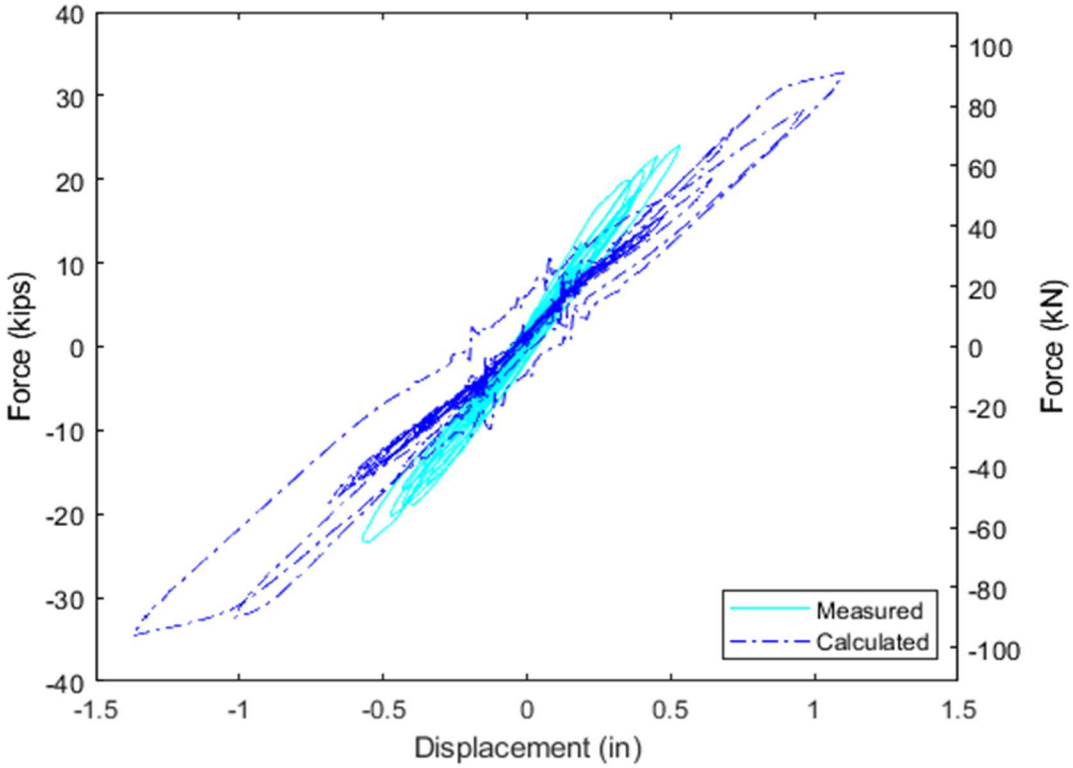

Figure 6.14 Comparison of force-displacement relationship for run 3

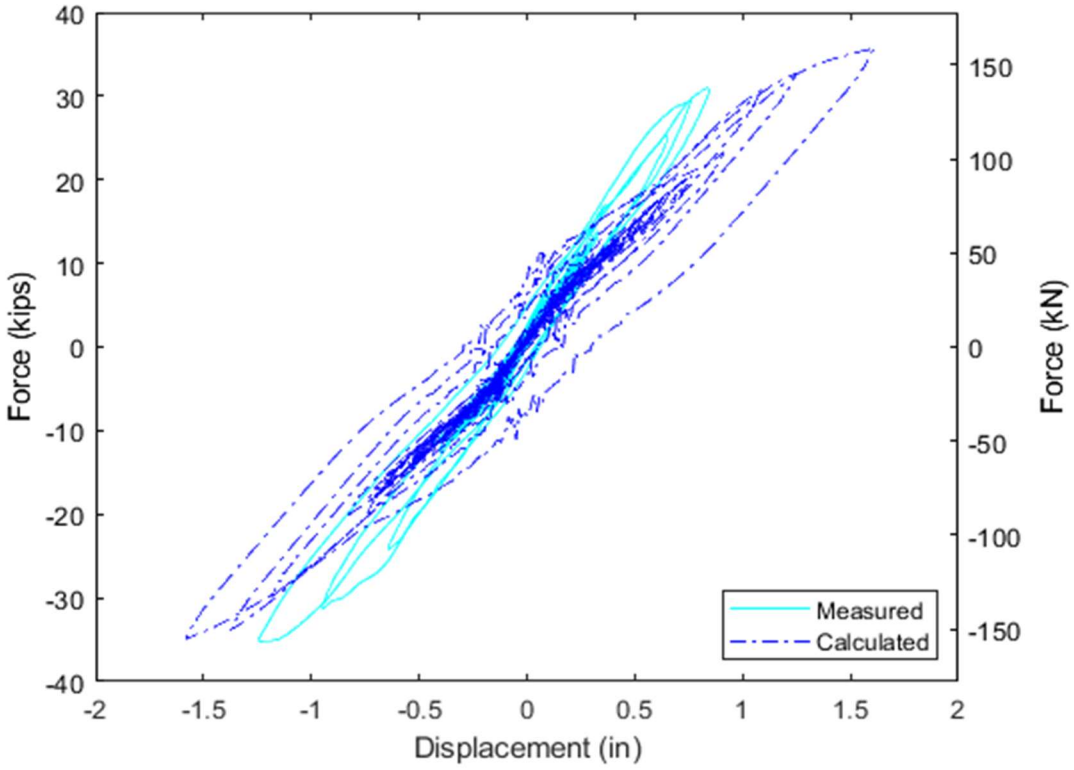

Figure 6.15 Comparison of force-displacement relationship for run 4

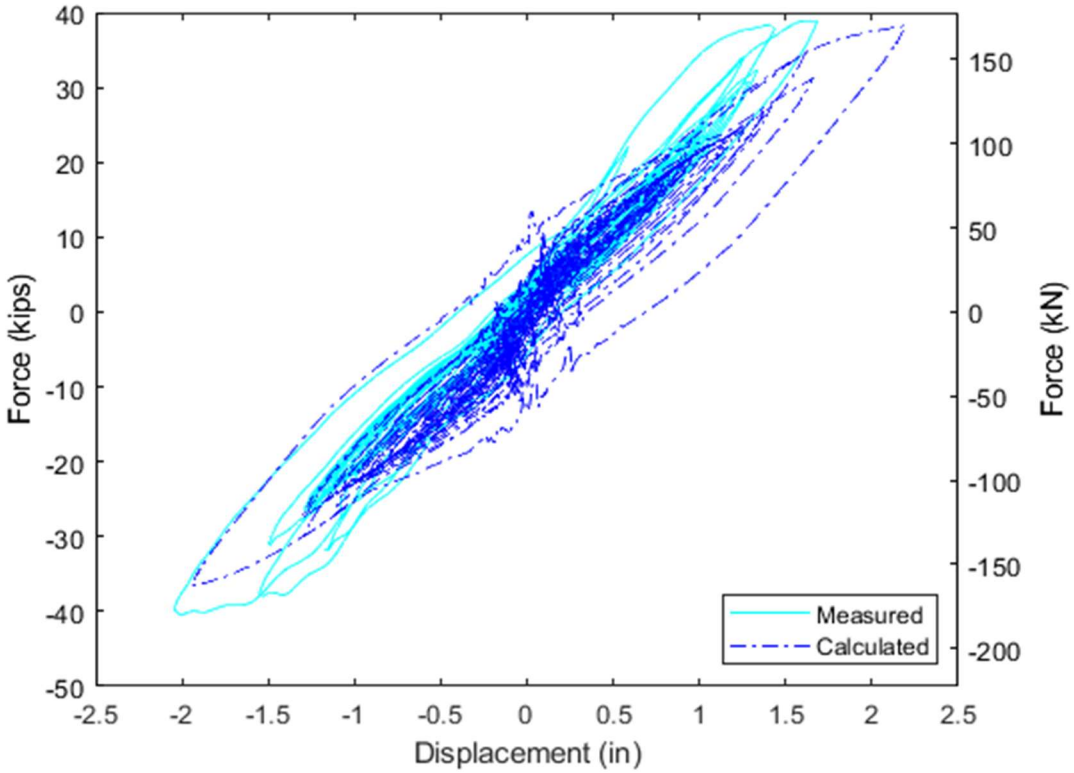

Figure 6.16 Comparison of force-displacement relationship for run 5

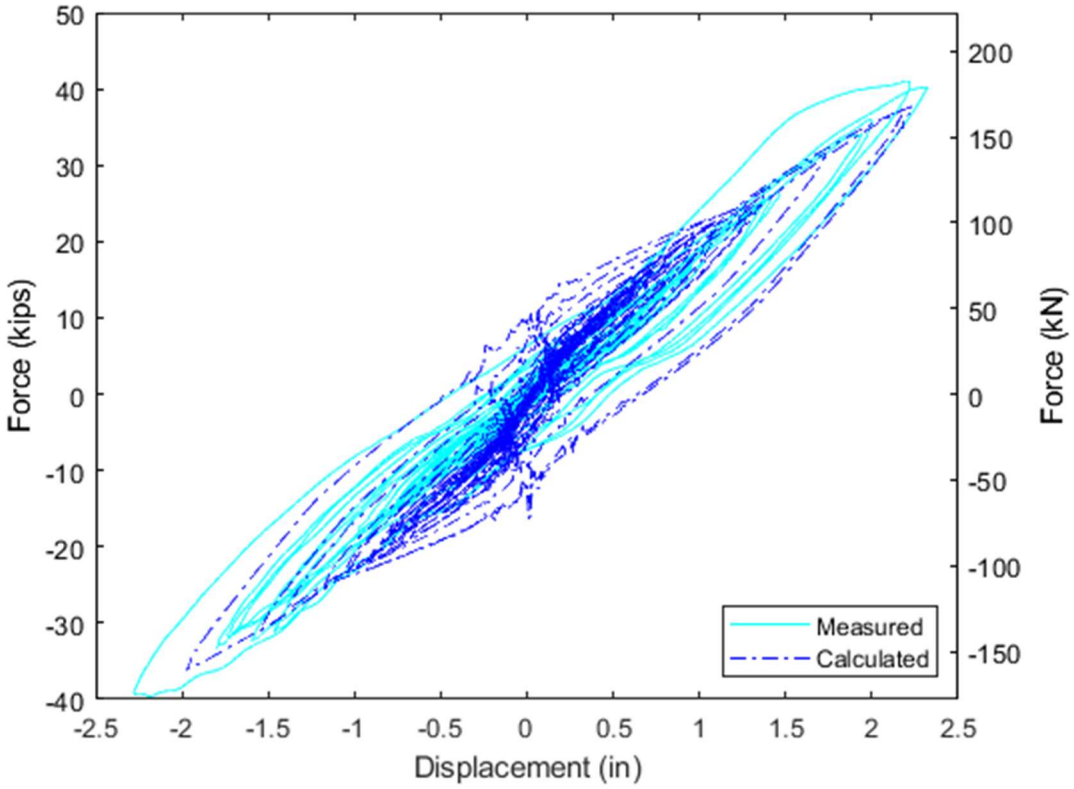

Figure 6.17 Comparison of force-displacement relationship for run 6

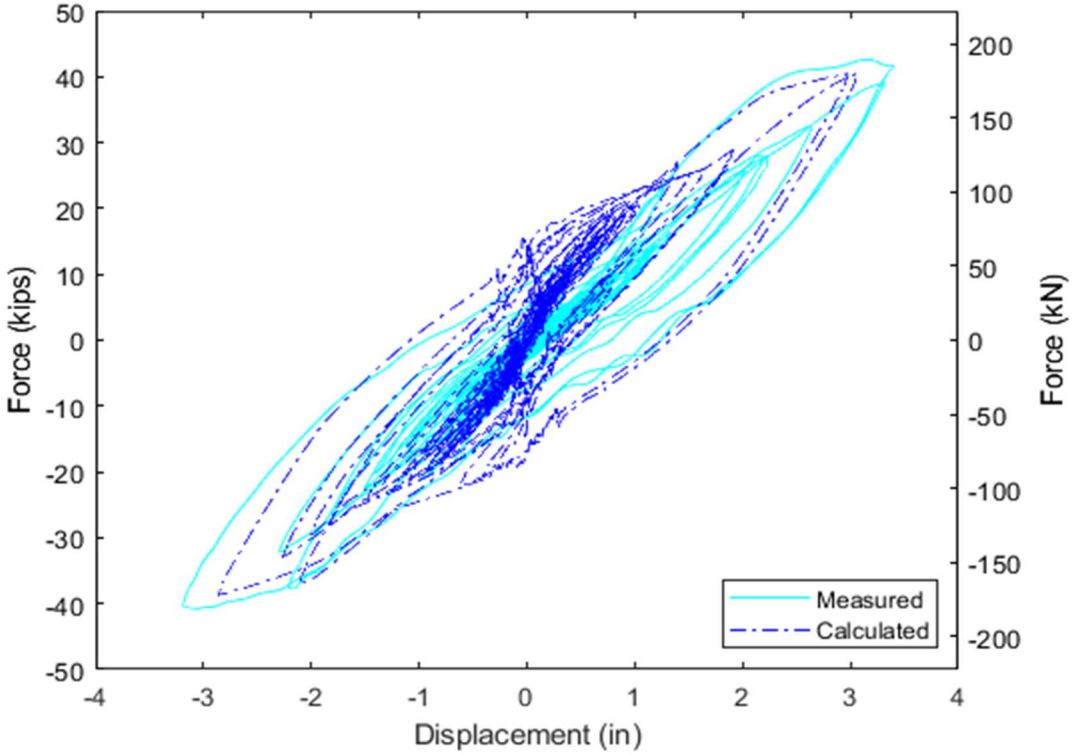

Figure 6.18 Comparison of force-displacement relationship for run 7

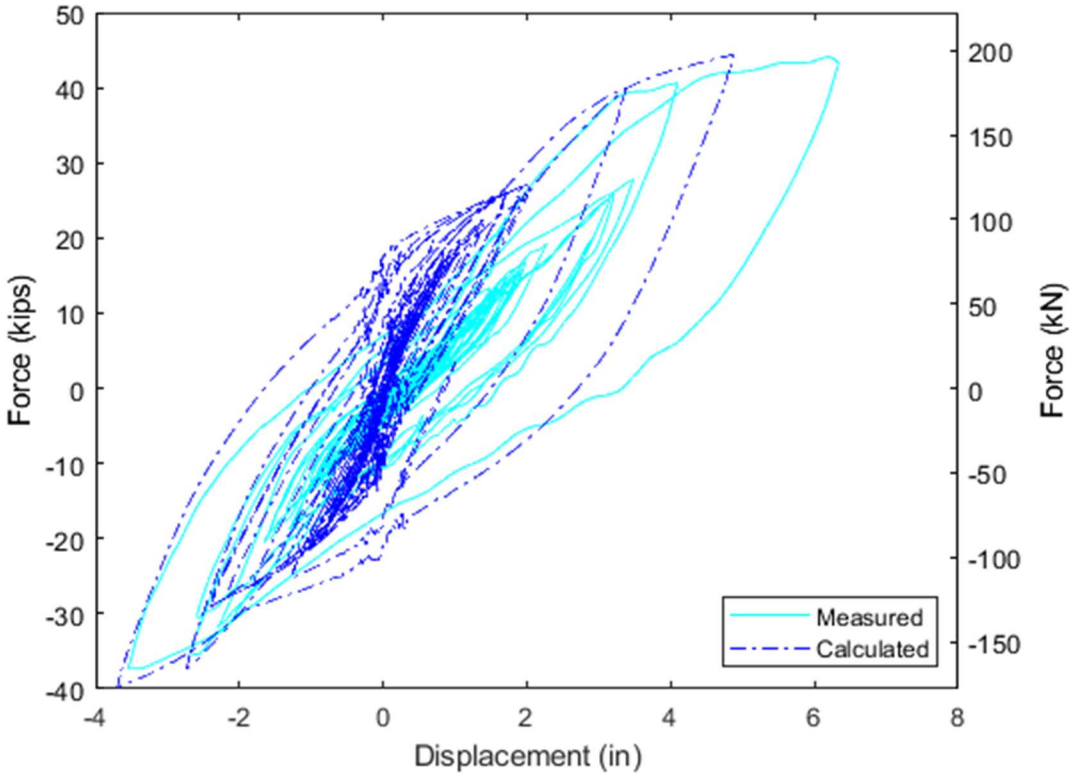

Figure 6.19 Comparison of force-displacement relationship for run 8

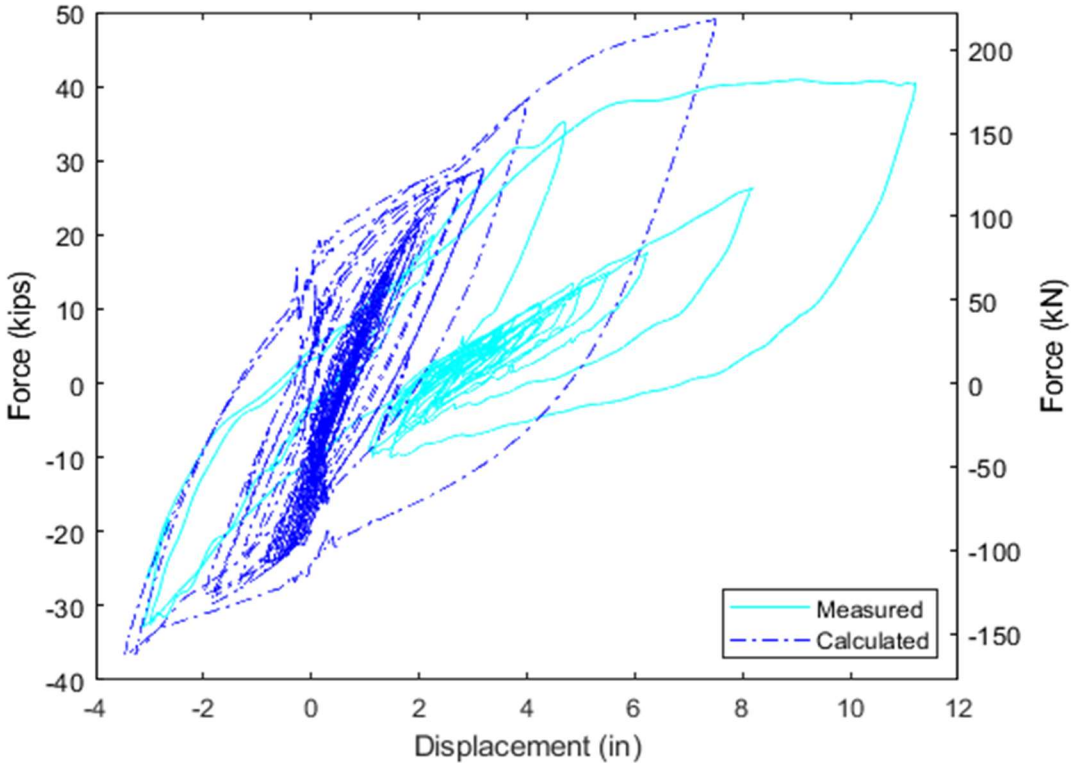

Figure 6.20 Comparison of force-displacement relationship for run 9

LIST OF CCEER PUBLICATIONS

Report No.	Publication
CCEER-84-1	Saiidi, M., and R. Lawver, "User's Manual for LZAK-C64, A Computer Program to Implement the Q-Model on Commodore 64," Civil Engineering Department, Report No. CCEER-84-1, University of Nevada, Reno, January 1984.
CCEER-84-1	Douglas, B., Norris, G., Saiidi, M., Dodd, L., Richardson, J. and Reid, W., "Simple Bridge Models for Earthquakes and Test Data," Civil Engineering Department, Report No. CCEER-84-1 Reprint, University of Nevada, Reno, January 1984.
CCEER-84-2	Douglas, B. and T. Iwasaki, "Proceedings of the First USA-Japan Bridge Engineering Workshop," held at the Public Works Research Institute, Tsukuba, Japan, Civil Engineering Department, Report No. CCEER-84-2, University of Nevada, Reno, April 1984.
CCEER-84-3	Saiidi, M., J. Hart, and B. Douglas, "Inelastic Static and Dynamic Analysis of Short R/C Bridges Subjected to Lateral Loads," Civil Engineering Department, Report No. CCEER-84-3, University of Nevada, Reno, July 1984.
CCEER-84-4	Douglas, B., "A Proposed Plan for a National Bridge Engineering Laboratory," Civil Engineering Department, Report No. CCEER-84-4, University of Nevada, Reno, December 1984.
CCEER-85-1	Norris, G. and P. Abdollaholiaee, "Laterally Loaded Pile Response: Studies with the Strain Wedge Model," Civil Engineering Department, Report No. CCEER-85-1, University of Nevada, Reno, April 1985.
CCEER-86-1	Ghusn, G. and M. Saiidi, "A Simple Hysteretic Element for Biaxial Bending of R/C in NEABS-86," Civil Engineering Department, Report No. CCEER-86-1, University of Nevada, Reno, July 1986.
CCEER-86-2	Saiidi, M., R. Lawver, and J. Hart, "User's Manual of ISADAB and SIBA, Computer Programs for Nonlinear Transverse Analysis of Highway Bridges Subjected to Static and Dynamic Lateral Loads," Civil Engineering Department, Report No. CCEER-86-2, University of Nevada, Reno, September 1986.
CCEER-87-1	Siddharthan, R., "Dynamic Effective Stress Response of Surface and Embedded Footings in Sand," Civil Engineering Department, Report No. CCEER-86-2, University of Nevada, Reno, June 1987.
CCEER-87-2	Norris, G. and R. Sack, "Lateral and Rotational Stiffness of Pile Groups for Seismic Analysis of Highway Bridges," Civil Engineering Department, Report No. CCEER-87-2, University of Nevada, Reno, June 1987.
CCEER-88-1	Orie, J. and M. Saiidi, "A Preliminary Study of One-Way Reinforced Concrete Pier Hinges Subjected to Shear and Flexure," Civil Engineering Department, Report No. CCEER-88-1, University of Nevada, Reno, January 1988.
CCEER-88-2	Orie, D., M. Saiidi, and B. Douglas, "A Micro-CAD System for Seismic Design of Regular Highway Bridges," Civil Engineering Department, Report No. CCEER-88-2, University of Nevada, Reno, June 1988.

CCEER-88-3 Orie, D. and M. Saiidi, "User's Manual for Micro-SARB, a Microcomputer Program for Seismic Analysis of Regular Highway Bridges," Civil Engineering Department, Report No. CCEER-88-3, University of Nevada, Reno, October 1988.

CCEER-89-1 Douglas, B., M. Saiidi, R. Hayes, and G. Holcomb, "A Comprehensive Study of the Loads and Pressures Exerted on Wall Forms by the Placement of Concrete," Civil Engineering Department, Report No. CCEER-89-1, University of Nevada, Reno, February 1989.

CCEER-89-2 Richardson, J. and B. Douglas, "Dynamic Response Analysis of the Dominion Road Bridge Test Data," Civil Engineering Department, Report No. CCEER-89-2, University of Nevada, Reno, March 1989.

CCEER-89-2 Vrontinos, S., M. Saiidi, and B. Douglas, "A Simple Model to Predict the Ultimate Response of R/C Beams with Concrete Overlays," Civil Engineering Department, Report NO. CCEER-89-2, University of Nevada, Reno, June 1989.

CCEER-89-3 Ebrahimpour, A. and P. Jagadish, "Statistical Modeling of Bridge Traffic Loads - A Case Study," Civil Engineering Department, Report No. CCEER-89-3, University of Nevada, Reno, December 1989.

CCEER-89-4 Shields, J. and M. Saiidi, "Direct Field Measurement of Prestress Losses in Box Girder Bridges," Civil Engineering Department, Report No. CCEER-89-4, University of Nevada, Reno, December 1989.

CCEER-90-1 Saiidi, M., E. Maragakis, G. Ghusn, Y. Jiang, and D. Schwartz, "Survey and Evaluation of Nevada's Transportation Infrastructure, Task 7.2 - Highway Bridges, Final Report," Civil Engineering Department, Report No. CCEER 90-1, University of Nevada, Reno, October 1990.

CCEER-90-2 Abdel-Ghaffar, S., E. Maragakis, and M. Saiidi, "Analysis of the Response of Reinforced Concrete Structures During the Whittier Earthquake 1987," Civil Engineering Department, Report No. CCEER 90-2, University of Nevada, Reno, October 1990.

CCEER-91-1 Saiidi, M., E. Hwang, E. Maragakis, and B. Douglas, "Dynamic Testing and the Analysis of the Flamingo Road Interchange," Civil Engineering Department, Report No. CCEER-91-1, University of Nevada, Reno, February 1991.

CCEER-91-2 Norris, G., R. Siddharthan, Z. Zafir, S. Abdel-Ghaffar, and P. Gowda, "Soil-Foundation-Structure Behavior at the Oakland Outer Harbor Wharf," Civil Engineering Department, Report No. CCEER-91-2, University of Nevada, Reno, July 1991.

CCEER-91-3 Norris, G., "Seismic Lateral and Rotational Pile Foundation Stiffnesses at Cypress," Civil Engineering Department, Report No. CCEER-91-3, University of Nevada, Reno, August 1991.

CCEER-91-4 O'Connor, D. and M. Saiidi, "A Study of Protective Overlays for Highway Bridge Decks in Nevada, with Emphasis on Polyester-Styrene Polymer Concrete," Civil Engineering Department, Report No. CCEER-91-4, University of Nevada, Reno, October 1991.

CCEER-91-5 O'Connor, D.N. and M. Saiidi, "Laboratory Studies of Polyester-Styrene Polymer Concrete Engineering Properties," Civil Engineering Department, Report No. CCEER-91-5, University of Nevada, Reno, November 1991.

CCEER-92-1 Straw, D.L. and M. Saiidi, "Scale Model Testing of One-Way Reinforced Concrete Pier Hinges Subject to Combined Axial Force, Shear and Flexure," edited by D.N. O'Connor, Civil Engineering Department, Report No. CCEER-92-1, University of Nevada, Reno, March 1992.

CCEER-92-2 Wehbe, N., M. Saiidi, and F. Gordaninejad, "Basic Behavior of Composite Sections Made of Concrete Slabs and Graphite Epoxy Beams," Civil Engineering Department, Report No. CCEER-92-2, University of Nevada, Reno, August 1992.

CCEER-92-3 Saiidi, M. and E. Hutchens, "A Study of Prestress Changes in A Post-Tensioned Bridge During the First 30 Months," Civil Engineering Department, Report No. CCEER-92-3, University of Nevada, Reno, April 1992.

CCEER-92-4 Saiidi, M., B. Douglas, S. Feng, E. Hwang, and E. Maragakis, "Effects of Axial Force on Frequency of Prestressed Concrete Bridges," Civil Engineering Department, Report No. CCEER-92-4, University of Nevada, Reno, August 1992.

CCEER-92-5 Siddharthan, R., and Z. Zafir, "Response of Layered Deposits to Traveling Surface Pressure Waves," Civil Engineering Department, Report No. CCEER-92-5, University of Nevada, Reno, September 1992.

CCEER-92-6 Norris, G., and Z. Zafir, "Liquefaction and Residual Strength of Loose Sands from Drained Triaxial Tests," Civil Engineering Department, Report No. CCEER-92-6, University of Nevada, Reno, September 1992.

CCEER-92-6-A Norris, G., Siddharthan, R., Zafir, Z. and Madhu, R. "Liquefaction and Residual Strength of Sands from Drained Triaxial Tests," Civil Engineering Department, Report No. CCEER-92-6-A, University of Nevada, Reno, September 1992.

CCEER-92-7 Douglas, B., "Some Thoughts Regarding the Improvement of the University of Nevada, Reno's National Academic Standing," Civil Engineering Department, Report No. CCEER-92-7, University of Nevada, Reno, September 1992.

CCEER-92-8 Saiidi, M., E. Maragakis, and S. Feng, "An Evaluation of the Current Caltrans Seismic Restrainer Design Method," Civil Engineering Department, Report No. CCEER-92-8, University of Nevada, Reno, October 1992.

CCEER-92-9 O'Connor, D., M. Saiidi, and E. Maragakis, "Effect of Hinge Restrainers on the Response of the Madrone Drive Undercrossing During the Loma Prieta Earthquake," Civil Engineering Department, Report No. CCEER-92-9, University of Nevada, Reno, February 1993.

CCEER-92-10 O'Connor, D., and M. Saiidi, "Laboratory Studies of Polyester Concrete: Compressive Strength at Elevated Temperatures and Following Temperature Cycling, Bond Strength to Portland Cement Concrete, and Modulus of Elasticity," Civil Engineering Department, Report No. CCEER-92-10, University of Nevada, Reno, February 1993.

CCEER-92-11 Wehbe, N., M. Saiidi, and D. O'Connor, "Economic Impact of Passage of Spent Fuel Traffic on Two Bridges in Northeast Nevada," Civil Engineering Department, Report No. CCEER-92-11, University of Nevada, Reno, December 1992.

CCEER-93-1 Jiang, Y., and M. Saiidi, "Behavior, Design, and Retrofit of Reinforced Concrete One-way

Bridge Column Hinges," edited by D. O'Connor, Civil Engineering Department, Report No. CCEER-93-1, University of Nevada, Reno, March 1993.

CCEER-93-2 Abdel-Ghaffar, S., E. Maragakis, and M. Saiidi, "Evaluation of the Response of the Aptos Creek Bridge During the 1989 Loma Prieta Earthquake," Civil Engineering Department, Report No. CCEER-93-2, University of Nevada, Reno, June 1993.

CCEER-93-3 Sanders, D.H., B.M. Douglas, and T.L. Martin, "Seismic Retrofit Prioritization of Nevada Bridges," Civil Engineering Department, Report No. CCEER-93-3, University of Nevada, Reno, July 1993.

CCEER-93-4 Abdel-Ghaffar, S., E. Maragakis, and M. Saiidi, "Performance of Hinge Restrainers in the Huntington Avenue Overhead During the 1989 Loma Prieta Earthquake," Civil Engineering Department, Report No. CCEER-93-4, University of Nevada, Reno, June 1993.

CCEER-93-5 Maragakis, E., M. Saiidi, S. Feng, and L. Flournoy, "Effects of Hinge Restrainers on the Response of the San Gregorio Bridge during the Loma Prieta Earthquake," (in final preparation) Civil Engineering Department, Report No. CCEER-93-5, University of Nevada, Reno.

CCEER-93-6 Saiidi, M., E. Maragakis, S. Abdel-Ghaffar, S. Feng, and D. O'Connor, "Response of Bridge Hinge Restrainers during Earthquakes -Field Performance, Analysis, and Design," Civil Engineering Department, Report No. CCEER-93-6, University of Nevada, Reno, May 1993.

CCEER-93-7 Wehbe, N., Saiidi, M., Maragakis, E., and Sanders, D., "Adequacy of Three Highway Structures in Southern Nevada for Spent Fuel Transportation," Civil Engineering Department, Report No. CCEER-93-7, University of Nevada, Reno, August 1993.

CCEER-93-8 Roybal, J., Sanders, D.H., and Maragakis, E., "Vulnerability Assessment of Masonry in the Reno-Carson City Urban Corridor," Civil Engineering Department, Report No. CCEER-93-8, University of Nevada, Reno, May 1993.

CCEER-93-9 Zafir, Z. and Siddharthan, R., "MOVLOAD: A Program to Determine the Behavior of Nonlinear Horizontally Layered Medium Under Moving Load," Civil Engineering Department, Report No. CCEER-93-9, University of Nevada, Reno, August 1993.

CCEER-93-10 O'Connor, D.N., Saiidi, M., and Maragakis, E.A., "A Study of Bridge Column Seismic Damage Susceptibility at the Interstate 80/U.S. 395 Interchange in Reno, Nevada," Civil Engineering Department, Report No. CCEER-93-10, University of Nevada, Reno, October 1993.

CCEER-94-1 Maragakis, E., B. Douglas, and E. Abdelwahed, "Preliminary Dynamic Analysis of a Railroad Bridge," Report CCEER-94-1, January 1994.

CCEER-94-2 Douglas, B.M., Maragakis, E.A., and Feng, S., "Stiffness Evaluation of Pile Foundation of Cazenovia Creek Overpass," Civil Engineering Department, Report No. CCEER-94-2, University of Nevada, Reno, March 1994.

CCEER-94-3 Douglas, B.M., Maragakis, E.A., and Feng, S., "Summary of Pretest Analysis of Cazenovia Creek Bridge," Civil Engineering Department, Report No. CCEER-94-3, University of Nevada, Reno, April 1994.

CCEER-94-4 Norris, G.M., Madhu, R., Valceschini, R., and Ashour, M., "Liquefaction and Residual

Strength of Loose Sands from Drained Triaxial Tests," Report 2, Vol. 1&2, Civil Engineering Department, Report No. CCEER-94-4, University of Nevada, Reno, August 1994.

CCEER-94-5 Saiidi, M., Hutchens, E., and Gardella, D., "Prestress Losses in a Post-Tensioned R/C Box Girder Bridge in Southern Nevada," Civil Engineering Department, CCEER-94-5, University of Nevada, Reno, August 1994.

CCEER-95-1 Siddharthan, R., El-Gamal, M., and Maragakis, E.A., "Nonlinear Bridge Abutment , Verification, and Design Curves," Civil Engineering Department, CCEER-95-1, University of Nevada, Reno, January 1995.

CCEER-95-2 Ashour, M. and Norris, G., "Liquefaction and Undrained Response Evaluation of Sands from Drained Formulation," Civil Engineering Department, Report No. CCEER-95-2, University of Nevada, Reno, February 1995.

CCEER-95-3 Wehbe, N., Saiidi, M., Sanders, D. and Douglas, B., "Ductility of Rectangular Reinforced Concrete Bridge Columns with Moderate Confinement," Civil Engineering Department, Report No. CCEER-95-3, University of Nevada, Reno, July 1995.

CCEER-95-4 Martin, T.., Saiidi, M. and Sanders, D., "Seismic Retrofit of Column-Pier Cap Connections in Bridges in Northern Nevada," Civil Engineering Department, Report No. CCEER-95-4, University of Nevada, Reno, August 1995.

CCEER-95-5 Darwish, I., Saiidi, M. and Sanders, D., "Experimental Study of Seismic Susceptibility Column-Footing Connections in Bridges in Northern Nevada," Civil Engineering Department, Report No. CCEER-95-5, University of Nevada, Reno, September 1995.

CCEER-95-6 Griffin, G., Saiidi, M. and Maragakis, E., "Nonlinear Seismic Response of Isolated Bridges and Effects of Pier Ductility Demand," Civil Engineering Department, Report No. CCEER-95-6, University of Nevada, Reno, November 1995.

CCEER-95-7 Acharya, S.., Saiidi, M. and Sanders, D., "Seismic Retrofit of Bridge Footings and Column-Footing Connections," Civil Engineering Department, Report No. CCEER-95-7, University of Nevada, Reno, November 1995.

CCEER-95-8 Maragakis, E., Douglas, B., and Sandirasegaram, U., "Full-Scale Field Resonance Tests of a Railway Bridge," A Report to the Association of American Railroads, Civil Engineering Department, Report No. CCEER-95-8, University of Nevada, Reno, December 1995.

CCEER-95-9 Douglas, B., Maragakis, E. and Feng, S., "System Identification Studies on Cazenovia Creek Overpass," Report for the National Center for Earthquake Engineering Research, Civil Engineering Department, Report No. CCEER-95-9, University of Nevada, Reno, October 1995.

CCEER-96-1 El-Gamal, M.E. and Siddharthan, R.V., "Programs to Computer Translational Stiffness of Seat-Type Bridge Abutment," Civil Engineering Department, Report No. CCEER-96-1, University of Nevada, Reno, March 1996.

CCEER-96-2 Labia, Y., Saiidi, M. and Douglas, B., "Evaluation and Repair of Full-Scale Prestressed Concrete Box Girders," A Report to the National Science Foundation, Research Grant CMS-9201908, Civil Engineering Department, Report No. CCEER-96-2, University of Nevada, Reno, May 1996.

CCEER-96-3 Darwish, I., Saiidi, M. and Sanders, D., "Seismic Retrofit of R/C Oblong Tapered Bridge

Columns with Inadequate Bar Anchorage in Columns and Footings," A Report to the Nevada Department of Transportation, Civil Engineering Department, Report No. CCEER-96-3, University of Nevada, Reno, May 1996.

CCEER-96-4 Ashour, M., Pilling, R., Norris, G. and Perez, H., "The Prediction of Lateral Load Behavior of Single Piles and Pile Groups Using the Strain Wedge Model," A Report to the California Department of Transportation, Civil Engineering Department, Report No. CCEER-96-4, University of Nevada, Reno, June 1996.

CCEER-97-1-A Rimal, P. and Itani, A. "Sensitivity Analysis of Fatigue Evaluations of Steel Bridges," Center for Earthquake Research, Department of Civil Engineering, University of Nevada, Reno, Nevada Report No. CCEER-97-1-A, September, 1997.

CCEER-97-1-B Maragakis, E., Douglas, B., and Sandirasegaram, U. "Full-Scale Field Resonance Tests of a Railway Bridge," A Report to the Association of American Railroads, Civil Engineering Department, University of Nevada, Reno, May, 1996.

CCEER-97-2 Wehbe, N., Saiidi, M., and D. Sanders, "Effect of Confinement and Flares on the Seismic Performance of Reinforced Concrete Bridge Columns," Civil Engineering Department, Report No. CCEER-97-2, University of Nevada, Reno, September 1997.

CCEER-97-3 Darwish, I., M. Saiidi, G. Norris, and E. Maragakis, "Determination of In-Situ Footing Stiffness Using Full-Scale Dynamic Field Testing," A Report to the Nevada Department of Transportation, Structural Design Division, Carson City, Nevada, Report No. CCEER-97-3, University of Nevada, Reno, October 1997.

CCEER-97-4-A Itani, A. "Cyclic Behavior of Richmond-San Rafael Tower Links," Center for Civil Engineering Earthquake Research, Department of Civil Engineering, University of Nevada, Reno, Nevada, Report No. CCEER-97-4, August 1997.

CCEER-97-4-B Wehbe, N., and M. Saiidi, "User's Manual for RCMC v. 1.2 : A Computer Program for Moment-Curvature Analysis of Confined and Unconfined Reinforced Concrete Sections," Center for Civil Engineering Earthquake Research, Department of Civil Engineering, University of Nevada, Reno, Nevada, Report No. CCEER-97-4, November, 1997.

CCEER-97-5 Isakovic, T., M. Saiidi, and A. Itani, "Influence of new Bridge Configurations on Seismic Performance," Department of Civil Engineering, University of Nevada, Reno, Report No. CCEER-97-5, September, 1997.

CCEER-98-1 Itani, A., Vesco, T. and Dietrich, A., "Cyclic Behavior of "as Built" Laced Members With End Gusset Plates on the San Francisco Bay Bridge," Center for Civil Engineering Earthquake Research, Department of Civil Engineering, University of Nevada, Reno, Nevada Report No. CCEER-98-1, March, 1998.

CCEER-98-2 G. Norris and M. Ashour, "Liquefaction and Undrained Response Evaluation of Sands from Drained Formulation," Center for Civil Engineering Earthquake Research, Department of Civil Engineering, University of Nevada, Reno, Nevada, Report No. CCEER-98-2, May, 1998.

CCEER-98-3 Qingbin, Chen, B. M. Douglas, E. Maragakis, and I. G. Buckle, "Extraction of Nonlinear Hysteretic Properties of Seismically Isolated Bridges from Quick-Release Field Tests," Center for Civil Engineering Earthquake Research, Department of Civil Engineering, University of Nevada, Reno, Nevada, Report No. CCEER-98-3, June, 1998.

CCEER-98-4 Maragakis, E., B. M. Douglas, and C. Qingbin, "Full-Scale Field Capacity Tests of a Railway Bridge," Center for Civil Engineering Earthquake Research, Department of Civil Engineering, University of Nevada, Reno, Nevada, Report No. CCEER-98-4, June, 1998.

CCEER-98-5 Itani, A., Douglas, B., and Woodgate, J., "Cyclic Behavior of Richmond-San Rafael Retrofitted Tower Leg," Center for Civil Engineering Earthquake Research, Department of Civil Engineering, University of Nevada, Reno. Report No. CCEER-98-5, June 1998

CCEER-98-6 Moore, R., Saiidi, M., and Itani, A., "Seismic Behavior of New Bridges with Skew and Curvature," Center for Civil Engineering Earthquake Research, Department of Civil Engineering, University of Nevada, Reno. Report No. CCEER-98-6, October, 1998.

CCEER-98-7 Itani, A and Dietrich, A, "Cyclic Behavior of Double Gusset Plate Connections," Center for Civil Engineering Earthquake Research, Department of Civil Engineering, University of Nevada, Reno, Nevada, Report No. CCEER-98-5, December, 1998.

CCEER-99-1 Caywood, C., M. Saiidi, and D. Sanders, "Seismic Retrofit of Flared Bridge Columns with Steel Jackets," Civil Engineering Department, University of Nevada, Reno, Report No. CCEER-99-1, February 1999.

CCEER-99-2 Mangoba, N., M. Mayberry, and M. Saiidi, "Prestress Loss in Four Box Girder Bridges in Northern Nevada," Civil Engineering Department, University of Nevada, Reno, Report No. CCEER-99-2, March 1999.

CCEER-99-3 Abo-Shadi, N., M. Saiidi, and D. Sanders, "Seismic Response of Bridge Pier Walls in the Weak Direction," Civil Engineering Department, University of Nevada, Reno, Report No. CCEER-99-3, April 1999.

CCEER-99-4 Buzick, A., and M. Saiidi, "Shear Strength and Shear Fatigue Behavior of Full-Scale Prestressed Concrete Box Girders," Civil Engineering Department, University of Nevada, Reno, Report No. CCEER-99-4, April 1999.

CCEER-99-5 Randall, M., M. Saiidi, E. Maragakis and T. Isakovic, "Restrainer Design Procedures For Multi-Span Simply-Supported Bridges," Civil Engineering Department, University of Nevada, Reno, Report No. CCEER-99-5, April 1999.

CCEER-99-6 Wehbe, N. and M. Saiidi, "User's Manual for RCMC v. 1.2, A Computer Program for Moment-Curvature Analysis of Confined and Unconfined Reinforced Concrete Sections," Civil Engineering Department, University of Nevada, Reno, Report No. CCEER-99-6, May 1999.

CCEER-99-7 Burda, J. and A. Itani, "Studies of Seismic Behavior of Steel Base Plates," Civil Engineering Department, University of Nevada, Reno, Report No. CCEER-99-7, May 1999.

CCEER-99-8 Ashour, M. and G. Norris, "Refinement of the Strain Wedge Model Program," Civil Engineering Department, University of Nevada, Reno, Report No. CCEER-99-8, March 1999.

CCEER-99-9 Dietrich, A., and A. Itani, "Cyclic Behavior of Laced and Perforated Steel Members on the San Francisco-Oakland Bay Bridge," Civil Engineering Department, University, Reno, Report No. CCEER-99-9, December 1999.

CCEER 99-10 Itani, A., A. Dietrich, "Cyclic Behavior of Built Up Steel Members and their Connections," Civil Engineering Department, University of Nevada, Reno, Report No. CCEER-99-10, December 1999.

CCEER 99-10-A Itani, A., E. Maragakis and P. He, "Fatigue Behavior of Riveted Open Deck Railroad Bridge Girders," Civil Engineering Department, University of Nevada, Reno, Report No. CCEER-99-10-A, August 1999.

CCEER 99-11 Itani, A., J. Woodgate, "Axial and Rotational Ductility of Built Up Structural Steel Members," Civil Engineering Department, University of Nevada, Reno, Report No. CCEER-99-11, December 1999.

CCEER-99-12 Sgambelluri, M., Sanders, D.H., and Saiidi, M.S., "Behavior of One-Way Reinforced Concrete Bridge Column Hinges in the Weak Direction," Department of Civil Engineering, University of Nevada, Reno, Report No. CCEER-99-12, December 1999.

CCEER-99-13 Laplace, P., Sanders, D.H., Douglas, B, and Saiidi, M, "Shake Table Testing of Flexure Dominated Reinforced Concrete Bridge Columns", Department of Civil Engineering, University of Nevada, Reno, Report No. CCEER-99-13, December 1999.

CCEER-99-14 Ahmad M. Itani, Jose A. Zepeda, and Elizabeth A. Ware "Cyclic Behavior of Steel Moment Frame Connections for the Moscone Center Expansion," Department of Civil Engineering, University of Nevada, Reno, Report No. CCEER-99-14, December 1999.

CCEER 00-1 Ashour, M., and Norris, G. "Undrained Lateral Pile and Pile Group Response in Saturated Sand," Civil Engineering Department, University of Nevada, Reno, Report No. CCEER-00-1, May 1999. January 2000.

CCEER 00-2 Saiidi, M. and Wehbe, N., "A Comparison of Confinement Requirements in Different Codes for Rectangular, Circular, and Double-Spiral RC Bridge Columns," Civil Engineering Department, University of Nevada, Reno, Report No. CCEER-00-2, January 2000.

CCEER 00-3 McElhaney, B., M. Saiidi, and D. Sanders, "Shake Table Testing of Flared Bridge Columns With Steel Jacket Retrofit," Civil Engineering Department, University of Nevada, Reno, Report No. CCEER-00-3, January 2000.

CCEER 00-4 Martinovic, F., M. Saiidi, D. Sanders, and F. Gordaninejad, "Dynamic Testing of Non-Prismatic Reinforced Concrete Bridge Columns Retrofitted with FRP Jackets," Civil Engineering Department, University of Nevada, Reno, Report No. CCEER-00-4, January 2000.

CCEER 00-5 Itani, A., and M. Saiidi, "Seismic Evaluation of Steel Joints for UCLA Center for Health Science Westwood Replacement Hospital," Civil Engineering Department, University of Nevada, Reno, Report No. CCEER-00-5, February 2000.

CCEER 00-6 Will, J. and D. Sanders, "High Performance Concrete Using Nevada Aggregates," Civil Engineering Department, University of Nevada, Reno, Report No. CCEER-00-6, May 2000.

CCEER 00-7 French, C., and M. Saiidi, "A Comparison of Static and Dynamic Performance of Models of Flared Bridge Columns," Civil Engineering Department, University of Nevada, Reno, Report No. CCEER-00-7, October 2000.

CCEER 00-8 Itani, A., H. Sedarat, "Seismic Analysis of the AISI LRFD Design Example of Steel Highway Bridges," Civil Engineering Department, University of Nevada, Reno, Report

No. CCEER 00-08, November 2000.

CCEER 00-9 Moore, J., D. Sanders, and M. Saiidi, "Shake Table Testing of 1960's Two Column Bent with Hinges Bases," Civil Engineering Department, University of Nevada, Reno, Report No. CCEER 00-09, December 2000.

CCEER 00-10 Asthana, M., D. Sanders, and M. Saiidi, "One-Way Reinforced Concrete Bridge Column Hinges in the Weak Direction," Civil Engineering Department, University of Nevada, Reno, Report No. CCEER 00-10, April 2001.

CCEER 01-1 Ah Sha, H., D. Sanders, M. Saiidi, "Early Age Shrinkage and Cracking of Nevada Concrete Bridge Decks," Civil Engineering Department, University of Nevada, Reno, Report No. CCEER 01-01, May 2001.

CCEER 01-2 Ashour, M. and G. Norris, "Pile Group program for Full Material Modeling a Progressive Failure," Civil Engineering Department, University of Nevada, Reno, Report No. CCEER 01-02, July 2001.

CCEER 01-3 Itani, A., C. Lanaud, and P. Dusicka, "Non-Linear Finite Element Analysis of Built-Up Shear Links," Civil Engineering Department, University of Nevada, Reno, Report No. CCEER 01-03, July 2001.

CCEER 01-4 Saiidi, M., J. Mortensen, and F. Martinovic, "Analysis and Retrofit of Fixed Flared Columns with Glass Fiber-Reinforced Plastic Jacketing," Civil Engineering Department, University of Nevada, Reno, Report No. CCEER 01-4, August 2001

CCEER 01-5 Not Published

CCEER 01-6 Laplace, P., D. Sanders, and M. Saiidi, "Experimental Study and Analysis of Retrofitted Flexure and Shear Dominated Circular Reinforced Concrete Bridge Columns Subjected to Shake Table Excitation," Civil Engineering Department, University of Nevada, Reno, Report No. CCEER 01-6, June 2001.

CCEER 01-7 Reppi, F., and D. Sanders, "Removal and Replacement of Cast-in-Place, Post-tensioned, Box Girder Bridge," Civil Engineering Department, University of Nevada, Reno, Report No. CCEER 01-7, December 2001.

CCEER 02-1 Pulido, C., M. Saiidi, D. Sanders, and A. Itani, "Seismic Performance and Retrofitting of Reinforced Concrete Bridge Bents," Civil Engineering Department, University of Nevada, Reno, Report No. CCEER 02-1, January 2002.

CCEER 02-2 Yang, Q., M. Saiidi, H. Wang, and A. Itani, "Influence of Ground Motion Incoherency on Earthquake Response of Multi-Support Structures," Civil Engineering Department, University of Nevada, Reno, Report No. CCEER 02-2, May 2002.

CCEER 02-3 M. Saiidi, B. Gopalakrishnan, E. Reinhardt, and R. Siddharthan, "A Preliminary Study of Shake Table Response of A Two-Column Bridge Bent on Flexible Footings," Civil Engineering Department, University of Nevada, Reno, Report No. CCEER 02-03, June 2002.

CCEER 02-4 Not Published

CCEER 02-5 Banghart, A., Sanders, D., Saiidi, M., "Evaluation of Concrete Mixes for Filling the Steel Arches in the Galena Creek Bridge," Civil Engineering Department, University of Nevada,

Reno, Report No. CCEER 02-05, June 2002.

CCEER 02-6 Dusicka, P., Itani, A., Buckle, I. G., "Cyclic Behavior of Shear Links and Tower Shaft Assembly of San Francisco – Oakland Bay Bridge Tower," Civil Engineering Department, University of Nevada, Reno, Report No. CCEER 02-06, July 2002.

CCEER 02-7 Mortensen, J., and M. Saiidi, "A Performance-Based Design Method for Confinement in Circular Columns," Civil Engineering Department, University of Nevada, Reno, Report No. CCEER 02-07, November 2002.

CCEER 03-1 Wehbe, N., and M. Saiidi, "User's manual for SPMC v. 1.0 : A Computer Program for Moment-Curvature Analysis of Reinforced Concrete Sections with Interlocking Spirals," Center for Civil Engineering Earthquake Research, Department of Civil Engineering, University of Nevada, Reno, Nevada, Report No. CCEER-03-1, May, 2003.

CCEER 03-2 Wehbe, N., and M. Saiidi, "User's manual for RCMC v. 2.0 : A Computer Program for Moment-Curvature Analysis of Confined and Unconfined Reinforced Concrete Sections," Center for Civil Engineering Earthquake Research, Department of Civil Engineering, University of Nevada, Reno, Nevada, Report No. CCEER-03-2, June, 2003.

CCEER 03-3 Nada, H., D. Sanders, and M. Saiidi, "Seismic Performance of RC Bridge Frames with Architectural-Flared Columns," Civil Engineering Department, University of Nevada, Reno, Report No. CCEER 03-3, January 2003.

CCEER 03-4 Reinhardt, E., M. Saiidi, and R. Siddharthan, "Seismic Performance of a CFRP/ Concrete Bridge Bent on Flexible Footings," Civil Engineering Department, University of Nevada, Reno, Report No. CCEER 03-4, August 2003.

CCEER 03-5 Johnson, N., M. Saiidi, A. Itani, and S. Ladkany, "Seismic Retrofit of Octagonal Columns with Pedestal and One-Way Hinge at the Base," Center for Civil Engineering Earthquake Research, Department of Civil Engineering, University of Nevada, Reno, Nevada, and Report No. CCEER-03-5, August 2003.

CCEER 03-6 Mortensen, C., M. Saiidi, and S. Ladkany, "Creep and Shrinkage Losses in Highly Variable Climates," Center for Civil Engineering Earthquake Research, Department of Civil Engineering, University of Nevada, Reno, Report No. CCEER-03-6, September 2003.

CCEER 03- 7 Ayoub, C., M. Saiidi, and A. Itani, "A Study of Shape-Memory-Alloy-Reinforced Beams and Cubes," Center for Civil Engineering Earthquake Research, Department of Civil Engineering, University of Nevada, Reno, Nevada, Report No. CCEER-03-7, October 2003.

CCEER 03-8 Chandane, S., D. Sanders, and M. Saiidi, "Static and Dynamic Performance of RC Bridge Bents with Architectural-Flared Columns," Center for Civil Engineering Earthquake Research, Department of Civil Engineering, University of Nevada, Reno, Nevada, Report No. CCEER-03-8, November 2003.

CCEER 04-1 Olaegbe, C., and Saiidi, M., "Effect of Loading History on Shake Table Performance of A Two-Column Bent with Infill Wall," Center for Civil Engineering Earthquake Research, Department of Civil Engineering, University of Nevada, Reno, Nevada, Report No. CCEER-04-1, January 2004.

CCEER 04-2 Johnson, R., Maragakis, E., Saiidi, M., and DesRoches, R., "Experimental Evaluation of Seismic Performance of SMA Bridge Restrainers," Center for Civil Engineering Earthquake Research, Department of Civil Engineering, University of Nevada, Reno, Nevada, Report No. CCEER-04-2, February 2004.

CCEER 04-3 Moustafa, K., Sanders, D., and Saiidi, M., "Impact of Aspect Ratio on Two-Column Bent Seismic Performance," Center for Civil Engineering Earthquake Research, Department of Civil Engineering, University of Nevada, Reno, Nevada, Report No. CCEER-04-3, February 2004.

CCEER 04-4 Maragakis, E., Saiidi, M., Sanchez-Camargo, F., and Elfass, S., "Seismic Performance of Bridge Restrainers At In-Span Hinges," Center for Civil Engineering Earthquake Research, Department of Civil Engineering, University of Nevada, Reno, Nevada, Report No. CCEER-04-4, March 2004.

CCEER 04-5 Ashour, M., Norris, G. and Elfass, S., "Analysis of Laterally Loaded Long or Intermediate Drilled Shafts of Small or Large Diameter in Layered Soil," Center for Civil Engineering Earthquake Research, Department of Civil Engineering, University of Nevada, Reno, Nevada, Report No. CCEER-04-5, June 2004.

CCEER 04-6 Correal, J., Saiidi, M. and Sanders, D., "Seismic Performance of RC Bridge Columns Reinforced with Two Interlocking Spirals," Center for Civil Engineering Earthquake Research, Department of Civil Engineering, University of Nevada, Reno, Nevada, Report No. CCEER-04-6, August 2004.

CCEER 04-7 Dusicka, P., Itani, A. and Buckle, I., "Cyclic Response and Low Cycle Fatigue Characteristics of Plate Steels," Center for Civil Engineering Earthquake Research, Department of Civil Engineering, University of Nevada, Reno, Nevada, Report No. CCEER-04-7, November 2004.

CCEER 04-8 Dusicka, P., Itani, A. and Buckle, I., "Built-up Shear Links as Energy Dissipaters for Seismic Protection of Bridges," Center for Civil Engineering Earthquake Research, Department of Civil Engineering, University of Nevada, Reno, Nevada, Report No. CCEER-04-8, November 2004.

CCEER 04-9 Sureshkumar, K., Saiidi, S., Itani, A. and Ladkany, S., "Seismic Retrofit of Two-Column Bents with Diamond Shape Columns," Center for Civil Engineering Earthquake Research, Department of Civil Engineering, University of Nevada, Reno, Nevada, Report No. CCEER-04-9, November 2004.

CCEER 05-1 Wang, H. and Saiidi, S., "A Study of RC Columns with Shape Memory Alloy and Engineered Cementitious Composites," Center for Civil Engineering Earthquake Research, Department of Civil Engineering, University of Nevada, Reno, Nevada, Report No. CCEER-05-1, January 2005.

CCEER 05-2 Johnson, R., Saiidi, S. and Maragakis, E., "A Study of Fiber Reinforced Plastics for Seismic Bridge Restrainers," Center for Civil Engineering Earthquake Research, Department of Civil Engineering, University of Nevada, Reno, Nevada, Report No. CCEER-05-2, January 2005.

CCEER 05-3 Carden, L.P., Itani, A.M., Buckle, I.G, "Seismic Load Path in Steel Girder Bridge Superstructures," Center for Civil Engineering Earthquake Research, Department of Civil Engineering, University of Nevada, Reno, Nevada, Report No. CCEER-05-3, January 2005.

CCEER 05-4 Carden, L.P., Itani, A.M., Buckle, I.G, "Seismic Performance of Steel Girder Bridge Superstructures with Ductile End Cross Frames and Seismic Isolation," Center for Civil Engineering Earthquake Research, Department of Civil Engineering, University of Nevada, Reno, Nevada, Report No. CCEER-05-4, January 2005.

CCEER 05-5 Goodwin, E., Maragakis, M., Itani, A. and Luo, S., "Experimental Evaluation of the Seismic Performance of Hospital Piping Subassemblies," Center for Civil Engineering Earthquake Research, Department of Civil Engineering, University of Nevada, Reno, Nevada, Report No. CCEER-05-5, February 2005.

CCEER 05-6 Zadeh M. S., Saiidi, S, Itani, A. and Ladkany, S., "Seismic Vulnerability Evaluation and Retrofit Design of Las Vegas Downtown Viaduct," Center for Civil Engineering Earthquake Research, Department of Civil Engineering, University of Nevada, Reno, Nevada, Report No. CCEER-05-6, February 2005.

CCEER 05-7 Phan, V., Saiidi, S. and Anderson, J., "Near Fault (Near Field) Ground Motion Effects on Reinforced Concrete Bridge Columns," Center for Civil Engineering Earthquake Research, Department of Civil Engineering, University of Nevada, Reno, Nevada, Report No. CCEER-05-7, August 2005.

CCEER 05-8 Carden, L., Itani, A. and Laplace, P., "Performance of Steel Props at the UNR Fire Science Academy subjected to Repeated Fire," Center for Civil Engineering Earthquake Research, Department of Civil Engineering, University of Nevada, Reno, Nevada, Report No. CCEER-05-8, August 2005.

CCEER 05-9 Yamashita, R. and Sanders, D., "Shake Table Testing and an Analytical Study of Unbonded Prestressed Hollow Concrete Column Constructed with Precast Segments," Center for Civil Engineering Earthquake Research, Department of Civil Engineering, University of Nevada, Reno, Nevada, Report No. CCEER-05-9, August 2005.

CCEER 05-10 Not Published

CCEER 05-11 Carden, L., Itani., A., and Peckan, G., "Recommendations for the Design of Beams and Posts in Bridge Falsework," Center for Civil Engineering Earthquake Research, Department of Civil Engineering, University of Nevada, Reno, Nevada, Report No. CCEER-05-11, October 2005.

CCEER 06-01 Cheng, Z., Saiidi, M., and Sanders, D., "Development of a Seismic Design Method for Reinforced Concrete Two-Way Bridge Column Hinges," Center for Civil Engineering Earthquake Research, Department of Civil Engineering, University of Nevada, Reno, Nevada, Report No. CCEER-06-01, February 2006.

CCEER 06-02 Johnson, N., Saiidi, M., and Sanders, D., "Large-Scale Experimental and Analytical Studies of a Two-Span Reinforced Concrete Bridge System," Center for Civil Engineering Earthquake Research, Department of Civil Engineering, University of Nevada, Reno, Nevada, Report No. CCEER-06-02, March 2006.

CCEER 06-03 Saiidi, M., Ghasemi, H. and Tiras, A., "Seismic Design and Retrofit of Highway Bridges," Proceedings, Second US-Turkey Workshop, Center for Civil Engineering Earthquake Research, Department of Civil Engineering, University of Nevada, Reno, Nevada, Report No. CCEER-06-03, May 2006.

CCEER 07-01 O'Brien, M., Saiidi, M. and Sadrossadat-Zadeh, M., "A Study of Concrete Bridge Columns Using Innovative Materials Subjected to Cyclic Loading," Center for Civil Engineering Earthquake Research, Department of Civil Engineering, University of Nevada, Reno, Nevada, Report No. CCEER-07-01, January 2007.

CCEER 07-02 Sadrossadat-Zadeh, M. and Saiidi, M., "Effect of Strain rate on Stress-Strain Properties and Yield Propagation in Steel Reinforcing Bars," Center for Civil Engineering Earthquake

Research, Department of Civil Engineering, University of Nevada, Reno, Nevada, Report No. CCEER-07-02, January 2007.

CCEER 07-03 Sadrossadat-Zadeh, M. and Saiidi, M., "Analytical Study of NEESR-SG 4-Span Bridge Model Using OpenSees," Center for Civil Engineering Earthquake Research, Department of Civil Engineering, University of Nevada, Reno, Nevada, Report No. CCEER-07-03, January 2007.

CCEER 07-04 Nelson, R., Saiidi, M. and Zadeh, S., "Experimental Evaluation of Performance of Conventional Bridge Systems," Center for Civil Engineering Earthquake Research, Department of Civil Engineering, University of Nevada, Reno, Nevada, Report No. CCEER-07-04, October 2007.

CCEER 07-05 Bahen, N. and Sanders, D., "Strut-and-Tie Modeling for Disturbed Regions in Structural Concrete Members with Emphasis on Deep Beams," Center for Civil Engineering Earthquake Research, Department of Civil Engineering, University of Nevada, Reno, Nevada, Report No. CCEER-07-05, December 2007.

CCEER 07-06 Choi, H., Saiidi, M. and Somerville, P., "Effects of Near-Fault Ground Motion and Fault-Rupture on the Seismic Response of Reinforced Concrete Bridges," Center for Civil Engineering Earthquake Research, Department of Civil Engineering, University of Nevada, Reno, Nevada, Report No. CCEER-07-06, December 2007.

CCEER 07-07 Ashour M. and Norris, G., "Report and User Manual on Strain Wedge Model Computer Program for Files and Large Diameter Shafts with LRFD Procedure," Center for Civil Engineering Earthquake Research, Department of Civil Engineering, University of Nevada, Reno, Nevada, Report No. CCEER-07-07, October 2007.

CCEER 08-01 Doyle, K. and Saiidi, M., "Seismic Response of Telescopic Pipe Pin Connections," Center for Civil Engineering Earthquake Research, Department of Civil Engineering, University of Nevada, Reno, Nevada, Report No. CCEER-08-01, February 2008.

CCEER 08-02 Taylor, M. and Sanders, D., "Seismic Time History Analysis and Instrumentation of the Galena Creek Bridge," Center for Civil Engineering Earthquake Research, Department of Civil Engineering, University of Nevada, Reno, Nevada, Report No. CCEER-08-02, April 2008.

CCEER 08-03 Abdel-Mohti, A. and Pekcan, G., "Seismic Response Assessment and Recommendations for the Design of Skewed Post-Tensioned Concrete Box-Girder Highway Bridges," Center for Civil Engineering Earthquake Research, Department of Civil and Environmental Engineering, University of Nevada, Reno, Nevada, Report No. CCEER-08-03, September 2008.

CCEER 08-04 Saiidi, M., Ghasemi, H. and Hook, J., "Long Term Bridge Performance Monitoring, Assessment & Management," Proceedings, FHWA/NSF Workshop on Future Directions," Center for Civil Engineering Earthquake Research, Department of Civil and Environmental Engineering, University of Nevada, Reno, Nevada, Report No. CCEER 08-04, September 2008.

CCEER 09-01 Brown, A., and Saiidi, M., "Investigation of Near-Fault Ground Motion Effects on Substandard Bridge Columns and Bents," Center for Civil Engineering Earthquake Research, Department of Civil and Environmental Engineering, University of Nevada, Reno, Nevada, Report No. CCEER-09-01, July 2009.

CCEER 09-02 Linke, C., Pekcan, G., and Itani, A., "Detailing of Seismically Resilient Special Truss Moment Frames," Center for Civil Engineering Earthquake Research, Department of Civil and Environmental Engineering, University of Nevada, Reno, Nevada, Report No. CCEER-09-02, August 2009.

CCEER 09-03 Hillis, D., and Saiidi, M., "Design, Construction, and Nonlinear Dynamic Analysis of Three Bridge Bents Used in a Bridge System Test," Center for Civil Engineering Earthquake Research, Department of Civil and Environmental Engineering, University of Nevada, Reno, Nevada, Report No. CCEER-09-03, August 2009.

CCEER 09-04 Bahrami, H., Itani, A., and Buckle, I., "Guidelines for the Seismic Design of Ductile End Cross Frames in Steel Girder Bridge Superstructures," Center for Civil Engineering Earthquake Research, Department of Civil and Environmental Engineering, University of Nevada, Reno, Nevada, Report No. CCEER-09-04, September 2so009.

CCEER 10-01 Zaghi, A. E., and Saiidi, M., "Seismic Design of Pipe-Pin Connections in Concrete Bridges," Center for Civil Engineering Earthquake Research, Department of Civil and Environmental Engineering, University of Nevada, Reno, Nevada, Report No. CCEER-10-01, January 2010.

CCEER 10-02 Pooranampillai, S., Elfass, S., and Norris, G., "Laboratory Study to Assess Load Capacity Increase of Drilled Shafts through Post Grouting," Center for Civil Engineering Earthquake Research, Department of Civil and Environmental Engineering, University of Nevada, Reno, Nevada, Report No. CCEER-10-02, January 2010.

CCEER 10-03 Itani, A., Grubb, M., and Monzon, E, "Proposed Seismic Provisions and Commentary for Steel Plate Girder Superstructures," Center for Civil Engineering Earthquake Research, Department of Civil and Environmental Engineering, University of Nevada, Reno, Nevada, Report No. CCEER-10-03, June 2010.

CCEER 10-04 Cruz-Noguez, C., Saiidi, M., "Experimental and Analytical Seismic Studies of a Four-Span Bridge System with Innovative Materials," Center for Civil Engineering Earthquake Research, Department of Civil and Environmental Engineering, University of Nevada, Reno, Nevada, Report No. CCEER-10-04, September 2010.

CCEER 10-05 Vosooghi, A., Saiidi, M., "Post-Earthquake Evaluation and Emergency Repair of Damaged RC Bridge Columns Using CFRP Materials," Center for Civil Engineering Earthquake Research, Department of Civil and Environmental Engineering, University of Nevada, Reno, Nevada, Report No. CCEER-10-05, September 2010.

CCEER 10-06 Ayoub, M., Sanders, D., "Testing of Pile Extension Connections to Slab Bridges," Center for Civil Engineering Earthquake Research, Department of Civil and Environmental Engineering, University of Nevada, Reno, Nevada, Report No. CCEER-10-06, October 2010.

CCEER 10-07 Builes-Mejia, J. C. and Itani, A., "Stability of Bridge Column Rebar Cages during Construction," Center for Civil Engineering Earthquake Research, Department of Civil and Environmental Engineering, University of Nevada, Reno, Nevada, Report No. CCEER-10-07, November 2010.

CCEER 10-08 Monzon, E.V., "Seismic Performance of Steel Plate Girder Bridges with Integral Abutments," Center for Civil Engineering Earthquake Research, Department of Civil and Environmental Engineering, University of Nevada, Reno, Nevada, Report No. CCEER-10-08, November 2010.

CCEER 11-01 Motaref, S., Saiidi, M., and Sanders, D., "Seismic Response of Precast Bridge Columns with Energy Dissipating Joints," Center for Civil Engineering Earthquake Research, Department of Civil and Environmental Engineering, University of Nevada, Reno, Nevada, Report No. CCEER-11-01, May 2011.

CCEER 11-02 Harrison, N. and Sanders, D., "Preliminary Seismic Analysis and Design of Reinforced Concrete Bridge Columns for Curved Bridge Experiments," Center for Civil Engineering Earthquake Research, Department of Civil and Environmental Engineering, University of Nevada, Reno, Nevada, Report No. CCEER-11-02, May 2011.

CCEER 11-03 Vallejera, J. and Sanders, D., "Instrumentation and Monitoring the Galena Creek Bridge," Center for Civil Engineering Earthquake Research, Department of Civil and Environmental Engineering, University of Nevada, Reno, Nevada, Report No. CCEER-11-03, September 2011.

CCEER 11-04 Levi, M., Sanders, D., and Buckle, I., "Seismic Response of Columns in Horizontally Curved Bridges," Center for Civil Engineering Earthquake Research, Department of Civil and Environmental Engineering, University of Nevada, Reno, Nevada, Report No. CCEER-11-04, December 2011.

CCEER 12-01 Saiidi, M., "NSF International Workshop on Bridges of the Future – Wide Spread Implementation of Innovation," Center for Civil Engineering Earthquake Research, Department of Civil and Environmental Engineering, University of Nevada, Reno, Nevada, Report No. CCEER-12-01, January 2012.

CCEER 12-02 Larkin, A.S., Sanders, D., and Saiidi, M., "Unbonded Prestressed Columns for Earthquake Resistance," Center for Civil Engineering Earthquake Research, Department of Civil and Environmental Engineering, University of Nevada, Reno, Nevada, Report No. CCEER-12-02, January 2012.

CCEER 12-03 Arias-Acosta, J. G., Sanders, D., "Seismic Performance of Circular and Interlocking Spirals RC Bridge Columns under Bidirectional Shake Table Loading Part 1," Center for Civil Engineering Earthquake Research, Department of Civil and Environmental Engineering, University of Nevada, Reno, Nevada, Report No. CCEER-12-03, September 2012.

CCEER 12-04 Cukrov, M.E., Sanders, D., "Seismic Performance of Prestressed Pile-To-Bent Cap Connections," Center for Civil Engineering Earthquake Research, Department of Civil and Environmental Engineering, University of Nevada, Reno, Nevada, Report No. CCEER-12-04, September 2012.

CCEER 13-01 Carr, T. and Sanders, D., "Instrumentation and Dynamic Characterization of the Galena Creek Bridge," Center for Civil Engineering Earthquake Research, Department of Civil and Environmental Engineering, University of Nevada, Reno, Nevada, Report No. CCEER-13-01, January 2013.

CCEER 13-02 Vosooghi, A. and Buckle, I., "Evaluation of the Performance of a Conventional Four-Span Bridge During Shake Table Tests," Center for Civil Engineering Earthquake Research, Department of Civil and Environmental Engineering, University of Nevada, Reno, Nevada, Report No. CCEER-13-02, January 2013.

CCEER 13-03 Amirihormozaki, E. and Pekcan, G., "Analytical Fragility Curves for Horizontally Curved Steel Girder Highway Bridges," Center for Civil Engineering Earthquake Research, Department of Civil and Environmental Engineering, University of Nevada, Reno, Nevada, Report No. CCEER-13-03, February 2013.

CCEER 13-04 Almer, K. and Sanders, D., "Longitudinal Seismic Performance of Precast Bridge Girders Integrally Connected to a Cast-in-Place Bentcap," Center for Civil Engineering Earthquake Research, Department of Civil and Environmental Engineering, University of Nevada, Reno, Nevada, Report No. CCEER-13-04, April 2013.

CCEER 13-05 Monzon, E.V., Itani, A.I., and Buckle, I.G., "Seismic Modeling and Analysis of Curved Steel Plate Girder Bridges," Center for Civil Engineering Earthquake Research, Department of Civil and Environmental Engineering, University of Nevada, Reno, Nevada, Report No. CCEER-13-05, April 2013.

CCEER 13-06 Monzon, E.V., Buckle, I.G., and Itani, A.I., "Seismic Performance of Curved Steel Plate Girder Bridges with Seismic Isolation," Center for Civil Engineering Earthquake Research, Department of Civil and Environmental Engineering, University of Nevada, Reno, Nevada, Report No. CCEER-13-06, April 2013.

CCEER 13-07 Monzon, E.V., Buckle, I.G., and Itani, A.I., "Seismic Response of Isolated Bridge Superstructure to Incoherent Ground Motions," Center for Civil Engineering Earthquake Research, Department of Civil and Environmental Engineering, University of Nevada, Reno, Nevada, Report No. CCEER-13-07, April 2013.

CCEER 13-08 Haber, Z.B., Saiidi, M.S., and Sanders, D.H., "Precast Column-Footing Connections for Accelerated Bridge Construction in Seismic Zones," Center for Civil Engineering Earthquake Research, Department of Civil and Environmental Engineering, University of Nevada, Reno, Nevada, Report No. CCEER-13-08, April 2013.

CCEER 13-09 Ryan, K.L., Coria, C.B., and Dao, N.D., "Large Scale Earthquake Simulation of a Hybrid Lead Rubber Isolation System Designed under Nuclear Seismicity Considerations," Center for Civil Engineering Earthquake Research, Department of Civil and Environmental Engineering, University of Nevada, Reno, Nevada, Report No. CCEER-13-09, April 2013.

CCEER 13-10 Wibowo, H., Sanford, D.M., Buckle, I.G., and Sanders, D.H., "The Effect of Live Load on the Seismic Response of Bridges," Center for Civil Engineering Earthquake Research, Department of Civil and Environmental Engineering, University of Nevada, Reno, Nevada, Report No. CCEER-13-10, May 2013.

CCEER 13-11 Sanford, D.M., Wibowo, H., Buckle, I.G., and Sanders, D.H., "Preliminary Experimental Study on the Effect of Live Load on the Seismic Response of Highway Bridges," Center for Civil Engineering Earthquake Research, Department of Civil and Environmental Engineering, University of Nevada, Reno, Nevada, Report No. CCEER-13-11, May 2013.

CCEER 13-12 Saad, A.S., Sanders, D.H., and Buckle, I.G., "Assessment of Foundation Rocking Behavior in Reducing the Seismic Demand on Horizontally Curved Bridges," Center for Civil Engineering Earthquake Research, Department of Civil and Environmental Engineering, University of Nevada, Reno, Nevada, Report No. CCEER-13-12, June 2013.

CCEER 13-13 Ardakani, S.M.S. and Saiidi, M.S., "Design of Reinforced Concrete Bridge Columns for Near-Fault Earthquakes," Center for Civil Engineering Earthquake Research, Department

of Civil and Environmental Engineering, University of Nevada, Reno, Nevada, Report No. CCEER-13-13, July 2013.

CCEER 13-14 Wei, C. and Buckle, I., "Seismic Analysis and Response of Highway Bridges with Hybrid Isolation," Center for Civil Engineering Earthquake Research, Department of Civil and Environmental Engineering, University of Nevada, Reno, Nevada, Report No. CCEER-13-14, August 2013.

CCEER 13-15 Wibowo, H., Buckle, I.G., and Sanders, D.H., "Experimental and Analytical Investigations on the Effects of Live Load on the Seismic Performance of a Highway Bridge," Center for Civil Engineering Earthquake Research, Department of Civil and Environmental Engineering, University of Nevada, Reno, Nevada, Report No. CCEER-13-15, August 2013.

CCEER 13-16 Itani, A.M., Monzon, E.V., Grubb, M., and Amirihormozaki, E. "Seismic Design and Nonlinear Evaluation of Steel I-Girder Bridges with Ductile End Cross-Frames," Center for Civil Engineering Earthquake Research, Department of Civil and Environmental Engineering, University of Nevada, Reno, Nevada, Report No. CCEER-13-16, September 2013.

CCEER 13-17 Kavianipour, F. and Saiidi, M.S., "Experimental and Analytical Seismic Studies of a Four-span Bridge System with Composite Piers," Center for Civil Engineering Earthquake Research, Department of Civil and Environmental Engineering, University of Nevada, Reno, Nevada, Report No. CCEER-13-17, September 2013.

CCEER 13-18 Mohebbi, A., Ryan, K., and Sanders, D., "Seismic Response of a Highway Bridge with Structural Fuses for Seismic Protection of Piers," Center for Civil Engineering Earthquake Research, Department of Civil and Environmental Engineering, University of Nevada, Reno, Nevada, Report No. CCEER-13-18, December 2013.

CCEER 13-19 Guzman Pujols, Jean C., Ryan, K.L., "Development of Generalized Fragility Functions for Seismic Induced Content Disruption," Center for Civil Engineering Earthquake Research, Department of Civil and Environmental Engineering, University of Nevada, Reno, Nevada, Report No. CCEER-13-19, December 2013.

CCEER 14-01 Salem, M. M. A., Pekcan, G., and Itani, A., "Seismic Response Control Of Structures Using Semi-Active and Passive Variable Stiffness Devices," Center for Civil Engineering Earthquake Research, Department of Civil and Environmental Engineering, University of Nevada, Reno, Nevada, Report No. CCEER-14-01, May 2014.

CCEER 14-02 Saini, A. and Saiidi, M., "Performance-Based Probabilistic Damage Control Approach for Seismic Design of Bridge Columns," Center For Civil Engineering Earthquake Research, Department Of Civil and Environmental Engineering, University of Nevada, Reno, Nevada, Report No. CCEER-14-02, May 2014.

CCEER 14-03 Saini, A. and Saiidi, M., "Post Earthquake Damage Repair of Various Reinforced Concrete Bridge Components," Center For Civil Engineering Earthquake Research, Department Of Civil and Environmental Engineering, University of Nevada, Reno, Nevada, Report No. CCEER-14-03, May 2014.

CCEER 14-04 Monzon, E.V., Itani, A.M., and Grubb, M.A., "Nonlinear Evaluation of the Proposed Seismic Design Procedure for Steel Bridges with Ductile End Cross Frames," Center For Civil Engineering Earthquake Research, Department Of Civil and Environmental Engineering, University of Nevada, Reno, Nevada, Report No. CCEER-14-04, July 2014.

CCEER 14-05 Nakashoji, B. and Saiidi, M.S., "Seismic Performance of Square Nickel-Titanium Reinforced ECC Columns with Headed Couplers," Center For Civil Engineering Earthquake Research, Department Of Civil and Environmental Engineering, University of Nevada, Reno, Nevada, Report No. CCEER-14-05, July 2014.

CCEER 14-06 Tazarv, M. and Saiidi, M.S., "Next Generation of Bridge Columns for Accelerated Bridge Construction in High Seismic Zones," Center For Civil Engineering Earthquake Research, Department Of Civil and Environmental Engineering, University of Nevada, Reno, Nevada, Report No. CCEER-14-06, August 2014.

CCEER 14-07 Mehrsoroush, A. and Saiidi, M.S., "Experimental and Analytical Seismic Studies of Bridge Piers with Innovative Pipe Pin Column-Footing Connections and Precast Cap Beams," Center For Civil Engineering Earthquake Research, Department Of Civil and Environmental Engineering, University of Nevada, Reno, Nevada, Report No. CCEER-14-07, December 2014.

CCEER 15-01 Dao, N.D. and Ryan, K.L., "Seismic Response of a Full-scale 5-story Steel Frame Building Isolated by Triple Pendulum Bearings under 3D Excitations," Center For Civil Engineering Earthquake Research, Department Of Civil and Environmental Engineering, University of Nevada, Reno, Nevada, Report No. CCEER-15-01, January 2015.

CCEER 15-02 Allen, B.M. and Sanders, D.H., "Post-Tensioning Duct Air Pressure Testing Effects on Web Cracking," Center For Civil Engineering Earthquake Research, Department Of Civil and Environmental Engineering, University of Nevada, Reno, Nevada, Report No. CCEER-15-02, January 2015.

CCEER 15-03 Akl, A. and Saiidi, M.S., "Time-Dependent Deflection of In-Span Hinges in Prestressed Concrete Box Girder Bridges," Center For Civil Engineering Earthquake Research, Department Of Civil and Environmental Engineering, University of Nevada, Reno, Nevada, Report No. CCEER-15-03, May 2015.

CCEER 15-04 Zargar Shotorbani, H. and Ryan, K., "Analytical and Experimental Study of Gap Damper System to Limit Seismic Isolator Displacements in Extreme Earthquakes," Center For Civil Engineering Earthquake Research, Department Of Civil and Environmental Engineering, University of Nevada, Reno, Nevada, Report No. CCEER-15-04, June 2015.

CCEER 15-05 Wieser, J., Maragakis, E.M., and Buckle, I., "Experimental and Analytical Investigation of Seismic Bridge-Abutment Interaction in a Curved Highway Bridge," Center For Civil Engineering Earthquake Research, Department Of Civil and Environmental Engineering, University of Nevada, Reno, Nevada, Report No. CCEER-15-05, July 2015.

CCEER 15-06 Tazarv, M. and Saiidi, M.S., "Design and Construction of Precast Bent Caps with Pocket Connections for High Seismic Regions," Center For Civil Engineering Earthquake Research, Department Of Civil and Environmental Engineering, University of Nevada, Reno, Nevada, Report No. CCEER-15-06, August 2015.

CCEER 15-07 Tazarv, M. and Saiidi, M.S., "Design and Construction of Bridge Columns Incorporating Mechanical Bar Splices in Plastic Hinge Zones," Center For Civil Engineering Earthquake Research, Department Of Civil and Environmental Engineering, University of Nevada, Reno, Nevada, Report No. CCEER-15-07, August 2015.

CCEER 15-08 Sarraf Shirazi, R., Pekcan, G., and Itani, A.M., "Seismic Response and Analytical Fragility Functions for Curved Concrete Box-Girder Bridges," Center For Civil

Engineering Earthquake Research, Department Of Civil and Environmental Engineering, University of Nevada, Reno, Nevada, Report No. CCEER-15-08, December 2015.

CCEER 15-09 Coria, C.B., Ryan, K.L., and Dao, N.D., "Response of Lead Rubber Bearings in a Hybrid Isolation System During a Large Scale Shaking Experiment of an Isolated Building," Center For Civil Engineering Earthquake Research, Department Of Civil and Environmental Engineering, University of Nevada, Reno, Nevada, Report No. CCEER-15-09, December 2015.

CCEER 16-01 Mehraein, M and Saiidi, M.S., "Seismic Performance of Bridge Column-Pile-Shaft Pin Connections for Application in Accelerated Bridge Construction," Center For Civil Engineering Earthquake Research, Department Of Civil and Environmental Engineering, University of Nevada, Reno, Nevada, Report No. CCEER-16-01, May 2016.

CCEER 16-02 Varela Fontecha, S. and Saiidi, M.S., "Resilient Earthquake-Resistant Bridges Designed For Disassembly," Center For Civil Engineering Earthquake Research, Department Of Civil and Environmental Engineering, University of Nevada, Reno, Nevada, Report No. CCEER-16-02, May 2016.

CCEER 16-03 Mantawy, I. M, and Sanders, D. H., "Assessment of an Earthquake Resilient Bridge with Pretensioned, Rocking Columns," Center For Civil Engineering Earthquake Research, Department Of Civil and Environmental Engineering, University of Nevada, Reno, Nevada, Report No. CCEER-16-03, May 2016.

CCEER 16-04 Mohammed, M, Biasi, G., and Sanders, D., "Post-earthquake Assessment of Nevada Bridges using ShakeMap/ShakeCast," Center For Civil Engineering Earthquake Research, Department Of Civil and Environmental Engineering, University of Nevada, Reno, Nevada, Report No. CCEER-16-04, May 2016.

CCEER 16-05 Jones, J, Ryan, K., and Saiidi, M, "Toward Successful Implementation of Prefabricated Deck Panels to Accelerate the Bridge Construction Process," Center For Civil Engineering Earthquake Research, Department Of Civil and Environmental Engineering, University of Nevada, Reno, Nevada, Report No. CCEER-16-05, August 2016.

CCEER 16-06 Mehrsoroush, A. and Saiidi, M., "Probabilistic Seismic Damage Assessment for Sub-standard Bridge Columns," Center For Civil Engineering Earthquake Research, Department Of Civil and Environmental Engineering, University of Nevada, Reno, Nevada, Report No. CCEER-16-06, November 2016.

CCEER 16-07 Nielsen, T., Maree, A., and Sanders, D., "Experimental Investigation into the Long-Term Seismic Performance of Dry Storage Casks," Center For Civil Engineering Earthquake Research, Department Of Civil and Environmental Engineering, University of Nevada, Reno, Nevada, Report No. CCEER-16-07, December 2016.

CCEER 16-08 Wu, S., Buckle, I., and Itani, A., "Effect of Skew on Seismic Performance of Bridges with Seat-Type Abutments," Center For Civil Engineering Earthquake Research, Department Of Civil and Environmental Engineering, University of Nevada, Reno, Nevada, Report No. CCEER-16-08, December 2016.

CCEER 16-09 Mohammed, M., and Sanders, D., "Effect of Earthquake Duration on Reinforced Concrete Bridge Columns," Center For Civil Engineering Earthquake Research, Department Of Civil and Environmental Engineering, University of Nevada, Reno, Nevada, Report No. CCEER-16-09, December 2016.

CCEER 16-10 Guzman Pujols, J., and Ryan, K., "Slab Vibration and Horizontal-Vertical Coupling in the Seismic Response of Irregular Base-Isolated and Conventional Buildings," Center For Civil Engineering Earthquake Research, Department Of Civil and Environmental Engineering, University of Nevada, Reno, Nevada, Report No. CCEER-16-10, December 2016.

CCEER 17-01 White, L., Ryan, K., and Buckle, I., "Thermal Gradients in Southwestern United States and the Effect on Bridge Bearing Loads," Center For Civil Engineering Earthquake Research, Department Of Civil and Environmental Engineering, University of Nevada, Reno, Nevada, Report No. CCEER-17-01, May 2017.

CCEER 17-02 Mohebbi, A., Saiidi, M., and Itani, A., "Development and Seismic Evaluation of Pier Systems w/Pocket Connections, CFRP Tendons, and ECC/UHPC Columns," Center For Civil Engineering Earthquake Research, Department Of Civil and Environmental Engineering, University of Nevada, Reno, Nevada, Report No. CCEER-17-02, May 2017.

CCEER 17-03 Mehrsoroush, A., Saiidi, M., and Ryan, K., "Development of Earthquake-resistant Precast Pier Systems for Accelerated Bridge Construction in Nevada," Center For Civil Engineering Earthquake Research, Department Of Civil and Environmental Engineering, University of Nevada, Reno, Nevada, Report No. CCEER-17-03, June 2017.

CCEER 17-04 Abdollahi, B., Saiidi, M., Siddharthan, R., and Elfass, S., "Shake Table Studies on Soil-Abutment-Structure Interaction in Skewed Bridges," Center For Civil Engineering Earthquake Research, Department Of Civil and Environmental Engineering, University of Nevada, Reno, Nevada, Report No. CCEER-17-04, July 2017.

CCEER 17-05 Shrestha, G., Itani, A., and Saiidi, M., "Seismic Performance of Precast Full-Depth Decks in Accelerated Bridge Construction," Center for Civil Engineering Earthquake Research, Department of Civil and Environmental Engineering, University of Nevada, Reno, Nevada, Report No. CCEER-17-05, September 2017.

CCEER 17-06 Wu, S., Buckle, I., and Ryan, K., "Large-Scale Experimental Verification of an Optically-Based Sensor System for Monitoring Structural Response," Center for Civil Engineering Earthquake Research, Department of Civil and Environmental Engineering, University of Nevada, Reno, Nevada, Report No. CCEER-17-06, October 2017.

CCEER 17-07 Nada, H., and Sanders, D., "Analytical Investigation into Bridge Column Innovations for Mitigating Earthquake Damage," Center For Civil Engineering Earthquake Research, Department Of Civil and Environmental Engineering, University of Nevada, Reno, Nevada, Report No. CCEER-17-07, October 2017.

CCEER 18-01 Maree, A. F., and Sanders, D., "Performance and Design of Anchorage Zones for Post-Tensioned Box Girder Bridges," Center for Civil Engineering Earthquake Research, Department of Civil and Environmental Engineering, University of Nevada, Reno, Nevada, Report No. CCEER-18-01, January 2018.

CCEER 18-02 Mostafa, K., and Sanders, D., "Improving the Long-Term Performance of Bridge Decks using Deck and Crack Sealers," Center for Civil Engineering Earthquake Research, Department of Civil and Environmental Engineering, University of Nevada, Reno, Nevada, Report No. CCEER-18-02, March 2018.

CCEER 18-03 Blount, S., Ryan, K., Henry, R., Lu, Y., and Elwood, K., "Evaluation of lower damage concepts for enhanced repairability of reinforced concrete walls," Center for Civil

Engineering Earthquake Research, Department of Civil and Environmental Engineering, University of Nevada, Reno, Nevada, Report No. CCEER-18-03, June 2018.

CCEER 18-04 Mohebbi, A., Jordan, E., and Saiidi, M., "Exploratory Experimental Studies of Spliced Cam Shape Memory Alloy Bars for Seismic Application," Center for Civil Engineering Earthquake Research, Department Of Civil and Environmental Engineering, University of Nevada, Reno, Nevada, Report No. CCEER-18-04, September 2018.

CCEER 19-01 Saint Pierre, E., Elfass, S., Watters, R., Norris, G., and Ashour, M. "Improving Strain Wedge Model Capabilities in Analyzing Laterally Loaded Drilled Shafts in Cemented Soils," Center for Civil Engineering Earthquake Research, Department of Civil and Environmental Engineering, University of Nevada, Reno, Nevada, Report No. CCEER-19-01, March 2019.

CCEER 19-02 Benjumea, J., Saiidi, M., and Itani, A., "Experimental and Analytical Seismic Studies of a Two-Span Bridge System with Precast Concrete Elements and ABC Connections," Center for Civil Engineering Earthquake Research, Department of Civil and Environmental Engineering, University of Nevada, Reno, Nevada, Report No. CCEER-19-02, May 2019.

CCEER 19-03 Subedi, D., Moustafa, M., and Saiidi, M., "Non-Proprietary UHPC for Anchorage of Large Diameter Column Bars in Grouted Ducts," Center for Civil Engineering Earthquake Research, Department of Civil and Environmental Engineering, University of Nevada, Reno, Nevada, Report No. CCEER-19-03, May 2019.

CCEER 19-04 Shoushtari, E, D., Saiidi, M., Itani, A., and Moustafa, M., "Shake Table Studies of a Steel Girder Bridge System with ABC Connections," Center for Civil Engineering Earthquake Research, Department of Civil and Environmental Engineering, University of Nevada, Reno, Nevada, Report No. CCEER-19-04, June 2019.

CCEER 19-05 Wu, S., Miah, M., and McCallen, D., "Four Canonical Steel Moment Frame Buildings and Inter-Code Comparisons of Nonlinear Building Response," Center for Civil Engineering Earthquake Research, Department of Civil and Environmental Engineering, University of Nevada, Reno, Nevada, Report No. CCEER-19-05, September 2019.

CCEER 20-01 Schwartz, T., Saiidi, M., and Moustafa, M., "Simplifying Cast-in-Place Joint Design Using ABC Pocket Connection Details in High Seismic Regions," Center for Civil Engineering Earthquake Research, Department of Civil and Environmental Engineering, University of Nevada, Reno, Nevada, Report No. CCEER-20-01, January 2020.

CCEER 20-02 Shrestha, G., Saiidi, M., and Sanders, D., "Seismic Studies of Spliced Columns and Anchorage of Large Diameter Bars in Grouted Duct," Center for Civil Engineering Earthquake Research, Department of Civil and Environmental Engineering, University of Nevada, Reno, Nevada, Report No. CCEER-20-02, February 2020.

CCEER 20-03 Ozsahin, E. and Pekcan, G., "Torsional Ground Motion Effects on the Seismic Response of Continuous Box-girder Highway Bridges," Center for Civil Engineering Earthquake Research, Department of Civil and Environmental Engineering, University of Nevada, Reno, Nevada, Report No. CCEER-20-03, April 2020.

CCEER 20-04 Wu, S., Eckert, E., Huang, J., and McCallen, D., "Evaluation of the Domain Reduction Method Applied to Broad-Band, Near-Fault Earthquake Ground Motions with Inter-Code

Comparisons," Center for Civil Engineering Earthquake Research, Department of Civil and Environmental Engineering, University of Nevada, Reno, Nevada, Report No. CCEER-20-04, June 2020.

CCEER 20-05 Jones, J., Saiidi, M., and Itani, A. "Experimental and Analytical Studies of a Two-Span Bridge System with Precast Elements Incorporating Rebar Hinge and Socket Connections," Center for Civil Engineering Earthquake Research, Department of Civil and Environmental Engineering, University of Nevada, Reno, Nevada, Report No. CCEER-20-05, August 2020.

CCEER 20-06 Camarena, C., Saiidi, M., and Moustafa, M. "Development and Seismic Evaluation of Cast-in-Place Emulating ABC Pocket Connections and SMA Reinforced Two-Way Column Hinges," Center for Civil Engineering Earthquake Research, Department of Civil and Environmental Engineering, University of Nevada, Reno, Nevada, Report No. CCEER-20-06, August 2020.

Nevada Department of Transportation
Kristina L. Swallow, P.E. Director
Ken Chambers, Research Division Chief
(775) 888-7220
kchambers@dot.nv.gov
1263 South Stewart Street
Carson City, Nevada 89712